



Faculteit Wetenschappen
Departement Fysica
Theorie van Kwantumsystemen en Complexe Systemen

**Ground-state properties of nanoshells: orbital-based
calculations versus a new orbital-free method**

**Grondtoestandseigenschappen van nanoschillen:
orbitaalgebaseerde berekeningen versus een nieuwe
orbitaalvrije methode**

Proefschrift voorgelegd tot het behalen van de graad van
doctor in de Wetenschappen aan de Universiteit Antwerpen
te verdedigen door Katrijn Putteneers

Promotoren: Prof. dr. Fons Brosens
Prof. dr. Jacques Tempère

Antwerpen, november 2012

Juryleden

- Prof. dr. Fons Brosens - Universiteit Antwerpen (promotor)
- Prof. dr. Jacques Tempère - Universiteit Antwerpen (promotor)
- Prof. dr. Bart Partoens - Universiteit Antwerpen (voorzitter)
- Prof. dr. Paul Scheunders - Universiteit Antwerpen (secretaris)
- Prof. dr. Jozef Devreese - Universiteit Antwerpen (oprichter van TFVS - TQC)
- Prof. dr. Paul Koenraad - Technische Universiteit Eindhoven, Nederland
- Prof. dr. Peter Nordlander - Rice University, Texas, USA

Contents

Abbreviations and symbols	vii
Thesis objective and overview	xi
I Introduction	1
1 Basic concepts	5
2 Density-functional theory (DFT)	15
2.1 Origin: (extended) Thomas-Fermi model	16
2.1.1 The Thomas atom	16
2.1.2 Inclusion of exchange	17
2.2 The Hohenberg-Kohn theorems	18
2.3 Orbital-based DFT	19
2.4 Orbital-free DFT	21
3 Nanoshells	23
3.1 System and notations	23
3.2 Fabrication	24
3.3 Working principle	25
3.4 Some related structures	26
3.5 Existing methods to calculate nanoshell properties	27
3.5.1 Mie theory	27
3.5.2 Hybridization theory	31
3.5.3 (Time-dependent) Kohn-Sham calculations	33
3.5.4 Comparison of results	37
3.6 Applications	39
3.6.1 Biosensor	39
3.6.2 Cancer treatment	41
3.6.3 Photothermal drug delivery	41
3.6.4 Enhancement of the efficiency of semiconductor devices	41
3.6.5 Plasmonics	42
3.6.6 Gauge for high-pressure measurements	43
4 Conventions and approximations	57
II Aspects of orbital-based calculations	59
5 Bookkeeping and determination of the orbitals	63
5.1 Radial differential equation, wave functions and density	63

5.2	Orbital bookkeeping	64
5.2.1	Smallest amount of orbital calculations, much bookkeeping	66
5.2.2	More efficient bookkeeping	67
5.3	Orbital calculation: Transfer Matrix Method	69
5.3.1	Basics	69
5.3.2	Application to spherically symmetric system	70
5.3.3	Expressions for the piecewise radial solutions	72
5.3.4	Counting nodes - bracketing	77
5.3.5	Advantages over some other methods	79
6	Ideal Fermi gas in a spherically symmetric potential well	81
6.1	Calculation details	81
6.1.1	Infinite well	81
6.1.2	Finite well	84
6.2	Results	86
6.2.1	Comparison of used approaches	86
6.2.2	Infinite versus finite well	87
6.2.3	Fermi energy as function of shell thickness	90
6.3	Conclusion	93
III	Orbital-free calculations: a new method	95
7	Useful background	99
7.1	Sampling random variates according to a given distribution	99
7.1.1	Transformation method	100
7.1.2	Rejection method	101
7.2	Optimization inspired by simulated annealing	102
7.2.1	Simulated annealing - Metropolis acceptance	103
7.2.2	Threshold acceptance	105
7.2.3	Temperature-independent acceptance	105
7.3	Generating free diffusion with random numbers	105
7.3.1	Diffusion Monte Carlo	106
7.3.2	Bernoulli walk	107
8	Density-functional Monte Carlo (DFMC)	109
8.1	Basic procedure	109
8.1.1	Construction of a trial density distribution	109
8.1.2	Modification of the distribution	110
8.1.3	Acceptance/rejection of the new distribution	110
8.1.4	Stopping criterion	110
8.2	Determination of appropriate run parameters	111
8.2.1	Step one: Δx_α and N_w	111
8.2.2	Step two: the other parameters	112
8.3	Determination of the work function	112
8.3.1	Based on ionization energies	112
8.3.2	Based on the expression of Lang and Kohn	113

9	DFMC for nanoshells	115
9.1	Considered model and nanoshells	115
9.2	Expressions for the energy contributions	116
9.2.1	Kinetic energy	116
9.2.2	Exchange energy	116
9.2.3	Correlation energy	117
9.2.4	Hartree-energy	117
9.2.5	Energy functional	118
9.3	Calculation details	119
9.3.1	Mesh characteristics	119
9.3.2	Construction of a trial distribution	119
9.3.3	Modification of the distribution	119
9.3.4	Acceptance/rejection of the new distribution	119
9.3.5	Determination of run parameters for benchmark nanoshell	121
9.3.6	Overview of the run parameters for all systems	125
9.3.7	Work function based on ionization energies	125
9.4	Results	127
9.4.1	Benchmark nanoshell	127
9.4.2	Comparison with Kohn-Sham calculations	128
9.4.3	Influence of the permittivities	128
9.4.4	Investigation of the influence of the size	132
10	Conclusion	135
11	Positioning and outlook	137
	Summary and general conclusion	139
	Samenvatting en algemeen besluit	141
	List of publications	143
	Dankwoord	145
A	Regarding part II - Orbital-based calculations	147
A.1	Radial wave function in the free-of-charge region	147
A.1.1	Introduction	147
A.1.2	Solutions of the radial differential equation	147
A.1.3	Limiting behavior as $r \rightarrow \infty$	150
A.2	Implementation of the basis functions and their derivatives	151
A.2.1	(Modified) spherical Bessel functions	152
A.2.2	Whittaker function $\mathcal{W}_{\kappa,\mu}(x)$	154
B	Regarding part III - Orbital-free calculations	161
B.1	Hartree energy for spherically symmetric systems	161
B.1.1	Expression for $u_H(r)$ as a double integral	161
B.1.2	Expression for $u_H(r)$ as a sum of two single integrals	163
B.2	Difference in Hartree energy ΔE_H	164
B.2.1	Key formulas	164
B.2.2	Difference ΔE_H due to walker movement	166
B.2.3	Difference ΔE_H due to walker removal	167

Abbreviations and symbols

Abbreviation	Description
DAC	Diamond Anvil Cell
DFMC	Density-functional Monte Carlo
DFT	Density-functional theory
LDA	Local Density Approximation
LSPR	Localized Surface Plasmon Resonance
SPR	Surface Plasmon Resonance

Symbol	Description
Δx_α	Grid spacing in direction α
$E_C[n]$	Correlation energy functional
E_{GS}	Ground-state energy
E_{\min}	Minimum energy found in a number of Monte Carlo iterations
$E_H[n]$	Hartree energy functional
$E_v[n]$	Energy functional
$E_X[n]$	Exchange energy functional
$E_{XC}^{HK}[n]$	“Hohenberg-Kohn” exchange-correlation energy functional
$E_{XC}^{KS}[n]$	“Kohn-Sham” exchange-correlation energy functional
ϵ	(Effective) single-particle energy, possibly indexed with quantum numbers
ϵ_b	Background permittivity in Drude formula
ϵ_C	Permittivity of the core
ϵ_E	Permittivity of the environment
ϵ_k	Permittivity of layer k
ϵ_S	Permittivity of the shell
$i_\ell(x)$	Modified spherical Bessel function of the first kind
i_{lower}	Number of Monte Carlo iterations after which to decrease P_a
i_{stop}	Sufficient number of iterations in which E_{\min} has not changed so that a Monte Carlo run can be ended
$j_\ell(x)$	Spherical Bessel function of the first kind
$k_\ell(x)$	Modified spherical Bessel function of the third kind
ℓ	Angular momentum quantum number
$L_p^\beta(x)$	Associated Laguerre polynomial
μ	Chemical potential
\mathbf{n}	Radial quantum number
n_0	Density of the homogeneous neutralizing background
N	Number of conduction electrons
N_{average}	Number of run results of which the average is calculated

Symbol	Description
$n(\mathbf{r})$	Electron concentration, electron particle density
$n_{GS}(\mathbf{r})$	Ground-state electron concentration
N_w	Number of Bernoulli walkers
P_a	Acceptance probability
P_{\min}	Value of P_a considered to be negligible
Q	Chi-square probability Q -value
Q'	Total charge in the system divided by the permittivity in the environment, $Q' = Q_{\text{tot}}/\epsilon_E$
Q_{tot}	Total charge in the system
r_F	Lower bound of the “free-of-charge” region, the region outside the nanoshell where no charge is present
$\mathfrak{R}(r)$	Normalized radial (part of the) single-particle wave function
$R(r)$	Unnormalized radial single-particle wave function
R_C	Radius of a nanoshell core
r_O	Outer radius of the region of constant potential energy in the core
R_S	Overall radius of a nanoshell
r_s	Wigner-Seitz radius
$\rho_b(\mathbf{r})$	Background charge density
$\rho_{exc}(\mathbf{r})$	Excess charge density, background charge density plus electron charge density
$T[n]$	Kinetic energy functional
$T_s[n]$	Kinetic energy functional for non-interacting electrons with density n
$U[n]$	Coulomb energy functional
$u_1(j, \epsilon, r_j)$	First piecewise basis function in interval j
$u_2(j, \epsilon, r_j)$	Second piecewise basis function in interval j
$u_C(\mathbf{r})$	Single-particle correlation energy
$U_{\text{Coul}}[n]$	Direct (classical) Coulomb energy functional
$u_{\text{eff}}(\mathbf{r})$	Effective single-particle energy, $u_{\text{eff}}(\mathbf{r}) = u_H(\mathbf{r}) + u_{XC}(\mathbf{r})$
$u_H(\mathbf{r})$	Single-particle Hartree energy
$u_X(\mathbf{r})$	Single-particle exchange energy
$u_{XC}(\mathbf{r})$	Single-particle exchange-correlation energy
V	Volume
$v(\mathbf{r})$	Potential energy for electrons due to background and/or external potential
W	Work function
$W_{\text{ionization}}$	Work function calculated based on ionization energies
W_{LK}	Work function calculated based on expression of Lang and Kohn
$\mathcal{W}_{\kappa,\mu}(x)$	Whittaker function
$Y_{\ell,m}(\theta, \varphi)$	Spherical harmonics
$y_\ell(x)$	Spherical Bessel function of the second kind

Thesis objective and overview

In 1994 it became possible to fabricate core-shell spherical nanoparticles called nanoshells. Since then, much experimental and theoretical research on these structures has been performed. This research is inspired by a number of interesting applications of such particles, ranging from biosensors over cancer treatment to faster data transfer on a small scale. Although the dimensions of nanoshells are in the nanometer regime, often macroscopic theoretical descriptions are applied to these structures. On the other hand, there exist quantum-mechanical calculations in which effective single-particle Schrödinger equations are solved self-consistently. Even though in that work an efficient algorithm was developed based on finite difference numerical integration of the Schrödinger equations, it was only possible to describe nanoshells that have sizes smaller than what is experimentally achievable at present.

The objective of this thesis is to calculate the ground-state density and work function of SiO₂-Au nanoshells of manufacturable sizes, with an inner core of at least 40 nm and a minimum shell thickness of 15 nm.

In order to derive the work function we considered a model without external potential, in which the electrostatic interaction of the conduction electrons of the shell with a homogeneous neutralizing background and with each other leads to a potential that confines the electrons mainly to the shell.

The thesis contains three parts and ends with a summary and general conclusion. The first part is the **introduction**. It starts with an appetizer that contains some basic concepts of non-relativistic quantum mechanics. Then we explain the general theory and the system considered in this thesis: density-functional theory and nanoshells. We also discuss the application of nanoshells as high-pressure gauge which was investigated during this Ph.D. To end the introduction, we present some conventions and approximations that are used in the rest of the thesis. The introduction is followed by part two on a feasibility study of performing **orbital-based calculations** for the nanoshells of interest. We start with setting out the bookkeeping that is involved for the degenerate orbitals of a spherically symmetric system, and explain how these orbitals can be determined with the Transfer Matrix Method. We then apply this method to noninteracting fermions in a finite and infinite spherically symmetric potential well. From these calculations, it is obvious that solving self-consistent equations for manufacturable nanoshells is very demanding and quickly becomes impossible when the size of the nanoshells increases. In part three on **orbital-free calculations**, we first give some background that is useful for the “density-functional Monte Carlo” (DFMC) method that we developed. Subsequently, the method is explained. We then compare the results of DFMC for a small nanoshell with those of Kohn-Sham calculations and study the influence of the permittivities and the size on the effective potential energy and work function of manufacturable nanoshells. The part is ended with a conclusion of the calculations and a positioning and outlook of DFMC.

Research funded by a Ph.D. grant of the Agency for Innovation by Science and Technology, Flanders (IWT Vlaanderen)

Part I

Introduction

The introduction is meant to give enough background to be able to understand the main parts of the thesis on orbital-based and orbital-free calculations. We start with a chapter in which some *basic concepts* are briefly repeated to set the stage for a thesis involving non-relativistic quantum mechanics. Afterwards, the theory on which this thesis is based is explained: *density-functional theory*. We discuss the origin of this theory and two types of implementations that are used at present. This chapter is followed by a chapter on *nanoshells*. We explain what they are, how they are made, how they work and which methods have been used to theoretically describe their properties. We end the chapter with some interesting applications. At the end of the introduction, the *conventions and approximations* used in this thesis are set out.

In this introductory part, mainly existing background material from the literature is summarized, supplemented with an original contribution in section 3.6.6.

Chapter 1

Basic concepts

The purpose of this chapter is to bring into mind some basic concepts of non-relativistic quantum mechanics, to just give a flavor of some more advanced topics and to have some expressions at hand. More extensive information can be found in basic quantum mechanics books.

First things first: **first quantization**. For static systems consisting of atoms one seeks in this formalism the solution of the Schrödinger equation

$$\hat{H}\Psi_{ec}(\mathbf{r}_1, \dots, \mathbf{r}_{N_e}, \mathbf{R}_1, \dots, \mathbf{R}_{N_c}) = E\Psi_{ec}(\mathbf{r}_1, \dots, \mathbf{r}_{N_e}, \mathbf{R}_1, \dots, \mathbf{R}_{N_c}). \quad (1.1)$$

In this equation, $\Psi_{ec}(\mathbf{r}_1, \dots, \mathbf{r}_{N_e}, \mathbf{R}_1, \dots, \mathbf{R}_{N_c})$ denotes the many-particle wave function for the electrons and the atomic cores, E an energy eigenvalue of the system, $\{\mathbf{r}_1, \dots, \mathbf{r}_{N_e}\}$ the positions of the N_e electrons in the system and $\{\mathbf{R}_1, \dots, \mathbf{R}_{N_c}\}$ the positions of the N_c atomic cores. The Hamiltonian (operator) \hat{H} for an unperturbed system is given by

$$\begin{aligned} \hat{H} = & -\frac{\hbar^2}{2m_e} \sum_{i=1}^{N_e} \nabla_i^2 + \frac{1}{2} \sum_{\substack{i,j=1 \\ j \neq i}}^{N_e} \frac{e^2}{|\mathbf{r}_i - \mathbf{r}_j|} \\ & -\frac{\hbar^2}{2} \sum_{I=1}^{N_c} \frac{1}{M_I} \nabla_I^2 + \frac{1}{2} \sum_{\substack{I,J=1 \\ J \neq I}}^{N_c} \frac{Z_I Z_J e^2}{|\mathbf{R}_I - \mathbf{R}_J|} \\ & - \sum_{i=1}^{N_e} \sum_{I=1}^{N_c} \frac{Z_I e^2}{|\mathbf{r}_i - \mathbf{R}_I|} \end{aligned}$$

with \hbar Planck's constant h divided by 2π , m_e the electron mass, ∇_i the nabla operator working on particle i , e the electron charge, M_I the mass of the atomic cores and Z_I the atomic mass number of atomic core I . The first line in the right-hand side contains the contribution of the kinetic energy of the electrons and the Coulomb interaction between the electrons, the second line contains the same kind of energy contributions for the atomic cores and the last line contains the contribution due to the interaction between the electrons and the atomic cores. For most systems it is impossible to solve the many-particle Schrödinger equation (1.1) exactly and approximations are unavoidable.

The **Born-Oppenheimer approximation** [13] is a first approximation that is often used. In this approximation the atomic cores are considered to be immobile. Because the atomic core coordinates $\{\mathbf{R}_1, \dots, \mathbf{R}_{N_c}\}$ are fixed, the wave function can be factorized as $\Psi_{ec}(\mathbf{r}_1, \dots, \mathbf{r}_{N_e}, \mathbf{R}_1, \dots, \mathbf{R}_{N_c}) = \Psi_e(\mathbf{r}_1, \dots, \mathbf{r}_{N_e}) \Psi_c(\mathbf{R}_1, \dots, \mathbf{R}_{N_c})$ with $\Psi_e(\mathbf{r}_1, \dots, \mathbf{r}_{N_e})$ the electron wave function and $\Psi_c(\mathbf{R}_1, \dots, \mathbf{R}_{N_c})$ the wave function of the atomic cores. In this way the

Schrödinger equation for the electronic problem is given by (in atomic units)

$$\left(\underbrace{-\frac{1}{2} \sum_{i=1}^{N_e} \nabla_i^2}_{\hat{T}} + \underbrace{\frac{1}{2} \sum_{\substack{i,j=1 \\ j \neq i}}^{N_e} \frac{1}{|\mathbf{r}_i - \mathbf{r}_j|}}_{\hat{U}} + \sum_{i=1}^{N_e} v_c(\mathbf{r}_i) \right) \Psi_e(\mathbf{r}_1, \dots, \mathbf{r}_{N_e}) = E \Psi_e(\mathbf{r}_1, \dots, \mathbf{r}_{N_e}) \quad (1.2)$$

in which $v_c(\mathbf{r}_i)$ contains the influence of the cores on the electrons.

If the system under study is a metal and one is only interested in the distribution of the conduction electrons, one often considers the wave functions of the core electrons to be the same as in the unperturbed atom. The electron wave function can then be written as a product of a wave function of the conduction electrons and a wave function of the core electrons. It is said that the conduction electrons are moving in a *background* of metal ions. In what follows, we denote the number of conduction electrons by the symbol N , the wave function of the conduction electrons by $\Psi(\mathbf{r}_1, \dots, \mathbf{r}_N)$ and the potential energy due to the background and a possible external static perturbation by $v(\mathbf{r})$. Then the Schrödinger equation for the conduction electrons becomes

$$\left(-\frac{1}{2} \sum_{i=1}^N \nabla_i^2 + \frac{1}{2} \sum_{\substack{i,j=1 \\ j \neq i}}^N \frac{1}{|\mathbf{r}_i - \mathbf{r}_j|} + \sum_{i=1}^N v(\mathbf{r}_i) \right) \Psi(\mathbf{r}_1, \dots, \mathbf{r}_N) = E \Psi(\mathbf{r}_1, \dots, \mathbf{r}_N). \quad (1.3)$$

A further approximation that one can use is the uniform-background or **jellium model**. In this model the background charges are supposed to be uniformly and homogeneously spread with a constant density equal to $n_0 = 3/(4\pi r_s^3)$ with r_s the Wigner-Seitz radius. This model is used in the thesis.

In equations (1.2) and (1.3) we used (Hartree) **atomic units**, abbreviated as a.u. We will use this system of units throughout the thesis. In practice the use of these units comes down to the following: everywhere one might expect a factor \hbar , m_e , e or $4\pi\epsilon_0$ (with ϵ_0 the permittivity of vacuum), these factors will not be there. This is because the units of mass M , charge Q , angular momentum L and “electric constant” \mathfrak{E} are given by

$$\begin{aligned} [M] &= m_e \\ [Q] &= [I] [t] = e \\ [L] &= [E] [t] = \frac{[M][L^2]}{[t]} = \hbar \\ [\mathfrak{E}] &= \frac{[M][L^3]}{[t^2][Q^2]} = \frac{1}{4\pi\epsilon_0} \end{aligned}$$

in which I denotes current, t denotes time, E denotes energy and the square brackets $[X]$ mean “unit of X ”. In this system of units, the units of length L and energy E are the Bohr radius a_B and the Hartree \mathbb{H} defined as

$$\begin{aligned} [L] &= a_B = \frac{4\pi\epsilon_0 \hbar^2}{m_e e^2} \\ [E] &= \mathbb{H} = \frac{m_e e^4}{\hbar^2} \left(\frac{1}{4\pi\epsilon_0} \right)^2. \end{aligned}$$

The following conversions between different length and energy units apply (SI stands for “système international”):

$$\begin{aligned} [L]_{\text{a.u.}} &= a_B \simeq 5.291772108 \times 10^{-11} [L]_{\text{SI}} \simeq 0.052918 \text{ nm} \\ [E]_{\text{a.u.}} &= \mathbb{H} \simeq 4.359744178 \times 10^{-18} [E]_{\text{SI}} \simeq 27.211 \text{ eV}. \end{aligned}$$

An important quantity in this thesis is the **electron (particle) density** $n(\mathbf{r})$ at position \mathbf{r} of the conduction electrons of a metal which is the number of particles per unit of volume such that $\int n(\mathbf{r}) d\mathbf{r} = N$.

Solving the many-particle electronic Schrödinger equation (1.2) or (1.3) can only be done exactly for very few systems, see e.g. Ref. [70] for an example. Therefore one has to resort to approximate methods. A picture that is of use for such methods is the picture of **non-interacting fermions**, also referred to as the ideal Fermi gas. In this picture, the Hamiltonian of equation (1.3) reduces to a sum of single-particle Hamiltonians \hat{H}_i :

$$\hat{H} = \sum_{i=1}^N \hat{H}_i = \sum_{i=1}^N \left(-\frac{1}{2} \nabla_i^2 + v(\mathbf{r}_i) \right). \quad (1.4)$$

For distinguishable particles, a wave function corresponding to the Hamiltonian (1.4) can be written as a product of single-particle wave functions. Fermions with the same spin are *indistinguishable* and subject to the Pauli exclusion principle: no two electrons with parallel spin can have the same spatial quantum numbers. It follows that the wave function $\Psi(\sigma; \mathbf{r}_{1\sigma}, \dots, \mathbf{r}_{N\sigma})$ for particles with the same spin σ has to be written as a Slater determinant of normalized single-particle *spin orbitals* $\psi_{\{q\}_k}(\sigma; \mathbf{r}_{j\sigma}) = \psi_{\{q\}_k}(\mathbf{r}_{j\sigma}) \sigma$ with a representation σ for the spin component, $\psi_{\{q\}_k}(\mathbf{r}_{j\sigma})$ single particle wave functions and $\{q\}_k$ a set of spatial quantum numbers (labeled with an index k for simplicity):

$$\Psi(\sigma; \mathbf{r}_{1\sigma}, \dots, \mathbf{r}_{N\sigma}) = \frac{1}{\sqrt{N_\sigma!}} \begin{vmatrix} \psi_{\{q\}_1}(\sigma; \mathbf{r}_{1\sigma}) & \psi_{\{q\}_2}(\sigma; \mathbf{r}_{1\sigma}) & \dots & \psi_{\{q\}_{N_\sigma}}(\sigma; \mathbf{r}_{1\sigma}) \\ \psi_{\{q\}_1}(\sigma; \mathbf{r}_{2\sigma}) & \psi_{\{q\}_2}(\sigma; \mathbf{r}_{2\sigma}) & \dots & \psi_{\{q\}_{N_\sigma}}(\sigma; \mathbf{r}_{2\sigma}) \\ \dots & \dots & \dots & \dots \\ \psi_{\{q\}_1}(\sigma; \mathbf{r}_{N_\sigma}) & \psi_{\{q\}_2}(\sigma; \mathbf{r}_{N_\sigma}) & \dots & \psi_{\{q\}_{N_\sigma}}(\sigma; \mathbf{r}_{N_\sigma}) \end{vmatrix}. \quad (1.5)$$

An experimental realization that is well described by the non-interacting many-body wave function (1.5) is the ultracold gas of spin polarized fermionic ^{40}K atoms in a magnetic trapping potential $v(\mathbf{r})$ [51]. For a system containing N_\uparrow particles with spin \uparrow , N_\downarrow particles with spin \downarrow and $N = N_\uparrow + N_\downarrow$, the wave function is then constructed as the product of the wave functions of the two spin components:

$$\Psi(\mathbf{r}_1, \dots, \mathbf{r}_N) = \Psi(\uparrow; \mathbf{r}_{1\uparrow}, \dots, \mathbf{r}_{N_\uparrow}) \Psi(\downarrow; \mathbf{r}_{1\downarrow}, \dots, \mathbf{r}_{N_\downarrow}). \quad (1.6)$$

Such wave function fulfills the Pauli exclusion principle. If two particles with the same spin would have the same spatial quantum numbers, then two columns of the Slaterdeterminant (1.5) would be identical and the determinant is equal to zero. As a consequence the wave function $\Psi(\sigma; \mathbf{r}_{1\sigma}, \dots, \mathbf{r}_{N_\sigma})$ would be zero and so would the total wave function (1.6): a system in which two particles with the same spin have the same spatial quantum numbers does not exist. A wave function that fulfills the Pauli exclusion principle is anti-symmetric under the exchange of particles with the same spin:

$$\Psi(\sigma; \mathbf{r}_{1\sigma}, \dots, \mathbf{r}_{i\sigma}, \dots, \mathbf{r}_{j\sigma}, \dots, \mathbf{r}_{N_\sigma}) = -\Psi(\sigma; \mathbf{r}_{1\sigma}, \dots, \mathbf{r}_{j\sigma}, \dots, \mathbf{r}_{i\sigma}, \dots, \mathbf{r}_{N_\sigma}). \quad (1.7)$$

The single-particle wave functions $\psi_{\{q\}_k}(\mathbf{r})$ can be found by solving N single-particle Schrödinger equations

$$\left(-\frac{1}{2} \nabla^2 + v(\mathbf{r}) \right) \psi_{\{q\}_k}(\mathbf{r}) = \epsilon_{\{q\}_k} \psi_{\{q\}_k}(\mathbf{r})$$

where particles with the same spin must have a different set of spatial quantum numbers.

It is useful to note that for non-interacting fermions the many-particle density $n(\mathbf{r})$ can be calculated as

$$n(\mathbf{r}) = \sum_{p=1}^N \left| \psi_{\{\mathbf{q}\}_p}(\mathbf{r}) \right|^2$$

with $\{\mathbf{q}\}_p = \{\{q\}_k, \uparrow\}$ or $\{\mathbf{q}\}_p = \{\{q\}_k, \downarrow\}$, and that the total energy is equal to

$$E = \sum_{p=1}^N \epsilon_{\{\mathbf{q}\}_p}. \quad (1.8)$$

At zero temperature and for fermionic particles, the lowest energy orbitals are subsequently filled by the number of particles up to a highest energy level called the *Fermi energy* ϵ_F . For systems at zero temperature and with spin balance the density and energy are equal to

$$\begin{aligned} n(\mathbf{r}) &= \sum_{p=1}^N \left| \psi_{\{\mathbf{q}\}_p}(\mathbf{r}) \right|^2 = 2 \sum_{k=1}^{N/2} \left| \psi_{\{q\}_k}(\mathbf{r}) \right|^2 \\ E &= \sum_{p=1}^N \epsilon_{\{\mathbf{q}\}_p} = 2 \sum_{k=1}^{N/2} \epsilon_{\{q\}_k}. \end{aligned}$$

We now briefly discuss some problems that are treated in basic quantum-mechanics courses in the framework of non-interacting particles and to which we will refer in the thesis. The first one is the one-dimensional **infinite square well** for which

$$v(\mathbf{r}) = v(x) = \begin{cases} 0 & 0 < x < a \\ \infty & \text{elsewhere} \end{cases}.$$

The boundary conditions for the single-particle wave functions are $\psi(x=0) = \psi(x=a) = 0$. The single-particle wave-functions and energies are given by

$$\begin{aligned} \psi_k(x) &= \sqrt{\frac{2}{a}} \sin\left(k \frac{\pi}{a} x\right) \\ \epsilon_k &= \frac{1}{2} \left(\frac{\pi}{a}\right)^2 k^2 \end{aligned}$$

with $k \in \mathbb{N}_0$. The lowest-energy single-particle wave functions are visualized in figure 1.1. A related but somewhat more complicated problem is that of the one-dimensional **finite square well**. This problem is characterized by the external potential

$$v(\mathbf{r}) = v(x) = \begin{cases} U_I & x < 0 \\ 0 & 0 < x < a \\ U_{III} & a < x \end{cases}$$

with $0 < U_I < \infty$ and $0 < U_{III} < \infty$. For particles that are bound to the well, the piecewise solutions in each region that lead to an integrable wave function are given by

$$\begin{aligned} \psi_I(x < 0) &= A \exp\left(\sqrt{2(U_I - \epsilon)}x\right) \\ \psi_{II}(0 < x < a) &= C \sin\left(\sqrt{2\epsilon}x\right) + D \cos\left(\sqrt{2\epsilon}x\right) \\ \psi_{III}(a < x) &= F \exp\left(-\sqrt{2(U_{III} - \epsilon)}x\right). \end{aligned}$$

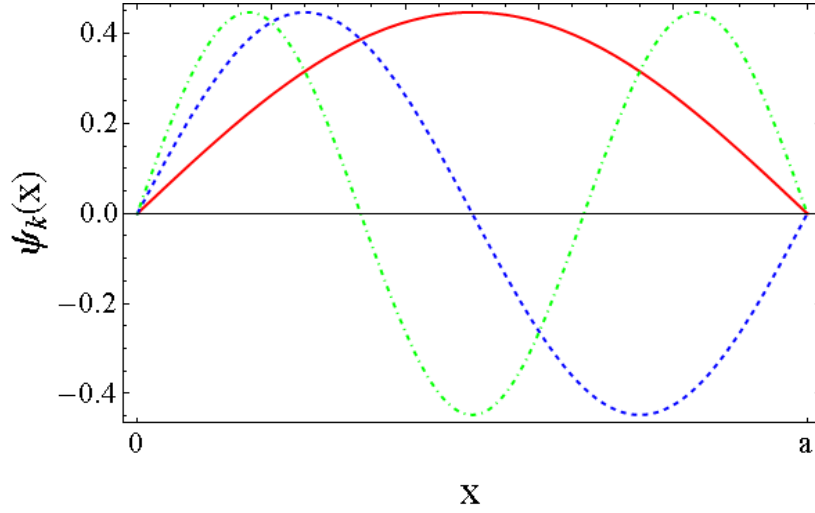


Figure 1.1: Single-particle wave functions $\psi_k(x)$ in a one-dimensional infinite potential well between $x = 0$ and $x = a$ corresponding to $k = 1$ (red solid line), $k = 2$ (blue dashed line) and $k = 3$ (green dash-dotted line).

The wave function and its derivative should be continuous everywhere. This leads to conditions from which the single-particle energies ϵ can be derived. It turns out that the energy levels are somewhat lower than the energy levels of an infinite square well with the same width. The wave functions are very similar to those of the infinite well, except that they are not zero at the well boundaries but that they show an exponential decay outside the well.

The last example we discuss is that of the **hydrogen-like atom**. The external potential in this problem is spherically symmetric:

$$v(\mathbf{r}) = v(r) = -\frac{Z}{r}.$$

For this spherically symmetric system one writes the single-particle wave functions as a product of a radial component and two angular components: $\psi(\mathbf{r}) = \mathfrak{R}(r) \Theta(\theta) \Phi(\varphi)$ with $r \in [0, \infty[$, $\theta \in [0, \pi[$, $\varphi \in [0, 2\pi[$. The angular part is described by spherical harmonics $Y_{\ell,m}(\theta, \varphi)$ with the angular quantum number $\ell \in \mathbb{N}$ and magnetic quantum number m for which $m = -\ell, \dots, \ell$. The differential equation for the radial part is then given by

$$\frac{d^2 \mathfrak{R}(r)}{dr^2} + \frac{2}{r} \frac{d\mathfrak{R}(r)}{dr} + \left[2 \left(\epsilon + \frac{Z}{r} \right) - \frac{\ell(\ell+1)}{r^2} \right] \mathfrak{R}(r) = 0.$$

The energy levels and the normalized radial single-particle wave functions of this problem are

$$\epsilon_{\mathbf{n}} = -\frac{Z^2}{2\mathbf{n}^2}$$

$$\mathfrak{R}_{\mathbf{n},\ell}(r) = \sqrt{\left(\frac{2Z}{\mathbf{n}}\right)^3 \frac{(\mathbf{n}-\ell-1)!}{2\mathbf{n}(\mathbf{n}+\ell)!}} \left(\frac{2Zr}{\mathbf{n}}\right)^\ell e^{-\frac{Zr}{\mathbf{n}}} L_{\mathbf{n}-\ell-1}^{(2\ell+1)}\left(\frac{2Zr}{\mathbf{n}}\right)$$

with $\mathbf{n} \in \mathbb{N}_0$ and $L_p^{(\beta)}(x)$ an associated Laguerre polynomial. The boundary conditions lead to the restriction $\ell \leq \mathbf{n} - 1$.

Before discussing some methods to treat the system of interacting particles approximately, we address a physical principle and two mathematical tools that were used to derive these methods.

The physical principle is the **variational principle** of quantum mechanics. It concerns the energy, or expectation value of the Hamiltonian, in a state described by the wave function $\Psi(\mathbf{r}_1, \dots, \mathbf{r}_N)$. The variational energy is defined as

$$E[\Psi] \equiv \langle \hat{H} \rangle \equiv \frac{\int \dots \int \Psi^*(\mathbf{r}_1, \dots, \mathbf{r}_N) \hat{H} \Psi(\mathbf{r}_1, \dots, \mathbf{r}_N) d\mathbf{r}_1 \dots d\mathbf{r}_N}{\int \dots \int \Psi^*(\mathbf{r}_1, \dots, \mathbf{r}_N) \Psi(\mathbf{r}_1, \dots, \mathbf{r}_N) d\mathbf{r}_1 \dots d\mathbf{r}_N} \quad (1.9)$$

with $\Psi^*(\mathbf{r}_1, \dots, \mathbf{r}_N)$ the complex conjugate of $\Psi(\mathbf{r}_1, \dots, \mathbf{r}_N)$ and where the integrals span the entire space. It turns out that the energy calculated from a guess $\Psi(\mathbf{r}_1, \dots, \mathbf{r}_N)$ for the ground-state wave function $\Psi_{GS}(\mathbf{r}_1, \dots, \mathbf{r}_N)$, is an upper bound to the true ground-state energy E_{GS} ,

$$E_{GS} \equiv E[\Psi_{GS}] \leq E[\Psi].$$

Stated differently: full minimization of $E[\Psi]$ with respect to the allowed N -electron wave functions will give the correct ground-state wave function $\Psi_{GS}(\mathbf{r}_1, \dots, \mathbf{r}_N)$ and energy E_{GS} :

$$E_{GS} = \min_{\Psi(\mathbf{r}_1, \dots, \mathbf{r}_N)} E[\Psi]. \quad (1.10)$$

The quantity $E[\Psi]$ to be minimized is not a function but a **functional**, which simply stated is a function of which the argument is a function (indicated between square brackets []). The derivative of such functional with respect to its argument is called functional derivative and is denoted as $\delta F[f] / \delta f(\mathbf{r})$. A rule that is used in the thesis is that if $F[f] = \int g(f(\mathbf{r})) d\mathbf{r}$ with $g(f(\mathbf{r}))$ containing no derivatives of $f(\mathbf{r})$, then

$$\frac{\delta F[f]}{\delta f(\mathbf{r})} = \left. \frac{\partial g(f)}{\partial f} \right|_{f=f(\mathbf{r})}.$$

For example if $F[f] = 3 \int [f(\mathbf{r})]^{4/3} d\mathbf{r}$, then $\delta F[f] / \delta f(\mathbf{r}) = 4 [f(\mathbf{r})]^{1/3}$.

Another mathematical tool is necessary because minimization will have to be performed under certain constraints. For such kind of “constrained minimization” one can use **Lagrange multipliers**. Say we want to minimize the function $f(x, y) = x + y$ but require that $\{x, y\}$ are points on the unit circle, so they are subject to the constraint $x^2 + y^2 = 1$ or $g(x, y) - 1 = x^2 + y^2 - 1 = 0$. This can be done by minimizing the auxiliary function

$$\Lambda(x, y, \lambda) = f(x, y) + \lambda [g(x, y) - 1] = x + y + \lambda (x^2 + y^2 - 1)$$

in which λ is the Lagrange multiplier. By equating the partial derivatives of $\Lambda(x, y, \lambda)$ to zero, we get a set of equations of which the solutions lead to the extrema of $f(x, y)$ that obey the required condition. We get

$$\begin{aligned} \frac{\partial \Lambda(x, y, \lambda)}{\partial x} &= 1 + 2\lambda x = 0 \\ \frac{\partial \Lambda(x, y, \lambda)}{\partial y} &= 1 + 2\lambda y = 0 \\ \frac{\partial \Lambda(x, y, \lambda)}{\partial \lambda} &= x^2 + y^2 - 1 = 0. \end{aligned}$$

From these equations it follows that $(x, y) = (-1/\sqrt{2}, -1/\sqrt{2})$ is the point on the unit sphere that gives a minimum value of $f(x, y)$. This is how Lagrange multipliers work for functions. One can require more constraints, and each constraint results in another Lagrange multiplier. The tool can also be used for extremizing functionals.

We now turn to the problem of **interacting electrons**.

A first approximation in order to deal with interacting particles was proposed by Hartree [39]. In the Hartree approximation, the many-particle wave function is written as a product of normalized single-particle wave functions

$$\Psi(\mathbf{r}_1, \dots, \mathbf{r}_N) = \psi_{\{\mathbf{q}\}_1}(\mathbf{r}_1) \dots \psi_{\{\mathbf{q}\}_N}(\mathbf{r}_N). \quad (1.11)$$

With \hat{H} given as in equation (1.3), application of the variational principle (1.10) of quantum mechanics to minimize $E[\Psi]$ under the constraint that the many-particle wave function has the form (1.11), leads to the so-called **Hartree equations**

$$\left(-\frac{1}{2}\nabla^2 + v(\mathbf{r}) + \sum_{\substack{p'=1 \\ p' \neq p}}^N \int \frac{\psi_{\{\mathbf{q}\}_{p'}}^*(\mathbf{r}') \psi_{\{\mathbf{q}\}_{p'}}(\mathbf{r}')}{|\mathbf{r} - \mathbf{r}'|} d\mathbf{r}' \right) \psi_{\{\mathbf{q}\}_p}(\mathbf{r}) = \epsilon_{\{\mathbf{q}\}_p} \psi_{\{\mathbf{q}\}_p}(\mathbf{r}). \quad (1.12)$$

In these effective single-particle equations, an electron is considered to move in a potential determined by the classical “mean field” Coulomb potential created by the other electrons (the third term between brackets). Because via this potential the wave function and energy of the considered electron depend on the wave functions of the other electrons, Hartree proposed to solve the equations **self-consistently**. This means that one solves equations (1.12) in subsequent iterations with in each iteration i the effective potential calculated from the wave functions in step $i - 1$:

$$\left(-\frac{1}{2}\nabla^2 + v(\mathbf{r}) + \sum_{\substack{p'=1 \\ p' \neq p}}^N \int \frac{[\psi_{\{\mathbf{q}\}_{p'}}^*(\mathbf{r}')]^{i-1} \psi_{\{\mathbf{q}\}_{p'}}^{i-1}(\mathbf{r}')}{|\mathbf{r} - \mathbf{r}'|} d\mathbf{r}' \right) \psi_{\{\mathbf{q}\}_p}^{(i)}(\mathbf{r}) = \epsilon_{\{\mathbf{q}\}_p}^{(i)} \psi_{\{\mathbf{q}\}_p}^{(i)}(\mathbf{r}).$$

These iterations are performed until all the wave functions converge to a solution. Under the assumption that the many-particle wave function can be factorized as (1.11), the density can be calculated as in the case of non-interacting particles:

$$n(\mathbf{r}) = \sum_{p=1}^N \left| \psi_{\{\mathbf{q}\}_p}(\mathbf{r}) \right|^2.$$

The wave function proposed by Hartree does not fulfill the anti-symmetric condition (1.7) of a fermionic wave function. Therefore a more correct result will be found if, instead of a wave function of the form (1.11), a wave function of the form (1.6) is assumed in the minimization of the energy $E[\Psi]$. This leads to the **Hartree-Fock equations** [33] which for systems with spin balance take the form

$$\left[\begin{array}{l} \left(-\frac{1}{2}\nabla^2 + v(\mathbf{r}) + \sum_{\substack{\sigma' \\ \{k', \sigma'\} \neq \{k, \sigma\}}} \sum_{k'=1}^{N/2} \int \frac{\psi_{\{q\}_{k'}}^*(\sigma'; \mathbf{r}') \psi_{\{q\}_{k'}}(\sigma'; \mathbf{r}')}{|\mathbf{r} - \mathbf{r}'|} d\mathbf{r}' \right) \psi_{\{q\}_k}(\sigma; \mathbf{r}) \\ - \left(\sum_{\substack{k'=1 \\ k' \neq k}}^{N/2} \int \frac{\psi_{\{q\}_{k'}}^*(\sigma; \mathbf{r}') \psi_{\{q\}_k}(\sigma; \mathbf{r}')}{|\mathbf{r} - \mathbf{r}'|} d\mathbf{r}' \right) \psi_{\{q\}_{k'}}(\sigma; \mathbf{r}) \end{array} \right] = \epsilon_{\{q\}_k} \psi_{\{q\}_k}(\sigma; \mathbf{r}).$$

In comparison with the Hartree equations (1.12) an extra term has appeared. This extra term is called the **exchange** contribution. It lowers the energy with respect to the energy found within the Hartree approximation. The exchange effect consists in a weakening of the effect of the classical Coulomb repulsion due to the fact that electrons with parallel spin are not allowed to occupy the same space. As in the cases of the non-interacting particles and the Hartree approximation, the density is calculated from

$$n(\mathbf{r}) = \sum_{p=1}^N \left| \psi_{\{\mathbf{q}\}_p}(\mathbf{r}) \right|^2.$$

Although the Hartree-Fock approximation is an improvement over the Hartree approximation, it still is an approximation. The exact wave function of a system of many interacting particles is often not a single determinant or a simple combination of a few determinants. The error that is made in using an approximate ansatz for solving the many-particle problem is called **correlation**. We note that “the” correlation correction does not exist because the correction depends on which approximation is made. So the difference $E_C^{(HF)}$ between the exact energy E and the Hartree-Fock energy E_{HF} ,

$$E_C^{(HF)} \equiv E - E_{HF},$$

is the correlation energy associated with the Hartree-Fock approximation. We will encounter another “type” of correlation energy below.

A small remark on the factors $\epsilon_{\{q\}_k}$ in the Hartree(-Fock) equations is in place. They are not single-particle energy levels. The only “meaning” that can really be assigned to them, is that they are the Lagrange multipliers - with the dimensions of an energy - used in the minimization of the energy functional to assure that the orbitals are normalized.

Before we go to the last topic of this chapter on basic concepts, we want to introduce a generalization of the formulation used above. The wave function $\Psi(\mathbf{r}_1, \dots, \mathbf{r}_N)$ which was introduced earlier is actually the representation of a general **state** $|\Psi\rangle$ in the basis of the spatial coordinates $|\mathbf{r}_1 \dots \mathbf{r}_N\rangle$, denoted as

$$\Psi(\mathbf{r}_1, \dots, \mathbf{r}_N) = \langle \mathbf{r}_1 \dots \mathbf{r}_N | \Psi \rangle.$$

The notation $|\Psi\rangle$ is called ket and the notation $\langle \Psi|$ is called bra. The inner product between two states is given in position representation by

$$\langle \Phi | \Psi \rangle = \int \dots \int \Phi^*(\mathbf{r}_1, \dots, \mathbf{r}_N) \Psi(\mathbf{r}_1, \dots, \mathbf{r}_N) d\mathbf{r}_1 \dots d\mathbf{r}_N.$$

An operator \hat{A} transforms a ket into another ket, $\hat{A}|\Psi\rangle = |\Psi'\rangle$, and its adjoint \hat{A}^\dagger transforms the corresponding bra: $\langle \Psi | \hat{A}^\dagger = \langle \Psi' |$. For operators corresponding to observables, $\hat{A} = \hat{A}^\dagger$. In position representation we write the expectation value of operator \hat{A} as

$$\langle \Phi | \hat{A} | \Psi \rangle = \int \dots \int \Phi^*(\mathbf{r}_1, \dots, \mathbf{r}_N) \hat{A} \Psi(\mathbf{r}_1, \dots, \mathbf{r}_N) d\mathbf{r}_1 \dots d\mathbf{r}_N.$$

In this notation the energy of a system in a certain state, expression (1.9), can be written as

$$E[\Psi] \equiv \frac{\langle \Psi | \hat{H} | \Psi \rangle}{\langle \Psi | \Psi \rangle}.$$

As a last topic of this chapter we want to address briefly the concept of **second quantization**. In this formalism, the description of states is not limited to a space with a fixed number of particles. Particles can be created and annihilated (destroyed). Operators that transform a state with a certain number of particles into a state with another number of particles, are called creation and annihilation operators. There are two types. The first type is discrete and is denoted by $\hat{a}_{\mathbf{k}}^\dagger$ and $\hat{a}_{\mathbf{k}}$ which create, respectively destroy, a particle characterized by the set of quantum numbers \mathbf{k} . The second type are the field operators $\hat{\psi}_\sigma^\dagger(\mathbf{r})$ and $\hat{\psi}_\sigma(\mathbf{r})$ which create or annihilate a particle at position \mathbf{r} with spin σ . For some of these operators it matters in which sequence they are applied to a state. This is for fermions indicated by the anti-commutation relations. The anti-commutator $\{\hat{A}, \hat{B}\}$ of two operators \hat{A} and \hat{B} is given by

$$\{\hat{A}, \hat{B}\} = \hat{A}\hat{B} + \hat{A}\hat{B}.$$

For the fermionic field operators the following anti-commutation relations hold:

$$\begin{aligned} \{\hat{\psi}_\sigma^\dagger(\mathbf{r}), \hat{\psi}_{\sigma'}^\dagger(\mathbf{r}')\} &= 0 \\ \{\hat{\psi}_\sigma(\mathbf{r}), \hat{\psi}_{\sigma'}(\mathbf{r}')\} &= 0 \\ \{\hat{\psi}_\sigma(\mathbf{r}), \hat{\psi}_{\sigma'}^\dagger(\mathbf{r}')\} &= \delta(\mathbf{r} - \mathbf{r}') \delta_{\sigma, \sigma'}. \end{aligned}$$

One can derive that the particle density can be written as

$$n(\mathbf{r}) = \sum_{\sigma} \langle \Psi | \hat{\psi}_\sigma^\dagger(\mathbf{r}) \hat{\psi}_\sigma(\mathbf{r}) | \Psi \rangle, \quad (1.13)$$

and that the Hamiltonian of (1.2) in second quantization with field operators looks like

$$\begin{aligned} \hat{H} &= -\frac{1}{2} \sum_{\sigma} \int \hat{\psi}_\sigma^\dagger(\mathbf{r}) \nabla^2 \hat{\psi}_\sigma(\mathbf{r}) d\mathbf{r} + \frac{1}{2} \sum_{\sigma, \sigma'} \int \frac{\hat{\psi}_\sigma^\dagger(\mathbf{r}) \hat{\psi}_{\sigma'}^\dagger(\mathbf{r}') \hat{\psi}_{\sigma'}(\mathbf{r}') \hat{\psi}_\sigma(\mathbf{r})}{|\mathbf{r} - \mathbf{r}'|} d\mathbf{r} d\mathbf{r}' \\ &+ \sum_{\sigma} \int v(\mathbf{r}) \hat{\psi}_\sigma^\dagger(\mathbf{r}) \hat{\psi}_\sigma(\mathbf{r}) d\mathbf{r}. \end{aligned}$$

The expression of the Hamiltonian that is used in the paper of Hohenberg and Kohn on density-functional theory [44], is found by performing partial integration to the first term and using the fact that there are no currents at the boundary of a system in the ground state.

Chapter 2

Density-functional theory (DFT)

In the previous chapter we have seen that a non-relativistic static quantum-mechanical system containing N conduction electrons can approximately be described by the time-independent Schrödinger equation (1.3). The solution of this equation is given by the many-particle wave function $\Psi(\mathbf{r}_1, \dots, \mathbf{r}_N)$, dependent on $3N$ variables, and the energy eigenvalues of the system. For the ground-state energy the variational principle (1.10) is valid. Because the many-particle Schrödinger equation is for most systems not exactly solvable, this variational principle was used to derive approximate self-consistent equations.

This wave-function formalism originated really at the beginning of the development of quantum mechanics. But already one year after the paper of Schrödinger in 1926, Thomas [123] and Fermi [32] developed a model in which not the many-particle wave function was used as the basic quantity, but the particle density $n(\mathbf{r})$. Using the density instead of the wave function as central variable has the advantage that $n(\mathbf{r})$ is dependent on 3 variables instead of $3N$. Thomas and Fermi did not prove that the particle density could be considered at the same footing as the many-particle wave function. Because of the lack of proof and because the results of the model were not that good as those of wave function calculations, the idea of using the density as basic variable moved to the background.

This changed in 1964 with the paper of Hohenberg and Kohn [44]. In this paper, it was proven that the density $n(\mathbf{r})$ determines implicitly all properties derivable from the many-particle Hamiltonian by solving the Schrödinger equation for the ground state. In this way, the ground-state energy could be written as a functional of the density. Moreover a variational principle for the ground-state energy functional with respect to $n(\mathbf{r})$ was derived. This work was considered to be so important that it was attributed a Nobel Prize in 1998 [62]. With the theorems of Hohenberg and Kohn, it was accomplished that considering the density as basic variable was not just a model anymore, it had become a theory: the density-functional theory (DFT). One year later, Kohn and Sham [60] used the density-functional variational principle to derive self-consistent equations that are similar to the Hartree or Hartree-Fock equations, but in which both exchange and correlation effects can be included. This type of implementation of DFT is called orbital-based DFT, as opposed to orbital-free DFT in which extensions of the Thomas-Fermi theory are used which are entirely based on the density.

In the rest of this chapter, we will give some more explanation on the original model, the theorems of Hohenberg and Kohn and the two implementation types of DFT that exist to date and that are widely applied in chemistry and physics [62, 92]. The text is based mainly on the original articles and on Ref. [89].

2.1 Origin: (extended) Thomas-Fermi model

2.1.1 The Thomas atom

The story of density-functional theory actually begins with the papers of Thomas [123] and Fermi [32]. Thomas wanted to find a way to calculate the effective electric field in atoms from purely theoretical considerations, without fitting to data. He developed a method that leads to approximate fields and that can only be used for heavy atoms (with a high electron density). To derive an equation he used the following assumptions:

1. Relativistic corrections can be neglected.
2. In the atom there is an effective field given by the potential $V(r)$ that is only dependent on the distance r from the core and that has the properties

$$\begin{aligned} V(r) &\rightarrow 0 \text{ if } r \rightarrow \infty \\ V(r)r &\rightarrow Q \text{ if } r \rightarrow 0 \end{aligned}$$

with Q the charge of the core.

3. The electrons are uniformly distributed in the six-dimensional phase space for the movement of the electron, i.e. they are distributed as $f(\mathbf{r}, \mathbf{p}) = f_0$, with two electrons per \hbar^3 of the six-dimensional volume. The part of phase space that contains electrons is limited to the part for which orbitals are closed (i.e. the orbitals are completely filled).
4. The potential $V(r)$ itself is determined by the core charge and the distribution of electrons.

Assumption 2 reflects in fact the limiting behavior of an atomic potential. In assumption 3 we recognize features of quantum mechanics being developed at that time: electrons with opposite spin can be in the same volume of phase space. The fourth assumption is actually that the potential is classical. This means that it can be defined from the Poisson equation $\Delta V(\mathbf{r}) = -4\pi\rho_{exc}(\mathbf{r})$ with $\rho_{exc}(\mathbf{r})$ the excess charge density which is the sum of the electron charge density $-n(\mathbf{r})$ and the background charge density $\rho_b(\mathbf{r})$, so $\rho_{exc}(\mathbf{r}) = \rho_b(\mathbf{r}) - n(\mathbf{r})$.

Under the assumptions 1 and 2 the Hamiltonian of the electron movement is given by

$$\hat{H} = \frac{\hat{p}^2}{2} - \hat{V}$$

with \hat{p} the momentum(operator) of the electron. Now Thomas used the following reasoning. An electron would escape from the atom if its energy is larger than or equal to $V(r \rightarrow \infty) = 0$. So for electrons that are part of the atom, one can determine an upper bound p_F for the momentum:

$$\frac{p_F^2(r)}{2} - V(r) = 0 \tag{2.1}$$

$$\begin{aligned} &\Downarrow \\ p_F(r) &= \sqrt{2V(r)}. \end{aligned} \tag{2.2}$$

Using assumption 3 one can find the following relation between \bar{p}_F and the density \bar{n} of a homogeneous electron gas:

$$\begin{aligned} \bar{n} &= (\text{density in phase space}) \times (\text{occupied part of phase space}) \\ &= \frac{2}{(2\pi)^3} \times \frac{4\pi}{3} \bar{p}_F^3 = \frac{1}{3\pi^2} \bar{p}_F^3. \end{aligned} \tag{2.3}$$

The next step is the most crucial one of the derivation. The relation (2.3) between the maximum momentum and density of a homogeneous electron gas is used *locally*, i.e. the electron density $n(r)$ in the atom is written as:

$$n(r) = \frac{1}{3\pi^2} p_F^3(r).$$

Combining this equation with the expression (2.2) for $p_F(r)$, we finally find a relation between $n(r)$ and $V(r)$:

$$n(r) = \frac{2}{(2\pi)^3} \frac{4\pi}{3} [2V(r)]^{3/2}.$$

The potential $V(r)$ and the density $n(r)$ can be derived by combining this equation with the Poisson equation.

For later use we note that with expression (2.3), the kinetic energy in equation (2.1) can be written as a function of the density. This results in the so-called Thomas-Fermi equation

$$\frac{1}{2} (3\pi^2)^{2/3} [n(r)]^{2/3} - V(r) = 0. \quad (2.4)$$

2.1.2 Inclusion of exchange

In the Thomas-Fermi model the potential energy was considered to be classical and for the kinetic energy the expression of a uniform electron gas was used locally. Some years later, Dirac [24] derived a way to include exchange in the Thomas-Fermi model. Like in the case of the kinetic energy, the expression of the Hartree-Fock exchange of the homogeneous electron gas was used locally. This led to the so-called Thomas-Fermi-Dirac equation

$$\frac{1}{2} (3\pi^2)^{2/3} [n(r)]^{2/3} - \left(\frac{3}{\pi}\right)^{1/3} [n(r)]^{1/3} - V(r) = 0$$

which has an extra term in comparison with the Thomas-Fermi equation (2.4) (a derivation of this term can also be found in e.g. Ref. [59]).

Dirac derived this term because he experienced in the early years of quantum theory that, as we said before, the solution of the many-particle Schrödinger equation is “far too complicated to be practical” and that the self-consistent effective single-particle equations were also “hardly practicable when one has to deal with very many electrons”. He already argued that the whole state of the atom is completely described simply by its (electric) density and that one thus can deal with any number of electrons by working with just one “matrix density function”. Apparently the argument of Dirac was not convincing enough, but that of Hohenberg and Kohn was. In the following section we will therefore discuss their theorems which really launched “density-functional theory”.

2.2 The Hohenberg-Kohn theorems

The formal justification of density-functional theory was originally given by two theorems proven by Hohenberg and Kohn [44, 62]. These theorems, which concern the ground state E_v of interacting particles in an external potential $v(\mathbf{r})$, can be formulated as follows:

1. The many-particle ground-state properties are uniquely determined by the particle density $n(\mathbf{r})$, at least for non-degenerate ground states and up to an arbitrary constant for $v(\mathbf{r})$. An important aspect of this theorem is that the ground-state energy E_v is a unique functional of $n(\mathbf{r})$:

$$E_v = E_v[n]. \quad (2.5)$$

2. The energy functional $E_v[n]$ has as its minimum value the correct ground-state energy E_{GS} associated with $v(\mathbf{r})$ if the number of particles $N[n] \equiv \int n(\mathbf{r}) d\mathbf{r}$ is kept constant:

$$E_{GS} \equiv E_v[n_{GS}] \stackrel{N[n]=N}{=} \min_{n(\mathbf{r})} E_v[n]. \quad (2.6)$$

The ground-state energy can be written as

$$E_v \equiv \langle \Psi | \hat{T} + \hat{V} + \hat{U} | \Psi \rangle = T[n] + V[n] + U[n].$$

In this expression, \hat{T} , \hat{V} and \hat{U} are the operators of the kinetic energy, the external potential energy and the electron interaction energy, and $T[n] \equiv \langle \Psi | \hat{T} | \Psi \rangle$, $V[n] \equiv \langle \Psi | \hat{V} | \Psi \rangle$ and $U[n] \equiv \langle \Psi | \hat{U} | \Psi \rangle$ are the corresponding functionals. Hohenberg and Kohn defined a “universal” functional $F[n(\mathbf{r})] \equiv \langle \Psi | \hat{T} + \hat{U} | \Psi \rangle = T[n] + U[n]$ which does not (formally) depend on the external potential $v(\mathbf{r})$. Then the energy functional can be written as

$$E_v[n] = \int v(\mathbf{r}) n(\mathbf{r}) d\mathbf{r} + F[n]. \quad (2.7)$$

If the universal functional $F[n]$ would be known exactly, then the exact ground-state electron density could be derived from equations (2.7) and (2.6). Unfortunately $F[n]$ is, to this date, only known approximately. For practical purposes one extracts from this functional the classical Coulomb interaction $U_{\text{Coul}}[n]$ so that

$$F[n] = U_{\text{Coul}}[n] + G[n] = \frac{1}{2} \int \int \frac{n(\mathbf{r}) n(\mathbf{r}')}{|\mathbf{r} - \mathbf{r}'|} d\mathbf{r} d\mathbf{r}' + G[n]$$

with $G[n]$ another universal functional that contains the kinetic energy and the non-classical part of the electron-electron interaction (exchange and correlation). Notice that $G[n]$ is for sure a functional of n because $F[n]$ is a functional of n from which we have extracted a part that is a functional of n . The energy functional (2.7) is then written as

$$E_v[n] = \int v(\mathbf{r}) n(\mathbf{r}) d\mathbf{r} + \frac{1}{2} \int \int \frac{n(\mathbf{r}) n(\mathbf{r}')}{|\mathbf{r} - \mathbf{r}'|} d\mathbf{r} d\mathbf{r}' + G[n] \quad (2.8)$$

with the universal functional $G[n]$ defined as

$$G[n] = T[n] + U[n] - U_{\text{Coul}}[n]. \quad (2.9)$$

2.3 Orbital-based DFT

This type of implementation of DFT is based on the self-consistent equations of Kohn and Sham [60]. There exist equations similar to the Hartree equations and equations similar to the Hartree-Fock equations. To see how self-consistent equations can be derived from the theorems of Hohenberg and Kohn, we follow the idea of the original paper which is somewhat more intuitive than the more rigorous derivation, which can be found in e.g. Ref. [89].

Kohn and Sham first proposed the following ansatz to the universal functional $G[n]$:

$$G[n] \equiv T_s[n] + E_{XC}^{(KS)}[n] \quad (2.10)$$

in which $T_s[n]$ is the kinetic energy of a system of non-interacting electrons with density n and $E_{XC}^{(KS)}[n]$ is, by the definition of Kohn and Sham¹, the exchange and correlation energy of an interacting system with density n . It follows from the theorems of Hohenberg and Kohn that for a system of non-interacting electrons, $T_s[n]$ is a unique functional of the density. For other systems it is an *assumption* that the universal functional $G[n]$ can be split up in terms to which the mentioned meaning can be attributed. With the ansatz (2.10), the energy functional is written as

$$E_v^{(KS)}[n] = T_s[n] + \int v(\mathbf{r}) n(\mathbf{r}) d\mathbf{r} + \frac{1}{2} \int \int \frac{n(\mathbf{r}) n(\mathbf{r}')}{|\mathbf{r} - \mathbf{r}'|} d\mathbf{r} d\mathbf{r}' + E_{XC}^{(KS)}[n]. \quad (2.11)$$

Under the assumption (2.10), Kohn and Sham derived two types of equations: Hartree-like and Hartree-Fock-like. We only discuss the first type because this is the one that is most often used.

To explain the idea of Kohn and Sham, we first consider the case of non-interacting particles. For this case the correct energy functional (2.5) and the Kohn-Sham energy functional (2.11) coincide. Constrained minimization of the energy functional, with a Lagrange multiplier λ to incorporate particle conservation, leads to the equation

$$\int \delta n(\mathbf{r}) \left[\frac{\delta T_s[n]}{\delta n(\mathbf{r})} + v(\mathbf{r}) - \lambda \right] d\mathbf{r} = 0. \quad (2.12)$$

Now we have seen in chapter 1 on basic concepts that the problem of non-interacting particles can be treated by solving N single-particle Schrödinger equations

$$\left(-\frac{1}{2} \nabla^2 + v(\mathbf{r}) \right) \psi_{\{q\}_k}(\mathbf{r}) = \epsilon_{\{q\}_k} \psi_{\{q\}_k}(\mathbf{r}) \quad (2.13)$$

from which the density can be calculated as

$$n(\mathbf{r}) = \sum_{p=1}^N \left| \psi_{\{\mathbf{q}\}_p}(\mathbf{r}) \right|^2$$

with $\{\mathbf{q}\}_p = \{\{q\}_k, \sigma\}$. In this case, the total kinetic energy can be calculated from the orbitals as follows. We have from equations (2.11) and (1.8) the equalities

$$\begin{aligned} E_v[n] &= T_s[n] + \int v(\mathbf{r}) n(\mathbf{r}) d\mathbf{r} \\ &= \sum_{p=1}^N \epsilon_{\{\mathbf{q}\}_p} = \sum_{p=1}^N \int \psi_{\{\mathbf{q}\}_p}^*(\mathbf{r}) \epsilon_{\{\mathbf{q}\}_p} \psi_{\{\mathbf{q}\}_p}(\mathbf{r}) d\mathbf{r} \\ &= -\frac{1}{2} \sum_{p=1}^N \int \psi_{\{\mathbf{q}\}_p}^*(\mathbf{r}) \nabla^2 \psi_{\{\mathbf{q}\}_p}(\mathbf{r}) d\mathbf{r} + \int v(\mathbf{r}) n(\mathbf{r}) d\mathbf{r} \end{aligned} \quad (2.14)$$

¹We attached the superscript (KS) to this part of the energy to indicate the difference with the correlation energy defined in the framework of the Hartree-Fock approximation.

so $T_s[n]$ can be calculated as:

$$T_s[n] = -\frac{1}{2} \sum_{p=1}^N \int \psi_{\{\mathbf{q}\}_p}^*(\mathbf{r}) \nabla^2 \psi_{\{\mathbf{q}\}_p}(\mathbf{r}) d\mathbf{r}.$$

In the case of interacting particles, constrained minimization of the Kohn-Sham energy functional (2.11) leads to the condition

$$\int \delta n(\mathbf{r}) \left[\frac{\delta T_s[n]}{\delta n(\mathbf{r})} + v(\mathbf{r}) + \int \frac{n(\mathbf{r}')}{|\mathbf{r} - \mathbf{r}'|} d\mathbf{r}' + u_{XC}(n) - \lambda \right] d\mathbf{r} = 0. \quad (2.15)$$

with $u_{XC}(n) = \delta E_{XC}^{(KS)}[n] / \delta n(\mathbf{r})$. Kohn and Sham saw an analogy between this equation and equation (2.12) for non-interacting particles. Using an *effective* potential energy

$$u_{\text{eff}}(\mathbf{r}) = v(\mathbf{r}) + \int \frac{n(\mathbf{r}')}{|\mathbf{r} - \mathbf{r}'|} d\mathbf{r}' + u_{XC}(\mathbf{r}), \quad (2.16)$$

the constrained minimization condition (2.15) for interacting particles is formally the same as the one for non-interacting particles (2.12):

$$\int \delta n(\mathbf{r}) \left[\frac{\delta T_s[n]}{\delta n(\mathbf{r})} + u_{\text{eff}}(\mathbf{r}) - \lambda \right] d\mathbf{r} = 0.$$

This led Kohn and Sham to propose that the problem of N interacting particles could be treated by solving self-consistently N *effective* single-particle Schrödinger equations of the form

$$\left[-\frac{1}{2} \nabla^2 + u_{\text{eff}}(\mathbf{r}) \right] \psi_{\{\mathbf{q}\}_k}(\mathbf{r}) = \epsilon_{\{\mathbf{q}\}_k} \psi_{\{\mathbf{q}\}_k}(\mathbf{r}) \quad (2.17)$$

with $u_{\text{eff}}(\mathbf{r})$ given by expression (2.16), and by calculating the density as for non-interacting particles:

$$n(\mathbf{r}) = \sum_{p=1}^N \left| \psi_{\{\mathbf{q}\}_p}(\mathbf{r}) \right|^2. \quad (2.18)$$

The energy minimization thus leads to Hartree-like equations in which the effective energy $u_{\text{eff}}(\mathbf{r})$ is dependent on the density (in the rigorous derivation the “eigenenergies” are again Lagrange multipliers used to fulfill the constraint that the “orbitals” are normalized). If we now calculate $T_s[n]$ from the orbitals as in expression (2.14) by integrating the Kohn-Sham equation (2.17), we find that the kinetic energy of the formally non-interacting particles can be calculated as

$$T_s^{(KS)}[n] = \sum_{p=1}^N \epsilon_{\{\mathbf{q}\}_p} - \int v(\mathbf{r}) n(\mathbf{r}) d\mathbf{r} - \int \int \frac{n(\mathbf{r}') n(\mathbf{r})}{|\mathbf{r} - \mathbf{r}'|} d\mathbf{r}' d\mathbf{r} - \int u_{XC}(\mathbf{r}) n(\mathbf{r}) d\mathbf{r}. \quad (2.19)$$

Combining expressions (2.11) and (2.19) we get the following expression for the total energy:

$$E^{(KS)} = \sum_{p=1}^N \epsilon_{\{\mathbf{q}\}_p} - \frac{1}{2} \int \int \frac{n(\mathbf{r}') n(\mathbf{r})}{|\mathbf{r} - \mathbf{r}'|} d\mathbf{r}' d\mathbf{r} + E_{XC}[n] - \int u_{XC}(\mathbf{r}) n(\mathbf{r}) d\mathbf{r}. \quad (2.20)$$

For the derivation given above, Kohn and Sham originally assumed an exchange-correlation energy of the form

$$E_{XC}[n] = \int n(\mathbf{r}) \epsilon_{XC}(n(\mathbf{r})) d\mathbf{r}. \quad (2.21)$$

We mention expression (2.21) because it is an approximation to the exchange-correlation energy that is often used, also in this thesis. It is called **Local Density Approximation (LDA)**. In this approximation, it is assumed that the exchange-correlation energy per particle $\epsilon_{XC}(\bar{n})$ of the homogeneous electron gas with density \bar{n} can be used locally, like is done with the kinetic energy in the Thomas-Fermi model and the exchange energy in the Thomas-Fermi-Dirac model. The approximation is supposed to give quite good results in two limiting cases: in the case the density is slowly varying and in the case the density is high. Kohn and Sham showed that in the first case, the energy (2.20) has errors of the order $|\nabla|^2$, or equivalently, of the order r_0^{-2} with r_0 the distance over which there is an appreciable change in density. They also showed that in this limit, the density is determined with a greater accuracy, of the order $|\nabla|^4$. In the limit of high density, the exchange-correlation energy is small in comparison with the kinetic energy and the inaccuracy in representing these energies becomes negligible.

The disadvantage of orbital-based calculations is that only a limited number of orbitals can be treated, so a limited number of particles or systems for which a large enough reduction by symmetry can be applied, e.g. in crystals where each periodic cell contains a sufficiently small number of particles or in spherically symmetric systems where the energy levels are degenerate. There exist some linearly scaled orbital-based DFT implementations (see e.g. references in Ref. [127]), but these are still complicated to implement and more computationally demanding than orbital-free DFT. Moreover, in these methods use is made of “orbital localization” which restricts the applicability to non-metallic systems for which the orbitals can be exponentially localized. For metallic systems that cannot be treated orbital-based, we thus have to rely on orbital-free DFT of which the existing implementation is explained in the next section.

2.4 Orbital-free DFT

From the theorems of Hohenberg and Kohn it follows that the particle density $n(\mathbf{r})$ can be considered as the basic quantity instead of the many-particle wave function $\Psi(\mathbf{r}, \mathbf{r}_2, \dots, \mathbf{r}_N)$. Based on these theorems, Kohn and Sham derived self-consistent effective single-particle equations. These equations have the advantage over the Hartree(-Fock) equations that in theory all quantum-mechanical many-particle effects can be included. But an attentive reader will have noticed that starting from a theory that is based on the particle density $n(\mathbf{r})$, a single-particle wave-function-like scheme was constructed. The Kohn-Sham formalism thus not remedies the drawback of the Hartree(-Fock) scheme that was mentioned by Dirac to be “hardly practicable when one has to deal with very many electrons”. Executing Kohn-Sham calculations is not feasible if the number of orbitals to be calculated becomes too large because in every iteration N differential equations have to be solved.

Today, there exist systems for which a rather large number of particles prevents a description based on Kohn-Sham calculations, but for which quantum-mechanical effects are large enough so that treating the systems classically would give erroneous results. Examples of such systems are nanoshells, stellar matter, quantum dots and other confined systems. For such systems one tries to calculate properties without making use of orbitals [43,96,112]. In standard² orbital-free DFT, one tries to solve as directly as possible the Euler equation

$$\left. \frac{\delta E_v[n]}{\delta n(\mathbf{r})} \right|_{N \text{ constant}} = \frac{\delta T[n]}{\delta n(\mathbf{r})} + v(\mathbf{r}) + \int \frac{n(\mathbf{r}')}{|\mathbf{r} - \mathbf{r}'|} d\mathbf{r}' + \frac{\delta E_{XC}^{(HK)}[n]}{\delta n(\mathbf{r})} = \mu. \quad (2.22)$$

that follows from the constrained minimization of the energy (2.8) where we have defined $E_{XC}^{(HK)}[n]$ as $E_{XC}^{(HK)}[n] \equiv U[n] - U_{\text{Coul}}[n]$. This equation is also referred to as the “Thomas-Fermi-Hohenberg-Kohn” equation. So in every iteration only one equation has to be solved.

²as opposed to the new orbital-free method we will propose in this thesis.

There are some drawbacks of this method. For the first one, we do not offer a solution with the new method proposed in this thesis. But our method offers a straightforward solution for the other issues for which before only quite artificial solutions were constructed. We will now discuss these issues briefly.

First of all, apart from rather well investigated expressions for $E_X[n]$ and $E_C[n]$ as needed in the Kohn-Sham scheme, a functional form of $T[n]$ is required. This is a topic of actual research [45, 93, 127] because up to date no functional has been found that reproduces all expected physical features like e.g. the shell structure in atoms.

Secondly, one needs a value for the Lagrange multiplier μ in eq. (2.22). This parameter is identified with the negative of the first ionization energy or with the chemical potential. If one does not know a value for this constant from experiment or other calculations, one has to do some more effort to incorporate the constraint, as is discussed in e.g. Ref. [127] on p. 158-160. Although a physical meaning might be attached to μ for the correct energy functional, it is not clear whether this meaning is justified when approximate functionals are used.

Another issue that arises in solving the Thomas-Fermi-Hohenberg-Kohn equation is that non-negativity of $n(\mathbf{r})$ is not guaranteed in general if $n(\mathbf{r})$ is used directly as the generalized coordinate in conventional optimization algorithms (see e.g. Refs. in Ref. [127]). One way in which this is bypassed is by using an artificial new variable $\varphi(\mathbf{r})$ for which $n(\mathbf{r}) = [\varphi(\mathbf{r})]^2$. Another way by which this issue is dealt with, is to set $n(\mathbf{r}) = 0$ wherever the density would become negative or complex.

Finally, if one manages to bypass all aforementioned problems, one is often left with a non-trivial differential, integral or integrodifferential equation to be solved if one wants to include a realistic external potential and quantum-mechanical many-particle effects.

Chapter 3

Nanoshells

3.1 System and notations

A nanoshell is a nanosize particle consisting of a dielectric core surrounded by a uniform conducting shell, as shown in figure 3.1. In this thesis, we will denote the radius of the core by R_C , the overall radius of the particle by R_S and the permittivity of the core, the shell and the environment by ε_C , ε_S and ε_E respectively.

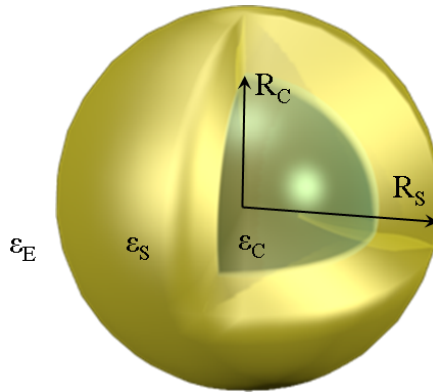


Figure 3.1: Visualization of a nanoshell. In the thesis the following notations will be used: R_C for the radius of the dielectric core, R_S for the outer radius of the metallic shell, and ε_C , ε_S and ε_E for the permittivity of the core, shell and environment respectively (figure of the nanoshell made by N. Van den Broeck).

We will investigate the influence of parameters such as permittivities and size on some properties of nanoshells, and we have therefore chosen a **benchmark nanoshell** for comparison. We considered a hollow nanoshell in vacuum, so $\varepsilon_C = \varepsilon_S = \varepsilon_E = 1$, with $R_C = 40$ nm and $R_S = 55$ nm. This nanoshell contains 2.5587435×10^7 conduction electrons. The sizes are the minimum sizes that can be achieved at the moment for nanoshells with a SiO_2 core and a golden shell [66]. SiO_2 -Au nanoshells of comparable dimensions are commercially available and are used in e.g. experiments on cancer treatment [82]. Figure 3.2 shows the relative magnitude of the benchmark nanoshell and the largest nanoshell that has been treated with Kohn-Sham calculations by Nordlander and Prodan [87].

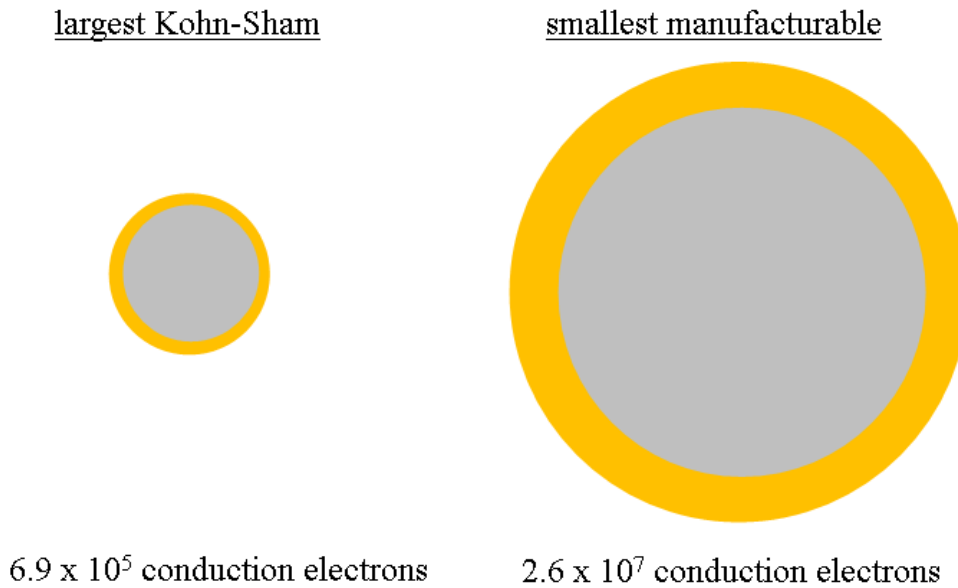


Figure 3.2: The relative magnitude of the smallest manufacturable nanoshell and the largest nanoshell that has been treated with Kohn-Sham calculations.

3.2 Fabrication

There exist nanoshells of different kinds of materials and each type of nanoshell has a distinct production process. In this section we explain briefly the fabrication of SiO_2 -Au nanoshells which are most relevant for the thesis. The basic steps in the fabrication of such nanoshells are visualized in figure 3.3 [88, 38, 53].

First a SiO_2 spherical nanoparticle is fabricated. This is done by the Stöber method [119]. With this method, one can fabricate particles that are quite uniform in size. The resulting core is amorphous [53].

Because both SiO_2 and gold are chemically quite inert, bifunctional molecules are attached to the core surface to enhance coverage of shell material.

To the functional surface, small gold colloid particles are bounded. Typically a surface coverage of approximately 25% is obtained.

The partially covered particle is then immersed in a electroless plating solution. The total amount of metal to be plated corresponds to the desired thickness of the shell. With this procedure, one can fabricate particles with a rather homogeneous distribution of the shell thickness.

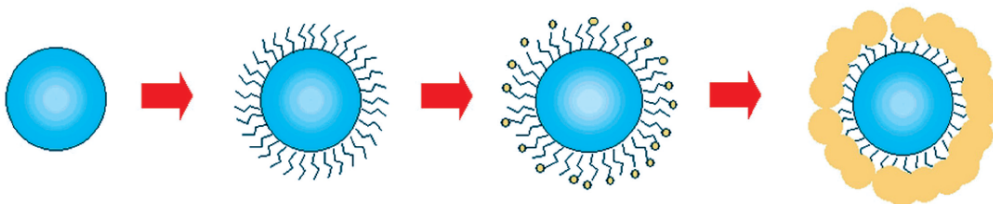


Figure 3.3: Basic steps in the fabrication of SiO_2 -Au nanoshells (figure taken from Ref. [38]).

3.3 Working principle

The interesting applications we will mention below are possible because of a phenomenon called **Localized Surface Plasmon Resonance (LSPR)** [53, 73].

When light is shone on a nanoshell, the conduction electrons of the shell will collectively oscillate. Hence the part “Plasmon” in the name: with a collective movement of electrons a kind of “quasiparticle” is associated, called a *plasmon*.

The inner part of the shell remains locally neutral, so the interesting physics takes place at the *surfaces* of the shell where charge excess is induced. For nanoshells that are small with respect to the wavelength of the light there will be a dipole distortion as shown in figure 3.4, for larger particles also higher order modes will be present.

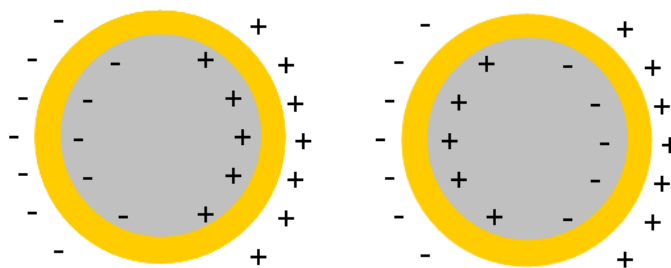


Figure 3.4: Possible surface excess charge densities induced in a nanoshell that is small with respect to the wavelength of the incident light.

At a certain frequency, the oscillation of the electrons becomes *resonant*, leading to enhanced absorption or scattering and a strongly enhanced near field in the immediate vicinity of the particle. This can be detected from e.g. the extinction spectrum which shows a peak at this frequency. As seen in figure 3.5, the resonance frequency can be tuned by changing the dimensions of the nanoshell. The tunability is more flexible than for solid metallic particles because of the interplay between the plasmons at the inner and outer surface of the shell. This tunability is important for applications in which one wants to have a resonance in a given part of the spectrum (e.g. near infrared for biomedical applications), or in which one wants to avoid response for certain wavelengths to exclude overlap with other signals. The resonance frequency not only depends on the dimensions of the nanoshell but also on the constituent materials, on the environment and on interaction with nearby nanoshells. For a fixed core/shell ratio, one can change the functional behavior of the nanoshell: in the small-particle or dipole limit, where the particle size is small with respect to the wavelength of the incident light, light will be absorbed at the resonance frequency. As the particle size is increased, light will become scattered at resonance [38]. This functional tunability is also important for applications, because it will depend on the application for which one wants to use a nanoshell whether absorption or scattering is desired or maybe unwanted. Nanoshells can be stored in a flask as seen in figure 3.6, with the color of the liquid dependent on which type of nanoshell is present¹.

There exists an analogous phenomenon in flat structures where the plasmons can travel along the surface. This is called “Surface Plasmon Resonance” (SPR). To make the distinction between this phenomenon and the mechanism we just described, where the electrons are *localized* on a nanoparticle, the word “Localized” was added to the term.

¹They have to be stored in the refrigerator, but not too close to a freezer compartment ...

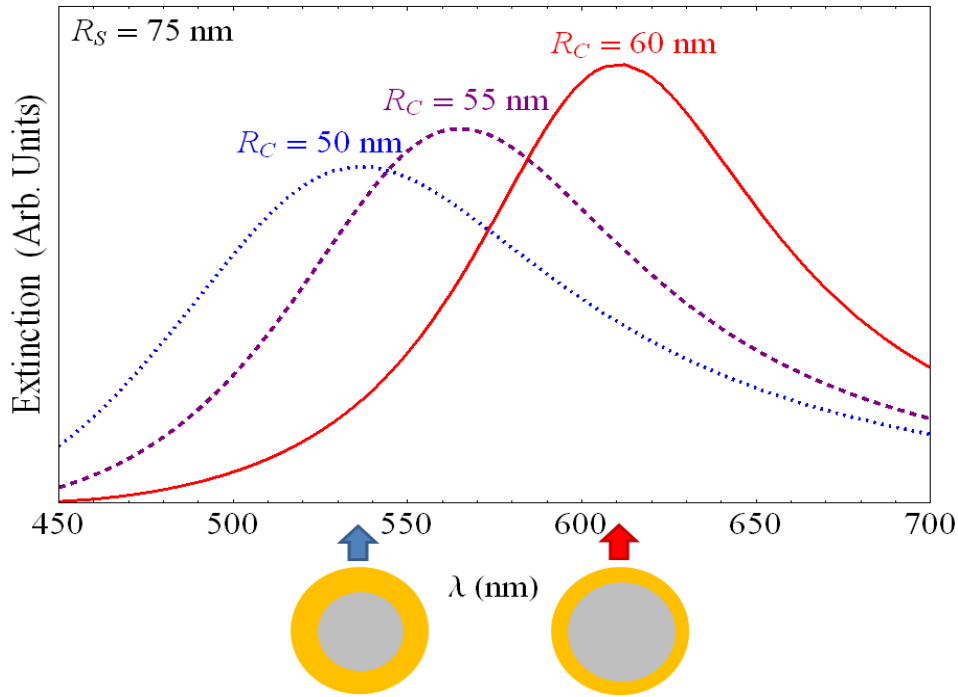


Figure 3.5: Optically most active dipole resonance of a SiO_2 -Au nanoshell for a fixed total radius of $R_S = 75$ nm and different core radii R_C ($R_C = 50$ nm, $R_C = 55$ nm and $R_C = 60$ nm). The spectrum is calculated using Mie theory (see section 3.5.1) with $\epsilon_C = 2.0449$ [111], $\epsilon_E = 1$ and for the frequency dependent dielectric function of the shell the Drude form $\epsilon(\omega) = \epsilon_b - \omega_p^2/\omega^2$ with ϵ_b a background contribution taken to be $\epsilon_b = 6.9$ [116] and ω_p the bulk plasmon frequency of gold.



Figure 3.6: Flasks containing nanoshells with different characteristics.

3.4 Some related structures

We have chosen to study SiO_2 -Au nanoshells because of their interesting (*in vivo*) biomedical applications, but there exist also other interesting structures of which the constituting materials or shape are such that the particles are most suited for a specific application. Not only the functionality (absorption or scattering, sharp edges for enhanced local fields or “hot spots”, ...) can be altered by considering different kinds of structures, also the resonance frequency differs among those structures, as is shown in figure 3.7. We mention some structures here to indicate that the field of LSPR offers many possibilities and it would be interesting to apply our new method also to these structures.

First of all, nanoshells themselves can be made of other materials than SiO_2 and gold. The first nanoshell that was fabricated had a Au_2S core and a golden shell [7]. Another metal that is used because it seems more appropriate for some applications, is silver. One can use other metals like e.g. copper which also has a resonance frequency close to the visible region of the spectrum [65]. Furthermore, combinations with semiconductors are possible [53].

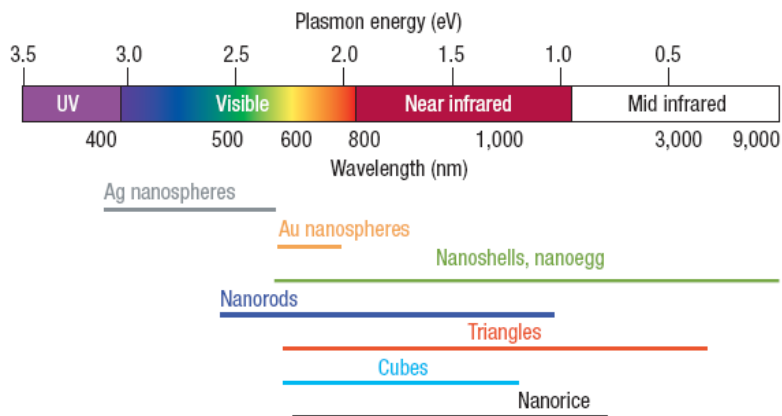


Figure 3.7: Region of possible resonance energies for a variety of particle morphologies (figure taken from Ref. [65]).

Advances in nanoparticle synthesis made it possible to fabricate other shapes of solid nanoparticles than spheres, like triangles, prisms, rods and cubes [65], and also nanorice, a prolate spheroidal particle invented at... Rice University [128].

As for core-shell nanoparticles, one can make multi-layered structures with alternating dielectric and conducting layers, called nanomatryushka after the Russian dolls. Another core-shell particle is a nanoegg: this is a nanoshell with an offset core [129].

Other interesting features emerge if nanoshells interact in e.g. dimers, trimers or quadrumers [129], or in monolayers [56]. For some applications the interaction of nanoparticles with a flat surface, e.g. a metallic film or an n-p junction, is of importance.

Because of their interesting features, also particles with a non-complete shell are studied, like nano-half-shells, nanocups, nanocaps and nanocrescents [135].

3.5 Existing methods to calculate nanoshell properties

Below in this thesis, also in the chapter on applications, we will refer to some existing methods to describe nanoshells theoretically. In this section, we will explain the basics of these methods and compare their results. The first two methods were used in the research on “nanoshells as high-pressure gauge” (see section 3.6.6), the third one is related to the orbital-based calculations in part II of this thesis.

3.5.1 Mie theory

Mie theory is used to solve the macroscopic Maxwell equations in systems with spherical symmetry. It was worked out for a homogeneous and isotropic sphere by Mie [79], an explanation with more modern notation is found in Ref. [121]. A nanoshell can be modeled as two concentric spheres. For this case the results originally derived by Mie for a single spherical interface were extended by Aden and Kerker [2]. Mie theory allows the calculation of the absorption, scattering and extinction cross section for an incident beam of radiation as a function of frequency. These quantities, of dimension $(\text{length})^2$, are defined as the ratio of the total scattered/absorbed/extincted energy per second to the energy flux of the incident wave. From the resulting cross section profile, the resonance frequencies can be determined numerically as the frequencies at which the cross section shows a maximum. For this method the input parameters are the sizes and permittivities of the particle layers.

The macroscopic Maxwell equations are

$$\begin{aligned}\nabla \cdot \mathbf{D}(\mathbf{r}, t) &= 4\pi\rho_{ext}(\mathbf{r}, t) \\ \nabla \cdot \mathbf{B}(\mathbf{r}, t) &= 0 \\ \nabla \times \mathbf{E}(\mathbf{r}, t) &= -\frac{1}{c} \frac{\partial \mathbf{B}(\mathbf{r}, t)}{\partial t} \\ \nabla \times \mathbf{H}(\mathbf{r}, t) &= \frac{1}{c} \frac{\partial \mathbf{D}(\mathbf{r}, t)}{\partial t} + \frac{4\pi}{c} \mathbf{J}_{ext}(\mathbf{r}, t)\end{aligned}$$

with c the speed of light and the following quantities that depend on position \mathbf{r} and time t : the electric and magnetic fields $\mathbf{E}(\mathbf{r}, t)$ and $\mathbf{H}(\mathbf{r}, t)$, the displacement vector $\mathbf{D}(\mathbf{r}, t)$, the magnetic induction $\mathbf{B}(\mathbf{r}, t)$, the external charge density $\rho_{ext}(\mathbf{r}, t)$ and the external current density $\mathbf{J}_{ext}(\mathbf{r}, t)$. In the derivations, the following assumptions are used:

1. the relevant quantities can be factorized in a position dependent and time dependent part, and the time dependent part $f(t)$ has the form $f(t) = e^{-i\omega t}$ with frequency ω ;
2. space (in each medium) is homogeneous and isotropic;
3. the relation between the magnetic induction $\mathbf{B}(\mathbf{r}, t)$ and the magnetic field $\mathbf{H}(\mathbf{r}, t)$ is given by $\mathbf{B}(\mathbf{r}, t) = \mu(\mathbf{r}, t) \mathbf{H}(\mathbf{r}, t)$ with μ the magnetic permeability considered independent of time and identical in each medium: $\mu(\mathbf{r}, t) = \mu$;
4. the relation between the displacement vector $\mathbf{D}(\mathbf{r}, t)$ and the electric field $\mathbf{E}(\mathbf{r}, t)$ is given by $\mathbf{D}(\mathbf{r}, t) = \varepsilon(\mathbf{r}, t) \mathbf{E}(\mathbf{r}, t)$ with $\varepsilon(\mathbf{r}, t)$ the dielectric function in a given medium, dependent on time (or equivalently, frequency ω) in metals and independent of time in dielectrics;
5. Ohm's law: $\mathbf{J}_{ext}(\mathbf{r}, t) = \sigma(\mathbf{r}, t) \mathbf{E}(\mathbf{r}, t)$ with $\sigma(\mathbf{r}, t)$ the conductivity of the medium;
6. there are no external charges: $\rho_{ext}(\mathbf{r}, t) = 0$.

The boundary conditions that are used, are

1. the tangential component of the electric field is continuous;
2. the tangential component of the magnetic field is continuous.

With the above mentioned assumptions, one can derive from the Maxwell equations a vector wave equation for the electric and magnetic fields $\mathbf{E}(\mathbf{r}, t)$ and $\mathbf{H}(\mathbf{r}, t)$. From these wave equations follows that for the *carthesian* components C_j of the fields (so C_j equals E_x, E_y, E_z, H_x, H_y or H_z) a *scalar* Helmholtz equation holds:

$$\nabla^2 C_j + k^2 C_j = 0 \quad (3.1)$$

with $k^2 = \omega^2/c^2$ in vacuum and $k^2 = (\omega^2/c^2)(\mu\varepsilon + i4\pi\mu\sigma/\omega)$ in a medium. One does not find a scalar Helmholtz equation in spherical coordinates, and that is why in Mie theory one uses basis functions defined from a scalar function $\Psi(\mathbf{r}, t)$ that does satisfy the Helmholtz equation (3.1). Factorized in a spatial and time-dependent part, these basis functions can be written as

$$\begin{aligned}\mathbf{L}(\mathbf{r}, t) &= \nabla \Psi(\mathbf{r}, t) = \mathbf{l}(\mathbf{r}) e^{-i\omega t} \\ \mathbf{M}(\mathbf{r}, t) &= \nabla \times \Psi(\mathbf{r}, t) \mathbf{a} = \mathbf{m}(\mathbf{r}) e^{-i\omega t} \\ \mathbf{N}(\mathbf{r}, t) &= \frac{1}{k} \nabla \times \mathbf{M}(\mathbf{r}, t) = \mathbf{n}(\mathbf{r}) e^{-i\omega t}\end{aligned}$$

in which \mathbf{a} is a vector in the radial direction. These functions are called vector spherical harmonics. The functions \mathbf{M} and \mathbf{N} are divergenceless, and the function \mathbf{L} is irrotational. One then expands the vector potential $\mathbf{A}(\mathbf{r}, t)$ in those vector spherical harmonics:

$$\mathbf{A}(\mathbf{r}, t) = \frac{i}{\omega} \sum_p (a_p \mathbf{M}_p + b_p \mathbf{N}_p + c_p \mathbf{L}_p).$$

From the relation $\mathbf{B}(\mathbf{r}, t) = \nabla \times \mathbf{A}(\mathbf{r}, t)$ and the fourth law of Maxwell, one then finds that in the used assumptions the fields can be written as

$$\begin{aligned}\mathbf{H}(\mathbf{r}, t) &= -\frac{k}{i\omega\mu} \sum_p (a_p \mathbf{N}_p + b_p \mathbf{M}_p) \\ \mathbf{E}(\mathbf{r}, t) &= -\sum_p (a_p \mathbf{M}_p + b_p \mathbf{N}_p).\end{aligned}\quad (3.2)$$

Using the fact that $\Psi(\mathbf{r}, t)$ satisfies the Helmholtz equation (3.1), and assuming that an incident plane wave with amplitude E_0 travels in the z -direction and is polarized in the x -direction, one then finds the following expressions for the fields:

$$\begin{aligned}\mathbf{H}(\mathbf{r}, t) &= -\frac{k}{\omega\mu} E_0 e^{-i\omega t} \sum_\ell i^\ell \frac{2\ell+1}{\ell(\ell+1)} \left[a_\ell \mathbf{n}_\ell^{(o)}(\mathbf{r}) - b_\ell \mathbf{m}_\ell^{(e)}(\mathbf{r}) \right] \\ \mathbf{E}(\mathbf{r}, t) &= -E_0 e^{-i\omega t} \sum_\ell i^\ell \frac{2\ell+1}{\ell(\ell+1)} \left[a_\ell \mathbf{m}_\ell^{(e)}(\mathbf{r}) + b_\ell \mathbf{n}_\ell^{(o)}(\mathbf{r}) \right]\end{aligned}\quad (3.3)$$

with

$$\begin{aligned}\mathbf{m}_\ell^{(e)}(\mathbf{r}) &= \mp \frac{1}{\sin(\theta)} z_\ell(kr) P_\ell^1(\cos(\theta)) \begin{pmatrix} \sin(\varphi) \\ \cos(\varphi) \end{pmatrix} \mathbf{e}_\theta \\ &\quad - z_\ell(kr) \frac{\partial P_\ell^1(\cos(\theta))}{\partial \theta} \begin{pmatrix} \cos(\varphi) \\ \sin(\varphi) \end{pmatrix} \mathbf{e}_\varphi \\ \mathbf{n}_\ell^{(o)}(\mathbf{r}) &= \frac{\ell(\ell+1)}{kr} z_\ell(kr) P_\ell^1(\cos(\theta)) \begin{pmatrix} \cos(\varphi) \\ \sin(\varphi) \end{pmatrix} \mathbf{e}_r \\ &\quad + \frac{1}{kr} \frac{\partial(rz_\ell(kr))}{\partial r} \frac{\partial P_\ell^1(\cos(\theta))}{\partial \theta} \begin{pmatrix} \cos(\varphi) \\ \sin(\varphi) \end{pmatrix} \mathbf{e}_\theta \\ &\quad \mp \frac{1}{kr \sin(\theta)} \frac{\partial(rz_\ell(kr))}{\partial r} P_\ell^1(\cos(\theta)) \begin{pmatrix} \sin(\varphi) \\ \cos(\varphi) \end{pmatrix} \mathbf{e}_\varphi.\end{aligned}$$

In these expressions, ℓ is the angular quantum number, $z_\ell(x)$ is a (modified) spherical Bessel function (or a linear combination of those functions), $P_\ell^m(\cos(\theta))$ is a Legendre polynomial and \mathbf{e}_r , \mathbf{e}_θ and \mathbf{e}_φ are the unit vectors in the r , θ and φ direction. Which functions are to be used for $z_\ell(x)$ depends on the radial boundary conditions in a given part of the system.

In a core-shell system there are the following fields in each part of space:

1. in the environment: incident (i) and scattered (s) fields, so that $\mathbf{E}_{\text{environment}}(\mathbf{r}, t) = \mathbf{E}_i(\mathbf{r}, t) + \mathbf{E}_s(\mathbf{r}, t)$, and analogous for the magnetic field.
2. in the shell: “shell transmitted” (st) and “shell scattered” (ss) - from the core - fields, so $\mathbf{E}_{\text{shell}}(\mathbf{r}, t) = \mathbf{E}_{st}(\mathbf{r}, t) + \mathbf{E}_{ss}(\mathbf{r}, t)$, and analogous for the magnetic field.
3. in the core: a “core transmitted” (ct) field, so $\mathbf{E}_{\text{core}}(\mathbf{r}, t) = \mathbf{E}_{ct}(\mathbf{r}, t)$, and analogous for the magnetic field.

From the requirement that the fields satisfy the appropriate boundary conditions, one can derive a set of equations from which one can find expressions for the coefficients $a_\ell^{(s)}$, $b_\ell^{(s)}$, $a_\ell^{(st)}$, $b_\ell^{(st)}$, $a_\ell^{(ss)}$, $b_\ell^{(ss)}$, $a_\ell^{(ct)}$ and $b_\ell^{(ct)}$.

The coefficients $a_\ell^{(s)}$ and $b_\ell^{(s)}$ can then be used to calculate the scattering cross section $Q_{\text{scatt}}(\omega)$, absorption cross section $Q_{\text{abs}}(\omega)$ or extinction/total cross section $Q_{\text{ext}}(\omega)$ which will show peaks as a function of ω at the resonance frequencies [121]:

$$\begin{aligned}
 Q_{\text{scatt}}(\omega) &= \frac{2\pi}{k_E^2(\omega)} \sum_{\ell=1}^{\infty} (2\ell+1) \left(\left| a_\ell^{(s)}(\omega) \right|^2 + \left| b_\ell^{(s)}(\omega) \right|^2 \right) \\
 Q_{\text{abs}}(\omega) &= -\frac{2\pi}{k_E^2(\omega)} \sum_{\ell=1}^{\infty} (2\ell+1) \left[\left| a_\ell^{(s)}(\omega) \right|^2 + \left| b_\ell^{(s)}(\omega) \right|^2 + \text{Re} \left(a_\ell^{(s)}(\omega) + b_\ell^{(s)}(\omega) \right) \right] \\
 Q_{\text{ext}}(\omega) &= Q_{\text{scatt}}(\omega) + Q_{\text{abs}}(\omega) = -\frac{2\pi}{k_E^2(\omega)} \sum_{\ell=1}^{\infty} (2\ell+1) \text{Re} \left(a_\ell^{(s)}(\omega) + b_\ell^{(s)}(\omega) \right).
 \end{aligned} \tag{3.4}$$

The term corresponding to $\ell = 1$ is called the dipole term, the term corresponding to $\ell = 2$ the quadrupole term, ... The first three multipole contributions to the extinction cross section $Q_{\text{ext}}(\omega)$ are shown in figure 3.8 as a function of wavelength λ . For each ℓ -value there is an optically more active peak at higher wavelengths and a less intense peak at lower wavelengths. The higher the order of the multipole contribution, the narrower the resonance peaks. This has consequences both for numerical calculations as for experimental determination. For a correct representation of the maximum of the quadrupole ($\ell = 2$) and hexapole ($\ell = 3$) term, a value for $Q_{\text{ext}}(\omega)$ had to be calculated every 0.1 nm, whereas a correct representation of the dipole contribution required only a value of $Q_{\text{ext}}(\omega)$ every 5 nm. If one scans the entire region where resonances might occur, the dipole peaks can be found with a wider mesh and thus more quickly and easily. Moreover only the lower-order contributions are relevant for experiment because the higher-order contributions do not contain enough spectral weight to be observed. In this way it is justified to calculate only the values of $Q(\omega)$ necessary to represent the first-order contributions well and to only take the first few terms of expressions (3.4) into account, the contributions that can be represented with the used mesh. The calculated spectrum does not change if terms are added for which the resonances cannot be shown with the used mesh.

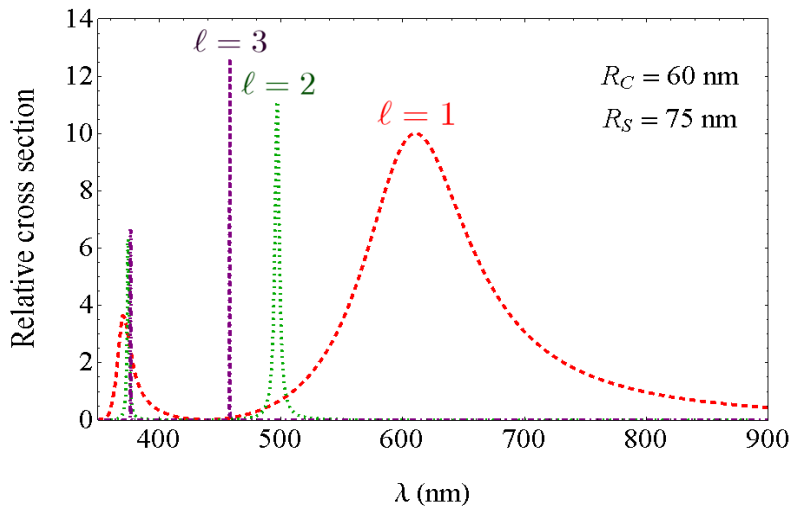


Figure 3.8: First three multipole contributions to the relative extinction cross section $Q_{\text{ext}}(\lambda) / (\pi R_S^2)$ of a SiO_2 -Au nanoshell with core radius $R_C = 60$ nm and total radius $R_S = 75$ nm. The parameters used in the Mie calculations are: $\varepsilon_C = 2.0449$ [111], $\varepsilon_E = 1$ and for the frequency dependent dielectric function of the shell the Drude form $\varepsilon(\omega) = \varepsilon_b - \omega_p^2/\omega^2$ with ε_b a background contribution taken to be $\varepsilon_b = 6.9$ [116] and ω_p the bulk plasmon frequency of gold.

Some side remarks

In the expansion (3.2) of the electric field in vector spherical harmonics, no longitudinal term has been incorporated: it is assumed that only transverse modes of the spherical particle exist. For a homogeneous sphere, Mie theory was extended by Ruppin to include the excitation of longitudinal polarization waves [114, 115]. Inclusion of the longitudinal component shifts the resonance peak of the transverse modes to somewhat higher frequencies (blue shift) and introduces some additional oscillations at higher frequencies. In [115] it is mentioned that for sodium particles of less than 50 Å radius the shift of the main resonance was indeed detected and that the additional oscillations appeared, not as individual oscillations but as a band due to size distribution.

In calculations based on Mie theory, a number of approximations are made. The crucial assumptions are the following. The fields are purely transverse. The relations $\mathbf{B}(\mathbf{r}, t) = \mu(\mathbf{r}, t) \mathbf{H}(\mathbf{r}, t)$, $\mathbf{J}_{ext}(\mathbf{r}, t) = \sigma(\mathbf{r}, t) \mathbf{E}(\mathbf{r}, t)$ and $\mathbf{D}(\mathbf{r}, t) = \varepsilon(\mathbf{r}, t) \mathbf{E}(\mathbf{r}, t)$ hold. For the dielectric function of a metallic layer one usually uses experimental bulk values or the Drude form

$$\varepsilon(\omega) = \varepsilon_b - \frac{\omega_p^2}{\omega^2 + i\gamma\omega}$$

in which ω_p is the bulk plasmon frequency, and in which the influence of the background ε_b is often set equal to $\varepsilon_b = 1$ and the damping coefficient γ is often set equal to $\gamma = 0$; Ruppin used the separate forms of the dielectric function for longitudinal and transverse response derived by Lindhard [71]. Sometimes size-corrections are added to the Drude dielectric function if the dimensions of the metal become smaller than the mean-free path ℓ_0 of the conduction electrons. For gold this mean-free path is of the order of $\ell_0 \approx 40$ nm. The model used for the dielectric function of the metallic shell is a determining factor for the width and the amplitude of the calculated resonance peaks.

If no assumptions are made the permittivity, permeability and conductivity will no longer be scalar functions, but complex tensors relating a field in one point to the values of other fields in different parts of space. Only if one assumes a certain degree of homogeneity, isotropy and locality will it be possible to define a quantity like the dielectric function. The mentioned assumptions might not be appropriate in the nanoregime, a rapidly developing research area. The question of applicability of the macroscopic Maxwell equations to nanostructures will be addressed in a Ph.D. thesis in our group by N. Van den Broeck.

3.5.2 Hybridization theory

Hybridization theory, developed by Prodan and Nordlander [107, 108], offers a fast-to-evaluate analytical form for the resonance frequencies of a multi-layer spherical particle. The advantage of hybridization theory over Mie theory is that the resonance frequencies are easily calculated from an analytical form, whereas in Mie theory one first has to calculate a spectrum and then determine numerically the location of the maxima. The drawbacks of hybridization theory are that the resonance frequencies only coincide with those of Mie theory for relatively small particles, smaller than ca. a tenth of the wavelength, and that it gives no information on the width of the resonance peaks.

Hybridization theory is a mesoscale electromagnetic analogue of the molecular-orbital theory used to predict how atomic orbitals interact to form molecular orbitals. In the theory, complex nanoparticle geometries are separated in simpler constituent parts. Then it is calculated how the plasmon resonances of the elementary parts interact with each other to generate the hybridized

²In Ref. [4], the expression $\ell_0 = r_s^2/\rho_\mu \times 92$ Å is given with $(\rho_\mu)_{\text{Au}} = 2.04 \mu\Omega$; with $(r_s)_{\text{Au}} = 3$ we thus find that $(\ell_0)_{\text{Au}} \simeq 40.5$ nm.

plasmon modes of the composite nanostructure. For a nanoshell it means that one combines two systems: a solid sphere with resonance frequency ω_S and a spherical cavity with resonance frequency ω_C . The interaction between the resonant modes of both constituent particles results in two “hybridized” modes: an anti-symmetric mode with a resonance frequency ω_+ and a symmetric mode with a resonance frequency ω_- (see figure 3.9). The resonance frequency of the anti-symmetric mode is higher than the resonance frequencies of the sphere and cavity, the resonance frequency of the symmetric mode is lower. The thinner the shell, the stronger the coupling and the larger the difference between the hybridized modes. Because the dipole moment of the symmetric plasmon mode is much larger than that of the anti-symmetric mode, the former couples much stronger to light than the latter.

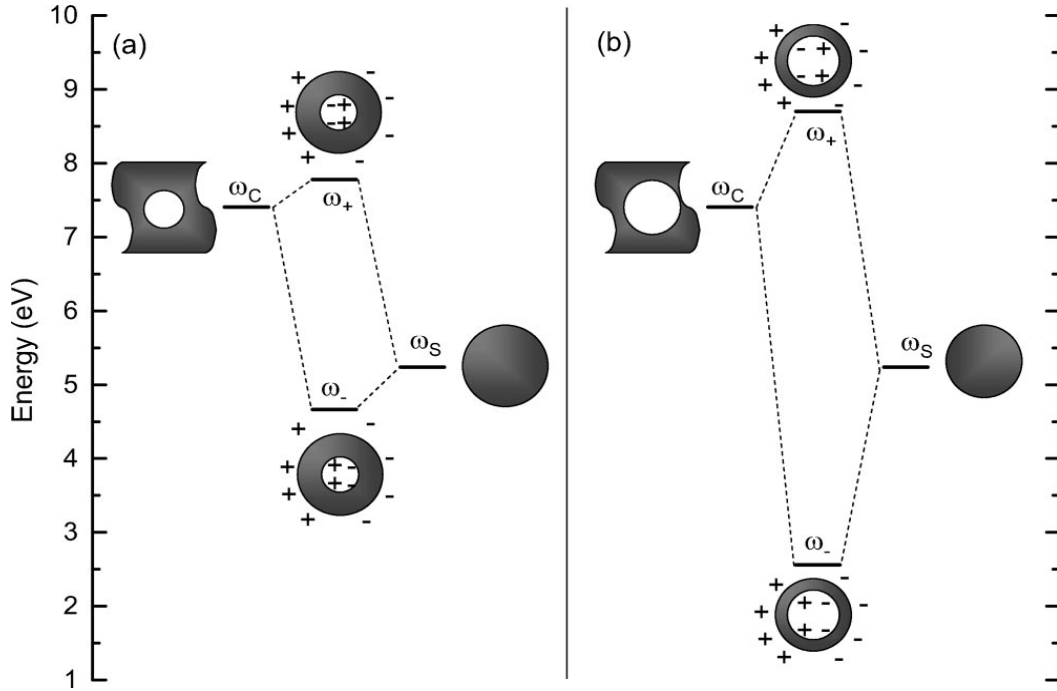


Figure 3.9: Two energy diagrams illustrating the plasmon hybridization in a metallic nanoshell. The energy levels marked with ω_C and ω_S represent the cavity and the sphere plasmon resonances. The energy levels marked with ω_{\mp} represent the symmetric, respectively, anti-symmetric plasmon modes of the metallic nanoshell. Panel (a) shows the diagram for a nanoshell with $(R_C, R_S) = (20, 40)$ nm and panel (b) shows a diagram for a nanoshell with $(R_C, R_S) = (28, 32)$ nm; in both cases $\varepsilon_C = \varepsilon_S = \varepsilon_E = 1$ (figure taken from Ref. [108]).

The derivation of the analytical expression for the resonance frequencies is based on the incompressible fluid model. In this model the conduction electrons of metallic layers are modeled as an incompressible, irrotational charged fluid with charge density $\rho(\mathbf{r})$ on top of a uniform positive background charge distribution n_0 representing the metal ion cores. The positive background charge extends only over the shell and the entire system is charge neutral. When the system is excited by an electromagnetic wave, the incompressible fluid will locally spill out an amount $n(\mathbf{r}) - n_0$ in the core or the environment. The basic equations that describe the incompressible, irrotational fluid are

$$\begin{aligned} \frac{\partial \rho(\mathbf{r}, t)}{\partial t} + \nabla \cdot \mathbf{j}(\mathbf{r}, t) &= 0 \\ \nabla \times \mathbf{j}(\mathbf{r}, t) &= 0 \\ \mathbf{j}(\mathbf{r}, t) &= \rho(\mathbf{r}, t) \mathbf{v}(\mathbf{r}, t). \end{aligned}$$

The first equation is the continuity equation in which $\mathbf{j}(\mathbf{r}, t)$ is the current density. The second equation states that there are no vortices present. The third equation is the definition of the current density in terms of the fluid velocity $\mathbf{v}(\mathbf{r}, t)$. Since $\mathbf{v}(\mathbf{r}, t) \propto \mathbf{j}(\mathbf{r}, t)$ it follows from the irrotationality condition that the velocity can be written as a gradient of a scalar function³ $\eta(\mathbf{r}, t)$, so $\mathbf{v}(\mathbf{r}, t) = \nabla\eta(\mathbf{r}, t)$, which satisfies the Laplace equation $\nabla^2\eta(\mathbf{r}, t) = 0$. From this equation one can find an expression for $\eta(\mathbf{r}, t)$ in each layer of the nanoparticle. These expressions in combination with the boundary conditions lead to expressions for the velocity and surface charge $\sigma = \lim_{\delta S \rightarrow 0} \frac{1}{\delta S} \int_{\delta V} (\rho - \rho_0) dV$ with S the surface. These quantities determine the Lagrangian L of the system:

$$L = \frac{1}{2} \int n_0 m_e \mathbf{v}^2 dV - \frac{1}{2} \int \int \frac{\sigma(\mathbf{r}, t) \sigma(\mathbf{r}', t)}{|\mathbf{r} - \mathbf{r}'|} dS_{\mathbf{r}} dS_{\mathbf{r}'}$$

If for the dielectric function of the metal shell the Drude form

$$\varepsilon_S(\omega) = \varepsilon_b - \frac{\omega_p^2}{\omega^2}, \quad (3.5)$$

is used, the equations of motion derived from the Lagrangian L with the correct solution for $\eta(\mathbf{r}, t)$ lead to the resonance frequencies

$$\begin{aligned} \omega_{\ell, \pm}^2 = & \frac{\omega_p^2}{\beta} \left(\begin{aligned} & (\ell + 1)^2 \varepsilon_E + 2\ell(\ell + 1) \varepsilon_b + \ell^2 \varepsilon_C \\ & + \ell(\ell + 1) (\varepsilon_E - 2\varepsilon_b + \varepsilon_C) x^{2\ell+1} \end{aligned} \right) \\ & \pm \left\{ \left[\ell^2 \varepsilon_C - (\ell + 1)^2 \varepsilon_E + \ell(\ell + 1) (\varepsilon_E - \varepsilon_C) x^{2\ell+1} \right]^2 \right. \\ & \left. + 4\ell(\ell + 1) [(\ell + 1) \varepsilon_E + \ell \varepsilon_C]^2 x^{2\ell+1} \right\}^{1/2} \end{aligned} \quad (3.6)$$

with $x = R_C/R_S$ and

$$\beta = 2 \left\{ [(\ell + 1) \varepsilon_b + \ell \varepsilon_C] [(\ell + 1) \varepsilon_E + \ell \varepsilon_b] + \ell(\ell + 1) (\varepsilon_b - \varepsilon_C) (\varepsilon_E - \varepsilon_b) x^{2\ell+1} \right\}.$$

The hybridization model has not only been applied to a nanoshell, but also to e.g. nanomaterials [108] and the system of a nanoshell near a metallic film [69].

3.5.3 (Time-dependent) Kohn-Sham calculations

Prodan and Nordlander performed (time-dependent) Kohn-Sham calculations for nanoshells in the Local Density Approximation within the jellium model [101, 102, 103, 104, 87, 106]. The aim was to calculate the optical absorption of manufacturable-size nanoshells and to compare the results with experiments. They managed to calculate the properties of a nanoshell with $(R_C, R_S) = (16, 19)$ nm [87], containing about 7×10^5 conduction electrons for which about 3000 orbitals have to be calculated in each iteration [106]. The algorithm they developed allowed for time-dependent calculations [105, 87, 106] of which the results could be compared with absorption spectra snapshots at $(R_C, R_S) = (4.1, 5.1)$ nm, $(R_C, R_S) = (8.6, 9.9)$ nm, $(R_C, R_S) = (13.1, 14.8)$ nm recorded during the growth of an Au₂S-Au nanoshell in aqueous solution [7]. At the stage the snapshots were taken, the nanoshells were not fully completed and had a rough surface. The shells were modeled as perfect shells and the “ideal” sizes were determined by comparing the spectra with results of Mie theory. In this way the Kohn-Sham calculations could be compared with experimental data, although complete shells of the mentioned (computable) sizes have not yet been fabricated experimentally.

³With $\eta(\mathbf{r})$ a scalar function, the identity $\nabla \times [\nabla\eta(\mathbf{r})] = 0$ holds.

The implementation of the Kohn-Sham equations for the mentioned large number of electrons is an enormous task, as indicated in the conclusion of the Ph.D. thesis of Prodan [106] : “The simulations presented in this thesis prove that the *ab initio* calculations can be pushed to a limit where real size metallic nanoparticles can be investigated”. To be able to do so, one needs an efficient algorithm. Before we discuss the basics of the algorithm developed by Prodan and Nordlander, we briefly mention some preliminary studies that they made to check whether the demanding calculations would make sense... something that was also of our interest when we wanted to perform orbital-based calculations as reported in this thesis.

Preliminary investigations

Before starting elaborate Kohn-Sham calculations, Prodan and Nordlander investigated the many-body effects in metallic nanoshells by comparing Hartree, Hartree-Fock and LDA calculations [100]. The results showed that the differences between the three approximations are similar to the differences for bulk metals for which the Hartree-Fock approximation overestimates the bandwidths and screening lengths. The differences appear even for very small nanoshells. From this study, Prodan and Nordlander concluded that correlation terms are important in nanoshells and that LDA is the most appropriate approach among the three investigated approximations.

Another topic that Prodan and Nordlander investigated, was the existence, uniqueness and the thermodynamic limit for the Kohn-Sham equations [99]. They remarked that for an exact exchange-correlation potential $u_{XC}(\mathbf{r})$ the equations are expected to have a unique solution far from a phase transition, but that this uniqueness is not obvious for the approximations to $u_{XC}(\mathbf{r})$ used in practical calculations. For finite temperatures, the LDA approximation does not cause any problems. But at zero temperature the Kohn-Sham equations do not have a unique solution in general. This occurs when the highest-energy level is not completely occupied. For an unperturbed electron system, each energy level is at least doubly degenerate because of spin. If there is only one electron that has an energy equal to the Fermi energy, its spin is undefined (in case of a spherically symmetric system also the values of the magnetic quantum number m are undefined). To overcome this problem, Prodan and Nordlander used the finite-temperature extension of DFT [77]. At finite temperature T , the electron density can be calculated from the single-particle wave functions $\psi_{\{\mathbf{q}\}_k}(\mathbf{r})$ as [60]

$$n(\mathbf{r}) = \sum_k \frac{|\psi_{\{\mathbf{q}\}_k}(\mathbf{r})|^2}{1 + e^{\beta(\epsilon_{\{\mathbf{q}\}_k} - \mu)}}$$

with $\beta = 1/(k_B T)$, k_B Boltzmann’s constant, μ the chemical potential and the summation running over all possible single-particles states. In this way, degenerate states have all a non-unity probability to occur. The chemical potential has to be adjusted so that the number of electrons N remains fixed:

$$N = \sum_k \frac{1}{1 + e^{\beta(\epsilon_{\{\mathbf{q}\}_k} - \mu)}}.$$

In principle, the finite temperature formalism involves an infinite set of orbitals to determine the density. Because in practice only states with an energy less than approximately $\mu + k_B T$ contribute substantially and because metals have a relatively large ionization potential, Prodan and Nordlander only included all the bound states and neglected the continuum states.

Orbital calculation

Prodan and Nordlander used the spherical symmetry and set the single-particle wave functions equal to⁴

$$\psi_{\mathbf{n},\ell,m}(\mathbf{r}) = \frac{u_{\mathbf{n},\ell}(r)}{r} Y_{\ell,m}(\Theta, \varphi),$$

with $Y_{\ell,m}(\Theta, \varphi)$ the spherical harmonics with angular quantum ℓ and magnetic quantum number m . They then considered the radial differential equations

$$\left(-\frac{1}{2} \frac{d^2}{dr^2} + \frac{\ell(\ell+1)}{2r^2} + u_{\text{eff}}(r) \right) u_{\mathbf{n},\ell}(r) = \epsilon_{\mathbf{n},\ell} u_{\mathbf{n},\ell}(r). \quad (3.7)$$

The effective potential energy $u_{\text{eff}}(r)$ was calculated as $u_{\text{eff}}(r) = U_{\text{ext}}(r) + u_H(r) + u_{XC}(r)$. In this expression the external potential energy $U_{\text{ext}}(r)$ was taken to be

$$U_{\text{ext}}(r) = \begin{cases} 0.02 \text{ a.u.} & r < R_C \\ -0.16 \text{ a.u.} & R_C < r < R_S \\ 0 \text{ a.u.} & R_S < r \end{cases} \quad (3.8)$$

in order that the ionization potential was approximately equal to 5.4 eV, appropriate for gold. The Hartree, or direct Coulomb, part $u_H(r)$ of the effective energy was calculated from the Poisson equation. The Wigner-Seitz radius r_s in the jellium model was taken to be $r_s = 3$ as for bulk gold. For the exchange and correlation potential energy $u_{XC}(r)$, the LDA form proposed in Ref. [90] was used. The electron concentration $n(r)$ was calculated as

$$n(r) = \frac{2}{r^2} \sum_{\mathbf{n},\ell} \frac{2\ell+1}{1 + e^{\beta(\epsilon_{\mathbf{n},\ell} - \mu)}} |u_{\mathbf{n},\ell}(r)|^2.$$

The global procedure to find the energy levels was as follows. For each value of ℓ , the value of the energy ϵ was swept from the bottom of the effective potential $u_{\text{eff}}(r)$ up to zero. For each couple $\{\ell, \epsilon\}$ the differential equation (3.7) was numerically integrated using 4-th order Runge-Kutta, a numerical finite-difference integration method (see e.g. Ref. [98]). This method was used to solve two initial boundary problems that started from the opposite sides of the considered radial domain. This resulted in two solutions of the differential equation (3.7): $u_{\mathbf{n},\ell}^{(1)}(r)$ and $u_{\mathbf{n},\ell}^{(2)}(r)$. Solution $u_{\mathbf{n},\ell}^{(1)}(r)$ had the boundary conditions

$$u_{\mathbf{n},\ell}^{(1)}(r) \approx r^{\ell+1}, \quad \frac{du_{\mathbf{n},\ell}^{(1)}(r)}{dr} \approx (\ell+1)r^\ell \quad \text{for } r \rightarrow 0,$$

and for $u_{\mathbf{n},\ell}^{(2)}(r)$ the initial values were given at the other side of the integration interval:

$$u_{\mathbf{n},\ell}^{(2)}(r) \approx e^{-\sqrt{2|\epsilon_{\mathbf{n},\ell}|}r}, \quad \frac{du_{\mathbf{n},\ell}^{(2)}(r)}{dr} \approx -\sqrt{2|\epsilon_{\mathbf{n},\ell}|} e^{-\sqrt{2|\epsilon_{\mathbf{n},\ell}|}r} \quad \text{for } r \rightarrow \infty.$$

For the numerical implementation of the initial condition for $u_{\mathbf{n},\ell}^{(2)}(r)$, a finite spherical volume with radius $R \gg R_S$ was used with R considered to be large enough to implement this condition.

⁴To have a consistent notation in the thesis, we used in this section for some of the quantities a different notation than in the work of Prodan and Nordlander. For example, we make use of a quantum number \mathbf{n} instead of subscripts k or E . The quantum number \mathbf{n} is defined as follows: $\mathbf{n} = 1$ is used for the lowest state that can be occupied for a given value of ℓ , $\mathbf{n} = 2$ for the second lowest state that can be occupied for a given ℓ -value, ...

A trial energy $\epsilon_{n,\ell}$ was accepted as an eigenvalue if the two solutions $u_{n,\ell}^{(1)}(r)$ and $u_{n,\ell}^{(2)}(r)$ became linear dependent, i.e. when the Wronskian $W \left\{ u_{n,\ell}^{(1)}(r), u_{n,\ell}^{(2)}(r) \right\}$ cancelled out:

$$W \left\{ u_{n,\ell}^{(1)}(r), u_{n,\ell}^{(2)}(r) \right\} = \left[u_{n,\ell}^{(1)}(r) \frac{du_{n,\ell}^{(2)}(r)}{dr} - \frac{du_{n,\ell}^{(1)}(r)}{dr} u_{n,\ell}^{(2)}(r) \right] = 0.$$

The cancellation of the Wronskian for a certain energy value ϵ should be valid for each value of r . To test whether the Wronskian is equal to zero, one should make sure that the r -value r_0 for which this condition is tested, is not a node of the two solutions. Therefore r_0 was taken to be located at a local minimum or maximum of $u_{n,\ell}^{(1)}(r)$, which was constructed in the direct integration.

To get an accuracy of at least four digits on the eigenvalues, 33000 grid points had to be used for the considered nanoshells of dimensions $(R_C, R_S) = (4.1, 5.1)$ nm, $(R_C, R_S) = (8.6, 9.9)$ nm and $(R_C, R_S) = (13.1, 15.1)$ nm which contained around 1.6×10^4 up to 3×10^5 electrons.

Determining the energy levels, the most time-consuming step of the calculations, could be somewhat simplified using the observation that for two consecutive angular quantum numbers, ℓ and $\ell + 1$, the corresponding energies $\epsilon_{n,\ell}$ and $\epsilon_{n,\ell+1}$ are very close to each other with respect to the size of the effective potential well and are related as $\epsilon_{n,\ell} < \epsilon_{n,\ell+1}$. This means that the energy ϵ had to be swept over a large interval only for $\ell = 0$ and the values of $\epsilon_{n,\ell>0}$ could be found in the vicinity of $\epsilon_{n,\ell-1}$.

Performing a lot of calculations, Prodan and Nordlander observed that the larger the nanoshell, the more difficult it is to make the iterative process converge. To overcome this convergence issue, a screened Coulomb potential was used for which the screening length λ was increased when convergence was reached for a certain value of λ , until increasing of λ did not have any effect on the first four digits of the eigenvalues (the ones that matter).

Static perturbation

Orbitals derived as outlined in the previous section were used to calculate the independent-electron polarization function $\Pi_0(\mathbf{r}, \mathbf{r}')$ of Lindhard

$$\Pi_0(\mathbf{r}, \mathbf{r}') = 2 \sum_{i,j} \psi_i^*(\mathbf{r}) \psi_j(\mathbf{r}) \frac{f_{FD}(\xi_i) - f_{FD}(\xi_j)}{\xi_i - \xi_j + i\delta} \psi_i(\mathbf{r}') \psi_j^*(\mathbf{r}')$$

in which $\xi_i = \epsilon_i - \mu$ and $f_{FD}(\xi_i)$ is the Fermi-Dirac distribution function. This polarization function was used to calculate the screening charge

$$\delta n(\mathbf{r}) = - \int \Pi(\mathbf{r}, \mathbf{r}') \frac{Z}{|\mathbf{r}' - \mathbf{r}_0|} d\mathbf{r}'$$

due to an impurity of charge Z at position $\mathbf{r}_0 = 0$, both in the independent-electron picture and in the Random Phase Approximation for which $\Pi_{RPA}(\mathbf{r}, \mathbf{r}') = \Pi_0(\mathbf{r}, \mathbf{r}') / (1 - V\Pi_0(\mathbf{r}, \mathbf{r}'))$ with V equal to the sum of the Coulomb interaction and $\delta u_{XC}(\mathbf{r}') = [du_{XC}(n(\mathbf{r})) / dn] \delta(\mathbf{r} - \mathbf{r}')$.

Time-dependent perturbation

The same orbital calculations were used to calculate the frequency-dependent polarization function $\Pi_0(\mathbf{r}, \mathbf{r}'; \omega)$ in the independent-particle picture which again was used to calculate the polarization in the Random Phase Approximation. With this polarization, the photoabsorption cross section $\sigma_{\text{abs}}(\omega)$ was calculated as

$$\sigma_{\text{abs}}(\omega) = \frac{2\pi}{c} \omega \text{Im}[\alpha(\omega)] = -\frac{8\pi^2}{3c} \omega \text{Im} \left[\int \int r^3 \Pi(\mathbf{r}, \mathbf{r}'; \omega) r'^3 dr dr' \right].$$

3.5.4 Comparison of results

Mie theory versus experiment

In Ref. [83] nanoshell scattering spectra calculated with Mie theory are compared with experimental spectra of single nanoshells. In the calculations the dielectric function $\varepsilon_S(\omega)$ of the golden shell was modeled by a function of the form

$$\varepsilon_S(\omega) = \varepsilon_{\text{interband}}(\omega) + \left(1 - \frac{\omega_p^2}{\omega^2 + i\omega\gamma_{\text{bulk}}}\right) \quad (3.9)$$

with ω_p the bulk plasmon frequency of gold. To obtain values for $\varepsilon_{\text{interband}}(\omega)$ and the bulk damping factor γ_{bulk} , the function (3.9) was fitted to the measured values of the bulk dielectric function obtained in Ref. [52].

Figure 3.10 shows the results for three single nanoshells in water (refractive index n taken to be $n = 1.33$). For all three nanoshells the calculated position of the resonance peak coincides with the measured resonance energy. For the nanoshell with $(R_C, R_S) = (60, 80)$ nm the width of the measured resonance peak is rather well reproduced by the calculations. The smaller the nanoshell, the more the theoretical and experimental peak width differ. This is an indication that the bulk description of the dielectric function and/or the Maxwell equations is not appropriate for nanoshells smaller than a critical size. For the nanoshells of the considered sizes, the description can however be used to determine the resonance energy.

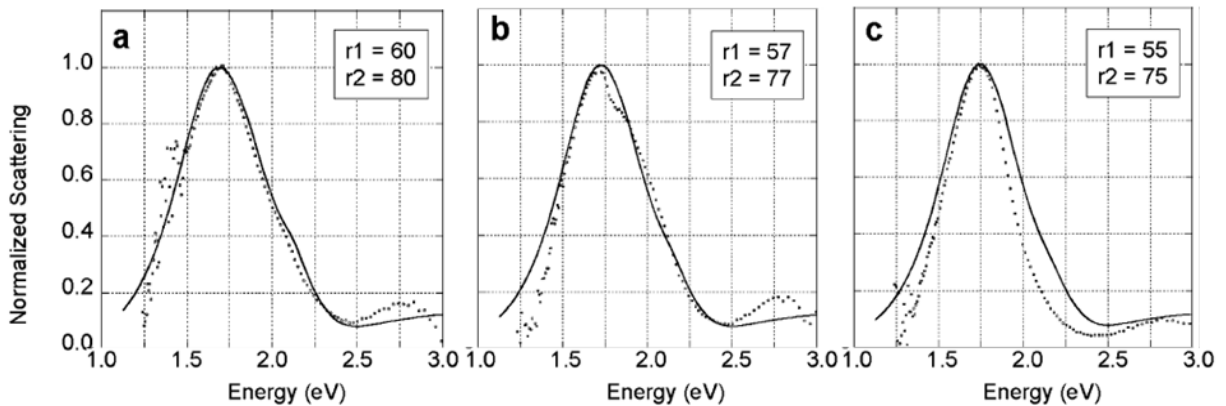


Figure 3.10: Scattering cross section versus energy for three different SiO_2 -Au nanoshells in water: a) $(R_C, R_S) = (60, 80)$ nm, b) $(R_C, R_S) = (57, 77)$ nm, c) $(R_C, R_S) = (55, 75)$ nm. The circles represent the experimental data and the solid line was calculated using Mie theory. The measured and calculated spectra are normalized to have a peak value of 1 (figures taken from Ref. [83]).

Hybridization theory versus Mie Theory

As already mentioned in section 3.5.2, hybridization theory has advantages and disadvantages in comparison with Mie theory. The advantage is that the resonance frequencies are easily calculated from an analytical formula, whereas in Mie theory one first has to calculate a spectrum and then determine the location of the maxima numerically. On the other hand, only for relatively small particles the resonance frequencies coincide with those of Mie theory (and thus with the results of extinction experiments, see previous section). This is illustrated in figure 3.11. Another drawback is that hybridization theory gives no information on the width of the resonance peaks.

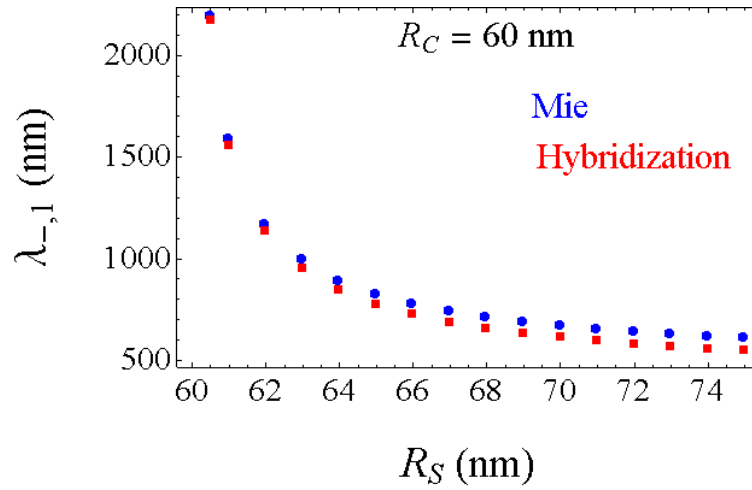


Figure 3.11: Resonance wave length $\lambda_{-,1}$ of the optical active dipole peak of SiO_2 -Au nanoshells as a function of total radius for nanoshells with $R_C = 60$ nm calculated with Mie theory (blue circles) and with hybridization theory (red squares). The permittivities of the core and environment were taken to be $\varepsilon_C = 2.0449$ [111] and $\varepsilon_E = 1$. For the dielectric function of the shell a Drude-type function was used: $\varepsilon_S(\omega) = \varepsilon_b - \omega_p^2/\omega^2$ with $\varepsilon_b = 6.9$ [116] and ω_p the bulk plasmon frequency of gold calculated as $\omega_p = \sqrt{ne^2/(m_e\varepsilon_0)}$ with e the electron charge, m_e the electron mass, ε_0 permittivity of free space and $n = 5.9 \times 10^{22} \text{ cm}^{-3}$ [58].

Time-dependent Kohn-Sham calculations versus experiment and Mie theory

In Ref. [105] results of time-dependent Kohn-Sham calculations were compared with absorption spectra snapshots recorded during the growth of an Au_2S -Au nanoshell in aqueous solution [7]. At the stage the snapshots were taken, the nanoshells were not fully completed and had a rough surface. The shells were modeled as perfect shells and the “ideal” sizes were determined by comparing the spectra with results of Mie theory. In this way the Kohn-Sham calculations could be compared with experimental data, although complete shells of the mentioned sizes (treatable with Kohn-Sham calculations) have not yet been fabricated experimentally. The experimental spectra showed two distinct peaks: one at the resonance wave length of nanoshells with the supposed size, and one at the resonance wave length of solid gold spheres that were also present in the solution. The resonance wave length calculated with the Kohn-Sham equations coincides with the resonance wave length of the nanoshells. The calculated and experimental width differ however substantially, with the experimental width much larger than the calculated width. This is attributed to an inhomogeneous size distribution in the experimental sample: at each moment during growth, nanoshells with different sizes are present in the solution. Introducing a size-inhomogeneity in the calculations can reproduce the experimental width. Since completed nanoshells with sizes treatable with Kohn-Sham calculations cannot be fabricated at the moment, the calculated results cannot be compared with experimental results of a single nanoshell as was done for Mie theory.

Results from Kohn-Sham calculations for a single nanoshell can be compared with results from Mie theory. This was done in Ref. [87] for nanoshells with the same size and different permittivities for the core and the environment, and for nanoshells of the same material but with different sizes. In the Mie calculations, the dielectric function of the shell was modeled by a pure Drude dielectric function, i.e. $\varepsilon(\omega) = 1 - \omega_p^2/\omega^2$. The results are shown in figure 3.12. The two calculation methods agree very well on the position of the resonance peak. No comparison was made regarding the width of the peaks.

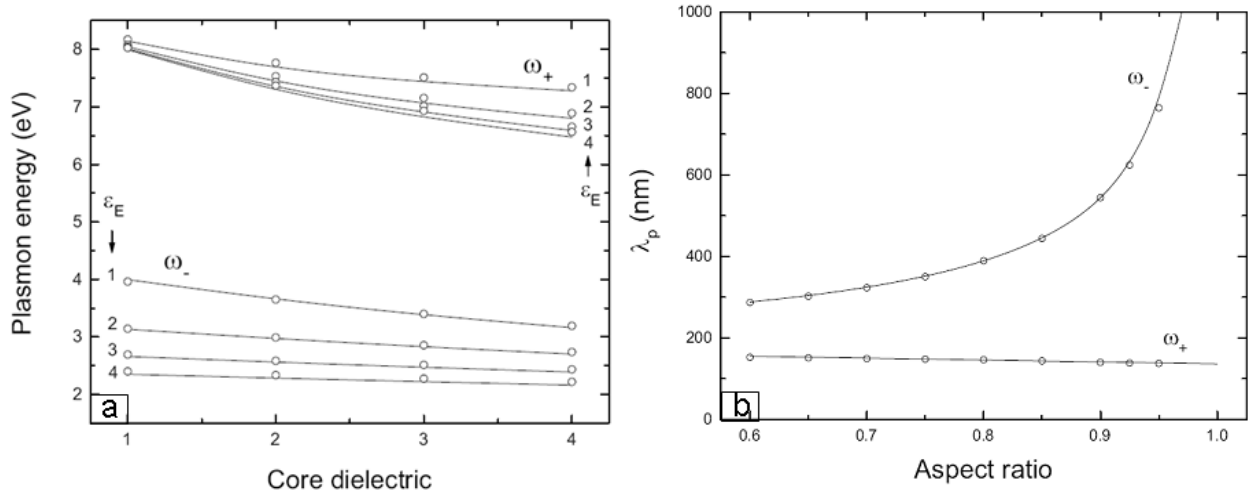


Figure 3.12: Optical active (ω_-) and optical inactive (ω_+) dipole resonance position calculated with time-dependent Kohn-Sham calculations (open circles) and with Mie theory (solid lines) in which the dielectric function of the shell was modeled as $\epsilon_S(\omega) = 1 - \omega_p^2/\omega^2$. Panel a: plasmon energy for nanoshells with $(R_C, R_S) = (60, 90)$ a.u. $\simeq (3.16, 4.76)$ nm and different permittivities in the core and the environment, as indicated in the figure. Panel b: plasmon wave lengths for nanoshells with $\epsilon_C = \epsilon_E = 1$ and $d = R_S - R_C = 17$ a.u. $\simeq 0.9$ nm for different aspect ratios, where the aspect ratio is defined as R_C/R_S . (Figures taken from Ref. [87])

3.6 Applications

The resonance frequency of SiO₂-Au nanoshells can easily be positioned in the near infrared (800 nm – 1300 nm) where absorption by biomatter is low [42]. Furthermore, gold is highly biocompatible because it is resistant to corrosion, has a very low toxicity level⁵, has inert chemical properties [42] and is resistant to ionizing radiation and high temperatures (in comparison to semiconductor structures) [120]. These properties make golden nanoshells qualified not only for *in vitro* applications, but also for *in vivo* applications. We give some more explanation on a couple of interesting examples of both types of applications.

3.6.1 Biosensor

As already mentioned, the response of nanoshells depends on the environment. This property can be used to create biosensors. As is illustrated in figure 3.13, antibodies can be attached to a nanoshell. Such an antibody is a chemical compound to which only one other specific compound, the analyte, can be bounded; the antibody can be viewed as a keyhole and the analyte as the fitting key. If one wants to determine whether and how much of a specific analyte is present in a solution, one attaches the right antibody to the nanoshell. From the change in response, one can determine the amount of analyte present.

There have already been developed quite some types of nanoshell biosensors, commercial and non-commercial, for e.g. streptavidine, antibiotine concanavaline, biomarkers for Alzheimer [137], biomolecular interactions in blood [130], detection of DNA, detection of food poisoning, screening of cancer markers (e.g. the Transmission Plasmon Biosensor of IMEC) [46], Escherichia coli [54], stanozolol [63], casein in milk [41], ...

⁵it is even eatable

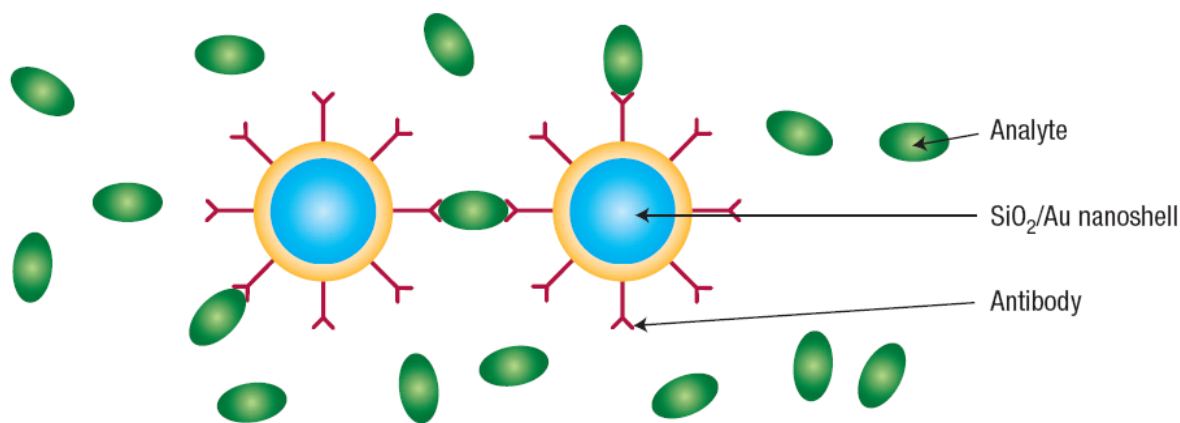


Figure 3.13: The response of a nanoshell changes when an analyte binds to an antibody that is fixed to the nanoshell. The change in optical response of nanoshells when the environment is changed is the reason why these nanoparticles can be used as biosensors (figure taken from Ref. [15]).

With this kind of biosensors, whole-blood immunoassays can be performed much faster than with more traditional methods like the Enzyme Linked Immunosorbant Assay (ELISA) which needs a time-consuming purification process, can be applied for *in vitro* use only and depends upon factors as temperature and pH. The assay based on antibody conjugated near infrared resonant nanoshells provides results within several minutes with sensitivity similar to an ELISA (see Ref. [42] and Refs. therein). Except for the shorter assay time, the nanoshell-based biosensors have the advantages that less reagents is used than for conventional biosensors, no carcinogenic substances are used, manufacturing and implementing the biosensors is rather easy and the nanoshells can easily be multiplied on a grid [46].

The possible enormous field enhancement due to surface plasmons can also lead to single-molecule sensitivity in surface-enhanced Raman spectroscopy [8, 11].

As already mentioned in section 3.3, there is an effect at bulk surfaces or films that is analogous to Localized Surface Plasmon Resonance and which is called Surface Plasmon Resonance (SPR). Biacore was the first company that used this principle to manufacture commercial biosensors and since then the effect has been used for e.g. medical diagnostics, environmental monitoring and screening of food safety [122]. There are some advantages of using Localized Surface Plasmon Resonance instead of Surface Plasmon Resonance. First of all, the simplicity of the geometry and the measurement technique of nanoparticle-based biosensors can lead to a higher portability than the relative large Surface Plasmon Resonance machine, making it possible to perform environmental or food measurements “in the field”. A related advantage is that nanoshells can be used *in vivo* where they can penetrate membranes and reach cells, organs and tissue that are unattainable for larger structures. Furthermore, there is an advantage with respect to the solvents that can be used [118]. Devices based on (flat) Surface Plasmon Resonance use microfluid channels that are not resistant to organic solvents which are often used to concentrate and extract elements from e.g. food. Therefore the samples have to be diluted. This problem is not present if one uses nanoshells, so that lower concentrations can be detected. Use of nanoshells can also lead to a smaller signal of non-specific bindings present in Surface Plasmon Resonance devices because the size of the particles can be tuned so that only the target binding molecule will attach [137]. Some other advantages can be found in a comparative table in Ref. [37].

3.6.2 Cancer treatment

With the aid of nanoshells, one cannot only trace diseases based on the optical response, one can also attempt treatment. A very interesting application is the destruction of cancer cells by a process called “photothermal ablation” [14, 10]. This process is based on the fact that the nanoshells heat up when intense laser light is shone on them for a sufficiently long time. This is due to the many collisions of the conduction electrons with ion cores and impurities when they are “shaken around” by the light of an appropriate wavelength. In this way the cancer cells and the blood vessels supplying them are “cooked” locally with minimal damage to the adjacent tissue. This procedure is much less invasive to the rest of the body as compared to e.g. chemotherapy. In 2004, the first animal tests proved that this kind of cancer treatment was effective [14]. At the moment, the patent-holding company Nanospectra Biosciences Inc. is conducting a pilot study in patients with refractory head and neck cancer, and plans to commence additional clinical studies in other cancers in the near future [82]. Because it is a combination of gold nanoshells and lasers, the commercial name of the method is “Aurolase[®] Therapy”.

The nanoparticles are delivered intravenously. Cancer vasculature grows very fast and is thus not very well formed. Unlike healthy blood vessels, it can have gaps as large as 2 microns. It is at the leaky vasculature that nanoshells can get out of the blood vessels and into tumors. This effect is called “enhanced permeability and retention effect” (EPR). After having done their job, nanoshells accumulate in the spleen and kidney from where they will be excreted.

3.6.3 Photothermal drug delivery

The phenomenon of heating is also used in photothermal drug delivery [38]. In this application, nanoshells are placed in a hydrogel together with the drug. A hydrogel is a kind of bag that collapses when being heated above a certain temperature. In this case this leads to the expulsion of the drug, which now can be delivered inside the body at a desired place. The collapse is reversible so that the action can be repeated at later times.

3.6.4 Enhancement of the efficiency of semiconductor devices

The light amplification properties of nanoshells open the way for enhancing the efficiency of existing devices. With nanoshells one would e.g. be able to enhance the emission of quantum dots and quantum wells, leading to a higher efficiency and brightness of solid-state LED’s [5]. A device called SPASER (Surface Plasmon Amplification of Stimulated Emission of Radiation) could possibly detect very small objects like small quantities of chemicals or viruses [5].

Also the enhancement of the efficiency of solar cells is a topic in which nanoshells could play a role. It is shown experimentally that incoupling of light into thin-film solar cells by scattering from solid plasmonic nanoparticles increases the photocurrent (see e.g. Refs. in Ref. [6]). These experimental observations inspired theoretical research in the TQC group on the effect of nanoshells on the efficiency of silicon solar cells. The results of this research are reported in a master thesis [124] and a bachelor thesis [21]. The effect that was investigated in these theses was that nanoshells on top of a Si n-p junction efficiently scatter the light that would otherwise impinge perpendicular to the surface, leading to a longer path of the light in the depletion layer as shown in figure 3.14. If the light travels a longer distance in the depletion layer, more charge carriers can be created that contribute to the photovoltaic current. For the calculations, the following descriptions were used. In the solar cell, the absorption of light was described by the law of Lambert-Beer and for the diffusion of charge carriers transport equations were used [84]. The response of the nanoshell was calculated with Mie theory in which the complex permittivity of the metallic shell was calculated from interpolation of experimental bulk results and only the “far-field” limit was considered.

In the master thesis [124] the following parameters were investigated in the search for an optimal configuration: the radii of the nanoshell, the density of nanoshells on the surface (for densities justifying a noninteracting nanoshell picture) and the material of the shell. The theoretical results were not decisive, because some important effects could not be incorporated in the limited framework of a master thesis. These effects include the refraction of the light at the surface of the solar cell, the angular dependence of the scattered light and near-field effects.

The topic of the bachelor thesis [21] was to derive the angular dependence of the scattered light and the refraction of this light at the surface of the solar cell. The results showed that more charge carriers are generated in the depletion layer than was found based on the calculations in which the effects were not incorporated.

Up to now, the effect of the near field has not been studied although it is expected to be important. Along with the near field, other configurations could also improve the results, e.g. placing nanoshells in or at the bottom of the solar cell, embed the nanoshells in a “cladding layer” with scatters the backscattered light from the nanoshell towards the solar cell again, ... The work of the theses is thus a first step towards more thorough study.

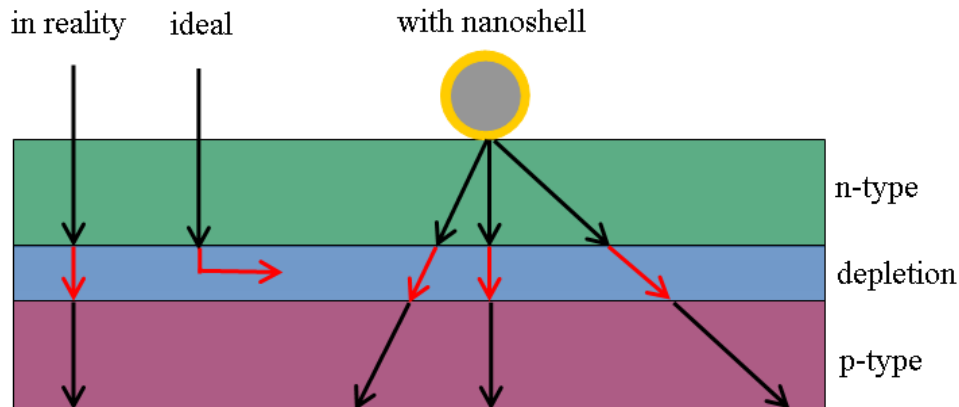


Figure 3.14: Effect of a nanoshell on a n-p Si solar cell as considered in Refs. [124, 21]: the nanoshell bends a big part of the incoming light so that the path of the light in the depletion layer is longer, leading to a higher probability to create charge carriers which contribute to the photovoltaic current.

3.6.5 Plasmonics

“Plasmonics” is a contraction of the words “plasmon” and “electronics”. The importance of this kind of electronics is visualized in figure 3.15. At the moment, we can send information around the globe quite fast and we can work on a computer that is somewhere else on the world performing difficult calculations in a reasonable amount of time. This is possible because of the existence of photonics and electronics. But as is seen in the figure and is experienced in daily life, those technologies have still a limitation on either the speed or the size that can be reached. Plasmonics can be seen as the bridge between optical fibre technology, which is limited by the diffraction limit, and electronics, which has a smaller capacity. In plasmonics, light is coupled to electrons. In this way, data can be transferred at the speed of light and this is possible in small devices because the wavelength of electrons is smaller than that of light. For this purpose one could use “photonic band gap materials” which consist of ordered rows or grids with nanoparticles. It was shown that in this kind of structures electromagnetic energy can be transported via short-field interactions between the particles [11]. This leads to the possibility of making optical networks on the nanoscale.

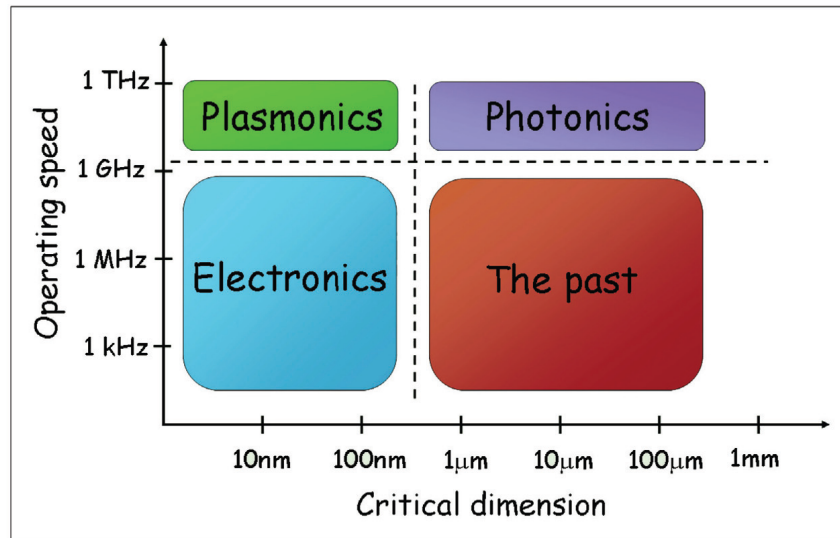


Figure 3.15: Operating speeds and critical dimensions of various chip-scale device technologies, highlighting the strengths of the different technologies (figure taken from Ref. [138]).

3.6.6 Gauge for high-pressure measurements

Together with N. Van den Broeck, J. Tempere and I. F. Silvera, I investigated the usefulness of nanoshells in the field of high-pressure physics [125], and more precisely Diamond Anvil Cell (DAC) pressure measurements [50]. The main idea behind the use of nanoshells as a pressure gauge is that the size of the nanoshell and the permittivity of the SiO_2 core and the environment will change under pressure, resulting in a shift of the resonance frequencies. The goal of the research was to calculate the optical response as a function of wavelength for a spatial distribution of non-interacting monodisperse nanoshells.

We performed the calculations for a nanoshell with parameters that are commercially available from Nanospectra Biosciences, Inc:

$$R_C = 60 \text{ nm}$$

$$R_S = 75 \text{ nm}$$

$$\varepsilon_C = \varepsilon_{\text{SiO}_2}$$

$$\varepsilon_S = \varepsilon_{\text{Au}}.$$

The first theoretical calculations for this spherically symmetric SiO_2 -gold nanoshell under pressure (up to 200 GPa) are presented, indicating clear measurable absorption peaks. There are however some problems when the nanoshells are placed in a DAC pressurization medium instead of in vacuum. It is shown below that these problems can be overcome by coating the nanoshell with an additional dielectric layer.

Except for the introduction on the diamond anvil cell, this section is largely based on N. Van den Broeck, K. Putteneers, J. Tempere, I. F. Silvera, *Nanoshells as a high-pressure gauge analyzed to 200 GPa*, *J. Appl. Phys.* **110**, 114318 (2011). The collaboration with experimentalists was facilitated by a work visit to the Silvera group (High-pressure measurements) in Harvard University, Boston, USA (January 30 - February 2, 2011).

The Diamond Anvil Cell (DAC)

A DAC is a device that can be used to perform high-pressure measurements with pressures up to 350 GPa, the pressure in the center of the earth. The device is used to recreate the pressure existing deep inside planets, creating materials and phases not observed under standard atmospheric conditions. In this way, the structure below the surface of planets can be studied without going “in the field”...

A sketch of the functional part of a DAC is shown in figure 3.16. The sample is placed between the tips of two diamonds that are cut in a “brilliant” shape. Via an external mechanism, force is applied to the table of the diamonds. This force is transferred to the tips of the diamonds. Because the pressure P on a surface A is related to the force F on the surface as

$$P = \frac{F}{A}, \quad (3.10)$$

one can create a very high pressure on the sample between the tips. The sample is placed in a metal gasket which offers the opportunity to put the sample in a fluid or a gas (the *pressurization medium*) to perform the experiment. Such pressurization medium is used to transform the uniaxial pressure generated by the diamond tips to a uniform hydrostatic pressure in the gasket. This results in an equally distributed pressure on the sample. The technique is quite demanding for the materials used, and both the gasket and diamonds have to be replaced regularly. Indeed, even one of the hardest materials on earth can be destroyed in such experiments. The advantage of diamond is of course that it does not break as easily as most materials, and that it will not deform under the high pressures. Another advantage of diamond is that it is transparent, not only in the visible spectrum, but also in the X-ray part of the spectrum. In this way, measurement techniques based on electromagnetic radiation are most of the time not hindered by the set-up itself. The measurement of the pressure is based on such techniques because the calculation of the pressure by the relation (3.10) is not very accurate. As indicated in the figure, a way to determine the pressure is to use ruby (Al_2O_3) crystals, which do not react with most samples. The shift in the fluorescence spectrum of those crystals is linearly dependent on pressure up to about 30 GPa [75,95].

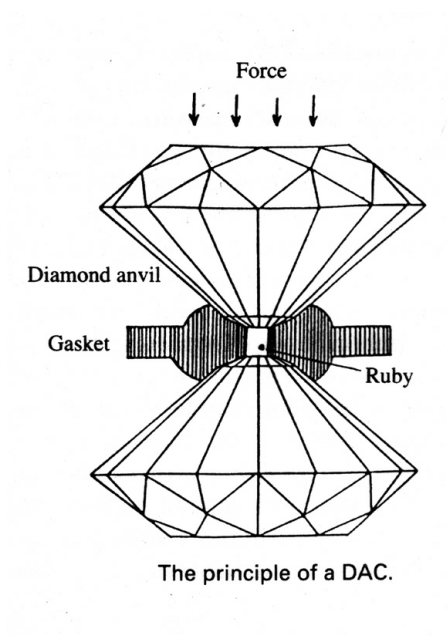


Figure 3.16: Sketch of the functional part of a Diamond Anvil Cell (figure taken from Ref. [49]).

Established measurement techniques

At present there are several pressure gauges used in high-pressure physics.

The prime pressure gauge is the shift of the peak of the ruby fluorescence spectrum with pressure [75,95], excited by laser pumping. In this case, micron sized ruby grains are embedded in the pressurization medium. Several problems can arise above a certain pressure [19,117]:

- At pressures above 100 GPa diamond fluorescence can become intense and mask the ruby line.
- Ruby grains can be blown away during loading or masked during pressurization.
- Above a few hundred GPa the standard method of pumping the ruby with a green or blue laser line becomes ineffective as the laser light is absorbed by the diamond anvil.

Although some of these problems can be overcome [18,30], the ruby method becomes challenging to use at very high pressure.

For cases where the ruby is lost or cannot be observed researchers have used the phonon Raman spectrum of the diamond from the high pressure culet or stressed region of the diamond. This is less precise and has some dependence on the diamond geometry [9].

Another method is to embed a grain of diamond in the pressurization medium, but this also has challenges and limitations [27].

An important gauge is the X-ray spectrum of metal “markers” embedded in the pressurization medium, but this is only useful at synchrotrons (and those devices are not commonly available).

Finally we mention that many of the pressure gauges have problems at high temperatures.

Advantages of nanoshells as high-pressure gauge

The advantages of nanoshells are the following:

- They can be painted onto the diamond culet in a thin invisible (to the eye) layer so they will not blow out, and they cover the entire culet flatly so they cannot easily be masked.
- They can maintain their sensitivity to the highest pressures.
- Optical spectroscopy is easy to implement with a large signal-to-noise ratio compared to fluorescence or Raman scattering.
- The spectroscopy will not be masked by fluorescence from the diamonds.
- We believe that nanoshells will maintain their sensitivity at high temperatures, but this requires further study.

Calculations

Applying a pressure P to a nanoshell will lead to a change of the volume of the core $V_C(P)$ and the shell $V_S(P)$. These changes can be calculated using the Vinet equation of state (EOS) [126]:

$$P = 3K_0 \frac{1 - \left(\frac{V}{V_0}\right)^{1/3}}{\left(\frac{V}{V_0}\right)^{2/3}} \exp \left\{ \frac{3}{2} (K_1 - 1) \left[1 - \left(\frac{V}{V_0}\right)^{1/3} \right] \right\}, \quad (3.11)$$

which gives the relation between the pressure P and the relative volume change V/V_0 with respect to a reference volume V_0 of a material at a certain temperature. Here K_0 and K_1 are material constants for which the values used in this thesis are presented in table 3.1. Using the Vinet EOS one can calculate the size change of the nanoshell under pressure where V_0 has

Material	K_0 (GPa)	K_1	ε
Amorphous SiO ₂	329 [26]	4.1 [26]	2.0449 [111]
Au	167 [136]	5.94 [136]	6.9 [116]

Table 3.1: The material properties used in the pressure calculations of the nanoshell. Parameters K_0 and K_1 are valid up to 580 GPa for gold and up to 150 GPa for amorphous silicon according to Ref. [136] and Ref. [26] respectively. The last column indicates the relative permittivity at ambient pressure. The permittivity indicated for gold is the background permittivity ε_b as defined in equation (3.5).

been taken as the original volume at zero pressure. This is done by considering the function $f(V/V_0) = P - (\text{r.h.s. of Eq. (3.11)})$. The zero of this function for a certain pressure is the relative volume at that pressure. Under pressure, the nanoshell will be compressed resulting in a different core and shell radius and a different bulk plasma frequency. For the pressure dependence of the core radius R_C we find, with V_C the core volume,

$$V_C = \frac{4\pi}{3} R_C^3 \implies R_C(P) = R_C(0) \left(\frac{V_C(P)}{V_C(0)} \right)^{1/3}. \quad (3.12)$$

For the shell radius R_S we get, with V_S the shell volume,

$$V_S = \frac{4\pi}{3} (R_S^3 - R_C^3) \xrightarrow{(3.12)} R_S(P) = \left[R_S^3(0) + R_C^3(0) \left(\frac{V_C(P)}{V_C(0)} - \frac{V_S(P)}{V_S(0)} \right) \right]^{1/3}.$$

For the bulk plasmon frequency the pressure dependence can be calculated from

$$\omega_p^2(P) = \frac{n(P) e^2}{\varepsilon_0 m} = \left(\frac{V_S(0)}{V_S(P)} \right) \omega_p^2(0), \quad (3.13)$$

where n is the bulk electron concentration defined as the number of electrons N per volume V ($n = N/V$), e is the electron charge, ε_0 is the permittivity of vacuum and m is the electron mass. The pressure dependency of the radii is shown in figure 3.17. When the nanoshell is compressed, the electron density will increase and so will the bulk plasma frequency (3.13). This will also influence the permittivity of the metal since the plasma frequency is an essential part of the Drude dielectric function $\varepsilon_S(\omega) = \varepsilon_b - \omega_p^2/\omega^2$ which is used to model the dielectric function of the metallic shell.

The pressure and frequency dependency of the permittivity of SiO₂ in the megabar regime remains, to the best of our knowledge, unknown. However it is possible to estimate the pressure dependency from the Vinet EOS using the Clausius-Mossotti relation [58]:

$$\frac{\varepsilon(\omega, P) - 1}{\varepsilon(\omega, P) + 2} = \frac{4\pi}{3} n(P) \alpha, \quad (3.14)$$

where α is the average atomic polarizability, assumed independent of pressure. This relation links the permittivity to the volume of a material. Dividing this expression with the same expression at zero pressure allows us to estimate

$$\varepsilon(\omega, P) = \frac{2 \frac{\varepsilon(\omega, 0) - 1}{\varepsilon(\omega, 0) + 2} + \frac{V_C(P)}{V_C(0)}}{\frac{V_C(P)}{V_C(0)} - \frac{\varepsilon(\omega, 0) - 1}{\varepsilon(\omega, 0) + 2}}, \quad (3.15)$$

where $V(P)/V(0)$ can be calculated from the Vinet EOS (3.11) and $\varepsilon(\omega, 0)$ represents the relative permittivity at zero pressure.

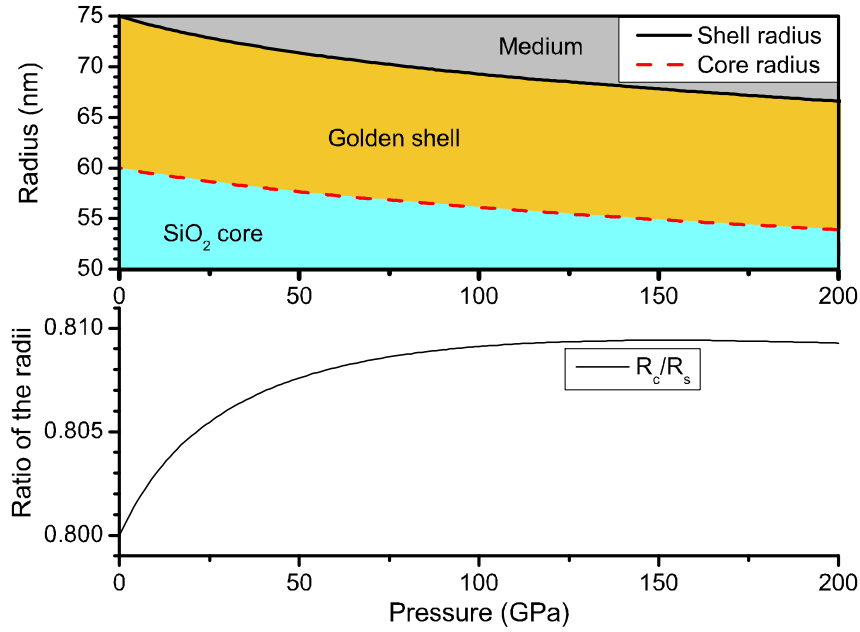


Figure 3.17: The behavior of the sizes of the nanoshell under pressure. The top panel presents the radii of the core and shell as a function of pressure. Notice that the golden shell will be compressed more strongly than the core until about 150 GPa where the core/shell ratio reaches a maximum. The bottom panel shows this ratio R_c/R_s , which is an important parameter for the optical response. The radii of the nanoshells in this research correspond to the size of commercially available nanoshells.

The pressure dependency of the permittivity of SiO₂ and of some possible pressurization media is given in table 3.2 and shown in figure 3.18. Notice that there is no phase change in the SiO₂ curve. In nature SiO₂ is in a crystalline phase at zero pressure and will switch to the amorphous phase at about 90 GPa. However, it has been reported [53] that the fabrication method of the SiO₂ particles results in cores that are in the amorphous state also at zero pressure.

Material	Refractive index n	P range (GPa)
He (fluid) [22]	$n = 0.8034 + 0.20256 (1 + P)^{0.12763}$	0.08 – 11.5
He (solid) [22]	$n = -0.1033 + (1 + P)^{0.052}$	11.7 – 20.2
H ₂ [31]	$n = -0.687343 + 0.00407826P + 1.86605 (0.29605 + P)^{0.0646222}$	0 – 100
Ne (fluid) [22]	$n = 0.668 + 0.33 (1 + 4.3P)^{0.076}$	0.7 – 4.7
Ne (solid) [22]	$n = 0.9860 + 0.08597P^{0.1953}$	5 – 27

Table 3.2: The refractive index of materials used as pressurization medium in a DAC as reported by Refs. [22] and [31]. The last column presents the pressure range of the data on which these fits are based. The dielectric function ϵ can be calculated by squaring the refractive index.

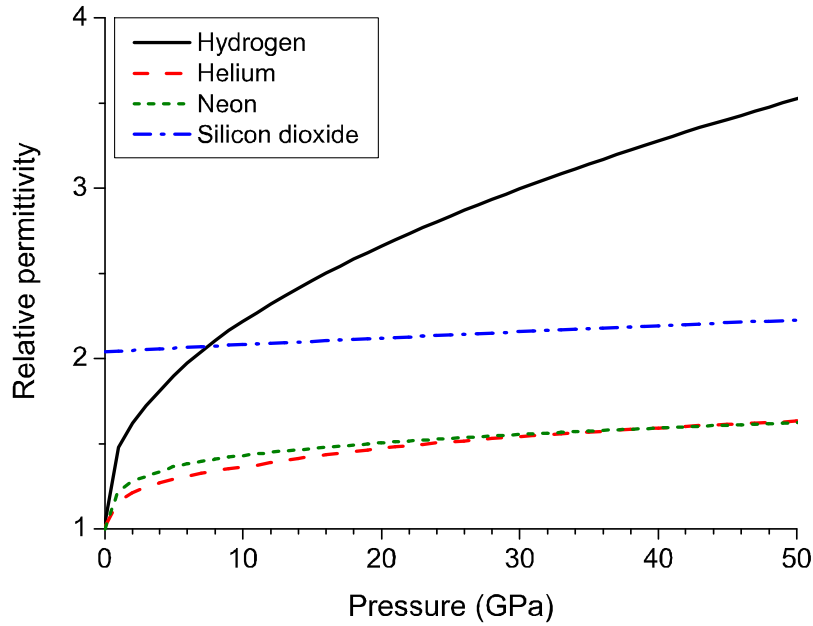


Figure 3.18: The pressure dependent permittivity of different materials. The permittivity of SiO_2 was calculated from the Vinet EOS and the Clausius-Mossotti relation. The other permittivities are given by the dependencies indicated in table 3.2 which were derived in Refs. [22, 31].

Results for an uncoated nanoshell

Figure 3.19 shows the relative cross section of the considered nanoshell placed in vacuum as calculated with Mie theory. The relative cross section is the total optical cross section $Q_{\text{ext}}(\omega)$ divided by πR_S^2 , the area of the projection of the nanoshell on a plane perpendicular to the incoming radiation. From this figure one can clearly see a substantial blue shift when 200 GPa pressure is applied. Another important observation concerns the width of the peak. This is important for increasing the precision in an experimental measurement since sharper peaks allow for a more accurate determination of the peak position. However, sharp resonance lines may elude experimental detection if they do not carry enough spectral weight. In Figure 3.19 one can see that the dipole peak (the rightmost peak) is a broad, clear and rather symmetric peak, while the quadrupole peak is much sharper and a good candidate for this type of experiments. Numerically however it is easier to track the broad dipole peak, thus all results presented here will be with regard to the dipole peak. It is seen that although the quantitative results differ for all peaks, the qualitative results presented here hold true for all resonance peaks.

In figure 3.20 the position of the dipole resonance peak is shown as a function of pressure for a nanoshell in a medium with constant permittivity equal to $\varepsilon = 1$. The black squares are calculated using Mie theory and a subsequent numerical determination of the peak maximum. Results from the hybridization theory are presented by the red circles. It is clear that the two theories do not agree on the exact position of the resonance peak for the considered nanoshell. The difference between the results of both theories at zero pressure thus remains at non-zero pressure. Still the hybridization model can prove to be useful because both theories agree well on the amount the peak shifts, as is shown in the inset of figure 3.20. The two theories diverge from each other only at higher pressures.

The results show that the nanoshell could be used to measure the pressure by determining the amount the resonance peak shifts. The inset is also an indication of the resolution that could be achieved. For this example nanoshell the dipole resonance peak shifts over 80 nm when 200 GPa pressure is applied (for rubies this would be 51.1 nm [19, 117]).

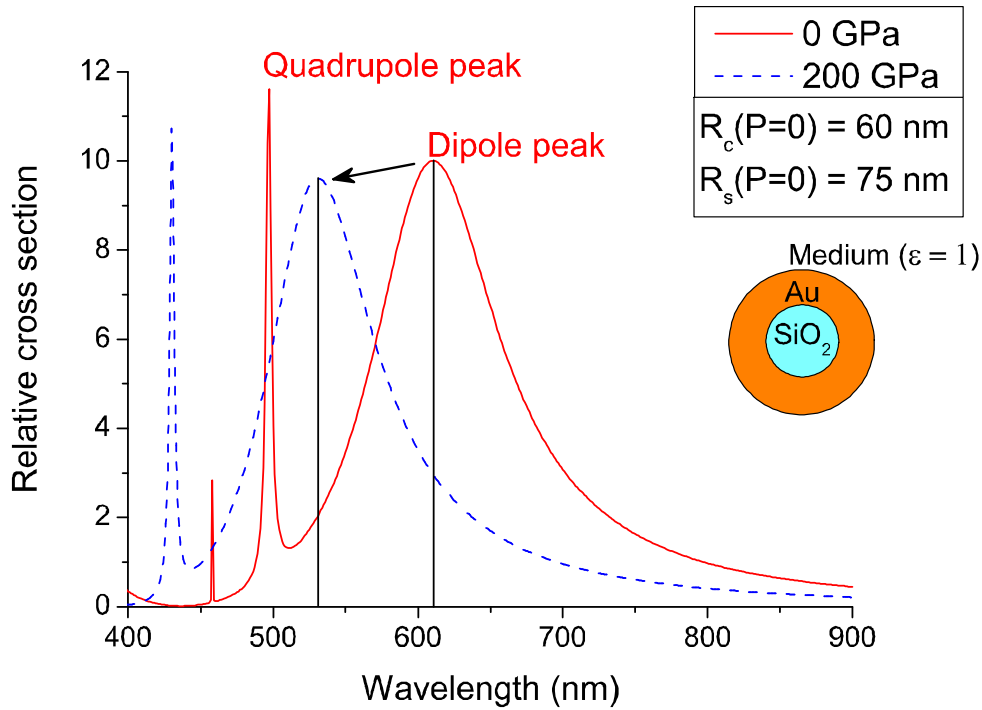


Figure 3.19: Relative cross section as function of wavelength for different pressures for a nanoshell with parameters as mentioned in the figure. Notice the pressure-induced blue shift of the dipole peak from 611 nm at 0 GPa to 531 nm at 200 GPa as indicated by the two black lines.

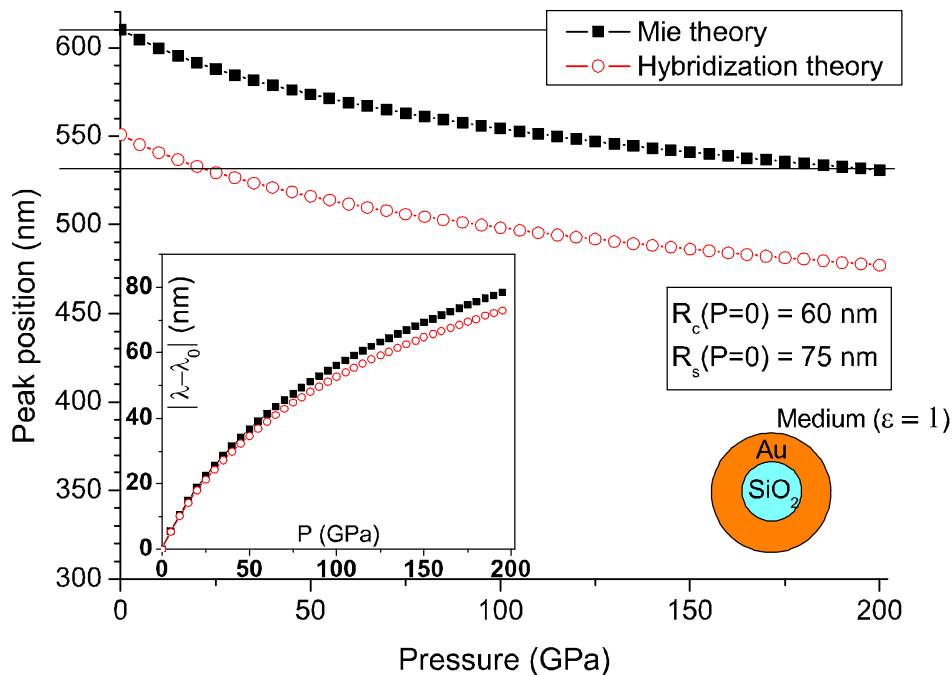


Figure 3.20: The position of the dipole resonance peak as a function of pressure for a nanoshell with parameters as mentioned on the figure. The two horizontal black lines correspond to the two black lines on figure 3.19. The blueshift from 611 nm at 0 GPa to 531 nm at 200 GPa as predicted by Mie theory is clearly visible. The red circles were calculated with hybridization theory and also indicate a blue shift, but predict a different peak position. The inset shows the peak shift as a function of pressure compared to the original position λ_0 at zero pressure.

The nanoshell's optical response depends on the dielectric function of the surrounding medium, and as such both the position of the resonance peaks and their pressure-induced shift will differ for different pressurization media. To determine the usefulness of nanoshells as a pressure gauge, calibration would thus be needed for every pressurization medium separately. The pressure dependency of the resonance peaks in different pressurization media was calculated using the pressure dependency of the refractive index of the media as given in table 3.2 and shown in figure 3.18. In Figure 3.21 one can see the pressure dependency of the position of the dipole resonance peak for different pressure media: helium, hydrogen and neon. The behavior of the medium under pressure clearly has a large influence on the optical response of the nanoshell. For these media, the blue shift that occurs in vacuum has turned into a red shift as pressure is increased. For neon and helium there is almost no shift of the resonance peak above a certain pressure, rendering the nanoshells ineffective as pressure gauges in that region. Although it is possible to calculate the optical response of nanoshells for much higher pressures, the results are not presented here because they are based on extrapolation of data from a limited pressure region and as such are considered unreliable.

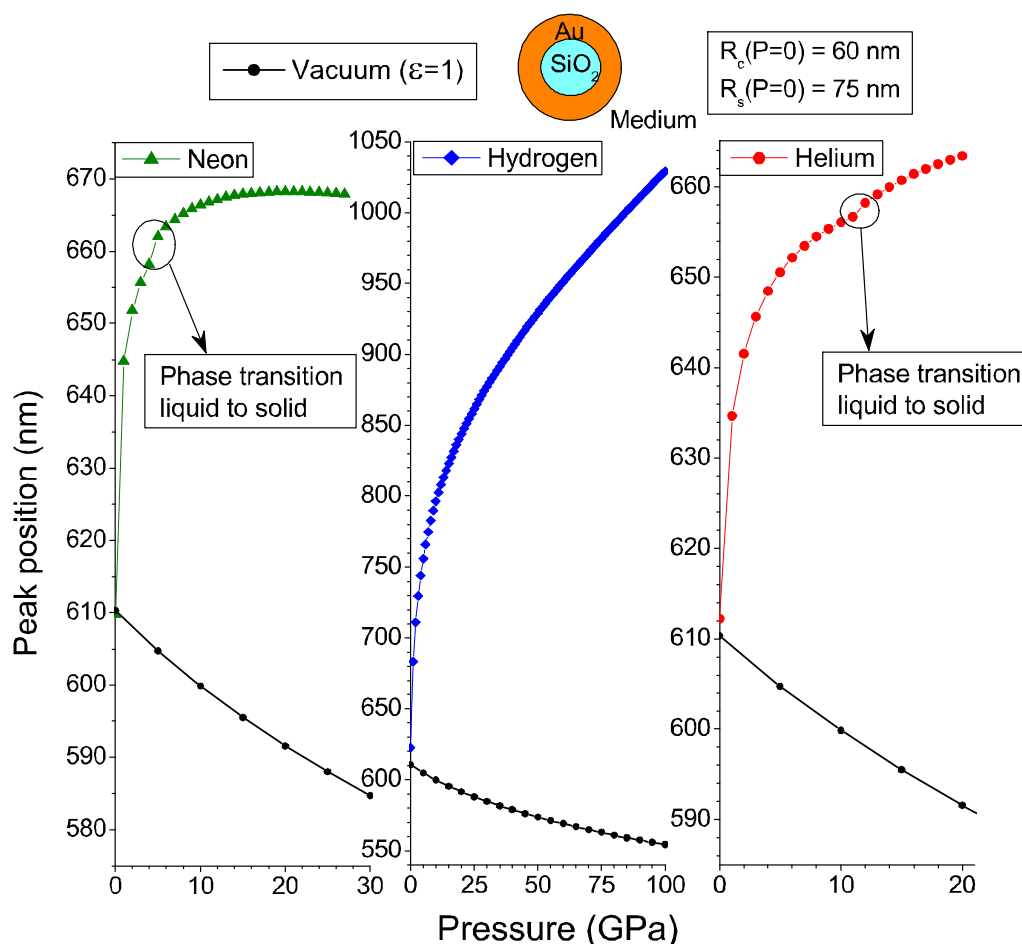


Figure 3.21: The position of the dipole peak as calculated with Mie theory for various pressure media: helium (red circles), hydrogen (blue diamonds) and neon (green triangles). In all figures the vacuum position is indicated in black for reference and the phase transition from liquid to solid in neon and helium is indicated. The plots only show the pressures for which experimental data are available.

Results for a coated nanoshell

As was seen in the previous section, the simple nanoshell geometry is not ideal for high-pressure experiments. Two draw-backs are apparent from figure 3.21:

1. The peak shift is affected by the pressurization medium, so calibration will be necessary for each nanoshell and medium.
2. For helium and, especially, for neon from a certain pressure on there will be almost no shift of the resonance peak, rendering the nanoshells ineffectual as pressure gauges in that region.

A possible solution would be to shield the nanoparticle from the effects of the medium, therefore allowing the shift of the resonance peak to be influenced only by the compression of the nanoparticle. The absence of the second problem when the nanoshell is placed in vacuum indicates that shielding the particle could indeed result in a pressure gauge that can be used in the entire pressure regime.

Shielding the nanoparticle from the environment means creating a barrier between the golden shell and the dielectric medium. This barrier should also be a dielectric. If not, another set of surface plasmons polaritons would arise on the interface between the outer layer and the environment, counteracting the intent of the extra layer. In the performed research the extra coating is achieved by adding an extra SiO_2 layer to the model. Henceforth we shall indicate this type of nanomatryushka [110] as “coated nanoshell”. The main questions to be answered are whether the coating has the desired effect and how thick this coating should be to effectively shield the nanoshell from the pressure effects on the dielectric function of the environment.

For the calculations we used Mie theory. Extending Mie theory to three concentric spheres, although not available in literature, does not provide any new problems in comparison with the two concentric sphere case solved by Aden and Kerker [2]. The final expressions for the electromagnetic fields in and around the coated nanoshell, as well as the optical cross section, are given in the appendix of Ref. [125]. Although the expression for the resonance frequency for multiple layered nanoshells derived with hybridization theory is available in literature [108], it is not considered here due to the expected deviations from the experimental values since the diameters of the coated nanoshell particles are two or three times larger than the nanoshell particles.

For reasons of comparison the core and the thickness of the golden shell are kept the same as for the nanoshell discussed before. Furthermore we have only studied the coated nanoshell in a helium environment since this is a commonly used quasi-hydrostatic pressure medium in DAC experiments. In neon the results will be almost the same because the dielectric functions of helium and neon are similar as was shown in figure 3.18. For hydrogen the counteracting effect is not present; therefore the results with nanoshells are adequate and no further improvements are necessary.

Figure 3.22 presents the dipole peak position for several coating thicknesses of the coated nanoshell as calculated by Mie theory. It can be seen that for the thinnest coatings the red shift due to the effect of the medium is still visible. At a certain pressure the peak position will reach a maximum and from there on the peak will undergo a blue shift which is due to the compression of the nanoshell similar to the results in vacuum (figure 3.20). This maximum is indicated by the black crosses and can be used as a measure for the pressure up to which the medium affects the optical response of the nanoparticle. It is clear that for thicker coatings the maximum shifts to lower pressures, suggesting that the influence of the medium indeed diminishes and thus that the coating effectively shields the nanoparticle. Unfortunately the red shift never disappears completely, meaning that the influence of the medium cannot be fully shielded by the dielectric layer. However, it is possible to position the maximum into a pressure region where it can do no harm for the pressure measurements.

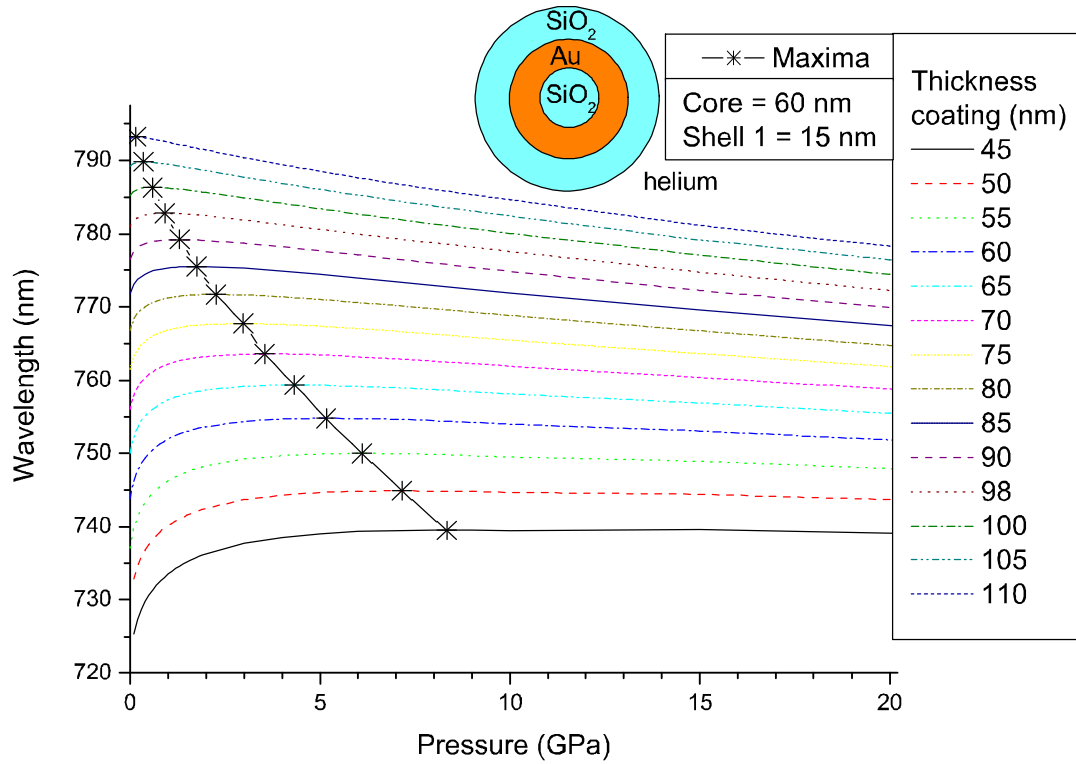


Figure 3.22: The dipole peak position as a function of pressure for the coated nanoshell with a 60 nm SiO_2 core, a 15 nm thick golden shell and for different thicknesses of the outer SiO_2 coating. For small coatings the red shift due to the influence of the pressurization medium is still clearly visible, while for thick coatings this effect seems to disappear. The black crosses indicate the pressure at which the wavelength peak position is maximal and where the red shift turns into a blue shift.

Apart from the position of the resonances, we observed that the optical response of the uncoated and the coated nanoshells also differed in the height of the relative cross section, i.e. the total optical cross section $Q_{\text{ext}}(\omega)$ divided by πR_{tot}^2 with R_{tot} the total radius of the considered particle. The maximum of the relative cross section of the coated nanoshell is lower than that of the uncoated nanoshell shown in figure 3.19. However, since the coated nanoshells are larger than the uncoated shell, their absolute optical cross section is larger. This means that less coated nanoshells than uncoated nanoshells are needed to obtain the same intensity. The nanoparticle density in the DAC can thus be kept low enough to avoid nanoparticle interaction and clustering.

The derivative of the curves in figure 3.22 gives a direct indication of the sensitivity achievable with the coated nanoshell structures. On average the sensitivity for the coated nanoshell with a 110 nm thick coating (upper curve on Figure 3.22) is approximately 0.90 nm/GPa. The resolution for ruby grains in the same pressure regime (0 GPa to 20 GPa) is approximately 0.36 nm/GPa [117] and for a nanoshell in vacuum, as was shown in figure 3.20 this would be 0.94 nm/GPa. From this we can conclude that the theory predicts a better resolution for (coated) nanoshells than for rubies in the pressure regime under consideration.

Discussion and Conclusions

We have carried out a theoretical analysis of nanoshells which can be designed so that they have absorption peaks in the IR-visible part of the optical spectrum due to scattering or absorption by localized surface plasmon polaritons. Calculations indicate that for nanoshells in vacuum these peaks have a substantial shift with pressure making them suitable as a pressure gauge for high-pressure research. A useful pressure gauge should have a calibration (peak wavelength versus pressure) independent of the pressurization medium. We found that for a simple nanoshell consisting of a SiO₂ core and a gold shell, the calibration differed with the pressurization medium; moreover it was double-valued and had a region of zero slope. The latter problem was resolved by coating the nanoshell with a SiO₂ cladding, resulting in a robust sensitive pressure gauge.

A possible implementation of the coated nanoshell would be to distribute them inside the DAC cell together with the ruby on the diamond culet. For low pressures both gauges can be used and the coated nanoshell can be calibrated by using the extensive knowledge of the behavior of ruby under pressure [117]. A possible challenge is the application of nanoshells to the surface of a diamond culet. A droplet can be placed on the culet and allowed to evaporate to produce a coverage bonded to the surface by van der Waals forces. Preliminary measurements show that to avoid clustering and segregation, it may prove useful to functionalize the diamond surface with a film of poly-4-vinylpyridine (PVP) which has dense sites that localize the nanoparticles [74]. For high pressures the ruby measurement would be difficult or no longer be possible. The spectra of the coated nanoshells however will still be measurable since these measurements are based on absorption and transmission. In this way nanoshells could be easily used and effectively extend pressure measurements to ultra high pressures.

Chapter 4

Conventions and approximations

First some word usage so that often used terminology is well-defined. With the term *potential well*, we refer to a well-shaped form of the potential energy (for a negative charge). If we talk about a *background charge*, we mean a positive unit charge (from an ion in the shell). Although no physical meaning can be attributed to the Lagrange multipliers ϵ in self-consistent calculations, we sometimes talk about the (*effective*) *single-particle energies*. We consider a spherically symmetric system, but we will not always put “radial” in front of the word *wave function*: the radial part of the wave function is the only part of interest in the calculations.

In the used methods, we do not have to consider the **boundary condition for infinite radius** at the finite radius of an “auxiliary sphere” as is done in the Kohn-Sham calculations in Refs. [101, 102, 103, 104, 87, 106]. Although the boundary condition will be satisfied rather close to the nanoshell, determining such a radius is artificial and could give densities different from the correct density. If the radius is chosen too close to the particle, the electrons are forced into a region that is smaller than the one in which they would be in reality. If the radius is chosen too large, electrons will have a larger density in a region where they would not be in reality.

The calculations are performed in the **jellium model** which was explained in section 1 and which was used in the Kohn-Sham calculations of Refs. [101, 102, 103, 104, 87, 106]. Calculations in Ref. [68] for a flat gold surface show that inclusion of a rather simple pseudopotential describing the periodic background potential, leads to an increase of the work function of 0% up to about 11% depending on the crystal face. This indicates that incorporating an effect of the spatial variations of the background will not appreciably alter the magnitude of the work function. The background charge density $\rho_b(\mathbf{r})$ is spherically symmetric, $\rho_b(\mathbf{r}) = \rho_b(r)$, and has the form

$$\rho_b(r) = \begin{cases} 0 & r < R_C \\ n_0 = \frac{N}{V_{shell}} = \frac{3}{4\pi} \frac{N}{R_S^3 - R_C^3} & R_C \leq r \leq R_S \\ 0 & R_S < r \end{cases} .$$

To calculate the work function, we consider **no external potential well** confining the conduction electrons in the shell. There is no external potential prohibiting the electrons to leave the metal; the only difference between the region inside and outside of the shell is that inside the shell there is a neutralizing background and outside of the shell there is not. If the electrons leave the metal, the shell will become positively charged. A positively charged shell will attract the electrons outside the metal. A mechanism arises that leads to an equilibrium situation in which the electrostatic interaction between the conduction electrons and the background and between the conduction electrons mutually causes a potential well by which the electrons mostly stay in the shell.

The influence of the **dielectric core** on the electrons is taken into account via a dielectric constant screening all electron interactions (Hartree, exchange, correlation).

Near-to-zero temperatures are assumed. In this context, no phonons are considered.

Part II

Aspects of orbital-based calculations

This part is a report on a feasibility study of performing orbital-based calculations for nanoshells with manufacturable sizes. Previously, Prodan and Nordlander succeeded to perform orbital-based calculations for small nanoshells (see section 3.5.3). In that work the solution method for the effective single-particle Schrödinger equations required 33000 grid points to get a sufficient accuracy for the eigenenergies of a nanoshell with $(R_C, R_S) = (13.1, 15.1)$ nm. For the smallest manufacturable SiO₂-Au nanoshell of $(R_C, R_S) = (40, 55)$ nm, the number of grid points would be unmanageably high. This is why we considered another method to determine the orbitals, namely the Transfer Matrix Method.

The part is divided in two chapters. In chapter 5, we explain how we determined the *orbitals* of the N conduction electrons of a nanoshell. We start with two sections on the general treatment of the degenerate orbitals of a spherically symmetric system. Then we explain the Transfer Matrix Method and how it is used to solve the effective single-particle radial Schrödinger equations. Chapter 6 contains a study of an ideal Fermi gas confined to a spherically symmetric infinite and finite *potential well* $u_{\text{well}}(r)$ between the radii R_C and R_S . These models of non-interacting fermions in a spherically symmetric potential well can be viewed as the simplest models for a nanoshell and show similarities and differences with the (in)finite square well discussed in chapter 1 on basic concepts. The problems can be solved exactly and provide a test for the Transfer Matrix Method which can be used in problems that are not exactly solvable. Although the Transfer Matrix Method appears to have advantages over finite difference integration in determining the orbitals, it will become clear that also with the Transfer Matrix Method an orbital-based treatment of nanoshells with manufacturable dimensions is not practicable.

Portions of the work discussed in this part were presented in three posters:

- “Nanoshells: calculation of the work function using non-standard methods” at Nanometa 2011, Seefeld, Austria (03-06/01/2011)
- “Electrons in a nanoshell ready to get excited” at Two days of theoretical and mathematical physics (Flanders), Koksijde (28-29/05/2010) and at ‘Fysica 2010’ - Dutch and Belgian Physical Society, Utrecht, Nederland (23/04/2010)
- “Non-interacting electrons in a nanoshell” at the Joint general scientific meeting - Belgian Physical Society and Belgian Biophysical Society, Hasselt (01/04/2009)

Chapter 5

Bookkeeping and determination of the spherically symmetric orbitals

5.1 Radial differential equation, wave functions and density

In general the three-dimensional static effective Schrödinger equation for a particle with wave function $\psi(\mathbf{r})$ in a potential energy $u_{\text{eff}}(\mathbf{r})$ is given by

$$-\frac{1}{2}\Delta\psi(\mathbf{r}) + u_{\text{eff}}(\mathbf{r})\psi(\mathbf{r}) = \epsilon\psi(\mathbf{r})$$

with ϵ an energy eigenvalue. In the case of a nanoshell the potential energy is spherically symmetric, $u_{\text{eff}}(\mathbf{r}) = u_{\text{eff}}(r)$, and it is convenient to formulate the Schrödinger equation in the spherical coordinates $r \in [0, \infty[$, $\theta \in [0, \pi[$, $\varphi \in [0, 2\pi[$. With the usual product ansatz $\psi(r, \theta, \phi) = \mathfrak{R}(r)\Theta(\theta)\Phi(\phi)$ one finds that the angular part can be written with the spherical harmonics $Y_{\ell,m}(\theta, \varphi)$, so that

$$\psi(r, \theta, \phi) = \mathfrak{R}(r)Y_{\ell,m}(\theta, \varphi), \quad (5.1)$$

and that the radial part $\mathfrak{R}(r)$ of the wave function satisfies the differential equation

$$\boxed{\frac{1}{r^2} \frac{d}{dr} \left(r^2 \frac{d}{dr} \right) \mathfrak{R}(r) + \left[2\epsilon - \left(2u_{\text{eff}}(r) + \frac{\ell(\ell+1)}{r^2} \right) \right] \mathfrak{R}(r) = 0.} \quad (5.2)$$

The single-particle energies and the form of the radial wave functions depend in general on three quantum numbers:

1. the angular quantum number $\ell = 0, 1, 2, \dots$
2. the radial or principal quantum number denoted by $\mathbf{n} = 1, 2, 3, \dots$ ($\mathbf{n} = 1$ for the lowest state that can be occupied for a given value of ℓ , $\mathbf{n} = 2$ for the second lowest state that can be occupied for a given ℓ -value, ...). We use this quantum number in analogy with the hydrogen atom but we will see below that the boundary conditions in the radial direction do not result in an analytical expression for the energy values as a function of \mathbf{n} , as it was the case for the hydrogen-like atom. In all problems we will discuss, the electrons will be confined in a kind of potential well. The physical meaning of the quantum number \mathbf{n} is then the same as that of the quantum number in e.g. the (in)finite square well: a wave function with quantum number \mathbf{n} has $\mathbf{n} - 1$ nodes in the well.

- the spin quantum number $\sigma = \pm 1/2$. In problems without spin polarization, like the problem under study, the radial wave function and energy for given ℓ and \mathbf{n} is the same for both values of the spin component.

Note that in contrast to the case of the hydrogen-like atom where the values of ℓ are bounded by $\ell < \mathbf{n}$, there is in general no restriction on the value of ℓ with respect to \mathbf{n} . This restriction in the case of the hydrogen-like atom followed from the boundary conditions imposed on the analytical solution of the radial Schrödinger equation with $u_{\text{eff}}(r) \propto -1/r$ in the entire considered region. Also in contrast to the hydrogen-like atom for which $\epsilon = \epsilon_{\mathbf{n}} \propto -1/\mathbf{n}^2$, the energy levels of a nanoshell are dependent on both \mathbf{n} and ℓ . Based on the mentioned quantum number dependency, we denote the radial wave functions as $\mathfrak{R}_{\mathbf{n},\ell}(r)$ and the single-particle energies as $\epsilon_{\mathbf{n},\ell}$.

For simplicity we consider zero temperature and assume that the highest energy level is completely occupied. For an unperturbed system with many electrons, there will be a negligible influence on the density whether the states of the highest energy level are completely or partially occupied. In this feasibility study on orbital-based calculations, no self-consistent calculations are performed. In this way the assumption of completely filled highest energy level also does not lead to problems of charge non-neutrality that would occur when using the resulting electrostatic potential energy for a next iteration. Using the product ansatz (5.1), the electron particle density $n(\mathbf{r}) = n(r, \theta, \varphi)$ can then be written as

$$n(r, \theta, \varphi) = \sum_{\mathbf{n}, \ell, m, \sigma} |\psi_{\mathbf{n}, \ell, m, \sigma}(r, \theta, \varphi)|^2 = 2 \sum_{\mathbf{n}, \ell} |\mathfrak{R}_{\mathbf{n}, \ell}(r)|^2 \sum_{m=-\ell}^{\ell} |Y_{\ell, m}(\theta, \varphi)|^2.$$

With the aid of the theorem of Unsöld,

$$\sum_{m=-\ell}^{\ell} Y_{\ell, m}^*(\theta, \varphi) Y_{\ell, m}(\theta, \varphi) = \frac{2\ell + 1}{4\pi},$$

we find that the electron density is spherically symmetric and can be calculated from the radial wave functions $\mathfrak{R}_{\mathbf{n}, \ell}(r)$ as:

$$n(r, \theta, \varphi) = n(r) = \frac{1}{4\pi} \sum_{\mathbf{n}=1}^{\mathbf{n}_{\max}} \sum_{\ell=0}^{\ell_{\max}(\mathbf{n})} 2(2\ell + 1) |\mathfrak{R}_{\mathbf{n}, \ell}(r)|^2$$

with \mathbf{n}_{\max} and $\ell_{\max}(\mathbf{n})$ defined such that all the considered particles are taken into account. The single-particle energies are $2(2\ell + 1)$ times degenerate.

5.2 Orbital bookkeeping

This section is devoted to the bookkeeping burden that arises when doing orbital-based calculations with degenerate energy levels.

We will use that at zero temperature all single-particle energy levels below an energy ϵ_{\max} are filled and all energy levels above ϵ_{\max} are empty. The highest occupied energy level ϵ_{\max} is often called the chemical potential μ , and in the case of non-interacting particles it is also called the Fermi-energy ϵ_F . To check whether enough orbitals are included, we use that the number of particles can be calculated in two different ways: as the mean density of particles \bar{n} times the volume V ,

$$N = N_{nV} = \bar{n} \times V,$$

and as the sum of the lowest-energy states,

$$N = N_{\text{states}} = \sum_{n=1}^{n_{\text{max}}} \sum_{\ell=0}^{\ell_{\text{max}}(n)} 2(2\ell + 1).$$

We can thus use the following function

$$f(\mathbf{n}', \ell'(\mathbf{n})) = N_{nV} - 2 \sum_{n=1}^{n'} \sum_{\ell=0}^{\ell'(\mathbf{n})} (2\ell + 1). \quad (5.3)$$

that will become zero if all electrons with an energy up to ϵ_{max} are included.

In cases where the energy is dependent on one integer quantum number k and $\epsilon_{k-1} < \epsilon_k$, as in the case for e.g. the one-dimensional (in)finite potential well or the hydrogen-like atom, one just has to calculate the orbitals subsequently for $k = 1, k = 2, \dots$ until there are enough orbitals calculated to represent all the N particles present in the considered system.

As we have seen in the previous section, the energy levels of a general spherically symmetric system depend on two quantum numbers: the angular quantum number ℓ and a quantum number that we denote by \mathbf{n} . There is no analytical relation between the energy and an integer $\mathbf{n} \in \mathbb{N}_0$. We *define* $\mathbf{n} = 1$ for the lowest state that can be occupied for a given ℓ -value, $\mathbf{n} = 2$ for the second lowest state that can be occupied for a given value of ℓ , ... With the definition of \mathbf{n} it is obvious that

$$\epsilon_{\mathbf{n}, \ell} < \epsilon_{\mathbf{n}' > \mathbf{n}, \ell}. \quad (5.4)$$

We will see later on that for a spherically symmetric potential well also the following relation holds for energy levels with different ℓ -values:

$$\epsilon_{\mathbf{n}, \ell} < \epsilon_{\mathbf{n}, \ell' > \ell}. \quad (5.5)$$

But in advance the relative magnitude of energy levels with different \mathbf{n} and ℓ is undetermined:

$$\epsilon_{\mathbf{n}, \ell} \stackrel{?}{\underset{>}{\lesssim}} \epsilon_{\mathbf{n}' \neq \mathbf{n}, \ell' \neq \ell}. \quad (5.6)$$

To answer this question we have to solve the corresponding Schrödinger equations.

Because of the question (5.6) we cannot easily calculate subsequent energy levels for a system which depends on more than one quantum number. In theory we could of course calculate millions of orbitals and then just keep the ones with the lowest energy. But this would take, gently stated, a lot of time.

We will discuss two ways of avoiding to calculate too many orbitals. For that purpose we use a fictitious energy spectrum as shown in figure 5.1. Real energy spectra can look very different, but we use this energy spectrum to sketch the bookkeeping ideas.

Knowing relations (5.4) and (5.5) one starts of course by solving the problem for the state with $\{\mathbf{n}, \ell\} = \{1, 0\}$ because this state has the lowest energy. This results in the wave function and energy of $2(2 \times 0 + 1) = 2$ electrons. There are then in theory two possibilities for which the energy level can be the next higher one: $\{\mathbf{n}, \ell\} = \{2, 0\}$ or $\{\mathbf{n}, \ell\} = \{1, 1\}$. Not knowing the energy spectrum in advance, one has to solve the Schrödinger equation for these two cases. If the energy spectrum is like in figure 5.1, then one will find that $\epsilon_{1,1} < \epsilon_{2,0}$. One includes the state $\{1, 1\}$ so one has found the wave function and energy of $2(2 \times 1 + 1) = 6$ additional electrons. Now one does not know in advance whether the state $\{2, 0\}$ will also be included later on. Because solving the Schrödinger equation takes some time, one would want to store the resulting energy and wave function.

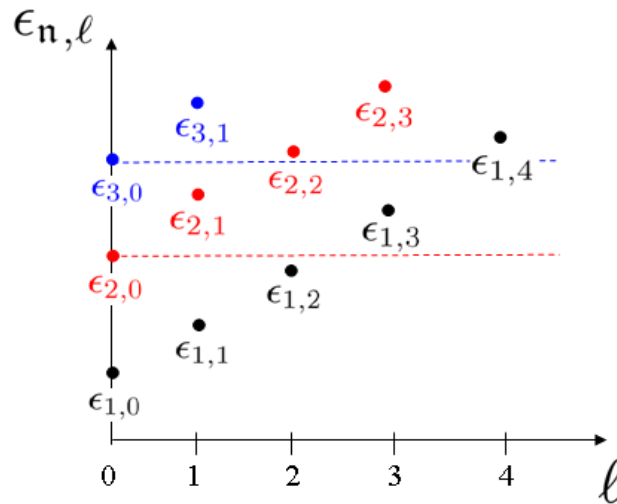


Figure 5.1: Fictitious energy spectrum to explain the bookkeeping of orbitals.

5.2.1 Smallest amount of orbital calculations, much bookkeeping

One way to proceed is like this: one stores the results of the retained states $\{1, 0\}$ and $\{1, 1\}$ and one stores the result for $\{\mathbf{n}, \ell\} = \{2, 0\}$ separately. Then one calculates the possible next higher energy $\epsilon_{1,2}$, and compares it with the stored value $\epsilon_{2,0}$. In our fictitious case we would find $\epsilon_{1,2} < \epsilon_{2,0}$ and accept the state $\{1, 2\}$, leaving the state $\{2, 0\}$ stored. Another possible next higher energy would now be $\epsilon_{1,3}$ so one solves the Schrödinger equation for $\{\mathbf{n}, \ell\} = \{1, 3\}$. Now $\epsilon_{1,3} > \epsilon_{2,0}$ so one accepts the state $\{2, 0\}$ and stores the state $\{1, 3\}$ in place. Now besides the calculated case $\{\mathbf{n}, \ell\} = \{1, 3\}$, there are two new possible cases with higher energy: $\{\mathbf{n}, \ell\} = \{2, 1\}$ and $\{\mathbf{n}, \ell\} = \{3, 0\}$. So the Schrödinger equation for these two cases has to be solved and the energies $\epsilon_{1,3}$, $\epsilon_{2,1}$ and $\epsilon_{3,0}$ have to be compared. The state with the lowest energy, $\{1, 3\}$, is retained and the other two states are stored. Except for these two states, there is another possible case with next higher energy, $\{\mathbf{n}, \ell\} = \{1, 4\}$, so there is one additional Schrödinger equation to be solved and the energies $\epsilon_{1,4}$, $\epsilon_{2,1}$ and $\epsilon_{3,0}$ have to be compared. In general, if \mathbf{n} is the highest \mathbf{n} -value that is in the running in the next-highest-energy competition, then $\mathbf{n} - 1$ states have to be stored for possible future use and each time \mathbf{n} energies have to be compared.

To keep track of which orbitals have to be calculated, one can use an array that contains for each \mathbf{n} -value up to which ℓ -value the orbitals are calculated. The procedure then looks like this for the first steps (-1 is the starting value for the ℓ -column if no orbitals are calculated yet):

\mathbf{n}	ℓ done	to do										
1	0	$\{1, 1\}$		1	$\{1, 2\}$		2	$\{1, 3\}$		3	$\{2, 1\}$	
2	-1	$\{2, 0\}$	→	0		→	0		→	0	$\{3, 0\}$	→ ...
3	-1			-1			-1			-1		
...		

So in every step, one Schrödinger equation has to be solved (for the $\{\mathbf{n}, \ell + 1\}$ -state), except when a state with $\ell = 0$ is accepted. In that case, two Schrödinger equations have to be solved: for $\{\mathbf{n}, 1\}$ and for $\{\mathbf{n} + 1, 0\}$. This is one part of the bookkeeping.

Another part of the bookkeeping concerns the energy comparison. A way to deal with this, is to have an array in which the energies from not-yet accepted states are sorted, lowest energy in the first place, and to which the corresponding quantum numbers and wave function are

linked. For step three we would have, before the acceptance of state $\{2, 0\}$:

$$\begin{aligned} \epsilon_{2,0} &\rightsquigarrow \{2, 0\}, \mathfrak{R}_{2,0}(r) \\ \epsilon_{1,3} &\rightsquigarrow \{1, 3\}, \mathfrak{R}_{1,3}(r) \end{aligned} .$$

With the orbitals sorted such that the lowest-energy orbital is in the first place, it is obvious that $\epsilon_{2,0}$ is the lowest energy and the state $\{2, 0\}$ has to be accepted. After one has solved the Schrödinger equation for states $\{2, 1\}$ and $\{3, 0\}$ and sorted the energies, one would get this situation:

$$\begin{aligned} \epsilon_{1,3} &\rightsquigarrow \{1, 3\}, \mathfrak{R}_{1,3}(r) \\ \epsilon_{2,1} &\rightsquigarrow \{2, 1\}, \mathfrak{R}_{2,1}(r) \\ \epsilon_{3,0} &\rightsquigarrow \{3, 0\}, \mathfrak{R}_{3,0}(r) \end{aligned}$$

and after acceptance of the state $\{1, 3\}$:

$$\begin{aligned} \epsilon_{2,1} &\rightsquigarrow \{2, 1\}, \mathfrak{R}_{2,1}(r) \\ \epsilon_{3,0} &\rightsquigarrow \{3, 0\}, \mathfrak{R}_{3,0}(r) \end{aligned}$$

in which then the state $\{1, 4\}$ has to be inserted on the right place.

In the procedure explained above, the results have to be sorted according to the energy each time new orbitals have been calculated. If the calculations proceed, more and more energies have to be sorted in each step. Now sorting is also a time-consuming task and very many times it is useless because the states will be included later on anyway. That is why we have used a more straightforward way with somewhat less bookkeeping and much less sorting.

5.2.2 More efficient bookkeeping

In this section we explain the procedure we have used. We first give a concrete exposition using the fictitious energy spectrum shown in figure 5.1. Afterwards we set out the formal generalization which is visualized in the flowchart of figure 5.2.

We performed subsequent steps p in which we considered “trial chemical potentials” $\mu(p)$. In each step, the orbitals with energies up to $\mu(p)$ were calculated. For the fictitious energy spectrum of figure 5.1, the procedure would be as follows if we take $\mu(p) = \epsilon_{p,0}$. The “first trial chemical potential” is $\mu(1) = \epsilon_{1,0}$. We check whether the function (5.3) changes sign if we would include the state $\{1, 0\}$. Denote the value of the function (5.3) after subtraction of the first states as $f^{(1)}$, so

$$f^{(1)} \equiv N_{nV} - \left[2 \sum_{n,\ell} (2\ell_{\epsilon_{n,\ell} \leq \mu(1)} + 1) \right] = N_{nV} - 2(2 \times \ell_{\epsilon_{1,0}} + 1) = N_{nV} - 2.$$

If the system contains more than 2 electrons, there would be no sign change: $f^{(1)} > 0$. In a second step we consider $\epsilon_{2,0}$ as second “trial chemical potential”, $\mu(2) = \epsilon_{2,0}$. We then calculate the orbitals $\{2, 0\}$, $\{1, 1\}$, $\{1, 2\}$ and $\{1, 3\}$, stopping with $\{1, 3\}$ because $\epsilon_{1,3} > \epsilon_{2,0}$. We then subtract from $f^{(1)}$ the number of orbitals corresponding to the states for which $\epsilon_{n,\ell} \leq \mu(2)$, so $\{1, 1\}$, $\{1, 2\}$ and $\{2, 0\}$. In this way we obtain the value of the function (5.3) for which all electrons with $\epsilon_{n,\ell} \leq \mu(2)$ are included: $f^{(2)} = f^{(1)} - 2[2(\ell_{\epsilon_{2,0}} + \ell_{\epsilon_{1,1}} + \ell_{\epsilon_{1,2}}) + 3] = N_{nV} - 20$. If the system contains more than 20 electrons, then we consider $\mu(3) = \epsilon_{3,0}$ as the new trial chemical potential, solve the Schrödinger equation for¹ $\{3, 0\}$, $\{2, 1\}$, $\{2, 2\}$ and $\{1, 4\}$, and calculate $f^{(3)} = f^{(2)} - 2[2(\ell_{\epsilon_{3,0}} + \ell_{\epsilon_{1,3}} + \ell_{\epsilon_{2,1}}) + 3] = N_{nV} - 42$. If there are more than 42 electrons in the system, we continue this procedure.

¹remember that the state $\{1, 3\}$ has already been calculated

Now suppose the system contains 34 electrons, so $N_{nV} = 34$. Then the function (5.3) has changed sign in the third step. We have now a rough estimate of the correct chemical potential μ , namely $\mu(2) < \mu < \mu(3)$. We also have a rough estimate of how many orbitals have to be included. Now it is time for refinement. Therefore we have to perform the only sorting task in the procedure: sorting the orbitals with energies between $\mu(2)$ and $\mu(3)$. After having sorted these energies, we start to add to $f^{(3)}$ the number of electrons of the highest energy levels, so we calculate first $f^{(3,1)} = f^{(3)} + 2(2\ell_{\epsilon_{3,0}} + 1) = N_{nV} - 40$ and then, because still $f^{(3,1)} < 0$, calculate $f^{(3,2)} = f^{(3,1)} + 2(2\ell_{\epsilon_{2,1}} + 1) = N_{nV} - 34 = 0$.

The procedure, which has been explained based on a specific fictitious energy spectrum, can be formalized as indicated in the flowchart of figure 5.2.

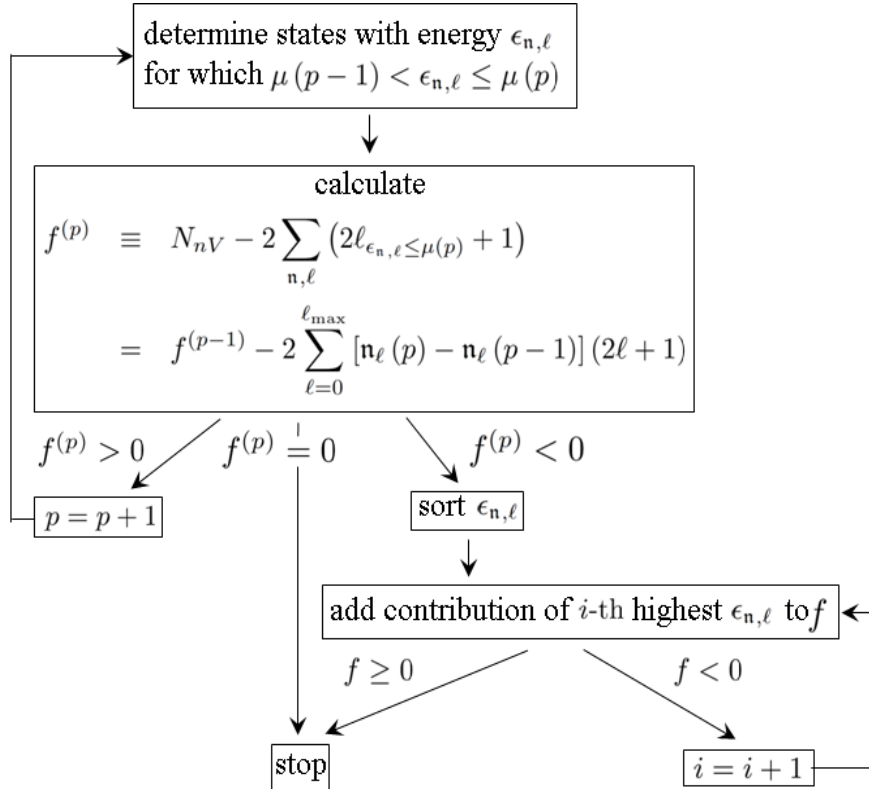


Figure 5.2: Visualization of the orbital bookkeeping for a spherically symmetric system. For such a system the single-particle energies ϵ depend on two quantum numbers: \mathbf{n} and ℓ . In iteration p a trial chemical potential $\mu(p)$ is considered ($\mu(0) = 0$). If all electrons are included then $f = f(\mathbf{n}', \ell'(\mathbf{n}))$, expression (5.3), has the value $f = 0$. N_{nV} is the number of electrons calculated from the average electron density n and the volume V , ℓ_{\max} is the highest ℓ -value for which states have been calculated in iteration p and $\mathbf{n}_\ell(p)$ is the total number of \mathbf{n} -values that was treated for a given ℓ -value up to iteration p .

We perform iterations in which for the p -th iteration we consider a trial chemical potential $\mu(p)$ and a value of the function (5.3) denoted as $f^{(p)}$ so that $f^{(p)} = N_{nV} - 2 \sum_{\mathbf{n}, \ell} (2\ell_{\epsilon_{\mathbf{n}, \ell} \leq \mu(p)} + 1)$. If $f^{(p)} < 0$, we sort the states with $\mu(p-1) < \epsilon_{\mathbf{n}, \ell} \leq \mu(p)$ according to energy and add energies $\epsilon_{\mathbf{n}, \ell} > \mu(p-1)$ to $f^{(p)}$, starting from the highest one, until the function (5.3) is equal to zero or changes sign again (the latter case occurs if the upper energy level is not completely filled). In an iteration we do not calculate all states for which $\epsilon_{\mathbf{n}, \ell} \leq \mu(p)$ because the states with $\epsilon_{\mathbf{n}, \ell} \leq \mu(p-1)$ were already calculated in previous iterations. Keeping track of which orbitals have already been calculated requires some bookkeeping. Therefore we store for each ℓ -value the number of \mathbf{n} -values that have been calculated up to iteration p , denoted as $\mathbf{n}_\ell(p)$. Then with

ℓ_{\max} the maximum ℓ -value for which orbitals have been calculated, the value of the function (5.3) in iteration p is calculated as

$$f^{(p)} = f^{(p-1)} - 2 \sum_{\ell=0}^{\ell_{\max}} [\mathbf{n}_{\ell}(p) - \mathbf{n}_{\ell}(p-1)] (2\ell + 1).$$

To sort the states according to energy we have used an index array so that the states do not have to be moved themselves. To order the index array we used the routine quicksort (see e.g. Ref. [98]) because this routine is fast in comparison with some other methods. Moreover there exists an algorithm reported in Ref. [97] based on this method in which one additional array (in this case with $\mathfrak{R}_{\mathbf{n},\ell}(r)$) is rearranged correspondingly to another array that is sorted (in this case the array with the energies $\epsilon_{\mathbf{n},\ell}$).

5.3 Orbital calculation: Transfer Matrix Method

We applied the Transfer Matrix Method to a nanoshell because it was already successfully applied to other confined systems, e.g. to calculate the charge distribution and leakage currents in ultrathin metal-insulator-semiconductor capacitors [72].

In this section, we first explain the basics of the method. Then we sketch how the transfer matrix and the boundary conditions look like in general for a spherically symmetric system. After that, we derive the piecewise wave functions. We then explain how the number of nodes of a single-particle wave function can be calculated. The section is ended with a list of some advantages of the Transfer Matrix Method as compared to finite difference implementations.

5.3.1 Basics

In the Transfer Matrix Method the considered domain is divided into intervals in which the potential energy can be approximated by a simpler function so that the Schrödinger equation in the intervals can be solved analytically. This results in piecewise wave functions. The solution of the entire problem is then obtained by requiring continuity of the wave functions and its derivative at the interval boundaries and by taking into account the boundary conditions of the problem which follow from the condition that the wave function should be integrable.

In one dimension we get in each interval j a piecewise Schrödinger equation

$$-\frac{1}{2}\Delta\psi_j(x) + u_{\text{eff},j}(x)\psi_j(x) = \epsilon\psi_j(x)$$

which results in a piecewise wave function

$$\psi_j(\epsilon, x) = a_j(\epsilon)u_1(j, \epsilon, x) + b_j(\epsilon)u_2(j, \epsilon, x)$$

with analytical basis functions $u_1(j, \epsilon, x)$ and $u_2(j, \epsilon, x)$ and coefficients $a_j(\epsilon)$ and $b_j(\epsilon)$. Imposing continuity of the wave function and its derivative between the intervals j and $j+1$,

$$\begin{aligned}\psi_j(\epsilon, x_{j+1}) &= \psi_{j+1}(\epsilon, x_{j+1}) \\ \psi'_j(\epsilon, x_{j+1}) &= \psi'_{j+1}(\epsilon, x_{j+1}),\end{aligned}$$

leads to a relation between the coefficients of neighboring intervals of the form

$$\begin{pmatrix} a_j(\epsilon) \\ b_j(\epsilon) \end{pmatrix} = \begin{pmatrix} A_j(\epsilon) & B_j(\epsilon) \\ C_j(\epsilon) & D_j(\epsilon) \end{pmatrix} \begin{pmatrix} a_{j+1}(\epsilon) \\ b_{j+1}(\epsilon) \end{pmatrix}. \quad (5.7)$$

The matrix $\begin{pmatrix} A_j(\epsilon) & B_j(\epsilon) \\ C_j(\epsilon) & D_j(\epsilon) \end{pmatrix}$ is called the transfer matrix. The matrix elements depend on ϵ and contain the functions $u_1(j, \epsilon, x)$, $u_2(j, \epsilon, x)$, $u_1(j+1, \epsilon, x)$ and $u_2(j+1, \epsilon, x)$ and their derivatives evaluated in $x = x_{j+1}$.

To find the eigenvalues ϵ which lead to a fulfillment of the boundary conditions of the problem, one fixes the boundary condition at one side, solves relation (5.7) recursively for each interval and checks whether the boundary condition at the other side of the system is fulfilled. This last boundary condition can be rewritten as a function of ϵ of which the zeros are the eigenvalues ϵ corresponding to the wave functions with the correct boundary conditions.

As a result, the unnormalized wave function $\psi_{\text{unnorm}}(x)$ is obtained which is related to the normalized wave function $\psi_{\text{norm}}(x)$ by a normalization factor C_{norm} as $\psi_{\text{norm}}(x) = C_{\text{norm}}\psi_{\text{unnorm}}(x)$. The normalization factor C_{norm} can be calculated from the M piecewise unnormalized wave functions $\psi_j(x)$ as

$$C_{\text{norm}} = \frac{1}{\sqrt{\sum_{j=1}^M \int_{x_j}^{x_{j+1}} |\psi_j(x)|^2 dx}}.$$

The problem of the finite square well mentioned in chapter 1, is actually solved with this method. In that case the potential energy is a different constant in three regions. The solution of the complete Schrödinger equation is found by solving the piecewise Schrödinger equation in the three regions and applying the boundary conditions at the well boundaries and at $x \rightarrow \pm\infty$.

5.3.2 Application to spherically symmetric system

In this and the next section we explain how a form for the unnormalized wave function $R(r)$ can be derived by solving the radial Schrödinger equation (5.2) with the Transfer Matrix Method. In section 5.3.3 we also explain how the contributions to the normalization integral can be calculated in order to determine the normalized wave function $\mathfrak{R}(r)$ from $R(r)$.

The general form of the piecewise radial wave function $R_j(\epsilon, r)$ in interval j is

$$R_j(\epsilon, r) = a_j u_1(j, \epsilon, r) + b_j u_2(j, \epsilon, r). \quad (5.8)$$

The condition that the wave function and its derivative should be continuous between subsequent intervals can be written as

$$\begin{aligned} u_1(j-1, \epsilon, r_j) a_{j-1} + u_2(j-1, \epsilon, r_j) b_{j-1} &= u_1(j, \epsilon, r_j) a_j + u_2(j, \epsilon, r_j) b_j \\ u_1'(j-1, \epsilon, r_j) a_{j-1} + u_2'(j-1, \epsilon, r_j) b_{j-1} &= u_1'(j, \epsilon, r_j) a_j + u_2'(j, \epsilon, r_j) b_j \end{aligned}$$

with $f'(r_j)$ defined as

$$f'(r_j) = \left. \frac{df(r)}{dr} \right|_{r=r_j}.$$

From these conditions, we can derive a transfer matrix which can be used to go from one end of the domain to the other by using forward or backward recurrence.

Transfer matrix

Expressing a_j and b_j as a function of a_{j-1} and b_{j-1} gives an expression that can be used for forward recurrence:

$$\begin{aligned} a_j &= \frac{u_1(j-1, \epsilon, r_j) u_2'(j, \epsilon, r_j) - u_1'(j-1, \epsilon, r_j) u_2(j, \epsilon, r_j)}{u_1(j, \epsilon, r_j) u_2'(j, \epsilon, r_j) - u_1'(j, \epsilon, r_j) u_2(j, \epsilon, r_j)} a_{j-1} \\ &\quad + \frac{u_2(j-1, \epsilon, r_j) u_2'(j, \epsilon, r_j) - u_2'(j-1, \epsilon, r_j) u_2(j, \epsilon, r_j)}{u_1(j, \epsilon, r_j) u_2'(j, \epsilon, r_j) - u_1'(j, \epsilon, r_j) u_2(j, \epsilon, r_j)} b_{j-1} \\ b_j &= \frac{u_1'(j-1, \epsilon, r_j) u_1(j, \epsilon, r_j) - u_1(j-1, \epsilon, r_j) u_1'(j, \epsilon, r_j)}{u_1(j, \epsilon, r_j) u_2'(j, \epsilon, r_j) - u_1'(j, \epsilon, r_j) u_2(j, \epsilon, r_j)} a_{j-1} \\ &\quad + \frac{u_2'(j-1, \epsilon, r_j) u_1(j, \epsilon, r_j) - u_2(j-1, \epsilon, r_j) u_1'(j, \epsilon, r_j)}{u_1(j, \epsilon, r_j) u_2'(j, \epsilon, r_j) - u_1'(j, \epsilon, r_j) u_2(j, \epsilon, r_j)} b_{j-1}. \end{aligned}$$

With the following function definitions

$$\begin{aligned} C_{\alpha, \beta}^{(\gamma, \delta)}(\epsilon, j) &= u_\alpha^{(\gamma)}(j, \epsilon, r_{j+1}) u_\beta^{(\delta)}(j+1, \epsilon, r_{j+1}) - u_\alpha^{(\delta)}(j, \epsilon, r_{j+1}) u_\beta^{(\gamma)}(j+1, \epsilon, r_{j+1}) \\ f^{(0)}(r_j) &= f(r_j); \quad f^{(1)}(r_j) = f'(r_j) \\ D(j, \epsilon, r_j) &= u_1(j, \epsilon, r_j) u_2'(j, \epsilon, r_j) - u_1'(j, \epsilon, r_j) u_2(j, \epsilon, r_j). \end{aligned} \quad (5.9)$$

we can write the relation between the coefficients of subsequent intervals in compact form as

$$\begin{pmatrix} a_j \\ b_j \end{pmatrix} = \frac{1}{D(j, \epsilon, r_j)} \begin{pmatrix} C_{1,2}^{(0,1)}(\epsilon, j-1) & C_{2,2}^{(0,1)}(\epsilon, j-1) \\ C_{1,1}^{(1,0)}(\epsilon, j-1) & C_{2,1}^{(1,0)}(\epsilon, j-1) \end{pmatrix} \begin{pmatrix} a_{j-1} \\ b_{j-1} \end{pmatrix}. \quad (5.10)$$

Expressing a_{j-1} and b_{j-1} as a function of a_j and b_j and then setting $j-1 = j$ gives an expression that can be used for backward recurrence:

$$\begin{pmatrix} a_j \\ b_j \end{pmatrix} = \frac{1}{D(j, \epsilon, r_{j+1})} \begin{pmatrix} C_{2,1}^{(1,0)}(\epsilon, j) & -C_{2,2}^{(0,1)}(\epsilon, j) \\ -C_{1,1}^{(1,0)}(\epsilon, j) & C_{1,2}^{(0,1)}(\epsilon, j) \end{pmatrix} \begin{pmatrix} a_{j+1} \\ b_{j+1} \end{pmatrix} \quad (5.11)$$

with the elements of the transfer matrix given by the expressions (5.9) and where we have used that $C_{\alpha, \beta}^{(\delta, \gamma)}(\epsilon, j) = -C_{\alpha, \beta}^{(\gamma, \delta)}(\epsilon, j)$.

Note that for all matrix elements of the transfer matrix, the denominators are proportional to the Wronskian of the linearly independent basic functions; they are thus different from zero.

During recurrence, underflow (of both coefficients) or overflow can be avoided by timely rescaling the coefficients a_j and b_j .

Boundary conditions

The boundary conditions for the radial wave function $\mathfrak{R}(r)$ of a spherically symmetric system are such that it is quadratically integrable, i.e. $\int_0^\infty |\mathfrak{R}(r)|^2 r^2 dr < \infty$. In the regions that contain the limiting values $r = 0$ and $r \rightarrow \infty$, there is one solution of the (piecewise) radial Schrödinger equation that is not quadratically integrable in the considered limit. We denote this solution as the basis function $u_2(j, \epsilon, r)$. The fact that this basis function gives rise to a non-integrable wave function means that the coefficient b_j of the intervals should be zero. Assigning the region which contains the origin the subscript "O" and the region which contains $r \rightarrow \infty$ the index " ∞ ", then $b_O = 0$ and $b_\infty = 0$ leads to special cases of relation (5.10) and relation (5.11):

$$a_{j_O+1} = \frac{C_{1,2}^{(0,1)}(\epsilon, j_O)}{D(j_O+1, \epsilon, r_O)} a_O; \quad b_{j_O+1} = \frac{C_{1,1}^{(1,0)}(\epsilon, j_O)}{D(j_O+1, \epsilon, r_O)} a_O \quad (5.12)$$

$$a_{j_\infty-1} = \frac{C_{2,1}^{(1,0)}(\epsilon, j_\infty-1)}{D(j_\infty-1, \epsilon, r_\infty)} a_\infty; \quad b_{j_\infty-1} = -\frac{C_{1,1}^{(1,0)}(\epsilon, j_\infty-1)}{D(j_\infty-1, \epsilon, r_\infty)} a_\infty, \quad (5.13)$$

with j_O the index of the last interval of the region that contains the origin, r_O the boundary of the region that contains the origin, j_∞ the first index of the region that contains the value $r \rightarrow \infty$ and r_∞ the boundary of the region that contains $r \rightarrow \infty$. Notice that the proportionality factors between the coefficients do not contain $u_2(j, \epsilon, r)$ in the limiting values for r .

In solving the differential equation (5.2) we find a function that still has to be normalized. This means that we can choose one of the coefficients: this will define the scaling factor of the solution but it does not have an influence on the physics. Suppose we fix a_O . Then by forward recurrence we can determine all coefficients $a_{j>j_O}$ and $b_{j>j_O}$. To check whether the boundary condition for $r \rightarrow \infty$ is satisfied we can construct a function that is zero if the boundary condition is fulfilled. This can be done as follows. If we eliminate a_∞ from the equations (5.13), then we find that the boundary condition for $r \rightarrow \infty$ is fulfilled if the function

$$\begin{aligned} f_\infty(\epsilon) &= \frac{C_{1,1}^{(1,0)}(\epsilon, j_\infty - 1)}{C_{2,1}^{(1,0)}(\epsilon, j_\infty - 1)} a_{j_\infty - 1} + b_{j_\infty - 1} \\ &= \frac{u'_1(j_\infty - 1, \epsilon, r_\infty) - u_1(j_\infty - 1, \epsilon, r_\infty) \frac{u'_1(j_\infty, \epsilon, r_\infty)}{u_1(j_\infty, v, r_\infty)}}{u'_2(j_\infty - 1, \epsilon, r_\infty) - u_2(j_\infty - 1, \epsilon, r_\infty) \frac{u'_1(j_\infty, \epsilon, r_\infty)}{u_1(j_\infty, \epsilon, r_\infty)}} a_{j_\infty - 1} + b_{j_\infty - 1} \end{aligned} \quad (5.14)$$

is equal to zero².

If we fix a_∞ , then by backward recurrence we can calculate all coefficients $a_{j<j_\infty}$ and $b_{j<j_\infty}$ and determine whether the boundary condition for $r = 0$ is satisfied by checking whether the function

$$f_O(\epsilon) = \frac{\frac{u'_1(j_O, \epsilon, r_O)}{u_1(j_O, \epsilon, r_O)} u_1(j_O + 1, \epsilon, r_O) - u'_1(j_O + 1, \epsilon, r_O)}{u'_2(j_O + 1, \epsilon, r_O) - \frac{u'_1(j_O, \epsilon, r_O)}{u_1(j_O, \epsilon, r_O)} u_2(j_O + 1, \epsilon, r_O)} a_{j_O + 1} - b_{j_O + 1} \quad (5.15)$$

is equal to zero.

To find a zero of a function we used the routine “zbrent” of Ref. [97].

5.3.3 Expressions for the piecewise radial solutions

We want to use the Transfer Matrix Method to solve the radial differential equation

$$\frac{1}{r^2} \frac{d}{dr} \left(r^2 \frac{d}{dr} \right) R(r) + \left[2\epsilon - \left(2u_{\text{eff}}(r) + \frac{\ell(\ell+1)}{r^2} \right) \right] R(r) = 0. \quad (5.16)$$

In this section we derive the piecewise wave functions that are of use in different models for a nanoshell. The form of these wave functions will depend on the approximation that can be made for the effective potential energy $u_{\text{eff}}(r)$ and for the centrifugal term $\ell(\ell+1)/r^2$.

In the model of an ideal Fermi gas in an infinite potential well between R_C and R_S , the effective potential in the well equals zero: $u_{\text{eff}}(R_C < r < R_S) = 0$. If we divide this region in sufficiently small intervals j , the centrifugal term can be approximated by a constant so that we can set $\ell(\ell+1)/(2r^2) = \ell(\ell+1)/(2r_j r_{j+1})$ with r_j the lower bound on interval j . This is shown in figure 5.3.

In the model of non-interacting fermions in a finite potential well between R_C and R_S , there are three regions defined by a constant potential energy:

$$u_{\text{eff}}(r) = \begin{cases} u_C & 0 \leq r \leq R_C \\ 0 & R_C < r < R_S \\ u_E & R_S \leq r < \infty \end{cases}$$

²We have written this zero function in a convenient form for later use.

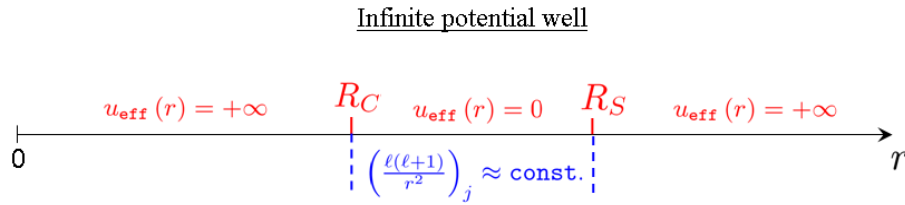


Figure 5.3: “Physical” characteristics of a nanoshell in the model of non-interacting fermions in an infinite potential well (red, above axis) and possible approximation to the potential energy in a sufficiently small interval j in the shell (blue, below axis).

with $0 \leq u_C < \infty$ and $0 \leq u_E < \infty$. Also in this case the shell region can be divided in sufficiently small intervals so that we can set $u_{\text{eff}}(r) + \ell(\ell+1)/(2r^2) = u_{\text{eff}}(j) + \ell(\ell+1)/(2r_j r_{j+1})$. In the region that contains the origin, the centrifugal term cannot be approximated by a constant. To implement the boundary condition for $r \rightarrow \infty$, it is also better not to use this approximation in the region $r > R_S$. The regions of the finite well and the possible approximation are shown in figure 5.4.

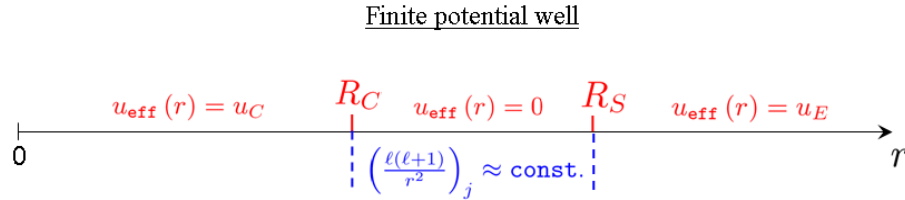


Figure 5.4: “Physical” characteristics of a nanoshell in the model of non-interacting fermions in a finite potential well (red, above axis) and possible approximation to the potential energy in a sufficiently small interval j in the shell (blue, below axis).

The most realistic model with interacting electrons also consists of three regions, as shown in figure 5.5.

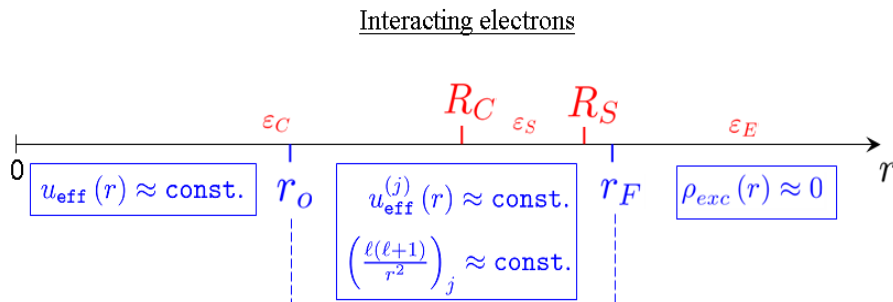


Figure 5.5: Physical regions of a nanoshells (red, above axis) and regions in which a certain approximation can be made (blue, below axis).

Like in the case of the finite well, there is a region near the origin where the centrifugal term cannot be approximated and where the potential energy is a constant. We denote the upper bound for this region as r_O and we will attach to every parameter in this region the subscript “O”. For $r > r_O$ intervals can be constructed so that the effective potential and the centrifugal potential can be approximated by a constant. The third region that can be

considered, is the region outside the nanoshell where the excess charge density is negligible, $\rho_{exc}(r) \approx 0$. In this region, which we will call the “free-of-charge” region, the effective potential energy has a $-1/r$ dependence and the piecewise Schrödinger equation can be solved without approximation for $u_{\text{eff}}(r)$ and the centrifugal term. We call the lower bound for this region r_F and we will attach to every parameter in this region the subscript “F”.

In the rest of this section we derive the piecewise basis functions in the different approximations for the effective and centrifugal potential. Where possible, we give an analytical expression for the contribution to the normalization integral. In appendix A.2 some details are given on the implementation of the basis functions and their derivatives to be used in the recurrence relations and boundary conditions as explained in section 5.3.2.

Approximation 1: $u_{\text{eff}}(r) = \text{constant} = u_{\text{eff}}(j)$

With this approximation, the differential equation (5.16) reduces to the differential equation of the (modified) spherical Bessel functions:

$$r^2 \frac{d^2 R(r)}{dr^2} + 2r \frac{dR(r)}{dr} + [\Lambda_j r^2 - \ell(\ell + 1)] R(r) = 0$$

with $\Lambda_j = 2[\epsilon - u_{\text{eff}}(j)]$. Basis functions of this differential equation are

	$\epsilon \geq u_{\text{eff}}(j)$	$\epsilon < u_{\text{eff}}(j)$
$u_1(j, \epsilon, r) =$	$j_\ell(\lambda_j r)$	$i_\ell(\lambda_j r)$
$u_2(j, \epsilon, r) =$	$y_\ell(\lambda_j r)$	$k_\ell(\lambda_j r)$

with $\lambda_j = \sqrt{|\Lambda_j|} = \sqrt{2|\epsilon - u_{\text{eff}}(j)|}$, $j_\ell(x)$ ($i_\ell(x)$) the (modified) spherical Bessel function of the first kind and $y_\ell(x)$ ($k_\ell(x)$) the (modified) spherical Bessel function of the second (third) kind.

The contribution to the normalization constant can be calculated by using the relation between the (modified) spherical Bessel functions $z_\ell(x)$ and the corresponding “non-spherical” (modified) Bessel functions $Z_\ell(x)$ [1, 36, 86, 109]:

$$z_\ell(x) = \sqrt{\frac{\pi}{2x}} Z_{\ell+\frac{1}{2}}(x). \quad (5.17)$$

The function $i_\ell(\lambda_j r)$ will only be used in the interval that contains the origin and $k_\ell(\lambda_j r)$ will only be used in the interval that contains $r \rightarrow \infty$ (for the finite potential well). Because of relation (5.17) we then can make use of the equalities [1, 36, 86, 109]

$$\int_0^x x I_\nu^2(\lambda x) dx = \frac{x^2}{2} \left[\left(1 + \frac{\nu^2}{\lambda^2 x^2} \right) I_\nu^2(\lambda x) - I_\nu'^2(\lambda x) \right] \quad (5.18)$$

$$\int x G_\nu(a x) F_\nu(a x) dx = \frac{1}{2} x^2 \left[\left(1 - \frac{\nu^2}{a^2 x^2} \right) G_\nu^2(a x) + G_\nu'^2(a x) \right] \quad (5.19)$$

$$\int_x^\infty x K_\nu^2(\lambda x) dx = \frac{x^2}{2} \left[K_\nu'^2(\lambda x) - \left(1 + \frac{\nu^2}{\lambda^2 x^2} \right) K_\nu^2(\lambda x) \right] \quad (5.20)$$

with

$$\begin{aligned} G_\nu(x) &= a J_\nu(x) + b Y_\nu(x) \\ f'(x) &= \frac{df(x)}{dx} \end{aligned} \quad (5.21)$$

to calculate the contribution to the normalization integral. Using

$$Z'_{\ell+\frac{1}{2}}(x) = \sqrt{\frac{2x}{\pi}} \left(\frac{z_\ell(x)}{2x} + z'_\ell(x) \right) \quad (5.22)$$

and introducing

$$g_\ell(\lambda_j r) = a_j j_\ell(\lambda_j r) + b_j y_\ell(\lambda_j r), \quad (5.23)$$

equations (5.17)-(5.23) lead to the following contributions to the normalization integral:

$$\int_0^{r_O} |\mathbf{R}_O(r)|^2 r^2 dr = a_O^2 \frac{r_O^3}{2} \left[\begin{array}{c} \left(1 + \frac{\ell(\ell+1)}{(\lambda_O r_O)^2}\right) i_\ell^2(\lambda_O r_O) \\ - \left(i'_\ell(\lambda_O r_O) + \frac{i_\ell(\lambda_O r_O)}{\lambda_O r_O}\right) i'_\ell(\lambda_O r_O) \end{array} \right] \quad (5.24)$$

$$\left[\int_{r_j}^{r_{j+1}} |\mathbf{R}_j(r)|^2 r^2 dr \right]_{\substack{j \geq j_O \\ j < j_{R_S}}} = \left\{ \frac{r^3}{2} \left[\begin{array}{c} \left(1 - \frac{\ell(\ell+1)}{(\lambda_j r)^2}\right) g_\ell^2(\lambda_j r) \\ + \left(g'_\ell(\lambda_j r) + \frac{g_\ell(\lambda_j r)}{\lambda_j r}\right) g'_\ell(\lambda_j r) \end{array} \right] \right\}_{r_j}^{r_{j+1}} \quad (5.25)$$

$$\int_{R_S}^{\infty} |\mathbf{R}_E(r)|^2 r^2 dr = b_E^2 \frac{R_S^3}{2} \left[\begin{array}{c} \left(k'_\ell(\lambda_E R_S) + \frac{k_\ell(\lambda_E R_S)}{\lambda_E R_S}\right) k'_\ell(\lambda_E R_S) \\ - \left(1 + \frac{\ell(\ell+1)}{(\lambda_E R_S)^2}\right) k_\ell^2(\lambda_E R_S) \end{array} \right] \quad (5.26)$$

with $\lambda_E = \sqrt{2|\epsilon - u_E|}$ and $r_O = R_C$ in the case of the finite potential well.

Approximation 2: $u_{\text{eff}}(r) + \ell(\ell+1)/(2r^2) = u_{\text{eff}}(j) + \ell(\ell+1)/(2r_j r_{j+1})$

In this approximation, only to be used in the shell and its close vicinity, the general differential equation (5.16) reduces to

$$\frac{d^2 \mathbf{R}_j(r)}{dr^2} + \frac{2}{r} \frac{d \mathbf{R}_j(r)}{dr} + W_j \mathbf{R}_j(r) = 0$$

with

$$W_j = 2\epsilon - \left(2u_{\text{eff}}(j) + \frac{\ell(\ell+1)}{r_j r_{j+1}} \right). \quad (5.27)$$

The basis functions for the solutions of this differential equation are³

	$W_j \geq 0$	$W_j < 0$
$u_1(j, \epsilon, r) =$	$\frac{\sin[w_j(r-r_j)]}{w_j r}$	$\frac{\sinh[w_j(r-r_j)]}{w_j r}$
$u_2(j, \epsilon, r) =$	$\frac{\cos[w_j(r-r_j)]}{r}$	$\frac{\cosh[w_j(r-r_j)]}{r}$

with

$$w_j = \sqrt{|W_j|} = \sqrt{\left| 2\epsilon - \left(2u_{\text{eff}}(j) + \frac{\ell(\ell+1)}{r_j r_{j+1}} \right) \right|}.$$

³Remark 1: We have chosen the arguments of the goniometric and hyperbolic functions to be $w_j(r - r_j)$ and not $w_j(r)$ for numerical reasons.

Remark 2: Although $\sin[w_j(r - r_j)]/r$ and $\sinh[w_j(r - r_j)]/r$ are solutions of the differential equation, the pairs of solutions $\{\sin[w_j(r - r_j)]/r, \cos[w_j(r - r_j)]/r\}$ and $\{\sinh[w_j(r - r_j)]/r, \cosh[w_j(r - r_j)]/r\}$ do not contain linearly independent basis functions because the Wronskian is equal to zero if $w_j = 0$. That is why $u_1(j, \epsilon, r)$ and $u_2(j, \epsilon, r)$ were chosen as mentioned.

The basis functions in a mesh point are given by

$$\begin{aligned} u_1(j, \epsilon, r_j) &= 0 \\ u_2(j, \epsilon, r_j) &= \frac{1}{r_j} \end{aligned}$$

from which it follows that the unnormalized radial wave function in a mesh point is simply equal to

$$R_j(r_j) = \frac{b_j}{r_j}.$$

The contribution to the normalization integral can be calculated as

$$\int_{r_j}^{r_{j+1}} |R_j(r)|^2 r^2 dr = \frac{1}{2} \left(s_{W_j} \frac{a_j^2}{w_j^2} + b_j^2 \right) h_j + \left[\frac{1}{2} \left(-s_{W_j} \frac{a_j^2}{w_j^2} + b_j^2 \right) u_2(j, \epsilon, r_{j+1}) + a_j b_j u_1(j, \epsilon, r_{j+1}) \right] u_1(j, \epsilon, r_{j+1}) r_{j+1}^2$$

with s_{W_j} the sign of W_j (expression (5.27)). The radial derivatives $u'_1(j, \epsilon, r)$ and $u'_2(j, \epsilon, r)$ for the transfer matrix can be simply calculated as

$$\begin{aligned} u'_1(j, \epsilon, r) &= \frac{du_1(j, \epsilon, r)}{dr} = -\frac{u_1(j, \epsilon, r)}{r} + u_2(j, \epsilon, r) \\ u'_2(j, \epsilon, r) &= \frac{du_2(j, \epsilon, r)}{dr} = -s_{w_j} w_j^2 u_1(j, \epsilon, r) - \frac{u_2(j, \epsilon, r)}{r}. \end{aligned}$$

The forward recurrence relations (5.10) then take the compact form

$$\begin{pmatrix} a_j \\ b_j \end{pmatrix} = r_j \begin{pmatrix} u_2(j-1, \epsilon, r_j) & -s_{w_{j-1}} w_{j-1}^2 u_1(j-1, \epsilon, r_j) \\ u_1(j-1, \epsilon, r_j) & u_2(j-1, \epsilon, r_j) \end{pmatrix} \begin{pmatrix} a_{j-1} \\ b_{j-1} \end{pmatrix}.$$

Approximation 3: $u_{\text{eff}}(r) = -Q'/r$

In the free-of-charge region, the effective potential energy is equal to $u_{\text{eff}}(r) = -Q'/r$ with $Q' = Q_{\text{tot}}/\epsilon_E$ in which Q_{tot} denotes the total charge in the system and ϵ_E the permittivity of the environment. With $u_{\text{eff}}(r) = -Q'/r$ we get from the differential equation (5.16) the piecewise differential equation

$$\frac{d^2 R_F(r)}{dr^2} + \frac{2}{r} \frac{dR_F(r)}{dr} + \left[\Lambda_F + 2 \frac{Q'}{r} - \frac{\ell(\ell+1)}{r^2} \right] R_F(r) = 0$$

with $\Lambda_F = 2\epsilon$. Because we are looking for bound states, for which $\epsilon < 0$, we will only have to consider the case $\Lambda_F < 0$. Then with $\lambda_F = \sqrt{2|\epsilon|} = \sqrt{-2\epsilon}$ the differential equation in the approximation considered here is given by

$$\frac{d^2 R_F(r)}{dr^2} + \frac{2}{r} \frac{dR_F(r)}{dr} + \left[-\lambda_F^2 + 2 \frac{Q'}{r} - \frac{\ell(\ell+1)}{r^2} \right] R_F(r) = 0.$$

It has the following solutions depending on whether Q'/λ_F is an integer or not (for the derivation of these basis functions, see appendix A.1):

$$u_1(j, \epsilon, r) = \begin{cases} \mathcal{W}_{\frac{Q'}{\lambda_F}, \ell + \frac{1}{2}}(2\lambda_F r) / r & \text{if } \frac{Q'}{\lambda_F} \notin \mathbb{N} \\ e^{-\frac{Q'}{p}r} r^\ell L_{p-\ell-1}^{(2\ell+1)}\left(2\frac{Q'}{p}r\right) & \text{if } \frac{Q'}{\lambda_F} = p \in \mathbb{N} \end{cases} \quad (5.28)$$

$$u_2(j, \epsilon, r) = \begin{cases} \mathcal{M}_{\frac{Q'}{\lambda_F}, \ell + \frac{1}{2}}(2\lambda_F r) / r & \text{if } \frac{Q'}{\lambda_F} \notin \mathbb{N} \\ \left(\int_0^r e^{2\frac{Q'}{p}r} / \left[r^{\ell+1} L_{p-\ell-1}^{(2\ell+1)}\left(2\frac{Q'}{p}r\right) \right]^2 dr + C \right) \\ \quad \times e^{-\frac{Q'}{p}r} r^\ell L_{p-\ell-1}^{(2\ell+1)}\left(2\frac{Q'}{p}r\right) & \text{if } \frac{Q'}{\lambda_F} = p \in \mathbb{N} \end{cases} \quad (5.29)$$

with $\mathcal{W}_{\kappa, \mu}(x)$ and $\mathcal{M}_{\kappa, \mu}(x)$ Whittaker functions, $L_p^{(\beta)}(x)$ an associated Laguerre polynomial and C a constant.

There are no analytic expressions for the contribution to the normalization integral. We thus have to rely on numerical integration. This is not a big problem because the contribution of this type of solution to the total integral is relatively small.

5.3.4 Counting nodes - bracketing

From section 5.2 on the orbital bookkeeping, it is clear that it is important for the process of finding eigenenergies that the quantum numbers \mathbf{n} and ℓ can be fixed. As for the ℓ -value, this is simple because it is an input parameter for the piecewise basis functions. Because there is no analytical relation between the quantum number \mathbf{n} and the wave function and energy of a state, this quantum number cannot be fixed easily. As mentioned in section 5.1, the principal quantum number \mathbf{n} is linked to the number of nodes of the wave function. Because in the Transfer Matrix Method the piecewise wave functions are given by an analytical function in the intervals, determining the number of nodes is relatively easy.

Number of nodes in an interval

We restrict the discussion of the determination of the number of nodes to the approximation $u_{\text{eff}}(r) + \ell(\ell+1)/(2r^2) = u_{\text{eff}}(j) + \ell(\ell+1)/(2r_j r_{j+1})$ because the wave functions will only have nodes in the region where this approximation can be used. There is a distinction between the cases $W_j = 2\epsilon - [2u_{\text{eff}}(j) + \ell(\ell+1)/(2r_j r_{j+1})] \geq 0$ and $W_j < 0$.

If $W_j \geq 0$ the wave function has nodes in the interval j where

$$\tan[w_j(r - r_j)] = -\frac{b_j w_j}{a_j}.$$

The function $\tan(cx)$ has a period T equal to $T = \pi/c$. So in the interval there will be at least

$$(\mathbf{n}_j)_{\min} = \text{int}\left(\frac{h_j}{T}\right) = \text{int}\left(\frac{w_j h_j}{\pi}\right)$$

nodes and at most one more. So the number of nodes \mathbf{n}_j in interval j lies between

$$(\mathbf{n}_j)_{\min} \leq \mathbf{n}_j \leq (\mathbf{n}_j)_{\min} + 1.$$

Whether n_j is even or odd can easily be determined from the values of the wave function at the interval boundaries (which were calculated and stored during the recurrence procedure): if $R(r_j) * R(r_{j+1}) > 0$ then n_j is even and if $R(r_j) * R(r_{j+1}) < 0$ then n_j is odd.

If $W_j < 0$ the piecewise wave function can have at most one node: if $R(r_j) * R(r_{j+1}) < 0$.

One has to pay attention to double counting if the wave function is zero in a mesh point.

Bracketing

Every routine for finding a zero x_0 of a function $f(x)$ needs a lower and an upper bound x_{lower} and x_{upper} for the argument in between which the zero has to be found. These bounding values x_{lower} and x_{upper} are called **brackets**. Determining good brackets is crucial for the process of finding a zero, but usually it is not easy. The brackets have to enclose the zero as tightly as possible and it is not allowed that the bracket interval contains more than one zero. Checking whether the interval $[x_{\text{lower}}, x_{\text{upper}}]$ contains an even or odd number of zeros can easily be done by calculating the product $A = f(x_{\text{lower}}) \times f(x_{\text{upper}})$. If A is positive, the interval contains an even number of nodes and the brackets have to be modified for sure. If A is negative, the interval contains an odd number of nodes, but one cannot tell whether it is just one or maybe three or five or ...

So in using the function (5.14) or (5.15) for finding the correct eigenvalue $\epsilon_{n,\ell}$, we need to supply the routine with values ϵ_{lower} and ϵ_{upper} in between which the eigenvalue $\epsilon_{n,\ell}$ is situated. There corresponds an “energy” ϵ_{lower} to a *trial wave function* $\mathcal{R}_{\epsilon_{\text{lower}}}(r)$ that has $n - 1$ nodes and fulfills the boundary condition at one end but not at the other end. Another trial wave function $\mathcal{R}_{\epsilon_{\text{upper}}}(r)$ that has n nodes and fulfills the boundary condition at one end but not at the other end, has an “energy” ϵ_{upper} . This is visualized in figure 5.6 for the case where a wave function with $n = 1$ is sought with as boundary conditions that the wave function is zero at $r = r_O$ and at $r = r_\infty$.

It is an important advantage of the Transfer Matrix Method that the number of nodes of a function can easily and (almost certainly) correctly be determined. In this way we can find good brackets for the search of an energy level $\epsilon_{n,\ell}$. We just have to find two “trial wave functions” with as input the correct ℓ -value and which satisfy only one boundary condition. One of those functions should have $n - 1$ nodes, with corresponding energy ϵ_{lower} , and one should have n nodes, with corresponding energy ϵ_{upper} .

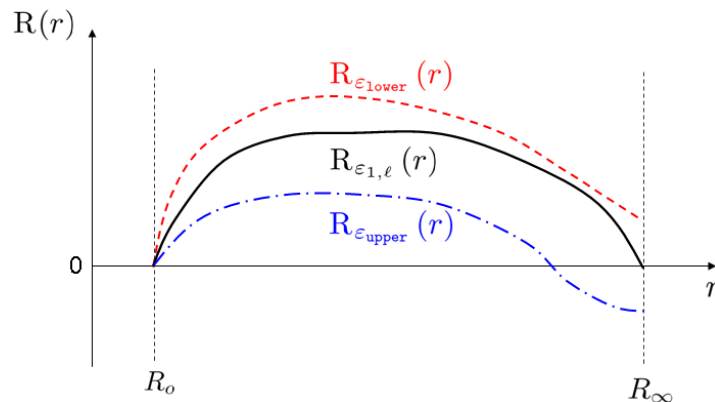


Figure 5.6: Visualization of the case where a wave function with $n = 1$ is sought with as boundary conditions that the wave function is zero at $r = R_O$ and at $r = R_\infty$. The black solid curve represents the correct wave function with energy $\epsilon_{n,\ell}$, the red dashed curve represents a trial wave function with “energy” ϵ_{lower} and the blue dash-dotted curve represents a trial wave function with “energy” ϵ_{upper} .

5.3.5 Advantages over some other methods

In some methods, like in the finite elements or the finite difference method, the values of the wave function are only known in the mesh points. In the Transfer Matrix Method also information of the wave function *in between* mesh points is known because of the use of piecewise analytical wave functions. This has advantages for

1. bracketing: because in “mesh-only methods” there is no information on the behavior of the wave function in between the mesh points, one cannot be sure that all nodes of the wave function are detectable: one has to rely on changes in sign of wave function values in subsequent mesh points. As seen in section 5.3.4, the Transfer Matrix Method allows for a quite certain determination of the number of nodes. This advantage is of course most important for highly oscillating wave functions.
2. the number of mesh points: because more information is known about the wave function in between mesh points, less mesh points are needed to determine the energies.
3. calculation of the normalization integral: in “mesh-only methods” one has to rely on numerical integration, e.g. linear interpolation, to calculate interval contributions to the normalization integral. This leads to a loss in accuracy. By using piecewise analytical wave functions, the contribution of an interval to the normalization integral can be calculated quickly and much more accurately.
4. implementing the boundary condition for $r \rightarrow \infty$: because an analytical solution can be derived for the region outside the nanoshell where no charge is present, the boundary condition for $r \rightarrow \infty$ does not have to be implemented in a finite mesh point.

Chapter 6

Ideal Fermi gas in a spherically symmetric potential well

The purpose of this chapter is to investigate whether with the Transfer Matrix Method orbital-based calculations can be performed for SiO₂-Au nanoshells of manufacturable sizes. For this purpose, we study two exactly solvable systems that can be considered as first approximations to the real nanoshell system: an infinite and a finite spherically symmetric potential well between R_C and R_S that confine non-interacting fermions. The results discussed in this chapter represent original, unpublished work derived in the framework of the current Ph.D. thesis.

The chapter consists of three sections. In the first section, the details of the calculations are given for the infinite as well as for the finite potential well, both in the exact approach and with the Transfer Matrix Method. The results of the calculations are shown in the second section, where we compare both approaches and both systems. We also comment on the size-dependency of the Fermi energy of the infinite well. The last section contains a conclusion.

6.1 Calculation details

The radial differential equation for the non-interacting electrons in a spherically symmetric well described by the potential energy $u_{\text{well}}(r)$ is given by

$$\frac{1}{r^2} \frac{\partial}{\partial r} \left(r^2 \frac{\partial}{\partial r} \right) R_{n,\ell}(r) + \left[2\epsilon - \left(2u_{\text{well}}(r) + \frac{\ell(\ell+1)}{r^2} \right) \right] R_{n,\ell}(r) = 0. \quad (6.1)$$

6.1.1 Infinite well

The infinite potential well is described by

$$u_{\infty\text{well}}(r) = \begin{cases} 0 & \text{for } R_C < r < R_S \\ \infty & \text{elsewhere} \end{cases}.$$

No approximation

The potential energy is zero inside the entire shell. Because $\epsilon_{n,\ell} > 0$ the wave function has the form (see section 5.3.3)

$$R_{n,\ell}(r) = \begin{cases} aj_\ell(\lambda_{n,\ell}r) + by_\ell(\lambda_{n,\ell}r) & \text{for } R_C < r < R_S \\ 0 & \text{elsewhere} \end{cases}$$

with $j_\ell(x)$ and $y_\ell(x)$ spherical Bessel functions and $\lambda_{n,\ell} = \sqrt{2\epsilon_{n,\ell}}$. The boundary conditions on the wave function are $R_{n,\ell}(R_C) = 0$ and $R_{n,\ell}(R_S) = 0$. Using the boundary condition at $r = R_C$

and the expression (5.25) for the definite integral of the piecewise wave function, we get the following analytical expression for the normalized wave function:

$$\mathfrak{R}_{n,\ell}(r) = \sqrt{\frac{2}{R_S^3 z_\ell'^2(\lambda_{n,\ell} R_S) - R_C^3 z_\ell'^2(\lambda_{n,\ell} R_C)}} z_\ell(\lambda_{n,\ell} r) \quad (6.2)$$

with

$$\begin{aligned} z_\ell(\lambda_{n,\ell} r) &= j_\ell(\lambda_{n,\ell} r) - \frac{j_\ell(\lambda_{n,\ell} R_C)}{y_\ell(\lambda_{n,\ell} R_C)} y_\ell(\lambda_{n,\ell} r) \\ z_\ell'(X) &= \left. \frac{dz_\ell(x)}{dx} \right|_{x=X}. \end{aligned} \quad (6.3)$$

From expressions (6.2), (6.3) and the boundary condition at $r = R_S$, the two boundary conditions can be summarized in one function

$$f_{\infty\text{well}}(\epsilon) = j_\ell(R_C \sqrt{2\epsilon}) y_\ell(R_S \sqrt{2\epsilon}) - j_\ell(R_S \sqrt{2\epsilon}) y_\ell(R_C \sqrt{2\epsilon}) \quad (6.4)$$

which is equal to zero if the boundary conditions are fulfilled. This function $f_{\infty\text{well}}(\epsilon)$ is shown in figure 6.1 for three different values of ℓ for the first three zeros, and in figure 6.2 for one value of ℓ but for a wider range of ϵ -values. From figure 6.1 it is clear that

$$\begin{aligned} \epsilon_{n,\ell} &< \epsilon_{n,\ell'>\ell} \\ \epsilon_{n,\ell} &< \epsilon_{n'>n,\ell} \\ \Delta\epsilon_{n,\Delta\ell=1} &\ll \Delta\epsilon_{\Delta n=1,\ell}. \end{aligned} \quad (6.5)$$

From figure 6.2 we see that for a given ℓ -value the spacing between zeros increases with increasing n -value:

$$\epsilon_{n+1,\ell} - \epsilon_{n,\ell} < \epsilon_{(n+i)+1,\ell} - \epsilon_{(n+i),\ell} \text{ with } i \in \mathbb{N}_0. \quad (6.6)$$

The energy levels for $\ell = 0$ can be calculated analytically: since $j_0(x) = \sin(x)/x$ and $y_0(x) = -\cos(x)/x$ [1, 86], a zero value of $f_{\infty\text{well}}(\epsilon_{n,0})$ is found for $\sin[(R_S - R_C) \sqrt{2\epsilon_{n,0}}] = 0$. Hence the zeros for $\ell = 0$ are given by

$$\epsilon_{n,0} = \frac{1}{2} \left(\frac{\pi}{R_S - R_C} \right)^2 n^2 \text{ with } n \in \mathbb{N}_0.$$

To find the single-particle energies for arbitrary ℓ -value numerically, we considered the dimensionless argument $x = R_C \sqrt{2\epsilon}$. Successive zeros of $f_{\infty\text{well}}(x_{n,\ell})$ for the same ℓ -value turn out to be approximately equally spaced. We then used the following brackets to find $x_{n,\ell}$:

$$\begin{aligned} x_{\text{lower}} &= \begin{cases} \begin{cases} x_{n,\ell-1} - \frac{x_{1,0}}{2} & n = 1 \\ x_{n-1,\ell} + \frac{x_{1,0}}{100} & n > 1 \end{cases} & \text{to start the } p\text{'th iteration} \\ x_{\text{higher},n-1,\ell} + \frac{\Delta x_{\text{brac}}}{2} & \text{during an iteration} \end{cases} \\ x_{\text{higher}} &= x_{\text{lower}} + i_{\text{sufficient}} \Delta x_{\text{brac}} \end{aligned}$$

with

$$\Delta x_{\text{brac}} = \begin{cases} \frac{x_{1,0}}{10} & n \leq 2 \\ \frac{x_{n-1,\ell} - x_{n-2,\ell}}{10} & n > 2 \end{cases}.$$

By ‘‘the p 'th iteration’’ is meant the iteration for which the p 'th trial chemical potential $\mu(p)$ is considered, as explained in section 5.2. The value of $i_{\text{sufficient}}$ was obtained by successively adding Δx_{brac} to x_{lower} until $f_{\infty\text{well}}(x_{\text{lower}}) \times f_{\infty\text{well}}(x_{\text{higher}}) < 0$. For the orbital bookkeeping we need estimates for $\mu(1)$ and $\mu(p)$. Because the chemical potential of a nanoshell is expected to be of the order of magnitude of the bulk Fermi energy $\epsilon_{F,\text{bulk}}$, but somewhat higher because of the confinement, we have used $\mu(1) = \epsilon_{F,\text{bulk}}$ and $\mu(p) = \mu(p-1) + \epsilon_{F,\text{bulk}}/100$.

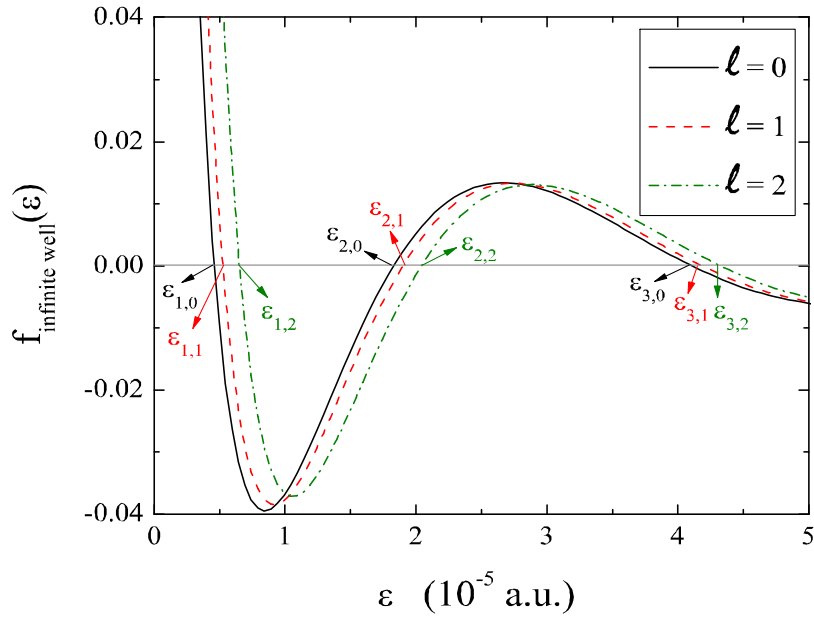


Figure 6.1: The function $f_{\infty\text{well}}(\epsilon)$, expression (6.4), for different ℓ -values - $\ell = 0$ (black solid line), $\ell = 1$ (red dashed line) and $\ell = 2$ (green dash-dotted line) - for a spherically symmetric infinite potential well with inner radius $R_C = 40$ nm and outer radius $R_S = 55$ nm in the energy range $0 \leq \epsilon \leq 5 \times 10^{-5}$ a.u.

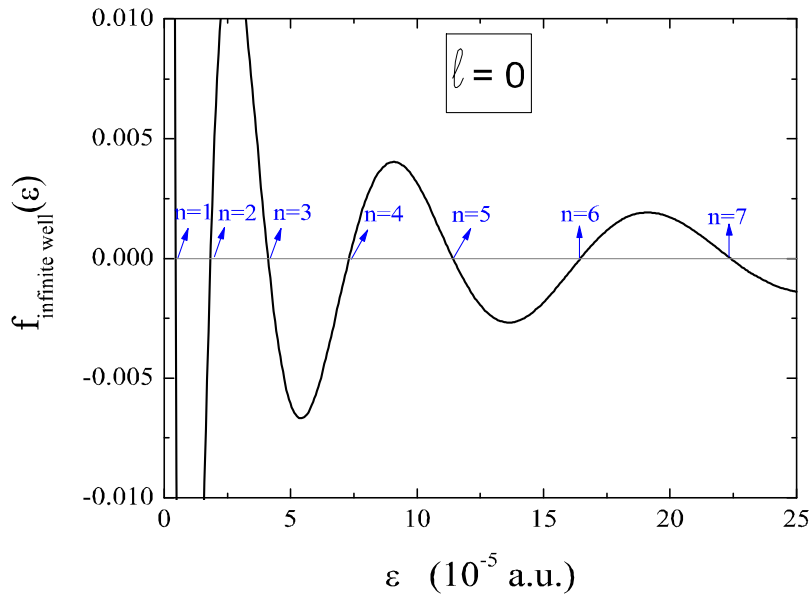


Figure 6.2: The function $f_{\infty\text{well}}(\epsilon)$, expression (6.4), for $\ell = 0$ for a spherically symmetric infinite potential well with inner radius $R_C = 40$ nm and outer radius $R_S = 55$ nm in the energy range $0 \leq \epsilon \leq 25 \times 10^{-5}$ a.u.

Approximation $[\ell(\ell+1)/r^2]_j = \ell(\ell+1)/(r_j r_{j+1})$

From section 5.3.3 on orbital calculation, we find that for $u_{\text{eff}}(r) = 0$ and if the approximation $[\ell(\ell+1)/r^2]_j = \ell(\ell+1)/(r_j r_{j+1})$ is used, the piecewise basis functions in the intervals are geometric or hyperbolic functions depending on whether ϵ is smaller or larger than the piecewise centrifugal term. The Transfer Matrix Method has the advantage that the number of nodes of a trial wave function can be calculated fast and accurately (see section 5.3.4), so in addition to using the knowledge of the approximate distance between successive energies we could check whether the guessed brackets were indeed good brackets and adjust them if necessary.

In the calculations we used forward recurrence with the coefficients $a_{j_{O+1}} = 1$ and $b_{j_{O+1}} = 0$ at $r = R_C$. The function that has to be zero for the correct boundary condition at $r = R_S$ was taken to be $f(\epsilon) = R_{n,\ell}(R_S) = b_{j_{R_S}}(\epsilon)/R_S$.

6.1.2 Finite well

When considering a finite potential well, values for the potential energies outside the well are needed. To determine a value for the potential energies in the core and the environment, we used the definition of the work function W . The work function is defined as the smallest amount of energy that is necessary to pull one electron out of a material. The electrons that are most easily pulled out, are the electrons at the Fermi surface. So the work function can be viewed as an energy barrier that electrons at the Fermi level should overcome to escape from the material. With this in mind, we used a finite potential well with the following characteristics:

$$u_{\text{finwell}}(r) = \begin{cases} u_C = \epsilon_F + W_{\text{Au} \rightarrow \text{SiO}_2} & \text{if } 0 \leq r \leq R_C \\ u_S = 0 & \text{if } R_C < r < R_S \\ u_E = \epsilon_F + W_{\text{Au} \rightarrow \text{vacuum}} & \text{if } R_S \leq r \end{cases} .$$

Because up to now only bulk values of the involved energy quantities are known, we rely on these values:

	value (eV)	Ref.
$\epsilon_{F,\text{bulk}}$	5.53	[58]
$W_{\text{Au} \rightarrow \text{SiO}_2,\text{bulk}}$	3.8	[35]
$W_{\text{Au} \rightarrow \text{vacuum},\text{bulk}}$	5.38	mean of values given in Ref. [40]

No approximation

We are looking for bound states, so $\epsilon_{n,\ell} < u_C$ and $\epsilon_{n,\ell} < u_E$. Then the normalized piecewise wave functions in the core (C), shell (S) and environment (E) which fulfill the boundary condition that the wave function is integrable, can be straightforwardly calculated as (see section 5.3.3):

$$\begin{aligned} \mathfrak{R}_{n,\ell}^{(C)}(r) &= G_\ell^{(1)}(\epsilon_{n,\ell}) \frac{i_\ell \left(\sqrt{2(u_C - \epsilon_{n,\ell})} r \right)}{i_\ell \left(\sqrt{2(u_C - \epsilon_{n,\ell})} R_C \right)} \\ \mathfrak{R}_{n,\ell}^{(S)}(r) &= G_\ell^{(1)}(\epsilon_{n,\ell}) \left[Q_\ell^{(1)}(\epsilon_{n,\ell}) j_\ell \left(\sqrt{2\epsilon_{n,\ell}} r \right) + Q_\ell^{(2)}(\epsilon_{n,\ell}) y_\ell \left(\sqrt{2\epsilon_{n,\ell}} r \right) \right] \\ \mathfrak{R}_{n,\ell}^{(E)}(r) &= D_\ell(\epsilon_{n,\ell}) G_\ell^{(1)}(\epsilon_{n,\ell}) \frac{k_\ell \left(\sqrt{2(u_E - \epsilon_{n,\ell})} r \right)}{k_\ell \left(\sqrt{2(u_E - \epsilon_{n,\ell})} R_C \right)} \end{aligned}$$

with the newly introduced functions defined as

$$\frac{1}{G_\ell^{(1)}(\epsilon)} = \sqrt{\frac{R_C^3}{2} \left[\begin{array}{c} \left(\frac{1}{2(u_C - \epsilon)R_C^2} + \frac{1}{2\epsilon R_C^2} \right) \times \left(\begin{array}{c} \ell(\ell+1) \\ - \left[G_\ell^{(2)} \left(\sqrt{2(u_C - \epsilon)R_C^2} \right) \right]^2 \\ - G_\ell^{(2)} \left(\sqrt{2(u_C - \epsilon)R_C^2} \right) \end{array} \right)^2 \\ - D_\ell^2(\epsilon) \frac{R_S}{R_C} \left(\frac{1}{2(u_E - \epsilon)R_C^2} + \frac{1}{2\epsilon R_C^2} \right) \\ \times \left(\begin{array}{c} \ell(\ell+1) \\ - \left[G_\ell^{(3)} \left(\sqrt{2(u_E - \epsilon)R_S} \right) \right]^2 \\ - G_\ell^{(3)} \left(\sqrt{2(u_E - \epsilon)R_S} \right) \end{array} \right)^2 \end{array} \right]} \\ \\ D_\ell(\epsilon) = \left[Q_\ell^{(1)}(\epsilon) j_\ell(\sqrt{2\epsilon}R_S) + Q_\ell^{(2)}(\epsilon) y_\ell(\sqrt{2\epsilon}R_S) \right] \\ Q_\ell^{(1)}(\epsilon) = \sqrt{2\epsilon}R_C \left[\begin{array}{c} \sqrt{2\epsilon}R_C y'_\ell(\sqrt{2\epsilon}R_C) \\ - G_\ell^{(2)} \left(\sqrt{2(u_C - \epsilon)R_C} \right) y_\ell(\sqrt{2\epsilon}R_C) \end{array} \right] \\ Q_\ell^{(2)}(\epsilon) = \sqrt{2\epsilon}R_C \left[\begin{array}{c} G_\ell^{(2)} \left(\sqrt{2(u_C - \epsilon)R_C} \right) j_\ell(\sqrt{2\epsilon}R_C) \\ - \sqrt{2\epsilon}R_C j'_\ell(\sqrt{2\epsilon}R_C) \end{array} \right] \\ G_\ell^{(2)}(z) = z \frac{i'_\ell(z)}{i_\ell(z)} \\ G_\ell^{(3)}(z) = z \frac{k'_\ell(z)}{k_\ell(z)}.$$

From the requirement that the wave function and its derivative should be continuous at the shell boundaries, we can again derive an analytical expression for a function which is equal to zero if and only if the boundary conditions are satisfied:

$$f_{\text{finwell}}(\epsilon) = \left\{ \begin{array}{c} T_\ell^{(1)}(\epsilon) \left[\begin{array}{c} \frac{R_C}{R_S} j_\ell(\sqrt{2\epsilon}R_S) G_\ell^{(3)} \left(\sqrt{2(u_E - \epsilon)R_S} \right) \\ - \sqrt{2\epsilon}R_C j'_\ell(\sqrt{2\epsilon}R_S) \end{array} \right] \\ + T_\ell^{(2)}(\epsilon) \left[\begin{array}{c} \frac{R_C}{R_S} y_\ell(\sqrt{2\epsilon}R_S) G_\ell^{(3)} \left(\sqrt{2(u_E - \epsilon)R_S} \right) \\ - \sqrt{2\epsilon}R_C y'_\ell(\sqrt{2\epsilon}R_S) \end{array} \right] \end{array} \right\}. \quad (6.7)$$

In this expression,

$$T_\ell^{(1)}(\epsilon) = \frac{Q_\ell^{(1)}(\epsilon)}{\sqrt{2\epsilon}R_C} = \left\{ \begin{array}{c} \sqrt{2\epsilon}R_C y'_\ell(\sqrt{2\epsilon}R_C) \\ - G_\ell^{(2)} \left(\sqrt{2(u_C - \epsilon)R_C} \right) y_\ell(\sqrt{2\epsilon}R_C) \end{array} \right\} \\ T_\ell^{(2)}(\epsilon) = \frac{Q_\ell^{(2)}(\epsilon)}{\sqrt{2\epsilon}R_C} = \left\{ \begin{array}{c} G_\ell^{(2)} \left(\sqrt{2(u_C - \epsilon)R_C} \right) j_\ell(\sqrt{2\epsilon}R_C) \\ - \sqrt{2\epsilon}R_C j'_\ell(\sqrt{2\epsilon}R_C) \end{array} \right\}.$$

The function (6.7) has globally the same behavior as the function (6.4) of the infinite well, with zeros for the same ℓ -value shifted to lower energy by a very small amount with respect to the distance between the zeros. We therefore used the same procedure to determine the relevant orbitals as in the case of the infinite well.

Approximation $[\ell(\ell+1)/r^2]_j = \ell(\ell+1)/(r_j r_{j+1})$ in the well

In the region that contains the origin, the modified spherical Bessel functions of the third kind is excluded by the boundary conditions so $b_O = 0$. The recurrence can thus be initiated by determining a_{j_O+1} and b_{j_O+1} from expression (5.12) and (5.9) with the appropriate basis functions and starting coefficient a_O . The recurrence can be ended in $r = R_S$ where the function (5.14) can be applied with a modified spherical Bessel function of the third kind, $k_\ell(\lambda_E R_S)$, for $u_1(j_\infty, \epsilon, R_\infty)$.

6.2 Results

We determined the occupied bounded states as explained in sections 5.2 and 5.3. For the infinite and finite well with $R_C = 40$ nm and $R_S = 55$ nm approximately 26×10^3 different radial orbitals had to be determined with $n_{\max} \simeq 57$ and $\ell_{\max}(n=0) \simeq 648$.

6.2.1 Comparison of used approaches

We quantitatively compared the energy levels of the infinite well obtained by the calculations without approximation and by the calculations with the Transfer Matrix Method (TMM) with 1, 10, 20 and 100 mesh points per nm. We looked at the relative error Δ_{rel} defined as $\Delta_{\text{rel}} = \left| \left(\epsilon_{n,\ell}^{(\text{exact})} - \epsilon_{n,\ell}^{(\text{TMM})} \right) / \epsilon_{n,\ell}^{(\text{exact})} \right|$. The mean relative error $\langle \Delta_{\text{rel}} \rangle$ and maximum relative error $(\Delta_{\text{rel}})_{\max}$ are given in the table below.

	$\langle \Delta_{\text{rel}} \rangle$	$(\Delta_{\text{rel}})_{\max}$
1 point per nm	4.5×10^{-4}	4.3×10^{-2}
10 points per nm	8.2×10^{-6}	9.1×10^{-4}
20 points per nm	2.7×10^{-6}	4.1×10^{-4}
100 points per nm	1.8×10^{-7}	1.6×10^{-6}

Already for 1 mesh point per nm (i.e. 15 mesh points in the shell), the mean relative error on the energy levels is as low as 4.5×10^{-4} . For a similar accuracy, 33000 grid points were needed when using finite element integration for nanoshells with an overall size smaller than 16 nm (the shell *thickness* we considered) and a shell thickness not larger than 2 nm [106]. The smaller number of mesh points is a big advantage of the Transfer Matrix Method since more mesh points lead to more round-off errors and more data to be stored.

Another advantage of the Transfer Matrix Method is that one does not need more “recurrence points” (points used for the recurrence to find the eigenenergies) if one wants to calculate or visualize the wave functions or density in more mesh points. For each “recurrence interval”, the basis functions and the values of their coefficients are known. This allows to calculate more values of the wave functions in the interval between the “recurrence points”.

We show in the table below the time needed for the calculation without approximation in which the wave functions and density are calculated in 20 mesh points, and with the Transfer Matrix Method (TMM) for different numbers of mesh points in the infinite potential well. In this table, t_ϵ denotes the time needed to calculate the energy levels and $t_{R,n}$ the time needed to calculate the wave functions and the density of the ideal Fermi gas. The calculation time for an ideal Fermi gas will be approximately equal to the calculation time of one iteration in a Kohn-Sham calculation. The calculations were performed on a 64 bit desktop (AMD Dual Core 3.0 GHz).

	t_ϵ (s)	$t_{R,n}$ (s)
exact, 20 points per nm	8	247
TMM, 1 point per nm	3	1
TMM, 10 points per nm	47	3
TMM, 20 points per nm	127	3

The calculation time is of course an increasing function of the number of mesh points. The calculation of the energy levels takes less time in the exact approach, except if only 1 mesh point per nm is considered in the Transfer Matrix Method. The calculation of the wave functions takes much more time in the exact approach for the considered numbers of mesh points. The analysis of the relative error on the energy levels showed that when using the Transfer Matrix Method, 20 mesh points per nm gives a sufficient high accuracy. With this number of mesh points the calculations for the benchmark nanoshell take a reasonable amount of time.

6.2.2 Infinite versus finite well

In figure 6.3 we show the single-particle density $|\mathbf{R}_{n,\ell}(r)|^2$ in the infinite well for different values of \mathbf{n} and ℓ . From this figure it is clear that the quantum number \mathbf{n} is indeed related to the number of nodes in the potential well. The single-particle density is not symmetric with respect to the center of the well as is the case for a one-dimensional square well (cfr. figure 1.1). There are two terms in the radial differential equation,

$$\frac{\partial^2 \mathbf{R}_{n,\ell}(r)}{\partial r^2} + \frac{2}{r} \frac{\partial \mathbf{R}_{n,\ell}(r)}{\partial r} + \left[2\epsilon - \left(2u_{\text{well}}(r) + \frac{\ell(\ell+1)}{r^2} \right) \right] \mathbf{R}_{n,\ell}(r) = 0,$$

that cause an opposite asymmetry of the single-particle density with respect to the center of the well. The term $\frac{2}{r} \frac{\partial \mathbf{R}_{n,\ell}(r)}{\partial r}$ results in more weight of the density in the inner half of the shell because of the $1/r$ factor which lowers the change $\partial \mathbf{R}_{n,\ell}(r) / \partial r$ in the wave function more with increasing r . This effect is clearly seen from the plot in figure 6.3 of the single-particle density of a state with $\ell = 0$. The centrifugal term $\ell(\ell+1)/r^2$ on the other hand leads to more weight in the outer half of the shell because it results in a lower effective potential energy at larger r -values. This term can lead to a very asymmetric single-particle density as is shown in figure 6.3 for two states with $\ell = 628$.

Although the highly asymmetric states with large ℓ -value each have a larger contribution to the density than a state with low ℓ -value, $n(r) = \frac{1}{4\pi} \sum \sum 2(2\ell+1) |\mathfrak{R}_{n,\ell}(r)|^2$, the total density is rather symmetric with respect to the center of the well, see figure 6.4. At the well boundaries the density shows strong oscillations around the homogeneous density. These are a consequence of the Gibbs phenomenon. This phenomenon occurs if in an eigenfunction expansion of a function at a discontinuity, only a finite set of eigenfunctions is taken into account. The density shown in figure 6.4 is constructed from a finite number of orbitals and as such displays the oscillatory behaviour of the radial wave functions. The amplitude of the oscillations decreases if more eigenfunctions are taken into account. This is clear from figure 6.5 in which the density is shown for two nanoshells that differ considerably in size and therefore also in number of orbitals. In the figure also an asymmetry with respect to the center of the well is observed. This asymmetry also decreases with the number of eigenfunctions taken into account.

Figure 6.4 shows that the density of the finite well is very similar to that of the infinite well and shows a small spill-out.

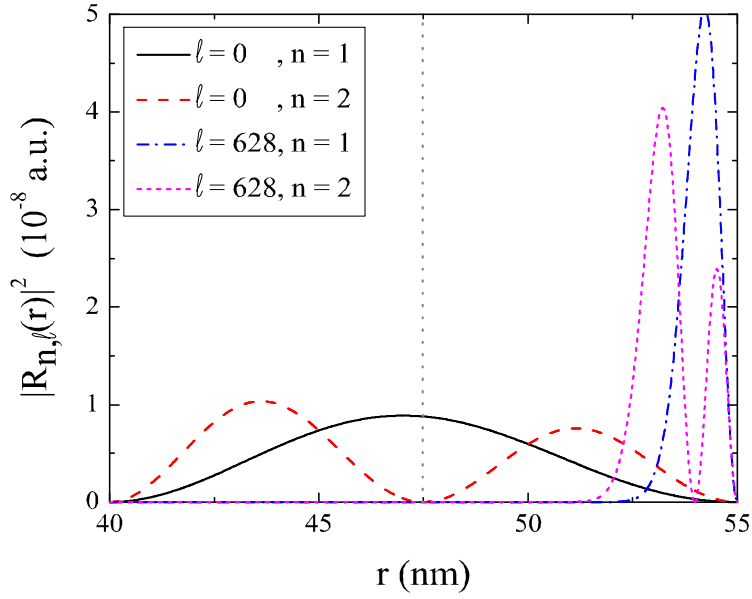


Figure 6.3: Single-particle density $|R_{n,\ell}(r)|^2$ in a spherically symmetric infinite potential well with $R_C = 40$ nm and $R_S = 55$ nm for $(\mathbf{n}, \ell) = (1, 0)$ (black solid line), $(\mathbf{n}, \ell) = (2, 0)$ (red dashed line), $(\mathbf{n}, \ell) = (1, 628)$ (blue dashed-dotted line) and $(\mathbf{n}, \ell) = (2, 628)$ (magenta short-dashed line).

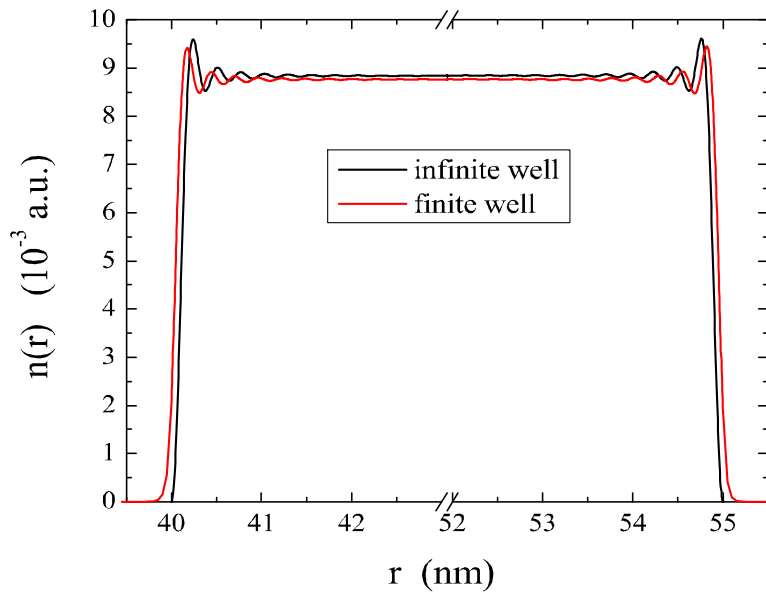


Figure 6.4: Density of non-interacting electrons in a spherically symmetric infinite (black line) and finite (red line) potential well with $R_C = 40$ nm and $R_S = 55$ nm.

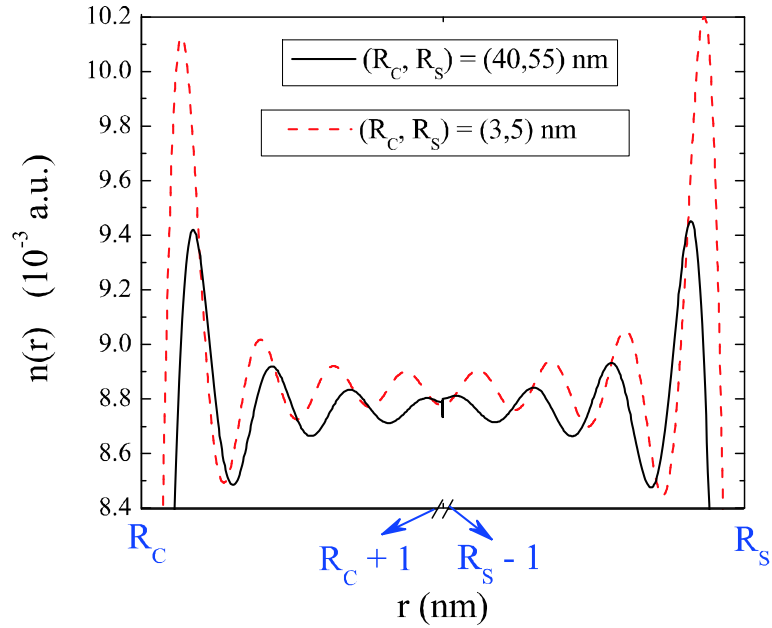


Figure 6.5: Part of the density of non-interacting fermions in a spherically symmetric finite potential well to illustrate the Gibbs phenomenon and asymmetry in a well with $(R_C, R_S) = (40, 55)$ nm (black solid line) and with $(R_C, R_S) = (3, 5)$ nm (red dashed line).

As for the energy spectrum, there is also a small difference between the infinite and the finite potential well, as shown in figure 6.6. The energy levels of the finite well are somewhat lower than those of the infinite well. One way to understand this is by looking at the analytical expression for the energy levels $\epsilon_{n,0}$ of the infinite potential well:

$$\epsilon_{n,0} = \frac{1}{2} \left(\frac{\pi}{R_S - R_C} \right)^2 n^2. \quad (6.8)$$

From this expression it is clear that if the well gets wider, the energy lowers. A wider well means that the electrons can spread out over a wider region. For a finite well, due to spill-out, the electrons also have a wider reach than in the infinite potential well with the same size. It also follows from expression (6.8) that the wider the well, the closer the energy levels. In the limit of an infinitely wide well there will thus be a continuous spectrum as expected for a bulk jellium system.

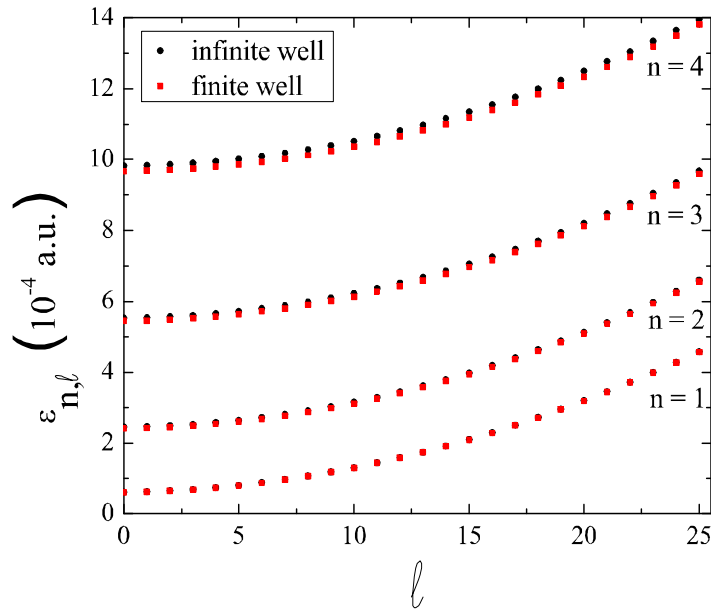


Figure 6.6: Part of the energy spectrum of the infinite (black circles) and finite (red squares) spherically symmetric potential wells with $R_C = 40$ nm and $R_S = 55$ nm.

6.2.3 Fermi energy as function of shell thickness

We calculated the Fermi energy for infinite wells with $R_C = 40$ nm and different R_S -values, of 55 nm and higher.

With the exact calculations we were able to reach $R_S = 90$ nm. From that radius on, the Fermi energy started to rise until at $R_S = 115$ nm it reached the maximum value allowed in the program, $\epsilon_F = 2\epsilon_{F,\text{bulk}}$. This unphysical behavior is probably caused by skipping energy levels. If energy levels are skipped, then energy levels will be taken into account to calculate the Fermi energy that are higher than the ones that are contributing in reality. This is possible because the calculation for a certain R_S is ended depending on the value of the function (5.3) in which no energy levels enter but only the ℓ -values of the calculated orbitals. It thus seems advisable also in this approach to check the number of nodes of the wave functions and to adjust the brackets if necessary. This means that a sufficient number of mesh points has to be considered, especially for higher energies. From this result it is again clear, as mentioned earlier, that an efficient bracketing procedure is crucial.

In the case with the approximation $[\ell(\ell+1)/r^2]_j = \ell(\ell+1)/(r_j r_{j+1})$ in the shell, we calculated the Fermi energy for $R_S = (55, 56, \dots, 90)$ nm, and for $R_S = 100$ nm, $R_S = 115$ nm, and $R_S = 130$ nm. In these calculations we considered 20 mesh points per nm. From the values of the Fermi energy of the wells with $R_S > 90$ nm, shown in figure 6.7, it is clear that the Fermi energy indeed does not rise if R_S increases. The calculations for $R_S = 100$ nm took about 24 hours and the calculations for $R_S = 130$ nm about 48 hours on a 64 bit desktop (AMD Dual Core 3.0 GHz). In the case $R_S = 130$ nm, 277093 states were calculated with $n_{\text{max}} = 345$ and $\ell_{\text{max}}(n=0) = 1543$.

Up to the outer radius that was reached in both approaches, the results are approximately the same, as shown in figure 6.7. The confinement of the electrons leads to a higher Fermi energy than the bulk value for gold and the Fermi energy lowers with increasing shell thickness.

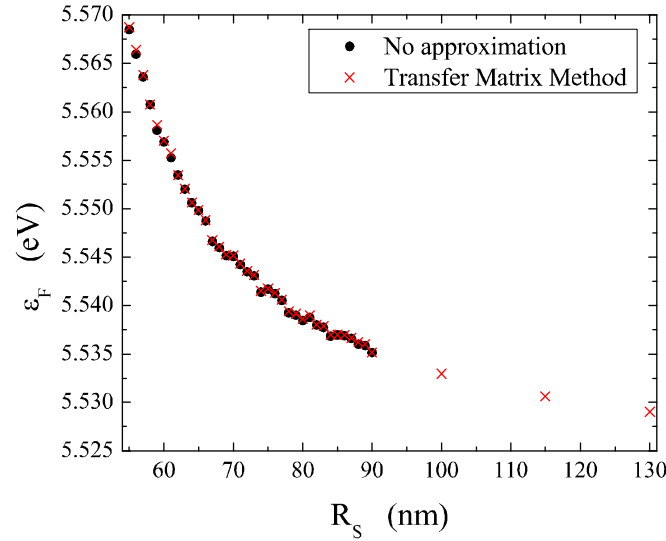


Figure 6.7: Fermi energy of a spherically symmetric infinite potential well with $R_C = 40$ nm as a function of R_S calculated without approximation (black circles) and with the Transfer Matrix Method with 20 mesh points per nm (red crosses).

To see from which overall radius on the difference with the bulk Fermi energy becomes negligible, we used Mathematica[®] to fit the calculated values to functions of the form $\epsilon'_F(R_S) = \epsilon'_{F,p}(\infty) + C'_p/R_S^p$ and $\epsilon_F(d) = \epsilon_{F,p}(\infty) + C_p/d^p$ with $d = R_S - R_C$ and $p \in \mathbb{N}_0$. These classes of functions have the correct behavior: descending as a function of R_S and tending to a finite value as $R_S \rightarrow \infty$. The χ^2 -values of fits with $p = 1, \dots, 5$ are:

p	χ^2 for $\epsilon'_F(R_S)$	χ^2 for $\epsilon_F(d)$
1	2.59×10^{-4}	4.80×10^{-6}
2	9.60×10^{-5}	1.31×10^{-4}
3	2.25×10^{-5}	4.13×10^{-4}
4	1.26×10^{-5}	7.33×10^{-4}
5	4.54×10^{-5}	1.04×10^{-3}

The class of functions $\epsilon_F(d)$ results in the best fit. This indicates that the quantity that determines the nanoshell properties is the shell thickness d and not the overall radius which seems to determine the properties of solid spheres like e.g. the work function [131]. Since $p = 1$ leads to the best fit, the Fermi energy of a nanoshell can then be written as a function of the shell thickness d as

$$\epsilon_F(d) = \epsilon_F(\infty) + \frac{C}{d}$$

with C a constant. With the Fermi energy expressed in eV and the shell thickness in nm, we find for $R_C = 40$ nm that the fitting parameters are equal to $\epsilon_F(\infty) = 5.52091$ eV and $C = 0.71875$ nm eV. The data points together with the best fit and $\epsilon_F(\infty)$ are shown in figure 6.8. The relative difference $[\epsilon_F(d) - \epsilon_F(\infty)]/\epsilon_F(\infty)$ is shown in figure 6.9 for the case $R_C = 40$ nm. This figure indicates that confinement effects are not negligible for nanoshells.

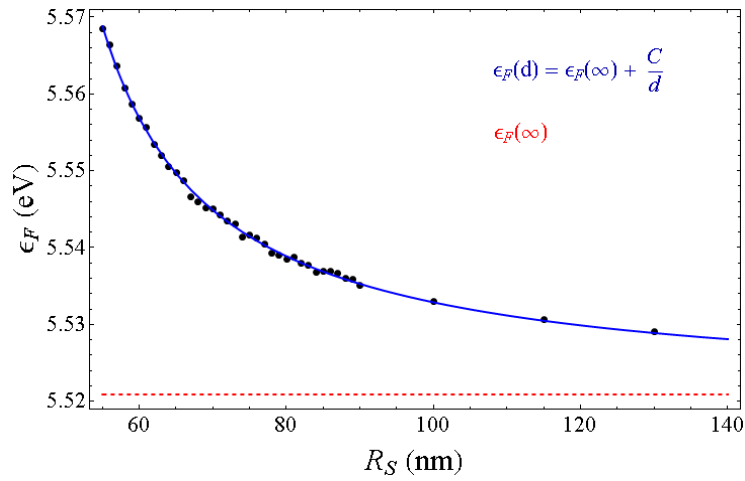


Figure 6.8: Calculated values of the Fermi energy of spherically symmetric infinite wells with $R_C = 40$ nm and different values of R_S (black dots), best fit of $\epsilon_F(d) = \epsilon_F(\infty) + C/d$ (blue solid line) and $\epsilon_{F,p}(\infty)$ of the best fit (red dashed line).

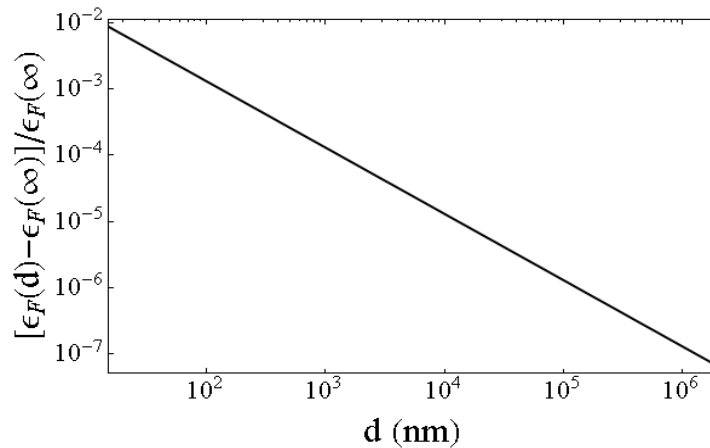


Figure 6.9: Relative difference between the Fermi energy $\epsilon_F(d)$ of a spherically symmetric infinite potential well and the bulk limit Fermi energy $\epsilon_F(\infty)$ as a function of the shell thickness d . The inner radius is equal to $R_C = 40$ nm. A log-log plot is used to indicate the orders of magnitude.

6.3 Conclusion

Comparison with analytical results of an ideal Fermi gas in a spherically symmetric potential well indicates that the Transfer Matrix Method is appropriate to calculate the orbitals of a nanoshell. It offers a way to solve the single-particle Schrödinger equations with a number of grid points that is about thousand times smaller than the number of grid points needed in the Kohn-Sham calculations for small nanoshells based on Runge-Kutta integration [106]. The method is also relatively fast and allows for secure bracketing of the eigenenergies.

Performing the calculations it became however clear that also an orbital-based treatment using the Transfer Matrix Method is very demanding for manufacturable-size SiO₂-Au nanoshells. We managed to treat this model for the benchmark nanoshell with $(R_C, R_S) = (40, 50)$ nm in a reasonable amount of time, but the calculation time rapidly increases with increasing shell thickness. Furthermore, memory problems arise because information on the orbitals has to be stored until the Fermi level is found and the density has been calculated.

To calculate the ground-state properties of nanoshells with dimensions that can be fabricated at present, we thus have to rely on methods without orbital calculations (which have the additional advantage that no orbital bookkeeping is involved). The next part of this thesis is dedicated to such a method.

Part III

Orbital-free calculations: a new method

In the previous part of this thesis it became clear that it is very demanding to perform orbital-based calculations for SiO₂-Au nanoshells for which at the moment the smallest manufacturable sizes are $(R_C, R_S) = (40, 55)$ nm. If the size of the nanoshells increases, an orbital-based treatment quickly becomes impossible. For nanoshells of these dimensions we thus have to rely on orbital-free methods. Because of the disadvantages of existing orbital-free methods mentioned in section 2.4, we developed a new orbital-free method called “density-functional Monte Carlo” (abbreviated as DFMC). Basically it is a direct numerical minimization of the energy functional by a Monte Carlo algorithm without the detour over the Euler equation (2.22) on which existing orbital-free implementations are based. In the DFMC method, the density is guaranteed to be non-negative in the entire domain and the number of particles is kept constant by construction. The algorithm is not based on solving a non-trivial differential, integral or integro-differential equation, but on the calculation of an integral, which is computationally easier.

This third part of the thesis contains four chapters. In chapter 7 some basic *background* is sketched concerning the Monte Carlo part of the method. That chapter is followed by an outline of the general procedure of the *DFMC* method. In chapter 9 we explain how we applied DFMC to *nanoshells* and what are the results. Chapter 10 contains a *conclusion* of the performed calculations. The part is ended with a *positioning and outlook* of DFMC.

The basics of the DFMC method and its application to the benchmark nanoshell are published as K. Putteneers, F. Brosens, *Monte Carlo implementation of density-functional theory*, Phys. Rev. B **86**, 085115 (2012).

Some of the material was also presented as a poster “Density-functional Monte Carlo for calculating properties of nanosystems”, resulting in the second prize of the European Physical Journal Best Poster Contest at the General Scientific Meeting of the Belgian Physical Society in Namur on May 25, 2011. This prize led to the invited publication K. Putteneers, *Density-functional Monte Carlo for calculating properties of nanosystems*, *BΦ*, Belgian Physical Society Magazine, nr. 3 (2011).

Chapter 7

Useful background

In this chapter some useful background is sketched for the newly developed density-functional Monte Carlo method. In the first section we explain how random numbers can be sampled according to a given distribution. This section is followed by an exposition of the minimization of a multidimensional function based on simulated annealing. The final section of this chapter outlines how free diffusion can be generated by using random numbers.

7.1 Sampling random variates according to a given distribution

For the method we propose, we need a way to generate random numbers according to a given probability distribution. Such a probability distribution is described by a function $p(\mathbf{x})$ of variables $\mathbf{x} = \{x_1, \dots, x_M\}$ on a domain Ω that has the properties

$$\forall \mathbf{x} \in \Omega : p(\mathbf{x}) \geq 0 \quad (7.1)$$

$$\int_{\Omega} p(\mathbf{x}) d\mathbf{x} = 1. \quad (7.2)$$

We thus want to generate random numbers with more numbers in the region where $p(\mathbf{x})$ has higher values, and less in the region where $p(\mathbf{x})$ has lower values. Such randomly drawn values of a variable are called **variates** or **deviates**.

In this section, we discuss three methods to generate such random numbers. In all methods, use is made of numbers that are uniformly distributed in the interval $[0, 1]$, which means that all numbers generated have an equal probability to occur in this interval. The probability of generating such a number between x and $x + dx$, is then given by

$$p(x) dx = \begin{cases} dx & 0 < x < 1 \\ 0 & \text{otherwise} \end{cases} . \quad (7.3)$$

This uniform distribution is denoted by $\mathcal{U}(0, 1)$. There exist numerous ready-to-use algorithms for drawing numbers according to this distribution. Below, we denote variates drawn according to this distribution by ξ , and variates that are drawn according to another distribution by η .

We discuss three ways to generate random numbers according to a distribution that differs from $\mathcal{U}(0, 1)$. The first two are classified as “transformation method”. The third one is called “rejection method”. We have only used the last method in our calculations, but the other methods can also be of use for DFMC calculations. More information can be found in e.g. Ref. [98].

7.1.1 Transformation method

Based on the Jacobian

The following rule can be used to generate random numbers according to a wanted distribution $\tilde{p}(\mathbf{y})$ starting from a distribution $p(\mathbf{x})$.

Suppose that we generate a deviate η_1 according to a one-dimensional probability distribution function $p(x)$ and take some prescribed function of it, $y(\eta_1)$. Then the probability distribution of y , denoted as $\tilde{p}(y) dy$, is determined by the fundamental transformation law of probabilities, which is

$$|\tilde{p}(y) dy| = |p(x) dx|$$

or

$$\tilde{p}(y) = \left| \frac{dx}{dy} \right| p(x). \quad (7.4)$$

In M dimensions this rule becomes

$$\tilde{p}(y_1, \dots, y_M) = J(\mathbf{x}, \mathbf{y}) p(x_1, \dots, x_M)$$

in which the Jacobian $J(\mathbf{x}, \mathbf{y})$ is given by the determinant

$$J(\mathbf{x}, \mathbf{y}) = \begin{vmatrix} \frac{\partial x_1}{\partial y_1} & \dots & \frac{\partial x_1}{\partial y_M} \\ \dots & \dots & \dots \\ \frac{\partial x_M}{\partial y_1} & \dots & \frac{\partial x_M}{\partial y_M} \end{vmatrix}.$$

As an illustration, suppose one wants to draw random numbers that are exponentially distributed, e.g. for simulating radioactive decay of nuclei. If we draw random numbers ξ according to $\mathcal{U}(0, 1)$, then the numbers $\eta = y(\xi) = -\ln(\xi)$ are distributed as $\exp(-y)$. Indeed:

$$\tilde{p}(y) = \left| \frac{dx}{dy} \right| p(x) \stackrel{\text{Eq. (7.3)}}{=} \left| \frac{d(e^{-y})}{dy} \right| = e^{-y}.$$

A famous transformation that makes use of the multi-dimensional version of this method is the Box-Muller transformation to generate normal (Gaussian) distributed random numbers based on uniformly distributed random numbers.

Based on the cumulative distribution function

This method can only be applied for one-dimensional distribution functions $\tilde{p}(y)$. Deriving variates according to $\tilde{p}(y)$ from uniformly distributed variates is, according to equation (7.4) and definition (7.3), equivalent to solving the differential equation

$$\frac{dx}{dy} = \tilde{p}(y).$$

But the solution of this differential equation is just $x = F(y)$, with $F(y) = \int_{-\infty}^y \tilde{p}(y') dy'$ the integral of $\tilde{p}(y)$ called the cumulative distribution function. This is a function that monotonically increases from $F(-\infty) = 0$ to $F(+\infty) = 1$. The desired transformation that takes a uniform deviate ξ into a deviate η that is distributed as $\tilde{p}(y)$, is therefore

$$\eta = F^{-1}(\xi)$$

with F^{-1} the inverse function of F . This is graphically visualized in figure 7.1.

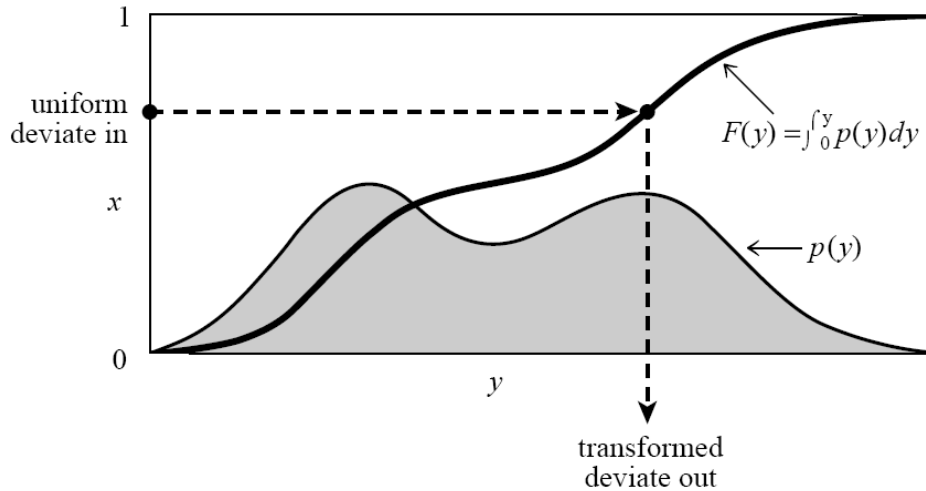


Figure 7.1: Visualization of the transformation method based on the use of the cumulative distribution function (figure taken from Ref. [98]).

Whether this method is feasible depends on whether the inverse function of the integral of $\tilde{p}(y)$ can be computed. If it is not possible to calculate this function analytically, a numerical version of the method might offer a solution. Therefore one constructs a grid with J grid points characterized by indices j and y -values y_j . One calculates the values of $\tilde{p}(y)$ on the grid, call these \tilde{p}_j . The value of the cumulative distribution function F_j in grid point j is then given by

$$F_j = \sum_{j'=1}^j \tilde{p}_{j'},$$

or a more sophisticated numerical calculation of the integral. The procedure is then to generate a variate $\xi \in \mathcal{U}(0, 1)$ and to check for which interval j this ξ fulfills the condition $F_j \leq \xi < F_{j+1}$. The variate according to $\tilde{p}(y)$ is then equal to y_j .

7.1.2 Rejection method

The rejection method is a general technique for generating random variates whose distribution function $\tilde{p}(\mathbf{y})$ is known and computable. The method does not require a computable cumulative distribution function, nor its inverse. It can be applied for multi-dimensional distribution functions, but the efficiency quickly decreases with increasing number of dimensions.

We will explain the principle based on the geometrical picture of a one-dimensional distribution, see figure 7.2. Draw a graph of the probability distribution $\tilde{p}(y)$ according to which one wants to generate deviates. The area under this curve in any range of y corresponds to the desired probability of generating a deviate η in that range. Now if we could generate (two-dimensional) random points (y, z) with uniform probability under the curve, then the y -values of those random points would have the desired distribution. Generating such uniform random points under the area can be done as follows. On the same graph, draw another curve $f(y)$ that has a finite area, lies everywhere above the probability function $\tilde{p}(y)$ and according to which one knows how to draw a random number. Now generate such a random number η according to $f(y)$. Then pick a random number ζ which is uniformly distributed between 0 and $f(\eta)$ (this can be done as $\zeta = f(\eta)\xi$ with $\xi \in \mathcal{U}(0, 1)$). If $\zeta \leq \tilde{p}(\eta)$, then accept η , else reject the variate.

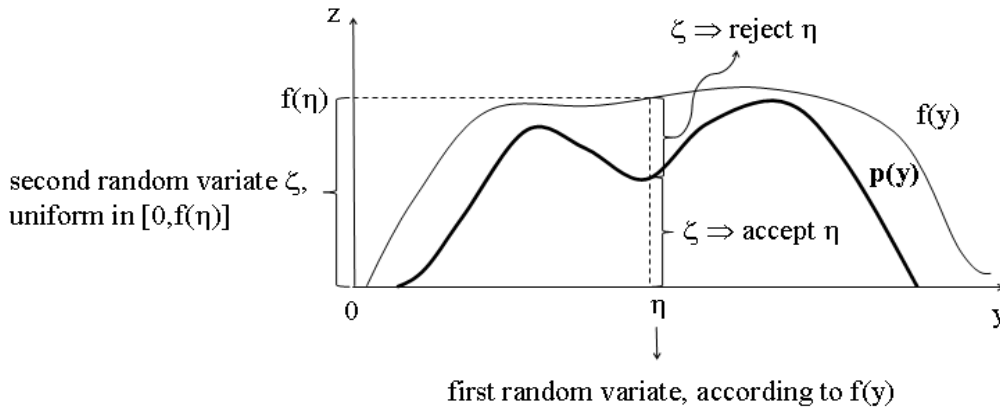


Figure 7.2: Geometrical picture of the rejection method in one dimension.

A well-known example in which the rejection method is used, is the calculation of π with random numbers. In this method one wants to generate points which are randomly distributed in a circle, say the unit circle. One does this by generating points (x, y) which are uniform randomly distributed in a square with side 1 ($x \in \mathcal{U}(0, 1)$ and $y \in \mathcal{U}(0, 1)$) and then only accept the points for which $r = \sqrt{x^2 + y^2} \leq 1$.

7.2 Optimization inspired by simulated annealing

The idea behind density-functional Monte Carlo is to perform a direct numerical minimization of the energy functional. Numerically, the density is given by $N_x \times N_y \times N_z$ values $n_{x,y,z}$ if N_α is the number of grid points in direction α . The energy then in fact depends on $N_x \times N_y \times N_z$ variables, the values of the density $n_{x,y,z}$ in the mesh points. Such a function that depends on many variables and that one wants to optimize, is called a **cost function** or **objective function**. The problem of minimizing a cost function is called multivariate or combinatorial optimization. In 1983 Kirkpatrick et al. [57] noticed that this difficult kind of problem can be solved with the aid of statistical mechanics if the size of such an optimization problem is large enough. The original idea, “simulated annealing”, is quite well-known and often used. We will explain it below, followed by two other methods that are derived from the basic idea. Although we have only used the third method in the DFMC calculations, the two other methods can equally well be used.

Before explaining the methods, we first briefly mention some related ways that can be used to perform a multivariate optimization, and how Kirkpatrick and co-workers came up with the idea that one could make a link with statistical mechanics.

Before the work of Kirkpatrick et al., there existed two solution types for the problem of multivariate optimization: “exact” methods, of which the computer effort scales exponentially with the number of variables M , and “heuristic” methods, of which the computational requirements are proportional to small powers of M . Of the last type there were two basic strategies. The first one is the **divide-and-conquer** method in which the problem is divided in subproblems that are solved separately and in the end patched back together. The second one is called **iterative improvement**. In this method, an initial configuration is rearranged until a configuration is found that improves the objective function. Then the procedure continues from this configuration. This process is carried on until no further improvements of the cost function can be found. Because only configurations are accepted that improve the objective function, the procedure usually gets stuck in a local minimum, and the sought global minimum is not found.

Therefore it was customary to repeat the process several times starting from different initial configurations, and to retain the best result.

Analysis of the results of the above mentioned methods were mainly focussed on “worst case situations” where the procedures do not perform well. Kirkpatrick et al. argued in their work [57] that as the size of the optimization problem increases, the worst-case analysis becomes less important, and the average performance of the algorithms dominates the analysis. This observation led them to make the link to statistical mechanics, the domain of the large number limit.

7.2.1 Simulated annealing - Metropolis acceptance

Kirkpatrick and co-workers remarked that the search in statistical mechanics for the ground state of systems with a large number of atoms can be used to solve optimization problems. In this search it was found that, although at low temperature ground states and configurations close to them dominate the collection of possible configurations, in practical contexts low temperature is not a sufficient condition for finding the ground state of a system. It appeared that the *procedure* to reach this state is of non-negligible importance. That is why in experiments to find the low-temperature state of a material, a process called “**annealing**” is used. In this process the substance is first melted. Then the temperature is lowered slowly and a long time is spent at temperatures in the vicinity of the freezing point. If one does not apply this careful melting-freezing procedure, then e.g. growing a single crystal from a melt can lead to a crystal with many defects or a glass with only metastable, locally optimal structures. This is for example the case in extremely rapid quenching from high temperatures to zero temperature, which can be viewed as the physical analogue of iterative improvement.

The importance of the careful annealing process can be understood using statistical mechanics of the canonical ensemble, an ensemble in which the number of particles is conserved but that can exchange energy with its environment. A possible configuration of particles in such an ensemble is defined by the set of particle positions $\{r_i\}$. In a canonical ensemble in thermal equilibrium at a given temperature T , each possible configuration of particles has a Boltzmann probability $P(\{r_i\})$ to occur which is given by

$$P(\{r_i\}) = \frac{1}{\mathcal{Z}} \exp\left(-\frac{E(\{r_i\})}{k_B T}\right) \quad (7.5)$$

with $E(\{r_i\})$ the energy of the configuration, k_B Boltzmann’s constant and \mathcal{Z} the canonical partition function. With this probability the ground state is the dominant state as temperature goes to zero. At high temperature also configurations with a high energy have nonzero probability to occur, although the configurations with a lower energy still have a somewhat higher probability.

What happens in (simulated) annealing is the following. At each temperature higher than $T = 0$, the atoms can rearrange themselves, and every configuration has a non-zero probability to occur. This is important because starting from a given configuration with $E = E^{(1)}$, it is possible that a small rearrangement leads to a configuration with a higher energy $E^{(2)} > E^{(1)}$, but nevertheless this “intermediate” configuration is necessary to get to a configuration with a lower energy $E^{(3)} < E^{(1)}$. If one does not allow the configuration with higher energy to occur, but cools rapidly, one will never find the configuration with $E = E^{(3)} < E^{(1)}$. This is shown simplified for a one-dimensional function in figure 7.3, from which also the difference between iterative improvement and annealing is clear.

With the annealing process it is more likely to find a global minimum than with rapid cooling. Understanding this, one is left with the question how to numerically simulate a canonical ensemble with the configuration distribution (7.5) at a given temperature T . This question was

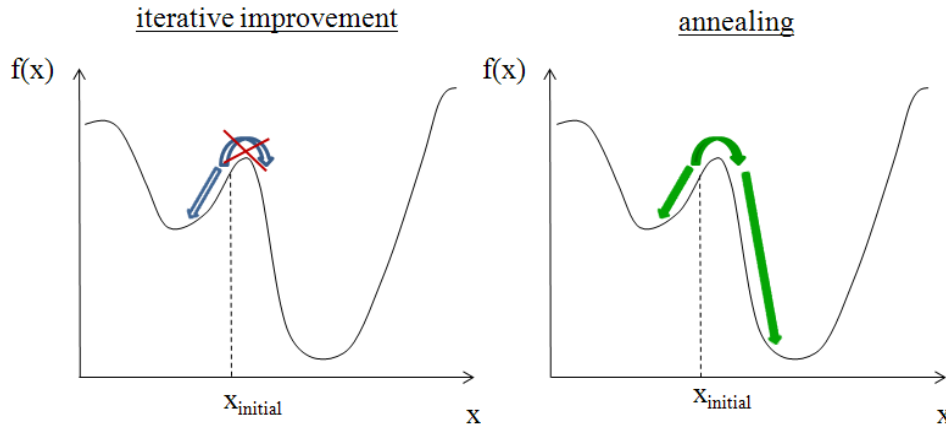


Figure 7.3: Simplified picture of the difference between iterative improvement and simulated annealing for a one-dimensional function. The arrows show the possible processes. Starting from an initial value of the variable, an iterative improvement algorithm can go only “downhill”. In simulated annealing the process has a probability to go uphill to look whether there is a deeper valley, a lower minimum, when going through a configuration with higher energy.

already answered by Metropolis et al. [78]. These researchers showed that a configuration could be chosen with probability $P(\{r_i\})$ at a given temperature T as in (7.5) in the following way. Starting from an initial configuration, one gives an atom a small random displacement and the resulting change in energy ΔE is calculated. If $\Delta E < 0$, i.e., if the move would bring the system to a state of lower energy, then the move is accepted and the configuration with the displaced atom is used as the starting point of the next step. If $\Delta E > 0$, the move is not always rejected as in iterative improvement: it is allowed with a probability $P(\Delta E) = \exp[-\Delta E/(k_B T)]$. This can be done in practice by generating a uniform random number $\xi \in \mathcal{U}(0, 1)$. If $\xi \leq P(\Delta E)$, then the move is accepted. If $\xi > P(\Delta E)$, the original configuration is used to start the next step. By repeating this basic step many times, one simulates the thermal motion of atoms in contact with a heat bath at temperature T . The choice of $P(\Delta E)$ has the consequence that the system evolves into a Boltzmann distribution.

The Metropolis procedure can be summarized as follows. Let $\{S\}$ be a set of variables of the problem. Then the probability $P(\{S'\})$ of accepting new values $\{S'\}$ of these variables is given by

$$P_{\text{Metropolis}}(\{S'\}) = \begin{cases} 1 & \text{if } \Delta E \leq 0 \\ \exp\left(-\frac{\Delta E}{k_B T}\right) & \text{if } \Delta E > 0 \end{cases} \quad (7.6)$$

with ΔE the difference in energy with the previous values.

In the above mentioned process geometrical ergodicity is assumed: after a sufficiently long time the system will have taken on all possible configurations and the result does not depend on the initial configuration.

In **simulated annealing** the physical annealing process is simulated by starting at a high temperature and gradually lowering the temperature, at each temperature performing the Metropolis procedure with a sufficient number of moves so that the system can reach a steady state at that temperature.

There is one practical problem when one wants to apply simulated annealing to a multi-variate optimization problem: there is no obvious equivalent of temperature in such problem. Therefore an “effective temperature” has to be defined, this means a starting temperature as well as a way in which to change this temperature and a time after which this temperature is changed. Therefore one first has to know the energy scale of the problem. One can derive this

scale by letting the variables change for some time and calculate the occurring energy differences ΔE . Based on this analysis, one can start at an effective temperature in which moves leading to higher energy are on average accepted with a user-defined probability.

7.2.2 Threshold acceptance

Some years after the work of Kirkpatrick et al., Moscato and Fontanari [81], and Dueck and Scheuer [28], proposed to use the following acceptance probability at temperature T :

$$P_{\text{threshold}}(\{S'\}) = \begin{cases} 1 & \text{if } \Delta E \leq T \\ 0 & \text{if } \Delta E > T \end{cases} \quad (7.7)$$

instead of the Metropolis probability (7.6). This deterministic update rule is called “threshold acceptance”. The authors claimed that the stochasticity of the updating rule is not essential to the good performance of simulated annealing and that threshold acceptance yields better results than simulated annealing. They showed with a number of examples in which threshold acceptance is compared with simulated annealing, that threshold acceptance indeed leads to good results. The advantage of the method is the gain in speed because no random numbers have to be calculated to decide on the acceptance and no exponential functions have to be calculated. The method still needs an “effective temperature” to be determined for the system under consideration.

7.2.3 Temperature-independent acceptance

Yet another minimization scheme that is based on the idea of simulated annealing, is a procedure for which no effective temperature has to be defined. The acceptance probability in this “temperature-independent acceptance” is given by

$$P_{T\text{-independent}}(\{S'\}) = \begin{cases} 1 & \text{if } \Delta E \leq 0 \\ p_k & \text{if } \Delta E > 0 \end{cases} ,$$

in which the probability $p_k < 1$ is relatively high at the beginning of the procedure and is gradually lowered during the minimization procedure. This is a probabilistic method like the Metropolis method, but which has the advantage that one does not have to determine a system-dependent effective temperature (in the Metropolis method, $p_k = \exp[-\Delta E / (k_B T)]$). Unlike in the other schemes, at each stage in the process large positive energy differences have an equal probability to be accepted as small positive energy differences. On the one hand, this can slow down convergence. On the other hand, it allows the system also at a later stage in the process to reach lower minima by going via configurations with much higher energies.

7.3 Generating free diffusion with random numbers

In this section we explain two ways in which free diffusion, also called Brownian motion, can be simulated by using random numbers: by diffusion Monte Carlo or by a Bernoulli walk. Both methods can be used in density-functional Monte Carlo. We used the Bernoulli walk in our calculations because of the easy bookkeeping of the corresponding density changes.

In a free diffusion process with constant diffusion coefficient D , the density of particles $n(\mathbf{r}, t)$ in a certain point \mathbf{r} at time t is given by the equation

$$\frac{\partial n(\mathbf{r}, t)}{\partial t} = D \nabla^2 n(\mathbf{r}, t). \quad (7.8)$$

With the initial distribution

$$n(\mathbf{r}, 0) = \delta(\mathbf{R}),$$

the solution of equation (7.8) is given by the normal (Gaussian) distribution

$$n_{\mathbf{R}}(\mathbf{r}, t) = \frac{1}{\sqrt{4\pi Dt}^3} \exp\left(-\frac{(\mathbf{r} - \mathbf{R})^2}{4Dt}\right).$$

The three-dimensional solution is a product of one-dimensional line-density solutions,

$$\begin{aligned} n_{\mathbf{R}}(\mathbf{r}, t) &= \left[\frac{1}{\sqrt{4\pi Dt}} \exp\left(-\frac{(x - X)^2}{4Dt}\right) \right] \left[\frac{1}{\sqrt{4\pi Dt}} \exp\left(-\frac{(y - Y)^2}{4Dt}\right) \right] \\ &\quad \times \left[\frac{1}{\sqrt{4\pi Dt}} \exp\left(-\frac{(z - Z)^2}{4Dt}\right) \right] \\ &= n_X(x, t) n_Y(y, t) n_Z(z, t), \end{aligned}$$

for which e.g.

$$\frac{\partial n(x, t)}{\partial t} = D \frac{\partial^2 n(x, t)}{\partial x^2}.$$

Therefore it is sufficient to explain how one-dimensional diffusion can be simulated with random numbers.

Both methods explained below have advantages and disadvantages. A big advantage of the Bernoulli walk is that it is easy to implement and the position that a particle reaches, is easy to track. An advantage of diffusion Monte Carlo is that the position changes are not restricted to a grid; for visualization or for further calculations however, the results are often binned.

7.3.1 Diffusion Monte Carlo

One method to implement the free diffusion time-evolution is by diffusion Monte Carlo (DMC). In this method, normally distributed random numbers are used (generated from uniformly distributed random numbers by e.g. the Box-Muller method). Say one wants to describe the diffusion of N particles with $D = 1/2$. Then one makes an array with length equal to the number of particles N . This array contains the positions x_α of the particles. Then in every time step k , the new position $x_\alpha^{(k)}$ of particle α is derived from the old one, $x_\alpha^{(k-1)}$, by generating a normally distributed random number with variance $\sigma^2 = \Delta t$ and mean μ equal to the old position, $\mu = x_\alpha^{(k-1)}$. If one has a random number generator that generates random numbers $\eta_{1,0}$ according to the standard normal distribution $\mathcal{N}(0, 1)$ with mean $\mu = 0$ and standard deviation $\sigma^2 = 1$, then a normal random number with different values for the mean μ and standard deviation σ^2 can be calculated from $\eta_{\mu,\sigma} = \sqrt{\sigma^2} \eta_{1,0} + \mu$.

The distribution of the particles can be visualized by constructing N_{bin} equidistant bins with width Δx and plotting the number of particles with a position in the corresponding interval. To obtain a normalized distribution, every particle is attributed a weight $w_\alpha = 1/(N \cdot \Delta x)$. Figure 7.4 shows a couple of time steps for the diffusion of particles that were originally situated in the origin. For comparison the analytical solution $n_0(x, t) = \exp(-x^2/(2k\Delta t)) / \sqrt{2\pi k\Delta t}$ is also plotted.

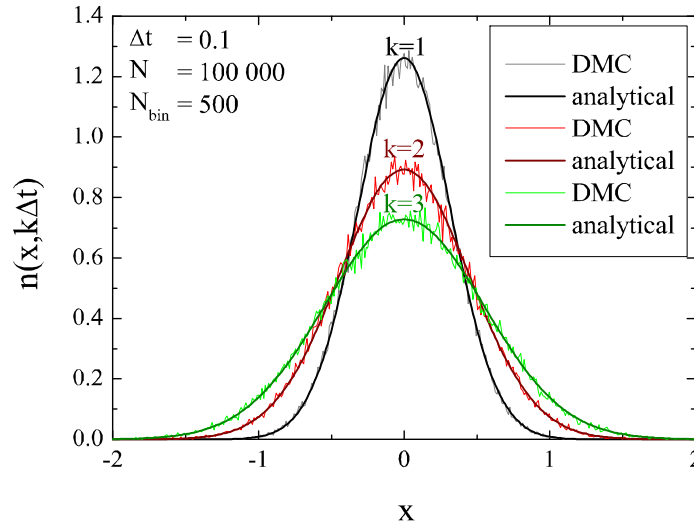


Figure 7.4: Three time steps in the diffusion process for which the particles were initially situated in the origin, calculated with diffusion Monte Carlo (DMC; thin, light lines) and from the analytical solution (thick, dark lines).

7.3.2 Bernoulli walk

Another way to implement the time evolution is to use a Bernoulli walk. In this method, Brownian motion is simulated by *walkers* on an equidistant grid with interval width Δx . In subsequent iterations (not to be confused with the time step Δt of diffusion Monte Carlo) the walkers make a step to an adjacent interval. To determine the direction of the move of a walker, one generates a random number $\xi \in \mathcal{U}(0, 1)$. In the case $\xi < q = 1/2$, the considered walker moves “to the left”, otherwise it moves “to the right”.

That such a process leads to a normal distribution can be understood if one calculates the probability $p(\Delta j, N_{\text{step}})$ that a walker reaches position $x(j) = j\Delta x$ on time $t(N_{\text{step}}) = N_{\text{step}}\Delta T$ after (a large number of) N_{step} time steps ΔT when he started on time $t = 0$ in the position $x(j_{\text{start}})$ with $\Delta j = j - j_{\text{start}}$. This position was reached by going μ steps to the right and ν steps to the left. Then

$$\begin{aligned} j - j_{\text{start}} &= \Delta j = \mu - \nu \\ \mu + \nu &= N_{\text{step}}. \end{aligned}$$

Now there are $\binom{N_{\text{step}}}{\mu}$ possibilities to perform Δj steps to the right. Then $p(\Delta j, N_{\text{step}})$ is given by

$$p(\Delta j, N_{\text{step}}) = \begin{cases} \binom{N_{\text{step}}}{\mu} q^{\mu} p^{\nu} = \frac{N_{\text{step}}!}{\left(\frac{N_{\text{step}} + \Delta j}{2}\right)! \left(\frac{N_{\text{step}} - \Delta j}{2}\right)!} \left(\frac{1}{2}\right)^{N_{\text{step}}} & \text{if } N_{\text{step}} - \Delta j \text{ even} \\ 0 & \text{if } N_{\text{step}} - \Delta j \text{ odd} \end{cases}.$$

Because N_{step} is large, we can make use of Stirling’s formula

$$s! \stackrel{s \text{ large}}{\simeq} \sqrt{2\pi s} s^{s+1/2} e^{-s}$$

so that $p(\Delta j, N_{\text{step}})$ can be rewritten as

$$p(\Delta j, N_{\text{step}}) = \sqrt{\frac{2}{\pi}} \sqrt{\frac{1}{N_{\text{step}} \left(1 - \frac{(\Delta j)^2}{N_{\text{step}}^2}\right)}} \left(\frac{1}{1 + \frac{\Delta j}{N_{\text{step}}}}\right)^{\frac{N_{\text{step}}}{2}} \left(\frac{1}{1 - \frac{\Delta j}{N_{\text{step}}}}\right)^{\frac{N_{\text{step}}}{2}} \left(\frac{1 - \frac{\Delta j}{N_{\text{step}}}}{1 + \frac{\Delta j}{N_{\text{step}}}}\right)^{\frac{\Delta j}{2}}.$$

Now because also $N_{\text{step}} \gg \Delta j$, we can perform a Taylor expansion. Making use of the equality $\exp(x) = \lim_{s \rightarrow \infty} (1 + x/s)^s$ we finally find that

$$\begin{aligned} p(\Delta j, N_{\text{step}}) &\simeq \sqrt{\frac{2}{\pi N_{\text{step}}}} \exp\left(\frac{(\Delta j)^2}{2N_{\text{step}}}\right) \\ &\simeq \sqrt{\frac{2\Delta T}{\pi t}} \exp\left(-\frac{\Delta T}{(\Delta x)^2} \frac{[x(j) - x(j_{\text{start}})]^2}{2t}\right). \end{aligned}$$

From this probability, the walker line density $n(x, t)$ per x -interval is found to be

$$\begin{aligned} n(x, t) &= \frac{p(\Delta j, N_{\text{step}})}{2\Delta x} = \sqrt{\frac{2}{\pi N_{\text{step}}}} \exp\left(\frac{(\Delta j)^2}{2N_{\text{step}}}\right) \\ &= \sqrt{\frac{\Delta T}{(\Delta x)^2} \frac{1}{2\pi t}} \exp\left(-\frac{\Delta T}{(\Delta x)^2} \frac{(x - X)^2}{2t}\right) \end{aligned}$$

where the factor 2 in the denominator originates from the fact that $n(\Delta j, N) = 0$ if $N - \Delta j$ is odd. To get a continuous expression for this density, we take the limits $\Delta x \rightarrow 0$ and $\Delta T \rightarrow 0$ where x and T are kept finite. Of course also the density $n(x, t)$ has to be finite and this can only be accomplished by keeping $\Delta T/\Delta x$ finite. The constant ratio

$$D = \frac{(\Delta x)^2}{2\Delta T}$$

serves as a diffusion constant and one can write

$$n(x, t) = \sqrt{\frac{1}{4\pi Dt}} \exp\left(-\frac{(x - X)^2}{4Dt}\right).$$

Chapter 8

Density-functional Monte Carlo (DFMC)

In this section some more explanation is given on the four basic steps of DFMC:

1. Construct a trial density distribution.
2. Change the density distribution.
3. Accept or reject the new distribution depending on the energy difference with the previous distribution.
4. Repeat steps 2 and 3 until a minimum value of the energy is found.

The entire process in which a minimum is found is called a **run**.

The procedure contains a number of parameters that have to be determined for each problem separately. In the section following the explanation of the basic steps we give a guideline of how appropriate run parameters can be derived. In the last section of this chapter we explain how the work function can be calculated in the framework of DFMC.

8.1 Basic procedure

8.1.1 Construction of a trial density distribution

In DFMC calculations, the density distribution of a system is simulated by walkers on a mesh that can for example be an equidistant grid. Let an interval be characterized by the indices $\{j_\alpha, j_\alpha + 1\}$ in each direction α and denote the volume of such interval by $V_{\mathbf{j}}$. The number of walkers in the interval is given by $(N_w)_{\mathbf{j}}$. Let there be N particles in the system represented by a total of N_w walkers. There is a one-to-one correspondence between the particle density $n_{\mathbf{j}}$ and $(N_w)_{\mathbf{j}}$ which is given by the relation

$$n_{\mathbf{j}} = \frac{N}{N_w} \frac{(N_w)_{\mathbf{j}}}{V_{\mathbf{j}}}. \quad (8.1)$$

The procedure is initiated by generating an initial walker distribution, drawn according to a trial distribution profile $N_{w,\text{trial}}(r)$ based on a trial density profile $n_{\text{trial}}(\mathbf{r})$ of the particles by use of e.g. the rejection method or the transformation method.

Finding a good trial density profile can be done in different ways. Usually when studying a system, one has a certain clue about the general behavior of the density. If this is not the case, one can for example solve an approximate version of the Thomas-Fermi-Hohenberg-Kohn equation (2.22) or one can calculate the energy functional of different profiles and take the density with the lowest value of the energy as the trial density.

8.1.2 Modification of the distribution

The density profile is changed by letting the walkers diffuse over the mesh: in a step s , a walker is moved to an adjacent interval with equal probability in each direction. This can be done by drawing for each direction α a random number $\xi_\alpha \in \mathcal{U}(0, 1)$, and letting the walker move from $\{j_\alpha, j_\alpha + 1\}$ to the direction $\{j_\alpha - 1, j_\alpha\}$ if $\xi_\alpha < 0.5$ and to the direction $\{j_\alpha + 1, j_\alpha + 2\}$ if $\xi_\alpha \geq 0.5$.

We have chosen to describe this diffusion process by Bernoulli walks rather than by diffusion Monte Carlo because of the easy bookkeeping of the corresponding density changes.

Unlike in solving the Thomas-Fermi-Hohenberg-Kohn equation (2.22), the condition $n(\mathbf{r}) \geq 0$ is automatically satisfied since no walker is moved from an interval with zero concentration.

8.1.3 Acceptance/rejection of the new distribution

After each step s , the energy difference

$$\Delta E^{(s)} = E^{(s)} [n^{(s)}(\mathbf{r})] - E^{(s-1)} [n^{(s-1)}(\mathbf{r})] \quad (8.2)$$

between the energy of the new density profile $n^{(s)}(\mathbf{r})$ and that of the previous one, $n^{(s-1)}(\mathbf{r})$, is calculated. Whether or not the new distribution is accepted depends on the sign of $\Delta E^{(s)}$:

- if $\Delta E^{(s)} \leq 0$, the new density profile $n^{(s)}(\mathbf{r})$ is accepted.
- if $\Delta E^{(s)} > 0$, the new density profile is accepted with probability $P_a < 1$, which gives the possibility of escaping from local minima. This acceptance probability can be constructed as a threshold acceptance, by Metropolis acceptance, ... The system configuration is allowed to stabilize by gradually lowering the acceptance probability P_a each i_{lower} iterations.

A note for people who are familiar with Quantum Monte Carlo: in order to fulfill the condition of the second Hohenberg-Kohn theorem that the number of particles has to be constant, no branching or killing accelerators are applied.

8.1.4 Stopping criterion

A minimization run is stopped if the acceptance probability P_a has reached a sufficiently low value P_{min} and if since then the minimum energy found so far has not changed for a number i_{stop} of iterations.

Despite the introduction of a probability P_a for accepting moves with increasing energy, the possibility of ending up in a local minimum cannot be avoided. Therefore several minimization runs have to be performed. If the run parameters i_{lower} , i_{stop} and the way in which P_a is changed are properly chosen, only a small part of the runs end up in a local minimum. A value can be considered to be a local minimum if it differs more with the lowest minimum of the runs than can be expected from numerical accuracy deviations. If more than half of the runs end in a local minimum, this can be an indication that the run parameters are not appropriate and as such the global minimum is actually not reached. It is then a good idea to change the run parameters.

In theory the ground-state energy is the lowest energy that can be found. In practice there are two problems to find the “theoretical” ground state.

First of all, it is impossible to simulate *all* possible walker profiles.

Furthermore, calculations are subject to truncation and round-off errors. To get an idea of the

error on the results one can average over the run results, but one wants of course to exclude the local minima. If with the chosen run parameters the share of local minima is lower than half of the performed runs, one can exclude these minima by only retaining the results which are equal to or lower than the median E_{med} of the minimum energies. One thus only retains the energies E_p for which

$$E_p \leq E_{\text{med}}.$$

In this way at least half of the run results are used for averaging to obtain a final result. One can thus decide in advance on the minimum number of data points that are used in the statistical processing of the DFMC results and perform as many runs as wanted.

8.2 Determination of appropriate run parameters

Some of the above mentioned parameters can be chosen independent of the system under investigation. These are:

1. the initial acceptance probability $P_a^{(0)}$: a good rule of thumb appears to take $P_a^{(0)} = 0.5$.
2. the way in which to change the acceptance probability: Metropolis acceptance, threshold acceptance or the temperature-independent acceptance.
3. the lowest value P_{min} of the acceptance probability from which one starts to count the number of iterations for which the minimum energy has not changed.

We are then left with the following parameters that have to be determined for each system separately:

1. the mesh spacing Δx_α in each direction α .
2. the total number of walkers N_w .
3. the number of iterations after which P_a is lowered, i_{lower} .
4. how much the acceptance probability is lowered (or how much the temperature is lowered).
5. the sufficient number of iterations in which the minimum has not changed and after which the run is ended, i_{stop} .

An appropriate value for these parameters can be derived as follows. Call an **iteration** a sweep over the entire mesh with a possible move of one walker in each mesh point. If one performs a **test run** with a fixed acceptance probability $P_a = 0.5$, then the minimum energy found in a number of iterations will typically first decrease some orders of magnitude until it does not change (much) in a larger number of iterations. How adequate run parameters can be derived from such a test run is explained in the next subsections.

8.2.1 Step one: Δx_α and N_w

Based on the minimum that is found in several test runs, one can decide on the number of mesh points and the number of walkers to be used in the calculations. Most of the time one has a clue about the spatial variation of the density, so one can start with a number of mesh points that seems appropriate. Then one performs test runs with different numbers of walkers. Because of the possibility that the calculation ends up in a local minimum, it is best to perform several runs and to consider for each value of N_w the run that ends in the lowest energy.

Typically one will notice the following behavior:

- the higher the number of walkers, the closer the minima for subsequent numbers of walkers.
- if the number of walkers increases, the number of iterations before a minimum is reached also increases.

The convergence of the minima if the number of walkers increases indicates that with a reasonable number of walkers an acceptable accuracy can be reached.

Based on which accuracy one finds sufficient, one can now decide on the number of walkers to be used. Say one tolerates a relative error of 0.001 for the minimum energy. Suppose that five test runs with $N_1 < \dots < N_5$ resulted in relative errors $\Delta_{\text{rel}} E_i = \left| \left(E_{\text{min}}^{(i)} - E_{\text{min}}^{(i+1)} \right) / E_{\text{min}}^{(i)} \right|$ equal to $\Delta_{\text{rel}} E_1 = 0.01$, $\Delta_{\text{rel}} E_2 = 0.005$, $\Delta_{\text{rel}} E_3 = 0.001$ and $\Delta_{\text{rel}} E_4 = 0.0005$. Then the appropriate number of walkers would be N_3 because runs with a lower number of walkers do not meet the accuracy criterion and runs with a higher number of walkers take more time than necessary.

8.2.2 Step two: the other parameters

With the number of mesh points and the number of walkers being chosen, a test run can determine the other necessary parameters.

The parameter i_{lower} can be set approximately equal to the number of iterations that was needed for the minimum energy to somewhat stabilize. The stabilization is an indication that the number of iterations over which the minimum energy has changed substantially is sufficient for the walkers to scout the entire domain in looking for a configuration with a lower energy.

The amount of lowering the acceptance probability or temperature depends on the details of the test runs.

The last parameter, i_{stop} , is best taken of the same order of magnitude as i_{lower} because this parameter is an indication of how long it takes to scan the domain for finding a configuration with a lower energy.

8.3 Determination of the work function

The work function is defined as the minimum energy required for removing one electron from a solid at temperature zero. We explain in this section two ways in which this quantity can be calculated in the framework of DFMC.

8.3.1 Based on ionization energies

One way in which we have determined the work function is with the following procedure:

1. Calculate the energy differences due to subsequent removal of walkers (the “*walker ionization energies*”). If ΔN_w walkers are removed from the system, the energy difference between the system with $N_w - \Delta N_w$ walkers and the system with N_w walkers is the $(\Delta N_w \times N/N_w)$ ’th “electron ionization energy”:

$$E_{\text{ionization}}(\Delta N_w) = E_{\text{ionization}} \left(\Delta N = \Delta N_w \frac{N}{N_w} \right).$$

2. Fit these data to a function $E_{\text{ionization}}(\Delta N)$ with as argument the number of removed electrons ΔN .
3. Evaluate the fitted function in $\Delta N = 1$, so $W_{\text{ionization}} = E_{\text{ionization}}(\Delta N = 1)$.

8.3.2 Based on the expression of Lang and Kohn

Lang and Kohn [68] derived an expression to calculate the work function at a metal surface in the framework of DFT. It reads:

$$W = \Delta\phi - \bar{\mu} = [\phi(\infty) - \langle\phi(\mathbf{r})\rangle] - \left\langle \frac{\delta G[n]}{\delta n(\mathbf{r})} \right\rangle$$

with $\Delta\phi$ the rise in mean electrostatic potential across the metal surface, $\bar{\mu}$ the bulk chemical potential of the electrons relative to the mean electrostatic potential in the metal interior, $G[n]$ the universal functional (2.9) and with the averages $\langle \rangle$ taken over the metal.

In the jellium model, the electron density in the metal interior has a constant value \bar{n} . In this case $\bar{\mu}$ takes on the form

$$\bar{\mu} = \frac{1}{2}k_F^2 + \mu_{xc}(\bar{n}) = \frac{1}{2}(3\pi^2\bar{n})^{2/3} + \left[\frac{d(n\epsilon_{xc}(n))}{dn} \right]_{n=\bar{n}}$$

with k_F the size of the Fermi wavevector and $\epsilon_{xc}(n)$ the exchange and correlation energy per particle of the uniform electron gas.

Now $d(n\epsilon_{xc}(n))/dn$ is just the effective single-particle exchange-correlation energy $u_{xc}(\mathbf{r})$. Furthermore, if the zero point of the energy is set at $r \rightarrow \infty$, the potential at infinity is equal to zero: $\phi(\infty) = 0$. We thus implemented the result of Lang and Kohn as

$$W_{\text{LK}} = u_H(R) - \left[\frac{1}{2}(3\pi^2\bar{n})^{2/3} + u_X(\bar{n}) + u_C(\bar{n}) \right] \quad (8.3)$$

with $u_H(r)$ the single-particle Hartree energy, R a value of r close to the outer surface and \bar{n} calculated as $\bar{n} = 3/(4\pi r_s^3)$ with r_s the bulk Wigner-Seitz radius. The expressions for $u_X(n)$ and $u_C(n)$ that we used in the calculations are given in the next chapter on the application of DFMC to a nanoshell.

Chapter 9

DFMC for nanoshells

9.1 Considered model and nanoshells

We consider the jellium model in the shell, without any external potential.

For comparison with Kohn-Sham calculations we derived the properties of a nanoshell with $(R_C, R_S) = (55, 95)$ a.u. $\simeq (2.9, 5.0)$ nm and $(\varepsilon_C, \varepsilon_S, \varepsilon_E) = (1, 1, 1)$ which contains about 2.56×10^4 conduction electrons.

The influence of the permittivities was investigated based on three nanoshells with the same size, $(R_C, R_S) = (40, 55)$ nm, and with permittivities $(\varepsilon_C, \varepsilon_S, \varepsilon_E) = (1, 1, 1)$, $(\varepsilon_C, \varepsilon_S, \varepsilon_E) = (4, 1, 1)$ and $(\varepsilon_C, \varepsilon_S, \varepsilon_E) = (1, 1, 4)$. The permittivity of SiO_2 is approximately equal to $\varepsilon_{\text{SiO}_2} \simeq 4$.

To test the influence of the nanoshell size on the work function, we have considered nanoshells with permittivities $(\varepsilon_C, \varepsilon_S, \varepsilon_E) = (1, 1, 1)$, core radius $R_C = 40$ nm and overall radii R_S ranging from $R_S = 55$ nm up to $R_S = 70$ nm. Nanoshells of these sizes contain 2.56×10^7 up to 6.97×10^7 conduction electrons.

The relative sizes of the nanoshell considered for comparison with Kohn-Sham calculations, the benchmark nanoshell and the largest considered nanoshell are visualized in figure 9.1.

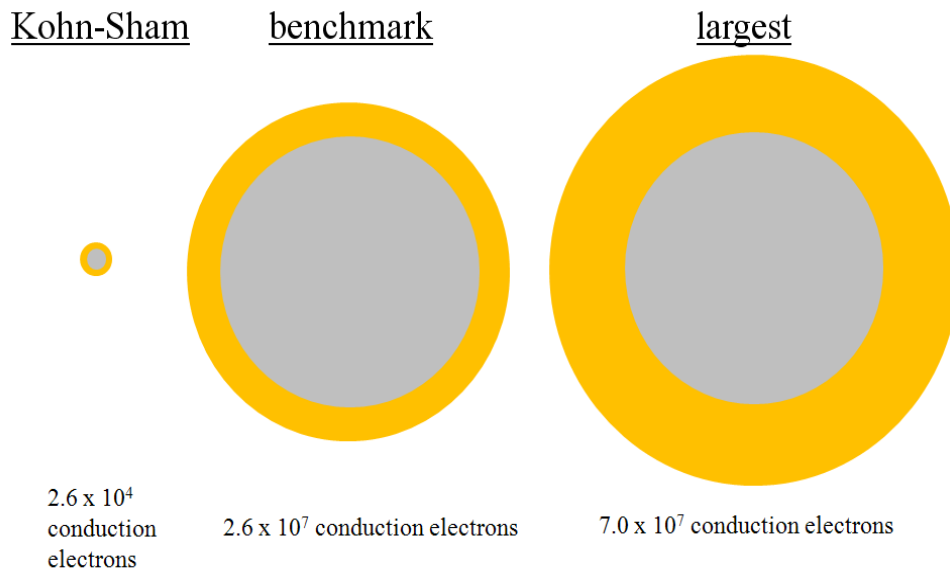


Figure 9.1: Relative sizes of the nanoshell considered for comparison with Kohn-Sham calculations, the benchmark nanoshell and the largest considered nanoshell.

9.2 Expressions for the energy contributions

We used the ansatz (2.10) for the universal functional $G[n]$ made by Kohn and Sham and we adopted the often used separation of the exchange-correlation energy in an exchange and a correlation part. In this way the energy functional of the nanoshell consists of four parts:

$$E[n(\mathbf{r})] = T_s[n(\mathbf{r})] + E_X[n(\mathbf{r})] + E_C[n(\mathbf{r})] + E_H[n(\mathbf{r})]$$

with $T_s[n(\mathbf{r})]$ the kinetic energy of non-interacting electrons with density n , $E_X[n(\mathbf{r})]$ the exchange energy, $E_C[n(\mathbf{r})]$ the correlation energy and $E_H[n(\mathbf{r})]$ the total Hartree energy due to the classical Coulomb interaction between conduction electrons mutually, between the background charges mutually and between the conduction electrons and the background charges. We limited the calculations to the local-density approximation. The energy functional $E[n(\mathbf{r})]$ can then be written as the integral over an ‘‘energy density’’ $\mathcal{E}(\mathbf{r})$:

$$E[n(\mathbf{r})] = \int \mathcal{E}(\mathbf{r}) d\mathbf{r} = \int \{T_s(\mathbf{r}) + \mathcal{E}_X(\mathbf{r}) + \mathcal{E}_C(\mathbf{r}) + \mathcal{E}_H(\mathbf{r})\} d\mathbf{r}. \quad (9.1)$$

For the calculation of the work function as in expression (8.3) we not only need the energy density of the Hartree-, exchange- and correlation contributions, but also the corresponding ‘single-particle’ potential energies $u_H(r)$, $u_X(r)$ and $u_C(r)$. These contributions are equal to

$$u_{H,X,C}(r) = \frac{\delta \mathcal{E}_{H,X,C}[n(r)]}{\delta n(r)}. \quad (9.2)$$

To be able to compare the results with the results of Kohn-Sham calculations and with results of calculations for a flat metallic surface, we used the same expression for the exchange and correlation energy as was used in Refs. [101, 102, 103, 104, 87, 106] and in Ref. [91].

9.2.1 Kinetic energy

For the kinetic energy per volume of the non-interacting electrons, $\mathcal{T}_s(\mathbf{r})$, we considered the Thomas-Fermi expression:

$$\mathcal{T}_s(\mathbf{r}) = (3/10) (3\pi^2)^{2/3} [n(r)]^{5/3}. \quad (9.3)$$

9.2.2 Exchange energy

The exchange energy density was taken to be the Hartree-Fock result introduced in the Thomas-Fermi equation by Dirac [24], but screened by a layer-dependent permittivity ε_k :

$$\mathcal{E}_X(\mathbf{r}) = -\frac{3}{4} \left(\frac{3}{\pi}\right)^{1/3} \frac{[n(r)]^{4/3}}{\varepsilon_k}. \quad (9.4)$$

Definition (9.2) results in the following expression for the single-particle exchange energy:

$$u_X(r) = -\left(\frac{3}{\pi}\right)^{1/3} \frac{[n(r)]^{1/3}}{\varepsilon_k}. \quad (9.5)$$

9.2.3 Correlation energy

For the correlation contribution we used the following combination that was proposed in Ref. [90] and used in Refs. [101, 102, 103, 104, 87, 106] and Ref. [91] without inclusion of the permittivity:

$$\mathcal{E}_C(\mathbf{r}) = \frac{n(r)}{\varepsilon_k} \begin{cases} A \ln(r_s) + B + Cr_s \ln(r_s) + Dr_s & \text{if } r_s(r) < 1 \\ \gamma / (1 + \beta_1 \sqrt{r_s} + \beta_2 r_s) & \text{if } r_s(r) \geq 1 \end{cases} \quad (9.6)$$

with $r_s(r) = \{3/[4\pi n(r)]\}^{1/3}$ the local Wigner-Seitz radius. The following constants were used for the high-density limit $r_s(r) < 1$ [34]

$$A = 0.0311; \quad B = -0.048; \quad C = 0.0020; \quad D = -0.0116$$

whereas for lower densities the following values of the constants were implemented [16, 17]

$$\gamma = -0.1423; \quad \beta_1 = 1.0529; \quad \beta_2 = 0.3334 .$$

For the implementation and for the derivation of the single-particle correlation energy it is useful to rewrite expression (9.6) entirely as a function of the density:

$$\mathcal{E}_C(r) = \frac{1}{\varepsilon_k} \begin{cases} \gamma n^{4/3}(r) / [n^{1/3}(r) + \beta_{1,E} n^{1/6}(r) + \beta_{2,E}] & \text{if } n(r) \leq \frac{3}{4\pi} \\ \left[\left(A + C_E \frac{1}{n^{1/3}(r)} \right) \ln \left(\left(\frac{3}{4\pi n(r)} \right)^{1/3} \right) \right. \\ \quad \left. + B + D_E \frac{1}{n^{1/3}(r)} \right] n(r) & \text{if } n(r) > \frac{3}{4\pi} \end{cases} \quad (9.7)$$

with the newly introduced constants defined by the relations $\beta_{1,E} = \left(\frac{3}{4\pi}\right)^{1/6} \beta_1$, $\beta_{2,E} = \left(\frac{3}{4\pi}\right)^{1/3} \beta_2$, $C_E = \left(\frac{3}{4\pi}\right)^{1/3} C$ and $D_E = \left(\frac{3}{4\pi}\right)^{1/3} D$.

Applying definition (9.2) to expression (9.7) for the correlation energy density, we find that the single-particle correlation energy $u_C(r)$ can be calculated as

$$u_C(r) = \frac{1}{\varepsilon_k} \begin{cases} \gamma \frac{n^{1/3}(r) + \beta_{1,u} n^{1/6}(r) + \beta_{2,u}}{(n^{1/3}(r) + \beta_{1,E} n^{1/6}(r) + \beta_{2,E})^2} n^{1/3}(r) & \text{if } n(r) \leq \frac{3}{4\pi} \\ \left[\begin{aligned} & D_C + B_A n^{1/3}(r) \\ & + (C_u + A n^{1/3}(r)) \ln \left(\left(\frac{3}{4\pi n(r)} \right)^{1/3} \right) \end{aligned} \right] / n^{1/3}(r) & \text{if } n(r) > \frac{3}{4\pi} \end{cases} \quad (9.8)$$

with the newly defined constants given by the expressions $\beta_{1,u} = 7\beta_{1,E}/6$, $\beta_{2,u} = 4\beta_{2,E}/3$, $D_C = (2D_E - C_E)/3$, $B_A = B - A/3$ and $C_u = 2C_E/3$.

9.2.4 Hartree-energy

The Hartree contribution to the energy density can be calculated from

$$\begin{aligned} \mathcal{E}_H(\mathbf{r}) &= \int \frac{1}{\varepsilon(\mathbf{r}')} \left(\frac{-\rho_b(\mathbf{r}') n(\mathbf{r})}{|\mathbf{r} - \mathbf{r}'|} + \frac{1}{2} \frac{\rho_b(\mathbf{r}') \rho_b(\mathbf{r}) + n(\mathbf{r}') n(\mathbf{r})}{|\mathbf{r} - \mathbf{r}'|} \right) d\mathbf{r}' \\ &= \frac{1}{2} \int \frac{\rho_{exc}(\mathbf{r}') \rho_{exc}(\mathbf{r})}{\varepsilon(\mathbf{r}') |\mathbf{r} - \mathbf{r}'|} d\mathbf{r}' = -\frac{1}{2} \rho_{exc}(\mathbf{r}) u_H(\mathbf{r}) \end{aligned}$$

in which $\rho_{exc}(\mathbf{r})$ is the excess charge density which is equal to the sum of the background charge density $\rho_b(\mathbf{r})$ and the electron charge density $-n(\mathbf{r})$, so $\rho_{exc}(\mathbf{r}) = \rho_b(\mathbf{r}) - n(\mathbf{r})$.

We derived two expressions for the Hartree energy $u_H(r)$ due to a spherically symmetric excess charge distribution $\rho_{exc}(r)$ (see appendix B.1 for the derivation). For calculating the $u_H(r)$ -profile itself, it is for accuracy reasons best to implement the double integral

$$u_H(r) = -4\pi \int_r^{+\infty} \frac{1}{\varepsilon(r'')} \frac{1}{r''^2} \left(\int_0^{r''} \rho_{exc}(r') r'^2 dr' \right) dr'' \quad (9.9)$$

In this case, one has to pay attention to the implementation for systems that are not charge-neutral because the potential energy is calculated on a finite mesh.

For the calculation of the direct energy difference in Hartree energy, ΔE_H , it is useful to write $u_H(r)$ as a sum of two single integrals instead of a double integral. With k the index of a material layer - so in the case of a single nanoshell $k_{\max} = 3$, $\{\varepsilon_1, \varepsilon_2, \varepsilon_3\} = \{\varepsilon_C, \varepsilon_S, \varepsilon_E\}$ and $\{R_1, R_2, R_3\} = \{R_C, R_S, +\infty\}$ - the Hartree energy in layer k can be written as follows¹:

$$u_H^{(k)}(r) = -4\pi \left\{ \begin{array}{l} \frac{1}{\varepsilon_k} \left[\frac{1}{r} \int_0^r \rho_{exc}(r') r'^2 dr' + \int_r^{R_k} \rho_{exc}(r') r' dr' \right] \\ + \sum_{k'=k}^{k_{\max}-1} \left[\left(\frac{1}{\varepsilon_{k'+1}} - \frac{1}{\varepsilon_{k'}} \right) \frac{1}{R_{k'}} \int_0^{R_{k'}} \rho_{exc}(r') r'^2 dr' \right. \\ \left. + \frac{1}{\varepsilon_{k'+1}} \int_{R_{k'}}^{R_{k'+1}} \rho_{exc}(r') r' dr' \right] \end{array} \right\} \quad (9.10)$$

9.2.5 Energy functional

To calculate the integral over the energy density $\mathcal{E}(\mathbf{r})$, the (charge) density was considered to be constant in the mesh intervals and for the potential energy linear interpolation was used. In this way the integrand is a linear combination of polynomials. Performing the integrals leads to terms containing the difference $r_{j+1}^p - r_j^p$ with r_j and r_{j+1} the lower and upper boundaries of interval j and p an integer. We did not implement this difference as is because of the possible large round-off errors in subtracting numbers of comparable magnitude. We used the equality $r_{j+1} = r_j + h_j$ with h_j the interval width so that $r_{j+1}^p - r_j^p$ can be written as a polynomial in h_j , i.e. $r_{j+1}^p - r_j^p = f(h_j) = \sum_{i=1}^p a_i (h_j)^i$. We then implemented this polynomial in Horner form $f(h_j) = h_j (a_1 + h_j (a_2 + \dots + h_j (a_{p-1} + a_p h_j) \dots))$ because this form of a polynomial is computationally more efficient and accurate than the form $f(h_j) = \sum_{i=1}^p a_i (h_j)^i$.

For the universal part $G[n] = T_S[n] + E_{XC}[n]$ we first calculated the energy density and then performed the integral in order to avoid as much as possible subtraction of numbers of comparable magnitude.

¹In Ref. [105] another transparent form is given which can be generalized as

$$u_H^{(k)}(r) = \frac{1}{\varepsilon_k} \tilde{u}_H(r) + \sum_{k'=k}^{k_{\max}} \frac{\varepsilon_{k'} - \varepsilon_{k'+1}}{\varepsilon_{k'} \varepsilon_{k'+1}} \tilde{u}_H(R_{k'})$$

with $\tilde{u}_H(r)$ the Hartree-energy if all permittivities are equal to $\varepsilon = 1$.

9.3 Calculation details

9.3.1 Mesh characteristics

We used a radial mesh with intervals characterized by an index j , a lower bound r_j , an upper bound r_{j+1} and a length $h_j = r_{j+1} - r_j$. An interval represents a three-dimensional volume $V_j = 4\pi (r_{j+1}^3 - r_j^3) / 3$. We considered 20 mesh points per nm, so about one mesh point per Bohr radius.

9.3.2 Construction of a trial distribution

We started with an almost homogeneous electron concentration in the shell. This initial density profile resembles the results obtained by the previously performed self-consistent wave-function-based calculations for a flat metallic surface [67, 68, 91] and for small nanoshells [101, 102, 87] which show an almost homogeneous electron distribution in the metal with a small spill-out outside the metal.

The distribution was constructed by first using the relation (8.1) between the electron concentration and the number of walkers in an interval to calculate an approximate walker distribution as

$$(N_w)_j = \text{floor} \left(\frac{V_j}{V_{\text{shell}}} N_w \right).$$

We then placed the rest $N_{\text{rest}} = N_w - \sum_j (N_w)_j$ of the walkers in the mesh by using the rejection method in which a uniform random point $\{x, y, z\}$ in a cube with side R_S is generated and a walker is put in the correct interval if $R_C \leq \sqrt{x^2 + y^2 + z^2} \leq R_S$.

9.3.3 Modification of the distribution

To modify the density we used a Bernoulli walk. The walkers were moved to an adjacent interval based on the value of a random number $\xi \in \mathcal{U}(0, 1)$. If

- $\xi < 0.5$, the walker was moved from interval $[j, j + 1[$ to interval $[j - 1, j[$
- $\xi \geq 0.5$, the walker was moved from interval $[j, j + 1[$ to interval $[j + 1, j + 2[$.

9.3.4 Acceptance/rejection of the new distribution

We used a temperature-independent acceptance probability of which the details are given in section 9.3.6.

The energy difference $\Delta E [n(r)]$ due to a walker move could be calculated directly for all energy contributions. With J the lowest index of the interval in which the density was changed, the difference in energy E_{local} for the local contributions (kinetic, exchange and correlation contribution) was calculated as

$$\Delta E_{\text{local}} [n(r)] = [E_{\text{local}} (n'_J) - E_{\text{local}} (n_J)] + [E_{\text{local}} (n'_{J+1}) - E_{\text{local}} (n_{J+1})]$$

with n'_j the actual density and n_j the density before the walker step.

Because of the use of Bernoulli walkers, we were able to derive an expression for calculating the difference in Hartree energy directly (see appendix B for the derivation):

$$\Delta E_H [n(r)] = \text{sgn} \times C_H \left[(\Delta \mathcal{U})_J S_J + \left(\begin{array}{l} [-\eta_J u_J + \rho'_J (\Delta \mathcal{U})_J] \cdot I_J^{(1)} \\ + [-\eta_J u_{J+1} + \rho'_J (\Delta \mathcal{U})_{J+1}] \cdot I_J^{(2)} \\ + [\eta_{J+1} u_{J+1} + \rho'_{J+1} (\Delta \mathcal{U})_{J+1}] \cdot I_{J+1}^{(1)} \\ + \eta_{J+1} u_{J+2} \cdot I_{J+1}^{(2)} \end{array} \right) \right]$$

with

$$\text{sgn} = \begin{cases} -1 & \text{if move to left} \\ +1 & \text{if move to right} \end{cases}$$

$$C_H = -\frac{\pi}{6}$$

$$S_j = \sum_{j_1=0}^{j-1} \rho_{j_1} \left(I_{j_1}^{(1)} + I_{j_1}^{(2)} \right)$$

$$\eta_j = \frac{N}{N_w} \frac{1}{V_j} = \frac{3}{4\pi} \frac{N}{N_w} \frac{1}{r_{j+1}^3 - r_j^3} \quad (9.11)$$

$$I_j^{(1)} = (r_{j+1}^2 + 2r_j r_{j+1} + 3r_j^2) h_j$$

$$I_j^{(2)} = (3r_{j+1}^2 + 2r_j r_{j+1} + r_j^2) h_j$$

and

$$\begin{aligned} (\Delta \mathcal{U})_J &= 3 \frac{N}{N_w} \left[\frac{1}{3} \left(\frac{1}{\varepsilon_{J+1}} - \frac{1}{\varepsilon_J} \right) \frac{1}{r_{J+1}} + \frac{1}{2} \left(\frac{1}{\varepsilon_J} \frac{r_{J+1}^2 - r_J^2}{r_{J+1}^3 - r_J^3} - \frac{1}{\varepsilon_{J+1}} \frac{r_{J+2}^2 - r_{J+1}^2}{r_{J+2}^3 - r_{J+1}^3} \right) \right] \\ (\Delta \mathcal{U})_{J+1} &= 3 \frac{N}{N_w} \frac{1}{\varepsilon_{J+1}} \left(\frac{1}{3r_{J+1}} - \frac{1}{2} \frac{r_{J+2}^2 - r_{J+1}^2}{r_{J+2}^3 - r_{J+1}^3} \right). \end{aligned}$$

The direct calculation of the energy difference,

$$\Delta E [n(r)] = \Delta E_{\text{local}} [n(r)] + \Delta E_H [n(r)],$$

instead of subtracting energy functionals has two advantages. First of all it is more accurate to calculate the energy difference directly than to derive it from subtraction of two numbers that are many orders of magnitude larger. Secondly, it is much faster than calculating the entire energy functional: for the local contribution only four terms are involved and the calculation of the *change* in Hartree energy is an $\mathcal{O}(N_{\text{interval}})$ process, whereas the calculation of the Hartree energy itself would require $\mathcal{O}(N_{\text{interval}}^2)$ calculations.

Because it is much faster, we also used this direct energy difference to calculate the total difference $\Delta E_{\text{min}}^{(\text{tot})}$ with the last found minimum energy to check whether the actual distribution resembles the ground-state density better. At the beginning of the calculations $\Delta E_{\text{min}}^{(\text{tot})} = 0$ because the energy of the trial distribution is the lowest energy calculated so far. Then each time a distribution is accepted, the addition $\Delta E_{\text{min}}^{(\text{tot})} = \Delta E_{\text{min}}^{(\text{tot})} + \Delta E [n(r)]$ is performed. Now if $\Delta E_{\text{min}}^{(\text{tot})} < 0$, then the actual energy is lower than the minimum found so far. If this situation occurs, the trial ground-state distribution $n_{\text{trial}}(r)$ is set equal to the actual distribution $n_{\text{actual}}(r)$, $\Delta E_{\text{min}}^{(\text{tot})}$ is set equal to $\Delta E_{\text{min}}^{(\text{tot})} = 0$, and adding starts again.

The above procedure leads to a fast program, but although calculating the direct difference is accurate for one move, adding up many little differences leads to an accumulation of round-off errors with a resulting error that can become much larger than the error of calculating and

subtracting energy functionals of two distributions. Therefore it is important that from time to time the total energy difference is determined by the difference of the two energy functionals that are calculated from the involved density distributions. The number of iterations after which such an update is necessary, i_{recalc} , depends on the system under consideration and on the other run parameters. It is to be determined after the other run parameters have been fixed. This can be done by performing a test run in which the calculations are based on the direct energy difference but for which the plotted minimum energy is calculated from the supposedly “best” walker distribution: the number of iterations after which the plotted “minimum energy found so far” increases gives an indication of the number of iterations after which an update is needed.

9.3.5 Determination of run parameters for benchmark nanoshell

To make the explanation concerning the determination of the run parameters more concrete, we now apply it to the nanoshell with $(R_C, R_S) = (40, 55)$ nm and $(\varepsilon_C, \varepsilon_S, \varepsilon_E) = (1, 1, 1)$. We have performed a similar analysis for most of the nanoshells considered and the resulting parameters are summarized in section 9.3.6.

Pre-determined parameters (for all nanoshells)

We took 20 mesh points per nm, fixed the initial acceptance probability at $P_a^{(0)} = 0.5$, used the temperature-independent acceptance probability and set $P_{\text{min}} = 0.001$.

Basic system-dependent run parameters

First we have to determine the basic system-dependent run parameters: the total number of walkers N_w , the number of iterations i_{lower} after which P_a is lowered, how much the acceptance probability is lowered and the sufficient number of iterations i_{stop} in which the minimum has not changed and after which the run is ended. In determining these parameters, acceptance or rejection was based on the directly calculated energy difference but after acceptance the entire energy functional was calculated and compared with the minimum energy found so far, in order to avoid cumulative round-off errors.

In figure 9.2 we show for different numbers of walkers the minimum energy found in a number of iterations. For each number of walkers we performed three runs of which the run that ended in the lowest minimum was used for the figure. Based on such runs one can decide on the number of walkers to use in the calculations. If one finds it sufficient that the accuracy on the energy is of the order of 10^4 eV, one can use 100000 walkers: more walkers give a change in the energy of that order. If one wants a better accuracy of about 10^3 eV, one at least needs 200000 walkers.

As already mentioned, using more walkers implies a longer run time. From figure 9.2 we can derive that appropriate choices for i_{lower} would be for example

$$\begin{aligned} N_w &= 100000 \longrightarrow i_{\text{lower}} = 2000 \\ N_w &= 200000 \longrightarrow i_{\text{lower}} = 3000 \\ N_w &= 300000 \longrightarrow i_{\text{lower}} = 8000. \end{aligned}$$

We decided to take 100000 walkers, to lower the acceptance probability each $i_{\text{lower}} = 2000$ iterations by a power $1/0.6$, so

$$P_a^{(\text{new})} = (P_a^{(\text{old})})^{1/0.6}$$

which corresponds to fictively lowering a temperature by a factor 0.6, and we have taken $i_{\text{stop}} = 1000$.

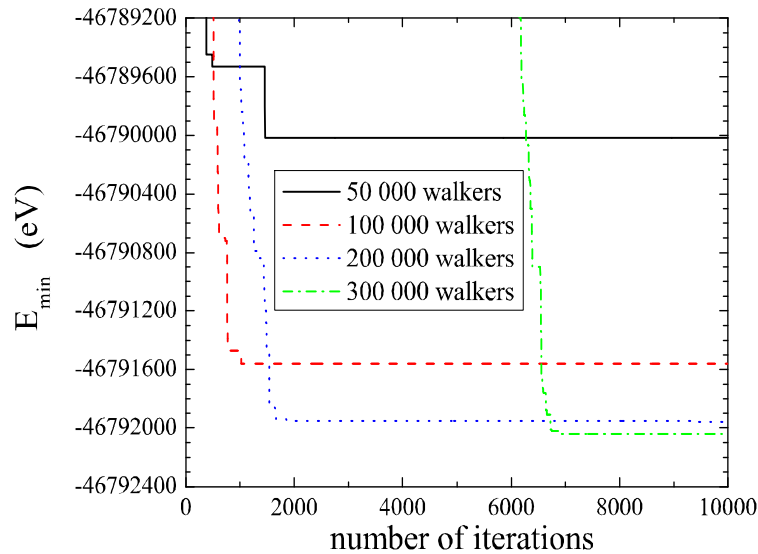


Figure 9.2: Minimum energy found in the indicated number of iterations calculated from test runs to determine an appropriate number of walkers for the benchmark nanoshell. Runs with different numbers of walkers: $N_w = 50000$ (black solid line), $N_w = 100000$ (red dashed line), $N_w = 200000$ (blue dotted line) and $N_w = 300000$ (green dash-dotted line).

Parameter due to use of direct energy difference

As already mentioned, there are two ways by which one can check whether a density distribution resembles the ground-state density better than the best distribution found so far. The first way is to calculate the energy from the distributions and to check which energy is the lowest. The second way is to sum directly calculated energy differences, as explained in section 9.3.4. The latter procedure is faster than the first one, but it suffers from accumulation of round-off errors. Therefore each i_{recalc} number of iterations a calculation of the energy from the distributions should be performed.

We derived a value for i_{recalc} in the following way. We performed test runs in which acceptance of a distribution as the best so far was based on the summation of energy differences. In each iteration we also calculated the energy from the supposedly best distribution. These energies are plotted in figure 9.3 for the benchmark nanoshell with 100000 walkers. Sometimes “the minimum energy found so far” increases. This is a sign that the cumulative error becomes too large: the procedure of summing energy differences does not lead to a distribution with a lower energy, but to one with a higher energy.

Because the solid red curve in figure 9.3 increases around the thousandth iteration, we decided to take $i_{\text{recalc}} = 1000$.

Check of parameters for given N_w and Δx_α

Before considering whether run results can be used to determine a specific result, one has to check whether the runs indeed most of the time lead to a global minimum (within acceptable accuracy). For this purpose, a plot of the minimum energies of the runs can be useful. Such a plot is given in figure 9.4 for the parameters mentioned above. Figure 9.5 shows the minima of this plot that are equal to or lower than the median. These minima do not differ more than

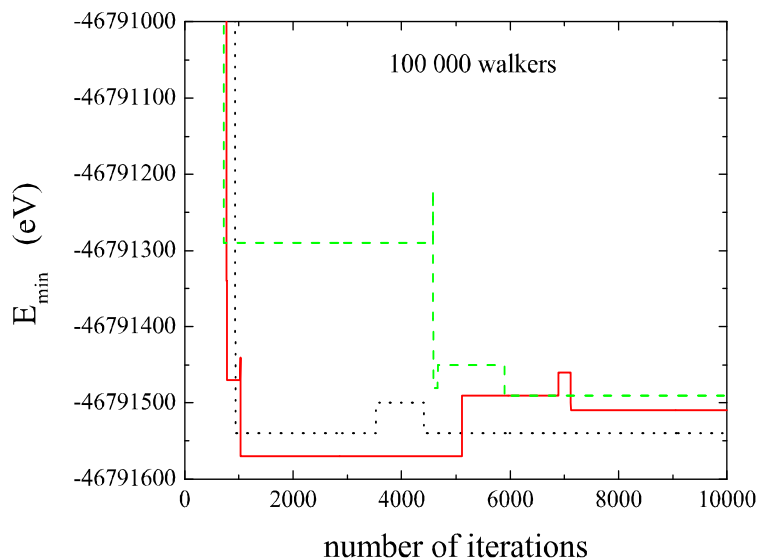


Figure 9.3: Minimum energy found in the indicated number of iterations for three test runs with 100000 walkers for the benchmark nanoshell to determine after how many iterations one has to perform an energy calculation from the walker distributions.

in the seventh digit with the lowest minimum found in all the runs. Because the calculations are performed in single precision, because there is a form of discreteness in the density and the mesh and because the energy functional is calculated with trapezoidal quadrature, the deviation from the lowest minimum can be explained by the numerical accuracy of the calculations. This is a confirmation that adequate run parameters were chosen.

One might comment that it would be better to use Metropolis acceptance so that it would not be necessary to check on the behavior of the run minima and one could use the program as a “blind user”. First of all, although this is almost never explicitly mentioned, also with Metropolis acceptance it is not sure that the algorithm finds a global minimum, so performing more than one run is also advisable if one uses this acceptance prescription. Furthermore, if one uses Metropolis acceptance (or threshold acceptance), one first has to define an effective temperature. One cannot do this blindfolded. Thirdly, a figure is illustrative but one can (“blindfolded”) also just let the program check whether the minimum and maximum included in the averaging do not differ more than a certain desired accuracy. Finally, numerical errors are always present; so it is a good idea anyway to have some more runs from which an average can be calculated.

Calculation time

With the mentioned parameters, one minimization run written in Fortran took about one minute on a 64 bit desktop (AMD Dual Core 3.0 GHz). With self-consistent Kohn-Sham calculations hundreds or even thousands of iterations would be required, each one taking more than two minutes.

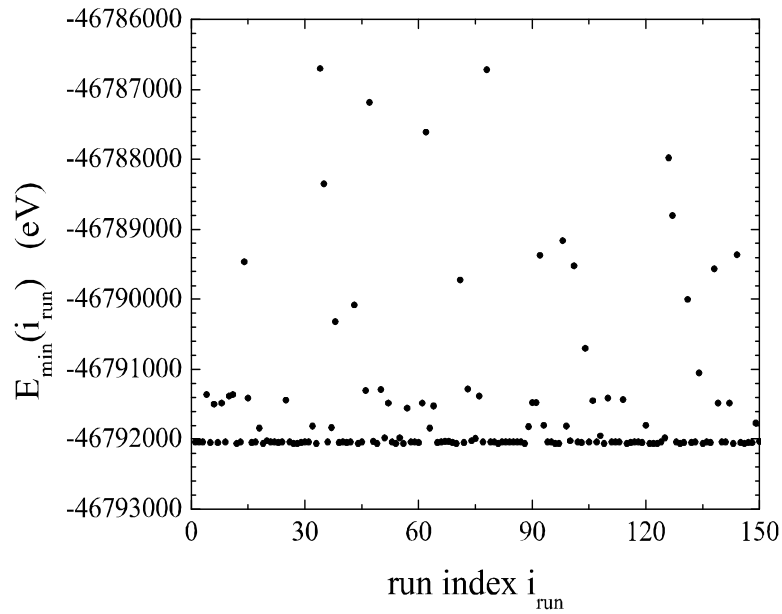


Figure 9.4: Minimum energies found in 150 DFMC runs for the benchmark nanoshell with the following parameters: 20 mesh points per nm, 100000 walkers, $P_a^{(\text{new})} = \left(P_a^{(\text{old})}\right)^{1/0.6}$, $i_{\text{low}} = 2000$, $i_{\text{stop}} = 1000$ and $i_{\text{recalc}} = 1000$.

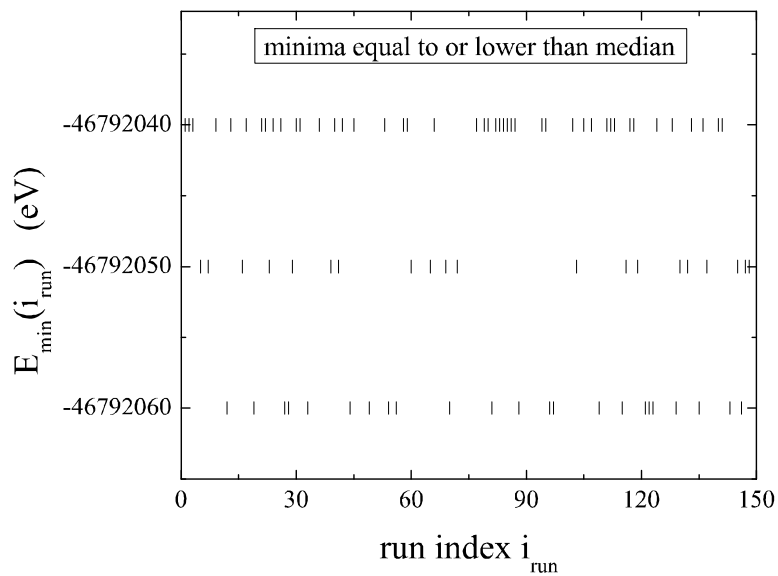


Figure 9.5: Minima of figure 9.4 that are equal to or lower than the median of all the minimum energies found in 150 runs.

9.3.6 Overview of the run parameters for all systems

For all considered nanoshells, we used some common parameters as described in the previous section:

1. 20 mesh points per nm
2. an initial acceptance probability $P_a^{(0)} = 0.5$.
3. the temperature-independent acceptance probability with $P_a^{(\text{new})} = \left(P_a^{(\text{old})}\right)^{1/0.6}$.
4. $P_{\text{min}} = 0.001$.

The other parameters were derived as in the previous section following the procedure described in section 8.2 and in the last paragraph of section 9.3.4.

For the nanoshell with $(R_C, R_S) = (55, 95)$ a.u. that we used for comparison with Kohn-Sham calculations, we took $N_w = 20000$, $i_{\text{lower}} = 3000$, $i_{\text{stop}} = 1000$ and $i_{\text{recalc}} = 50$.

For all larger nanoshells we used $i_{\text{lower}} = 2000$, $i_{\text{stop}} = 1000$ and $i_{\text{recalc}} = 1000$. To be able to compare the results for different sizes, we chose the number of walkers for the considered nanoshells such that the error on the energy was approximately the same as for the benchmark nanoshell (about 400 eV as shown in figure 9.2). We used the following number of walkers for each nanoshell:

(R_C, R_S) nm	(40, 55)	(40, 56)	(40, 57)	(40, 58)	(40, 59)	(40, 60)	(40, 61)	(40, 62)
N_w	100000	110000	120000	130000	140000	150000	150000	170000
(R_C, R_S) nm	(40, 63)	(40, 64)	(40, 65)	(40, 66)	(40, 67)	(40, 68)	(40, 69)	(40, 70)
N_w	180000	190000	200000	220000	230000	245000	260000	275000

9.3.7 Work function based on ionization energies

For each run, we calculated the ionization energies due to removal of one up to six walkers. We removed the walkers one by one from the same interval J and let the system relax after each removal by performing a minimization.

Direct energy difference due to walker removal

The energy difference between the system with N_w walkers and the system with $N_w - \Delta N_w$ walkers *before relaxation*, can be directly calculated with the formulas (see appendix B for the derivation of the Hartree contribution)

$$\begin{aligned} \Delta E_{\text{local}} &= E_{\text{local}}(n'_J) - E_{\text{local}}(n_J) \\ \Delta E_H &= C_H \left[\begin{aligned} &\Delta u_J S_J + \sum_{j=J+1}^{j_{\text{max}}-1} \rho_j \left(I_j^{(1)} \Delta u_{j>J} + I_j^{(2)} \Delta u_{j+1>J} \right) \\ &+ (-\text{sgn} \cdot \eta_J \Delta N_w u_J + \rho'_J \Delta u_J) I_J^{(1)} \\ &+ (-\text{sgn} \cdot \eta_J \Delta N_w u_{J+1} + \rho'_J \Delta u_{J+1}) I_J^{(2)} \end{aligned} \right] \end{aligned}$$

with sgn , C_H , S_j , η_j , $I_j^{(1)}$ and $I_j^{(2)}$ as in expressions (9.11) and

$$\begin{aligned} \Delta u_{j \leq J}^{(k)} &= \frac{N}{N_w} \Delta N_w \left[\sum_{k'=k}^{k_{\text{max}}-1} \left(\frac{1}{\varepsilon_{k'+1}} - \frac{1}{\varepsilon_{k'}} \right) \frac{1}{R_{k'}} + \frac{3}{2\varepsilon_k} \frac{r_{J+1}^2 - r_J^2}{r_{J+1}^3 - r_J^3} \right] \\ \Delta u_{j > J}^{(k)} &= \frac{N}{N_w} \Delta N_w \left[\sum_{k'=k}^{k_{\text{max}}-1} \left(\frac{1}{\varepsilon_{k'+1}} - \frac{1}{\varepsilon_{k'}} \right) \frac{1}{R_{k'}} + \frac{1}{\varepsilon_k} \frac{1}{r_j} \right] \end{aligned}$$

with k the layer in which interval j is located.

It should be emphasized that relaxation after removal of a walker leads to almost negligible energy changes. The largest part of the energy difference between systems with a different number of walkers comes from the instant removal of a walker. Therefore it is important that this difference is calculated as accurately as possible.

Work function as first ionization energy

Plotting the ionization energies, we observed a quadratic dependence as a function of the number of removed electrons ΔN . This is shown in figure 9.6 for the benchmark nanoshell. Taking into account that $E_{\text{ionization}}(\Delta N = 0) = 0$, we fitted these six calculated points to the quadratic function

$$E_{\text{ionization}}(\Delta N) = b \times (\Delta N) + c \times (\Delta N)^2$$

with the least square method (routine “svdfit.f90” of Ref. [97]). In this method, one determines the values for the parameters that are most likely the correct values given the data, by minimizing the chi-square value χ^2 which is in this case given by

$$\chi^2 = \sum_{i=1}^6 \left(\frac{E_{\text{ionization}}^{(i)} - E_{\text{ionization}}((\Delta N)_i; b, c)}{\sigma_i} \right)^2.$$

In this expression, $E_{\text{ionization}}^{(i)}$ is one of the six calculated “walker” ionization energies from averaging over run results, σ_i is the standard deviation on these values and $(\Delta N)_i$ is the number of electrons corresponding to removal of the first i walkers.

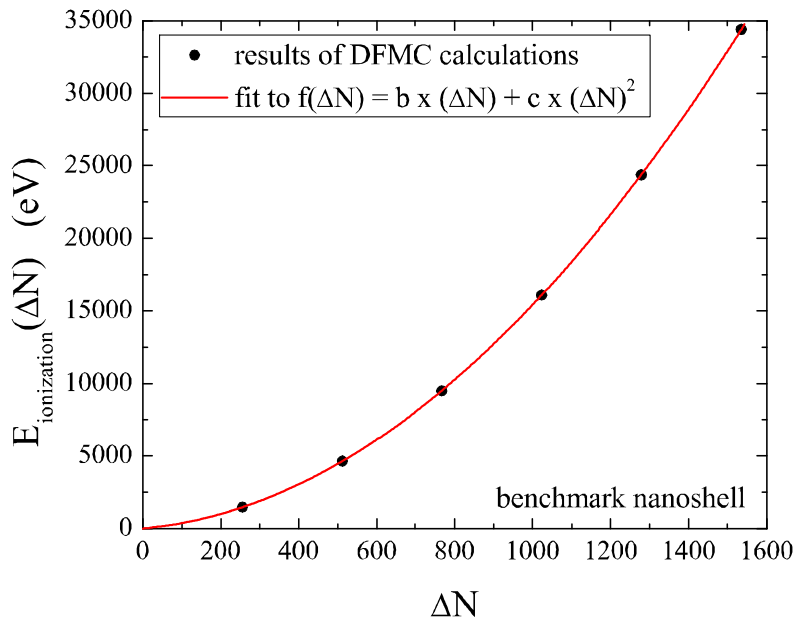


Figure 9.6: Ionization energies of the benchmark nanoshell as a function of the number of removed electrons ΔN calculated with the DFMC method (black dots) and fitting function of the form $f(\Delta N) = b \times (\Delta N) + c \times (\Delta N)^2$ (red line). The error bars are not visible in the figure.

The work function was then calculated as $W_{\text{ionization}} = E_{\text{ionization}}(\Delta N = 1)$ and its standard deviation with error propagation as $\sigma_W = \sqrt{\sigma_b^2 + \sigma_c^2 + 2\text{cov}(b, c)}$ with σ_b^2 and σ_c^2 the variances on the parameter b and c respectively and $\text{cov}(b, c)$ the covariance between the parameters b and c .

To check whether $E_{\text{ionization}}(\Delta N)$ is indeed quadratic, we calculated the χ^2 -probability Q -value which gives an indication of the “goodness-of-fit” of the model (see e.g. Ref. [98]). This Q -value gives, under the assumption that the measurement errors are normally distributed, the probability that in another experiment or set of runs, one will find a higher value of χ^2 by chance. It is defined as

$$Q(\chi^2|\nu) = Q\left(\frac{\nu}{2}, \frac{\chi^2}{2}\right) = \frac{\Gamma\left(\frac{\nu}{2}, \frac{\chi^2}{2}\right)}{\Gamma\left(\frac{\nu}{2}\right)}$$

with $\Gamma(a, x) = \int_x^\infty e^{-t} t^{a-1} dt$ the incomplete gamma function and $\Gamma(a) = \Gamma(a, 0)$ the gamma function. The parameter ν is the number of degrees of freedom which is defined as from the number of data points N_{data} and the number of parameters N_{param} as $\nu = N_{\text{data}} - N_{\text{param}}$; so in this case $\nu = 6 - 2 = 4$. In general, a model is accepted if Q lies between 0.001 and 1.

9.4 Results

9.4.1 Benchmark nanoshell

Based on the median of the minimum energies of 150 runs, 77 results were retained for averaging.

For the work function we found a value of $W_{\text{ionization}} = (2.364 \pm 0.017)$ eV with a Q -value of $Q = 0.39$, and $W_{\text{LK}} = 2.368$ eV. Both ways of calculating the work function thus result in values that are of the same order of magnitude. Given the relatively large dimensions of the nanoshell, its work function can be expected to be of the order of the bulk work function of gold, for which measured values are in the range [5.31 – 5.47] eV depending on the crystal face being measured [40]. The calculated work function of several eV thus has indeed the correct order of magnitude. The difference with the experimental value can be attributed entirely to the used model for the background and the approximate forms of the kinetic energy functional and the exchange-correlation energy. This can be seen from the results of Ref. [91] concerning a flat metallic surface. The calculations reported in this paper were based on the uniform background model and the same expression for the exchange and correlation energy as used in this thesis. For $r_s = 3$, Kohn-Sham calculations resulted in a work function $W = 3.35$ eV, which is also a few eV lower than the experimental bulk value. Furthermore, orbital-free calculations in which the kinetic energy was treated in the Thomas-Fermi framework led to a work function value of $W = 2.11$ eV. Expecting a somewhat higher work function for the nanoshell because of confinement, we consider the DFMC value for the work function to be consistent with the calculations performed for a flat surface. The difference of several eV with experiment is thus not due to the used method but due to the used approximations.

Note that the work function $W_{\text{ionization}}$, a quantity of the order of a few eV, is obtained from the total energy of a system, a quantity with a magnitude of several 10^7 eV. This shows that the Monte Carlo calculations reach an acceptable level of accuracy for the energy.

The resulting density is shown in figure 9.7. The global behavior is as can be expected: approximately homogeneous in the shell with a small spill-out into the core and the environment.

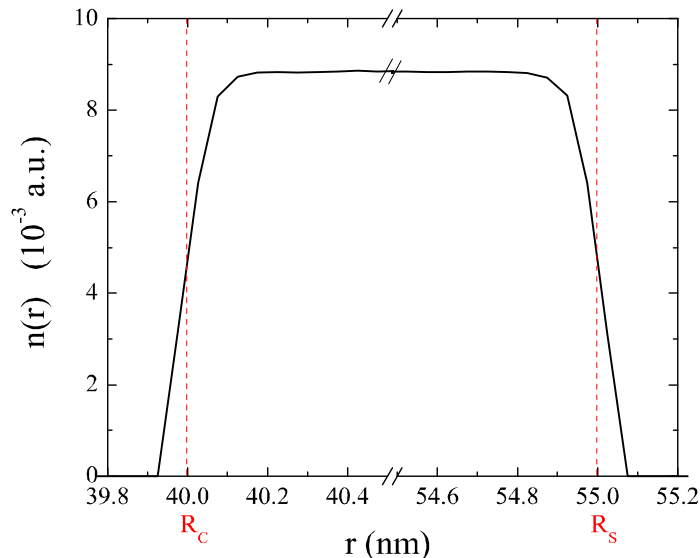


Figure 9.7: Calculated ground-state density of the benchmark nanoshell from averaging over 77 retained DFMC run results corresponding to the global minimum. The relative error is of the order $10^{-4} - 10^{-3}$ which results in error bars that are not visible in the figure.

9.4.2 Comparison with Kohn-Sham calculations

We have performed calculations for a nanoshell with $(R_C, R_S) = (55, 95)$ a.u. $\simeq (2.9, 5.0)$ nm and $(\varepsilon_C, \varepsilon_S, \varepsilon_E) = (1, 1, 1)$ for which previously Kohn-Sham calculations were performed [101] with the same approximations for the background and for the exchange and correlation energy as used in this thesis. The resulting density from averaging over 95 run results is given in figure 9.8 together with the data of the Kohn-Sham calculations [64]. Comparison of both curves shows that the resulting density profile is globally the same: almost homogeneous inside the shell with a spill-out into the core and the environment; the spill-out is of comparable accuracy in both treatments. The observable differences can be entirely attributed to the different treatment of the kinetic energy in both approaches. We found a value for the work function equal to $W_{\text{ionization}} = (2.518 \pm 0.002)$ eV from a fit of $E_{\text{ionization}}(N)$ with a Q -value of $Q \simeq 0.999$, and $W_{\text{LK}} = 2.385$ eV from the Lang-Kohn formalism.

9.4.3 Influence of the permittivities

We performed calculations for nanoshells of size $(R_C, R_S) = (40, 55)$ nm with either the core permittivity or the environment permittivity equal to $\varepsilon = 4$. This permittivity is of the order of the permittivity of SiO_2 and was also considered in Kohn-Sham calculations for nanoshells of size $(R_C, R_S) = (40, 80)$ a.u. containing 16592 electrons [102]. The results for the effective potential energy $u_{\text{eff}}(r)$ are given in figure 9.9. Our results are qualitatively similar to the results shown in figure 1 of Ref. [102]. In the core the effective potential energy of the shell with $\varepsilon_E = 4$ is higher than that of the benchmark nanoshell, and the effective potential energy of the nanoshell with $\varepsilon_C = 4$ is lower. In the shell the effective potential energies of the benchmark nanoshell and the nanoshell with $\varepsilon_C = 4$ coincide and the potential well of the nanoshell with $\varepsilon_E = 4$ is less shallow. This static result already indicates that nanoshells can be used as biosensor: the charge and potential profile depend on the permittivity of the environment.

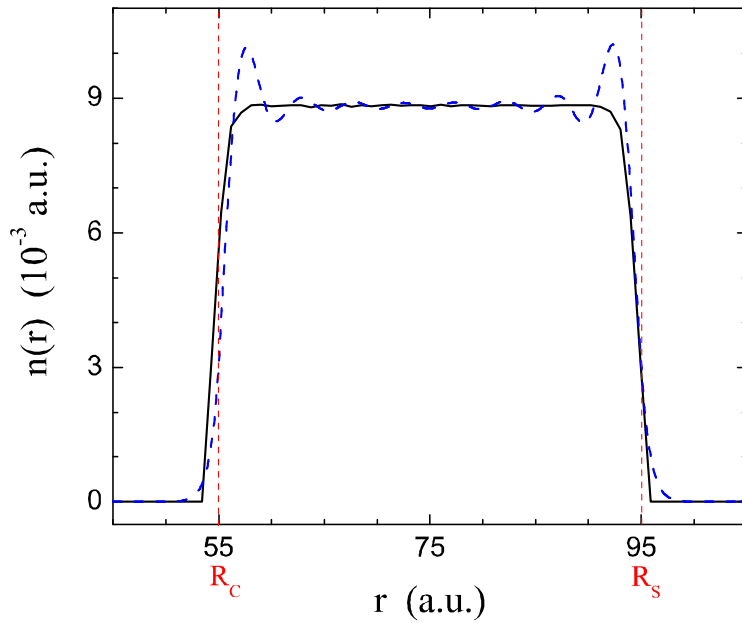


Figure 9.8: Ground-state density of a nanoshell with $(R_C, R_S) = (55, 95)$ a.u. $\simeq (2.9, 5.0)$ nm and $(\varepsilon_C, \varepsilon_S, \varepsilon_E) = (1, 1, 1)$ calculated with DFMC (black solid line) and with Kohn-Sham calculations [64] (blue dashed line). Error bars are not visible in the figure.

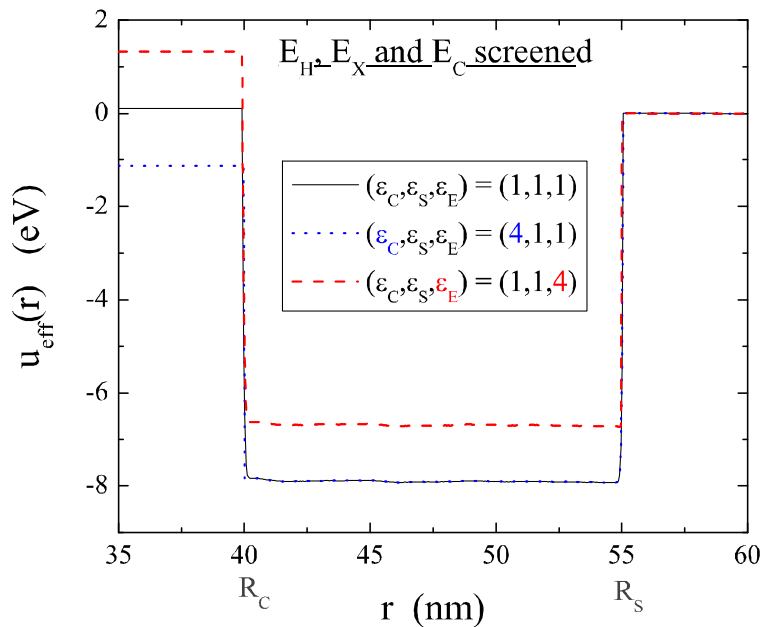


Figure 9.9: Effective potential energy $u_{\text{eff}}(r)$ as a function of r for nanoshells with size $(R_C, R_S) = (40, 55)$ nm and different permittivities: $(\varepsilon_C, \varepsilon_S, \varepsilon_E) = (1, 1, 1)$ (black solid line), $(\varepsilon_C, \varepsilon_S, \varepsilon_E) = (4, 1, 1)$ (blue dotted line), $(\varepsilon_C, \varepsilon_S, \varepsilon_E) = (1, 1, 4)$ (red dashed line). In the calculations the Hartree energy and the exchange-correlation energy were screened.

Quantitatively there are differences between the effective potential energies from our calculations and those from the Kohn-Sham calculations. A first remark that can be made is that the potential energy resulting from both methods is shifted even for the curve in absence of screening. The explanation of this behavior is that in the Kohn-Sham calculations an external potential $U_{\text{ext}}(r)$ was considered, given by expression (3.8), and in the DFMC calculations no external potential was introduced. A second feature is that the difference between the potential energies corresponding to different permittivities is larger in our results than in the Kohn-Sham results. To check whether the difference between the results of the two methods is attributed to the size difference between the considered nanoshells, we performed also calculations for the nanoshells with $(R_C, R_S) = (40, 80)$ a.u. We found nearly the same potential energies in the core and the shell as for the nanoshell with $(R_C, R_S) = (40, 55)$ nm, so the differences between the results of Ref. [102] and of the DFMC calculations cannot to be attributed to the size difference. The calculations also show that the difference in effective potential energy between nanoshells with different permittivities is almost not size-dependent. The reason for the different influence of the permittivities resulting from the Kohn-Sham and DFMC calculations seems to be that in the DFMC calculations the exchange-correlation potential was screened, whereas in the Kohn-Sham calculations it was not: if in the DFMC calculations we omit the screening of this contribution, we find the same order of magnitude of the difference between the effective potential energies corresponding to different permittivities, as is seen in figure 9.10. There is thus quite a large effect from the screening of the exchange-correlation energy. Comparison between figures 9.9, 9.10 and 9.11 shows that the largest screening effect stems from the exchange energy and that the effect of screening the correlation energy is negligible.

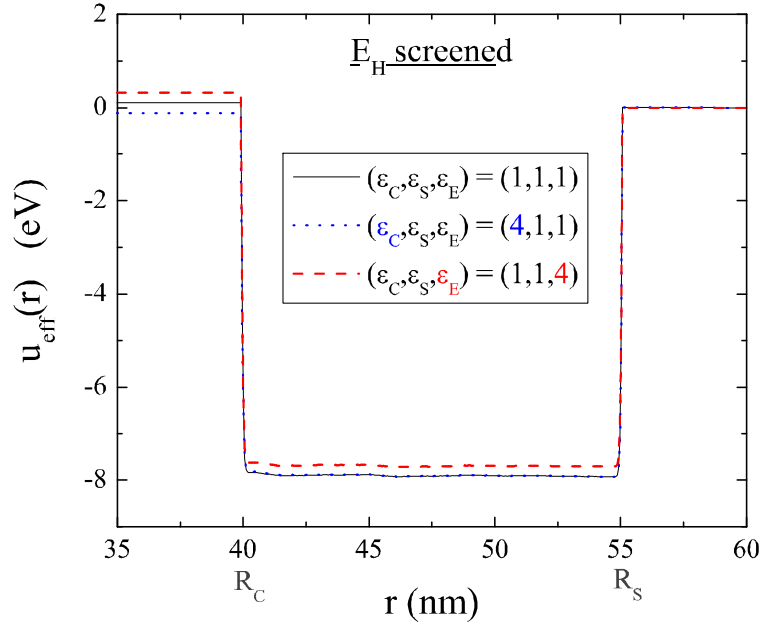


Figure 9.10: Effective potential energy $u_{\text{eff}}(r)$ as a function of r for nanoshells with size $(R_C, R_S) = (40, 55)$ nm and different permittivities: $(\epsilon_C, \epsilon_S, \epsilon_E) = (1, 1, 1)$ (black solid line), $(\epsilon_C, \epsilon_S, \epsilon_E) = (4, 1, 1)$ (blue dotted line), $(\epsilon_C, \epsilon_S, \epsilon_E) = (1, 1, 4)$ (red dashed line). In the calculations only the Hartree energy was screened, not the exchange-correlation energy.

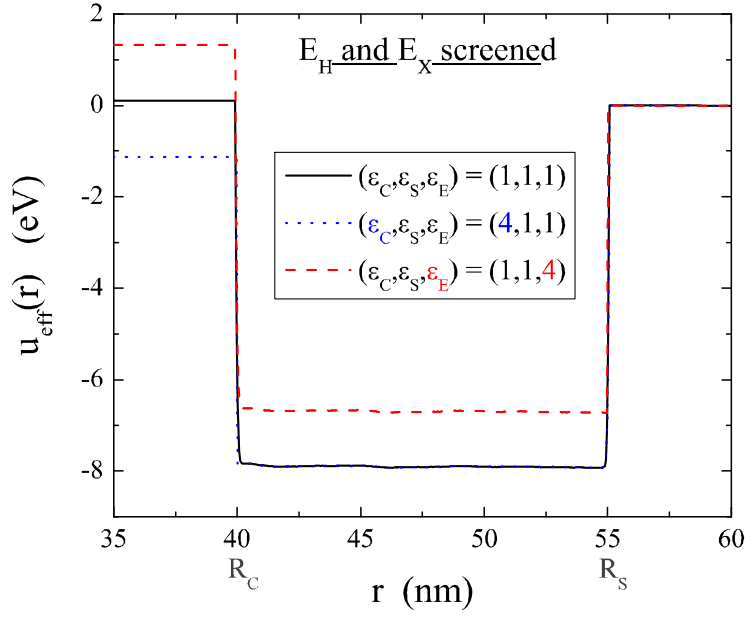


Figure 9.11: Effective potential energy $u_{\text{eff}}(r)$ as a function of r for nanoshells with size $(R_C, R_S) = (40, 55)$ nm and different permittivities: $(\varepsilon_C, \varepsilon_S, \varepsilon_E) = (1, 1, 1)$ (black solid line), $(\varepsilon_C, \varepsilon_S, \varepsilon_E) = (4, 1, 1)$ (blue dotted line), $(\varepsilon_C, \varepsilon_S, \varepsilon_E) = (1, 1, 4)$ (red dashed line). In the calculations the Hartree and exchange energy were screened, not the correlation energy.

The resulting work functions are given in table 9.1. The influence on the work function is low when the permittivity of the core is changed, and high when the permittivity of the environment is changed. The calculated work functions with $\varepsilon_E = 1$ and $\varepsilon_E = 4$ are somewhat less than half of the experimental bulk value, which is for gold to vacuum about $W_{\text{Au} \rightarrow \text{vac}} \approx 5.3$ eV [40] and for gold to SiO_2 about $W_{\text{Au} \rightarrow \text{SiO}_2} \approx 3.8$ eV [35]. The same behavior is also present when the screening of the exchange and/or correlation contribution is not included. In both cases the work function is about $W_{\text{LK}} \simeq 2.368$ eV and $W_{\text{ionization}} \simeq 2.365$ eV if $\varepsilon_C = 4$ and $\varepsilon_E = 1$. The results for the case $\varepsilon_C = 1$ and $\varepsilon_E = 4$ reflect again that the screening of the exchange contribution has the largest effect: if only the Hartree term is screened then $W_{\text{LK}} \simeq 2.153$ eV and $W_{\text{ionization}} \simeq 2.128$ eV, and if the Hartree and exchange contribution are screened then $W_{\text{LK}} \simeq 1.154$ eV and $W_{\text{ionization}} \simeq 1.173$ eV.

$(\varepsilon_C, \varepsilon_S, \varepsilon_E)$	W_{LK} (eV)	$W_{\text{ionization}}$ (eV)	σ_W (eV)	Q	N_{average}
(1, 1, 1)	2.368	2.364	0.017	0.39	77
(4, 1, 1)	2.368	2.361	0.016	0.30	90
(1, 1, 4)	1.154	1.173	0.012	0.10	103

Table 9.1: Work function values W_{LK} and $W_{\text{ionization}}$ and statistical error σ_W on the work function $W_{\text{ionization}}$ for nanoshells with $(R_C, R_S) = (40, 55)$ nm and with the mentioned permittivities, together with the Q -value of the fit for $E_{\text{ionization}}(N)$ and the number of run results of which the averages are taken, N_{average}

9.4.4 Investigation of the influence of the size

In figure 9.12 we show for nanoshells with $(\varepsilon_C, \varepsilon_S, \varepsilon_E) = (1, 1, 1)$, $R_C = 40$ nm and different values of R_S the work function values W_{LK} and $W_{\text{ionization}}$ and the standard deviation σ_W on the work function $W_{\text{ionization}}$, together with the number of run results of which the averages were taken, N_{average} . The table below shows the corresponding Q -values of the fit for $E_{\text{ionization}}(N)$.

R_S (nm)	55	56	57	58	59	60	61	62
Q	0.39	0.87	0.83	0.68	0.73	0.90	0.98	0.58
R_S (nm)	63	64	65	66	67	68	69	70
Q	0.66	0.59	0.88	0.60	0.091	0.62	0.021	0.059

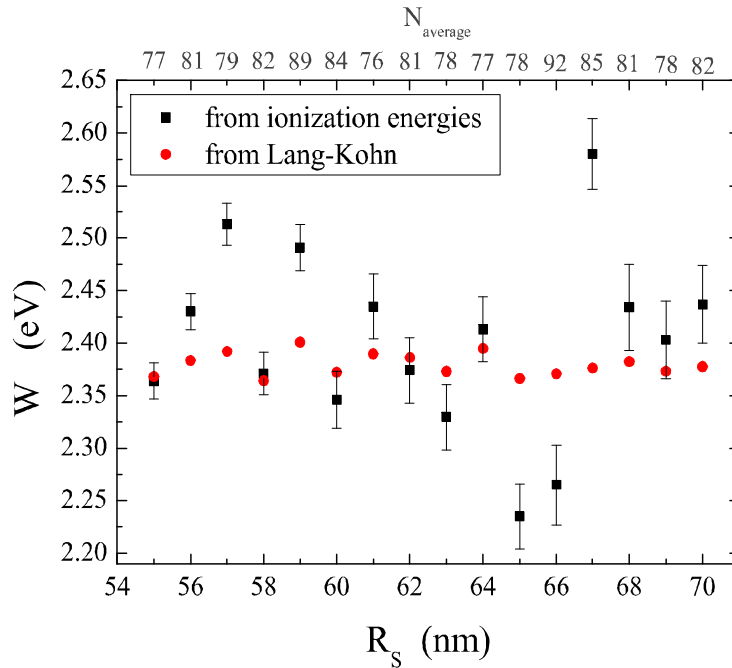


Figure 9.12: Work function as a function of R_S for a nanoshell with $(\varepsilon_C, \varepsilon_S, \varepsilon_E) = (1, 1, 1)$ and $R_C = 40$ nm calculated based on a fit of the “walker ionization energies” (black squares) and calculated from the expression (8.3) of Lang and Kohn (red circles).

All work function values are higher than $W = 2.11$ eV, the calculated value at a flat metallic surface [91]. This effect is due to the confinement of the electrons.

The absolute value of the relative difference, $|(W_{\text{LK}} - W_{\text{ionization}})/W_{\text{LK}}|$, ranges from 0.0041 (for $R_S = 55$ nm) up to 0.086 (for $R_S = 67$ nm). The results thus confirm the conclusion stated for the benchmark nanoshell: both ways of calculating the work function result in values of the same order of magnitude. Thus for the purpose of determining an estimate of the work function, the two methods can be used.

The difference $W_{\text{LK}} - W_{\text{ionization}}$ is however not constant: the sign and magnitude of it depend on the value of R_S . It is not obvious whether one method is better than the other. For $W_{\text{ionization}}$ fitting was used to calculate $E_{\text{ionization}}(\Delta N = 1) \approx 1$ eV from values of $E_{\text{ionization}}(\Delta N)$ with ΔN ranging from $\Delta N \approx 10^2$ up to $\Delta N \approx 10^3$ and $E_{\text{ionization}}$ ranging from $E_{\text{ionization}} \approx 10^4$ eV up to $E_{\text{ionization}} \approx 10^5$ eV. This procedure requires a very high accuracy of the calculated values. To attain a sufficiently high accuracy with a stochastic

method is actually not evident. It is already very satisfactory to find a value that has the correct order of magnitude.

The calculation of W_{LK} is based on an expression derived from the Euler equation (2.22) [68]. As already mentioned in section 2.4 it is not entirely clear whether the use of this equation is justified if approximate energy functionals are used.

That both W_{LK} and $W_{\text{ionization}}$ have a realistic order of magnitude is actually a confirmation that both procedures to calculate the work function are acceptable.

In neither $W_{\text{LK}}(R_S)$ nor $W_{\text{ionization}}(R_S)$ a simple pattern is observed. One would expect the work function to be globally decreasing as a function of R_S , like in the case of the Fermi energy of a spherically symmetric infinite potential well (shown in figure 6.7) or the work function of small metallic spheres [29]. The most likely reason why such effect is not observed is that the size of the effect is too small to detect with the accuracy of the performed calculations. For the Fermi energy of the potential well, the confinement effect for a nanoshell with $R_S = 55$ nm is only about $\epsilon_F(d = 15 \text{ nm}) - \epsilon_F(\infty) \simeq 0.05$ eV. The largest difference in work function value for the Na spheres studied in Ref. [29] is approximately equal to $[W(R) - W(\infty)]_{\text{max}} \simeq 2$ eV, but this difference occurs at a particle radius of only $R \simeq 8$ a.u. $\simeq 0.4$ nm. Figure 1 of Ref. [29] shows pronounced oscillatory behavior in $W(R)$ for the Na spheres in the considered interval $R \in [5, 20]$ a.u.: in this interval of about 1 nm the work function resulting from the orbital-based calculations is at a maximum whenever an orbital is completely filled and drops an amount when a new orbital starts to fill up. The difference between the attained maxima and the bulk work function decreases rapidly as a function of R , from $\Delta W(R \simeq 0.4 \text{ nm}) \simeq 2$ eV to $\Delta W(R \simeq 1 \text{ nm}) \simeq 1$ eV. The oscillatory behavior decreases correspondingly.

It is not likely that the oscillating-type behavior of the work function seen in figure 9.12 is attributed to shell effects. Theoretical and experimental results for the work function of small metallic spheres [29, 132] suggest that the work function is globally decreasing as the outer radius increases and that for metallic shells of the considered sizes ($R_C = 40$ nm, $R_S > 55$ nm) oscillations due to shell effects would be negligible as compared to this global trend. The behavior of the Fermi energy as a function of shell thickness (figure 6.7) supports this idea. Therefore we expect that the oscillating behavior indicates that the real behavior is out of reach of the accuracy of the performed calculations and that the real error on the work function is several times larger than the standard deviation indicated in figure 9.12. As explained in section 9.3.7, this statistical error was determined based on a fit through six ionization energies which each were calculated as the mean of a number of run results. All performed statistical calculations contained the implicit assumption that the errors on the data points are normally distributed. The invalidity of this assumption leads to an underestimation of the real error.

We showed in figure 9.5 that the minimum energies of the retained results for the benchmark nanoshell differ in the seventh digit. This is the highest accuracy that can be reached with the single-precision calculations we used. One might be tempted to just perform the calculations in double precision, but this is of not much use if no refinements are made regarding the integration method, the grid spacing and the ratio of the number of electrons per walker. Other factors that can lead to an incorrect behavior are the used model for the background and the kinetic, exchange and correlation contribution to the energy functional.

Chapter 10

Conclusion

We conclude that density-functional Monte Carlo is a relatively simple method for calculating the ground-state properties of rather large many-particle systems. The method, which consists of a direct numerical minimization of the energy functional by use of a Monte Carlo algorithm, is a pure implementation of density-functional theory because the particle density for N particles is the basic ingredient and no mathematically introduced Lagrange multiplier is required to incorporate particle conservation.

We showed that DFMC allows to treat nanoshells with manufacturable dimensions, which are hardly accessible to orbital-based DFT methods. The results are comparable to results of other calculation methods. The DFMC density in small nanoshells is globally the same as the density resulting from Kohn-Sham calculations, with a difference that can be entirely attributed to the different treatment of the kinetic energy in both approaches. The work function values are slightly higher than the value found from calculations for a flat surface, as can be expected for confined systems. The influence of the permittivity of the core and the environment on the behavior of the effective potential energy is essentially the same in the DFMC and the Kohn-Sham calculations. Screening of the exchange energy has the largest effect, the effect of screening the correlation energy is negligible.

Chapter 11

Positioning and outlook

In this thesis we have performed a Monte Carlo implementation of the basic Hohenberg-Kohn theorems of DFT to calculate ground-state properties of a nanoshell without making use of orbitals. The Hohenberg-Kohn theorems were proven for a non-degenerate ground state, but Kohn demonstrated that the requirement of nondegeneracy can be lifted [61].

The original paper of Hohenberg and Kohn was not only followed by generalizations concerning the electronic ground state of a system. Two of the other generalizations were already mentioned in the exposition of the existing Kohn-Sham calculations for nanoshells: finite-temperature DFT [77] and time-dependent DFT [94, 113, 133, 23]. Other examples can be found in e.g. Refs. [89, 25, 62]¹. Like the original Hohenberg-Kohn theorems, the generalizations are most often practically worked out with orbital-based Kohn-Sham calculations. Because of the limited number of orbitals that can be determined in practice, research is also performed in order to implement the generalizations orbital-free; see e.g. Ref. [55] for the extension to finite temperature and Ref. [85] for time-dependent orbital-free DFT which opens the way to the orbital-free calculation of response properties that are of interest for applications. Like the research for an adequate exchange and correlation energy for both orbital-based and orbital-free DFT [92, 93] and a static kinetic energy functional and pseudopotential for orbital-free DFT [127, 43, 45], the research to develop orbital-free implementations for the extensions of the Hohenberg-Kohn theorems is still ongoing. It is however possible to implement the existing results in DFMC to find approximate results, like was done in this thesis to calculate the ground-state properties of a nanoshell with local energy-density functionals and assuming a Jellium background in the shell.

As already mentioned in the introduction, DFMC is the first direct numerical minimization of the energy functional and removes some draw-backs from existing orbital-free implementations since the number of particles is kept constant by construction, no negative or complex density can occur in the minimization process and no non-trivial differential, integral or integro-differential equation has to be solved. Because of the conceptual simplicity, the DFMC method can even be used as a tool to check the validity of newly derived expressions for orbital-free kinetic energy functionals and pseudopotentials.

An approximation to the ground-state properties in the framework used in this thesis can relatively easily be obtained for other systems than nanoshells to which DFMC can be applied, e.g. atoms, molecules, graphene, nanowires, quantum dots and other confined systems.

Two further topics have to be addressed for each system separately: the construction of a mesh with an adequate description of possible material boundaries and the simulation of an initial walker density on the mesh. If the system is not (effectively) one-dimensional, solving

¹The Hohenberg-Kohn theorems are generally accepted, but in applying generalizations one should be careful. See e.g. Refs. [133, 23] for a discussion of the often cited time-dependent generalization proposed in Ref. [113].

the Poisson equation and integrating the energy density will have to be done differently than was described in this thesis. A solution of the Poisson equation can for example be obtained by using a relaxation method like the Jacobi method or the Gauss-Seidel method, possibly with successive overrelaxation (see e.g. Ref. [98] section 19.5). For multidimensional integration several approaches have been worked out (see e.g. Ref. [98] section 4.6) and the most appropriate approach depends on the behavior of the integrand and the desired accuracy, which can be increased at the end of a run to refine a rough approximation.

Some parameters of DFMC can be altered to obtain a better *numerical* accuracy: the use of single or double precision, the integration method, the mesh spacing (which can be non-uniform) and the number of walkers. Although adjusting these numerical parameters can lead to a higher numerical accuracy, the largest improvement of the results will probably be obtained by using a better description of the energy functional and the background.

As long as no appropriate functionals and pseudopotentials exist, more accurate results for systems with a moderate size might be obtained by first determining an approximate result from DFMC and afterwards performing one or a few orbital-based iterations. If adequate descriptions for the kinetic energy and background potential are found, accurate results might be obtained directly with DFMC not only for relatively large systems, but also for systems that can be described by orbital-based DFT. Then the research on very small systems would also profit from the benefits of an orbital-free treatment.

Summary and general conclusion

The objective of this thesis was to calculate the ground-state density and work function of SiO₂-Au nanoshells with sizes that are manufacturable at this moment, i.e. with a core radius of at least 40 nm and a minimum shell thickness of 15 nm.

We first investigated whether this goal can be achieved by performing orbital-based self-consistent Kohn-Sham calculations. Previously, Prodan and Nordlander developed an efficient Kohn-Sham algorithm in which the single-particle Schrödinger equations were solved by finite difference numerical integration [101]. However with this method it was only possible to describe nanoshells with an overall radius of about 20 nm and a shell thickness of a few nm. We examined whether nanoshells of manufacturable sizes can be treated orbital-based if the single-particle Schrödinger equations are solved by using the Transfer Matrix Method. In this method the entire domain is divided into sufficiently small intervals such that the potential energy can be piecewise approximated as a constant. In each interval the piecewise Schrödinger equation can then be solved analytically. Applying the correct boundary conditions results in the single-particle energies and the wave functions in the entire region. Calculations for an ideal Fermi gas in a spherically symmetric potential well show that the Transfer Matrix Method is an appropriate method to calculate orbitals and has some advantages in comparison with numerical integration. However, manufacturable nanoshells seem also out of reach for this method: orbital-based calculations for nanoshells of these dimensions suffer from long calculations times and memory issues.

Because of the limitations of orbital-based calculations, we devised another method to achieve our goal. Therefore we went back to the basics of density-functional theory. This theory is based on two theorems concerning the ground state of a system of interacting particles in an external potential $v(\mathbf{r})$. From the first theorem it follows that the particle density $n(\mathbf{r})$ can be used as a basic variable in quantum-mechanical ground-state calculations, so there is no need for a wave function description. In the second theorem it is stated that the energy functional $E_v[n]$ of a system reaches its minimum value at the correct ground-state density if the number of particles of the system is kept constant. Based on these two theorems, we developed a method in which the energy functional $E_v[n]$ is minimized numerically by use of a Monte Carlo algorithm: density-functional Monte Carlo (DFMC). In this method, the density distribution is simulated by a distribution of Bernoulli walkers on a mesh. The method contains the following basic steps. First a trial distribution is constructed. Then the distribution is changed by letting subsequently for each interval a walker move to an adjacent interval. After each walker move, the energy functional is compared with the value of the previous distribution and the new distribution is accepted or rejected based on the energy difference. The second and third step are repeated until in a sufficient number of iterations no lower energy is found. Using the DFMC method, we calculated the ground-state density and work function of nanoshells with different permittivities in the core and the environment and with different sizes. For this purpose, we used a model without external potential in which the interaction between the conduction electrons of the shell with a homogeneous neutralizing background and with each other leads to a self-consistent potential confining the electrons mainly to the shell. The

calculated electron density and effective potential energy in small nanoshells are in rather good agreement with the results of Kohn-Sham calculations. The work function values from the DFMC calculations for nanoshells are somewhat higher than the value resulting from orbital-free calculations for a flat golden surface, as can be expected for confined systems. Calculations with different permittivities in the core and the environment show that the largest effect of screening stems from the exchange contribution and that the effect of screening the correlation contribution is negligible. To investigate the effect of the shell size on the work function, some refinements would have to be made in order to attain a higher accuracy than that obtained in the presented calculations.

This thesis has two conclusions concerning the calculation of ground-state properties of SiO₂-Au nanoshells with sizes that are manufacturable at present. The first conclusion is that it is not feasible to use orbital-based calculations to achieve that goal. The second conclusion is that the newly developed density-functional Monte Carlo method opens better perspectives for doing so.

Samenvatting en algemeen besluit

Het doel van deze thesis was om de grondtoestandsdichtheid en werkfunctie te berekenen van SiO₂-Au nanoschillen die op dit ogenblik kunnen gefabriceerd worden, met een kernstraal van ten minste 40 nm en een minimum schildikte van 15 nm.

We hebben eerst onderzocht of dit doel kan bereikt worden met orbitaalgebaseerde zelfconsistente Kohn-Sham berekeningen. Eerder ontwikkelden Prodan en Nordlander een efficiënt Kohn-Sham algoritme waarin de ééndeeltjes-Schrödingervergelijkingen opgelost werden met numerieke integratie via de methode van de eindige verschillen [101]. Met deze aanpak was het echter enkel mogelijk om nanoschillen te beschrijven met een totale straal van ongeveer 20 nm en een schildikte van een aantal nm. We hebben nagegaan of nanoschillen met fabriceerbare grootte orbitaalgebaseerd kunnen behandeld worden als de ééndeeltjes-Schrödingervergelijkingen opgelost worden met de Transfermatrixmethode. In deze methode wordt het beschouwde gebied opgedeeld in voldoende kleine intervallen zodat de potentiële energie stuksgewijs als constant kan benaderd worden. Dan kan in elk interval de stuksgewijze Schrödingervergelijking analytisch opgelost worden. Toepassen van de correcte randvoorwaarden resulteert in de ééndeeltjesenergieën en de golffuncties in het hele gebied. Berekeningen voor een ideaal Fermigas in een sferisch symmetrische potentiaalput tonen aan dat de Transfermatrix Methode een geschikte manier is om orbitalen te berekenen en een aantal voordelen heeft in vergelijking met numerieke integratie. Fabriceerbare nanoschillen kunnen echter ook met deze methode niet behandeld worden: orbitaalgebaseerde berekeningen voor nanoschillen met deze afmetingen vergen lange berekeningstijden en leiden tot geheugenproblemen.

Vanwege de beperkingen van orbitaalgebaseerde berekeningen bedachten we een andere manier om het doel van deze thesis te bereiken. Daarvoor gingen we terug naar de basis van dichtheidsfunctionaaltheorie. Deze theorie is gebaseerd op twee theorema's in verband met de grondtoestand van een systeem van interagerende deeltjes in een externe potentiaal $v(\mathbf{r})$. Uit het eerste theorema volgt dat de deeltjesdichtheid $n(\mathbf{r})$ kan beschouwd worden als basisvariabele in kwantummechanische grondtoestandsberekeningen; er is hiervoor dus geen golffunctiegebaseerde beschrijving nodig. In het tweede theorema wordt gesteld dat, indien het aantal deeltjes behouden blijft, de energiefunctieaal $E_v[n]$ van een systeem minimaal is bij evaluatie in de correcte grondtoestandsdichtheid. Gebaseerd op deze twee theorema's ontwikkelden we een methode waarin de energiefunctieaal numeriek geminimaliseerd wordt met behulp van een Monte Carlo algoritme: dichtheidsfunctionaal Monte Carlo (DFMC). In deze methode wordt de dichtheidsverdeling gesimuleerd door een verdeling van Bernoulli wandelaars op een maze. De methode bestaat uit de volgende basisstappen. Eerst wordt een probeerverdeling geconstrueerd. Daarna wordt de verdeling gewijzigd door achtereenvolgens uit elk interval een wandelaar te verplaatsen naar een aanliggend interval. Na elke wandelaarsverplaatsing wordt de energiefunctieaal $E_v[n]$ vergeleken met de waarde van de vorige verdeling en de nieuwe verdeling wordt aanvaard of verworpen afhankelijk van het energieverval. De tweede en derde stap worden herhaald totdat in een voldoende aantal iteraties geen lagere energie gevonden wordt. Met deze DFMC methode berekenden we de grondtoestandsdichtheid en werkfunctie van nanoschillen met verschillende permittiviteiten in de kern en de omgeving en met verschillende

afmetingen. Hiervoor gebruikten we een model zonder externe potentiaal, waarin de interactie tussen de geleidingselektronen in de schil met een homogeen neutralizerende achtergrond en met elkaar leidt tot een zelf-consistente potentiaal waardoor de elektronen voornamelijk in de schil voorkomen. De berekende elektrondichtheid en effectieve potentiële energie in kleine nanoschillen vertonen goede overeenkomst met de resultaten van Kohn-Sham berekeningen. De waarden voor de werkfunctie van nanoschillen berekend met DFMC zijn iets hoger dan de waarden resulterend uit orbitaalvrije berekeningen aan een vlak gouden oppervlak, zoals te verwachten is voor ingeperkte systemen. De resultaten voor nanoschillen met verschillende permittiviteiten in de kern en de omgeving tonen aan dat het grootste effect van afscherming voortkomt van de uitwisselingsbijdrage en dat het effect van het afschermen van de correlatiebijdrage verwaarloosbaar is. Om het effect van de schildikte op de werkfunctie te kunnen onderzoeken zouden een aantal verfijningen moeten doorgevoerd worden om een hogere nauwkeurigheid te verkrijgen dan diegene die bereikt werd in de getoonde berekeningen.

Deze thesis levert twee besluiten betreffende het berekenen van de grondtoestandseigenschappen van SiO_2 -Au nanoschillen met afmetingen die op dit ogenblik fabricerbaar zijn. Het eerste besluit is dat het praktisch niet haalbaar is om dit doel te bereiken met orbitaalgebaseerde berekeningen. Het tweede besluit is dat de nieuw ontwikkelde dichtheidsfunctionaal Monte Carlo methode betere perspectieven biedt om dit te doen.

List of publications and award

Journals

Peer-reviewed

- K. Putteneers, F. Brosens, *Monte Carlo implementation of density-functional theory*, Phys. Rev. B **86**, 085115 (2012); doi: 10.1103/PhysRevB.86.085115
- N. Van den Broeck, K. Putteneers, J. Tempere, I. Silvera, *Nanoshells as a high-pressure gauge analyzed to 200 GPa*, J. Appl. Phys. **110**, 114318 (2011); doi: 10.1063/1.3665649

Other

K. Putteneers, *Density-functional Monte Carlo for calculating properties of nanosystems*, $B\Phi$, Belgian Physical Society Magazine, nr. 3 (2011)

Conference proceedings

- Poster “Density-functional Monte Carlo for calculating properties of nanosystems” and gong show (10 min) “A Monte Carlo implementation of density-functional theory”, Two days of theoretical and mathematical physics (Flanders), Koksijde (08-09/06/2012)
- Poster and gong show (3 min) “Density-functional Monte Carlo for calculating properties of nanosystems”, Two days of theoretical and mathematical physics (Flanders), Koksijde (27-28/05/2011)
- Poster “Density-functional Monte Carlo for calculating properties of nanosystems”, General Scientific Meeting of the Belgian Physical Society, Namur (25/05/2011)
- Poster “Nanoshells: calculation of the work function using non-standard methods”, Nanometa 2011, Seefeld, Austria (03-06/01/2011)
- Lecture “Nanoshells: introduction and biomedical applications” and poster “Electrons in a nanoshell ready to get excited”, Condensed Matter Theory (CMD) 23, Warschau, Polen (29/08/2010-02/09/2010)
- Poster and gong show (3 min) “Electrons in a nanoshell ready to get excited”, Two days of theoretical and mathematical physics (Flanders), Koksijde (28-29/05/2010)
- Poster “Electrons in a nanoshell ready to get excited”, ‘Fysica 2010’ - Dutch and Belgian Physical Society, Utrecht, Nederland (23/04/2010)
- Poster “Non-interacting electrons in a nanoshell”, Joint general scientific meeting- Belgian Physical Society and Belgian Biophysical Society, Hasselt (01/04/2009)

Mentor of a master thesis

N. Van den Broeck, *Metallische nanoschillen op een zonnecel - Metallic nanoshells on a solar cell*, master thesis, supervisor: Prof. dr. J. Tempere, mentor: K. Putteneers

Award

Second place of the European Physical Journal Best Poster Contest for the poster “Density-functional Monte Carlo for calculating properties of nanosystems”, awarded at the meeting of the Belgian Physica Society in Namur on May 25, 2011. This poster can be viewed at <http://www.ua.ac.be/main.aspx?c=.TQC&n=97200>.

Dankwoord

Ik bedank iedereen liever persoonlijk want het blijkt onmogelijk voor mij om dat op een blaadje papier te doen. Iets dat enigzins mogelijk is, is om een beperkte lijst te geven van mensen die mij altijd zijn blijven steunen en vaak meer begrip toonden voor mijn beperktheid dan ikzelf. Ik heb het ontzettende geluk dat ik gedurende al die jaren zowel een toffe werkomgeving als een fijne familie- en vriendenkring had. In alfabetische volgorde ziet de beperkte lijst er uit als volgt:

- collega's en ex-collega's van TQC/WN: Ben, Damiaan, Dries, Enya, Erik, Giovanni, Hamed, Jeroen, Linghzi, Maarten, Nick, Selma, Serghei, Stijn, Tobias, Vladimir, Wim
- mijn echtgenoot Wim
- familie: mijn ouders Gie en Ingrid, mijn broer Bram en zijn vriendin Anne, mijn grootouders Pam en Simone, mijn schoonouders Francis en Maria, mijn schoonzussen Annemie en Marleen en co., mijn tantes en nonkels, neven en nichten
- de Heilige Rita
- professoren van TQC/WN: Prof. dr. Jozef Devreese, Prof. dr. Jan Naudts, Prof. dr. Michiel Wouters
- promotoren: Prof. dr. Fons Brosens, Prof. dr. Jacques Tempère
- vrienden: mijn beste vriendin Sandrien (die echt bestaat) en alle andere vrienden die nog niet genoemd zijn: An, Bieke, Eva, Evi, Geert, Liesbeth, Petra, ...

Alle andere mensen die ik in de loop van de jaren heb ontmoet, bedank ik voor leuke en interessante babbels.

Tijdens mijn doctoraat zijn een aantal anekdotes en gewoontes ontstaan. Om de herinnering eraan niet verloren te laten gaan, worden ze hier in trefwoorden vermeld: attack of the clones, bamilezingen, bevallen tijdens verdediging, Boston's topattractie = eekhoortjes voeren, meest controversiële thesisverdediging, grafeenkikker, ijsberg die pinguïns wil waarschuwen, imaginaire vriendin, Jasper computervirus, Katrijn is een kip, Kittel in de koelkast, lelijk hemd, logo TQC, Monoke, noemen, poezenkalender, proffen slaan, rekkertjes verzamelen, de rol van de Schelde, trouwkleregesprek (?) met mannelijke fysici, verborgen camera, vergeten worden, wit eten.

Appendix A

Regarding part II - Orbital-based calculations

A.1 Radial wave function in the free-of-charge region

A.1.1 Introduction

In the free-of-charge region (i.e., outside the nanoshell at distances where the electron density is negligible) the piecewise radial Schrödinger equation has the form

$$\frac{d^2 f(r)}{dr^2} + \frac{2}{r} \frac{df(r)}{dr} + \left[-A + \frac{B}{r} - \frac{\ell(\ell+1)}{r^2} \right] f(r) = 0 \quad (\text{A.1})$$

with ℓ the angular quantum number which has integer values. The parameters A and B are related to physical quantities of the problem as

$$\begin{aligned} A &= \lambda_F^2 = 2|\epsilon| \\ B &= 2Q' = 2 \frac{Q_{\text{tot}}}{\epsilon_E} \end{aligned}$$

with ϵ the single-electron energy, Q_{tot} the total charge in the system and ϵ_E the permittivity of the environment.

We looked into the derivation of solutions of equation (A.1) to check the conditions for the continued fractions that we used to implement the Whittaker function.

In the following sections we first discuss the solutions of this differential equation because we did not find much information in the literature and we face the special case that ℓ is an integer. We also discuss the limiting behavior of the solutions as $r \rightarrow \infty$ in order to decide which solution can be used to represent the piecewise radial wave function in the free-of-charge region.

A.1.2 Solutions of the radial differential equation

Derivation

For the second order differential equation (A.1) we have to find two linearly independent solutions, regardless the value of ϵ : the value of the energy will be determined by imposing boundary conditions. We now look for two solutions of this differential equation that are linearly independent for all values of A and B .

The direct series solution in which we set

$$f(\alpha, r) = r^\alpha \sum_{k=0}^{\infty} c_k r^k \text{ with } c_0 \neq 0$$

leads to the solutions

$$f(r) = \begin{cases} r^\ell \sum_{k=0}^{\infty} c_k r^k & \text{with } c_k = \frac{-Bc_{k-1} + A^2 c_{k-2}}{(2\ell+1+k)_k} \\ r^{-\ell-1} \sum_{k=0}^{\infty} c_k r^k & \text{with } c_k = \frac{-Bc_{k-1} + A^2 c_{k-2}}{k(-2\ell-1+k)} \end{cases}.$$

The second solution is in general not bounded for ℓ a positive integer because the denominator of $c_{2\ell+1}$ is equal to zero. Finding a solution that is linearly independent of the first one is not that easy if the three-term recurrence relation is used.

A two-term recurrence relation can be obtained if we factorize out the behavior of the solution near the essential singularity $r \rightarrow \infty$ (see e.g. Ref. [76] p. 19). The two resulting solutions are

$$\begin{aligned} f_1(r) &= e^{-Ar} r^\ell \sum_{k=0}^{\infty} \frac{(\ell - \frac{B}{2A} + 1)_k}{k! (2\ell + 2)_k} (2Ar)^k \\ &= e^{-Ar} r^\ell M\left(\ell - \frac{B}{2A} + 1; 2\ell + 2; 2Ar\right) \\ &= \frac{1}{(2A)^{\ell+1}} \frac{\mathcal{M}_{\frac{B}{2A}, \ell + \frac{1}{2}}(2Ar)}{r} \\ f_{2, \text{ second attempt}}(r) &= e^{-Ar} r^{-\ell-1} \sum_{k=0}^{\infty} \frac{(-\frac{B}{2A} - \ell)_k}{k! (-2\ell)_k} (2Ar)^k \\ &= e^{-Ar} r^{-\ell-1} M\left(-\frac{B}{2A} - \ell; -2\ell; 2Ar\right) \\ &= \frac{1}{(2A)^\ell} \frac{\mathcal{M}_{\frac{B}{2A}, -\ell - \frac{1}{2}}(2Ar)}{r} \end{aligned} \tag{A.2}$$

with $(b)_k$ the Pochhammer symbol defined as $(b)_k = b(b+1)\dots(b+k-1) = \Gamma(b+k)/\Gamma(b)$, $M(a; c; x)$ a Kummer function and $\mathcal{M}_{\kappa, \mu}(x)$ a Whittaker function. The second solution is again not bounded in general. We thus still have to look for a second solution that is linearly independent of $f_1(r)$.

Two rather straightforward ways that are sometimes used to derive a second solution, cannot be applied. First of all, a transformation to a function with variable x for which $r = 1/x$, does not lead to a convergent series because $x = 0$ is an irregular singular point, except at $r = \infty$ (Ref. [80] p. 554). Furthermore, multiplying the series of $f_{2, \text{ second attempt}}(r)$ with the divergent factor, $(-2\ell)_{2\ell+1} = 1/\Gamma(-2\ell)$, leads to a solution that is linearly dependent on $f_1(r)$. We thus have to find another way.

A solution that is linearly independent of $f_1(r)$ can be derived by combining $f_1(r)$ and $f_{2, \text{ second attempt}}(r)$ and using the rule of l'Hôpital. The derivation is based on that of the Bessel function of the second kind $Y_n(x)$ with integer order n as given in Ref. [3] on p. 694 ff.

The linear combination

$$w\left(\ell - \frac{B}{2A} + 1; c; 2Ar\right) e^{-Ar} r^\ell = \left[\begin{array}{c} \frac{M\left(\ell - \frac{B}{2A} + 1; c; 2Ar\right)}{\Gamma\left(\ell - \frac{B}{2A} + 2 - c\right)\Gamma(c)} \\ - \frac{(2Ar)^{-2\ell-1} M\left(\ell - \frac{B}{2A} + 2 - c; 2 - c; 2Ar\right)}{\Gamma\left(\ell - \frac{B}{2A} + 1\right)\Gamma(2-c)} \end{array} \right] e^{-Ar} r^\ell$$

is just a linear combination of solutions if $c \neq 2\ell + 2$. But in $f_1(r)$ and $f_{2, \text{second attempt}}(r)$ the parameter c is equal to $c = 2\ell + 2$. In this case it seems that $w\left(\ell - B/(2A) + 1; c; 2Ar\right)$ is equal to zero but this appears not to be the case. We rewrite $w\left(\ell - B/(2A) + 1; c; 2Ar\right)$ with use of the relations [86]

$$\begin{aligned} \Gamma(x+1) &= x\Gamma(x) \\ \Gamma(x)\Gamma(1-x) &= \frac{\pi}{\sin(\pi x)} \end{aligned}$$

as

$$w\left(\ell - \frac{B}{2A} + 1; c; 2Ar\right) = \frac{\sin(c\pi)}{\pi} \frac{\left\{ \begin{array}{c} \Gamma\left(\ell - \frac{B}{2A} + 1\right)\Gamma(2-c)M\left(\ell - \frac{B}{2A} + 1; c; 2Ar\right) \\ - \left[\begin{array}{c} \Gamma\left(\ell - \frac{B}{2A} + 2 - c\right)\Gamma(c)(2Ar)^{-2\ell-1} \\ \times M\left(\ell - \frac{B}{2A} + 2 - c; 2 - c; 2Ar\right) \end{array} \right] \end{array} \right\}}{(1-c)\Gamma\left(\ell - \frac{B}{2A} + 2 - c\right)\Gamma\left(\ell - \frac{B}{2A} + 1\right)}.$$

Then in the limit $c \rightarrow 2\ell + 2$, the numerator and denominator of

$$\frac{w\left(\ell - \frac{B}{2A} + 1; c; 2Ar\right)}{\frac{\sin(c\pi)}{\pi}} = \frac{\pi \left[\frac{M\left(\ell - \frac{B}{2A} + 1; c; 2Ar\right)}{\Gamma\left(\ell - \frac{B}{2A} + 2 - c\right)\Gamma(c)} - \frac{(2Ar)^{-2\ell-1} M\left(\ell - \frac{B}{2A} + 2 - c; 2 - c; 2Ar\right)}{\Gamma\left(\ell - \frac{B}{2A} + 1\right)\Gamma(2-c)} \right]}{\sin(c\pi)}$$

tend to zero. We can then determine the limit of this ratio using the rule of l'Hôpital:

$$\lim_{c \rightarrow 2\ell+2} \frac{\pi w\left(\ell - \frac{B}{2A} + 1; c; 2Ar\right)}{\sin(c\pi)} = \pi \lim_{c \rightarrow 2\ell+2} \frac{\frac{d}{dc} w\left(\ell - \frac{B}{2A} + 1; c; 2Ar\right)}{\frac{d}{dc} \sin(c\pi)}.$$

It can be identified with the Kummer function $U(a; c; x)$ that is found in literature [1, 20, 76, 86]:

$$\begin{aligned} U\left(\ell - \frac{B}{2A} + 1; c; 2Ar\right) &= \frac{\pi}{\sin(c\pi)} \left[\begin{array}{c} \frac{M\left(\ell - \frac{B}{2A} + 1; c; 2Ar\right)}{\Gamma\left(\ell - \frac{B}{2A} + 2 - c\right)\Gamma(c)} \\ - \frac{(2Ar)^{-2\ell-1} M\left(\ell - \frac{B}{2A} + 2 - c; 2 - c; 2Ar\right)}{\Gamma\left(\ell - \frac{B}{2A} + 1\right)\Gamma(2-c)} \end{array} \right] \\ &= \frac{\Gamma(1-c)}{\Gamma\left(\ell - \frac{B}{2A} + 2 - c\right)} M\left(\ell - \frac{B}{2A} + 1; c; 2Ar\right) \\ &\quad + \left[\begin{array}{c} (2Ar)^{-2\ell-1} \Gamma(c-1) / \Gamma\left(\ell - \frac{B}{2A} + 1\right) \\ \times M\left(\ell - \frac{B}{2A} + 2 - c; 2 - c; 2Ar\right) \end{array} \right]. \end{aligned}$$

Executing the rule of l'Hôpital if $c = \mathbf{n}_1 + 1$ with $\mathbf{n}_1 \in \mathbb{N}$ leads to expressions (13.2.9) and (13.2.10) of [86]. The second solution $f_2(r)$ of the differential equation (A.1) can thus be written as (with $\mathcal{W}_{\kappa, \mu}(x)$ another Whittaker function) [86]

$$f_2(r) = e^{-Ar} r^\ell U\left(\ell - \frac{B}{2A} + 1; 2\ell + 2; 2Ar\right) = \frac{\mathcal{W}_{\frac{B}{2A}, \ell + \frac{1}{2}}(2Ar)}{r}. \quad (\text{A.3})$$

The solutions $f_1(r)$ and $f_2(r)$ are linearly independent if $Q'/\lambda_E \neq \mathbf{n} \in \mathbb{N}$. If $Q'/\lambda_E = \mathbf{n}$, they are linearly dependent and proportional to $f(r) = e^{-Q'r/\mathbf{n}} r^\ell L_{\mathbf{n}-\ell-1}^{(2\ell+1)}(2Q'r/\mathbf{n})$ with $L_p^{(\beta)}(x)$ an associated laguerre polynomial. A linearly independent solution $f_3(r)$ can in this case be found by applying the method of the reduced order (see e.g. Ref. [76] p. 11-12). This results in the expression

$$f_3(r) = \left[C_3 \int_0^r \frac{e^{2\frac{Q'}{\mathbf{n}}r}}{\left[r^{\ell+1} L_{\mathbf{n}-\ell-1}^{(2\ell+1)}\left(2\frac{Q'}{\mathbf{n}}r\right) \right]^2} dr + C_4 \right] f_1(\mathbf{n}, Q'; r) \quad (\text{A.4})$$

with C_3 and C_4 constants.

Conclusion

We have found for all values of the involved parameters two linearly independent solutions of the Schrödinger equation in the free-of-charge region that are bounded.

If $Q'/\lambda_E \neq \mathbf{n}$, the functions, denoted as $f_1(\lambda_F, Q'; r)$ and $f_2(\lambda_F, Q'; r)$, can be expressed as a series, with Kummer functions $M(a; c; x)$ or $U(a; c; x)$, and with Whittaker functions $\mathcal{M}_{\kappa, \mu}(x)$ or $\mathcal{W}_{\kappa, \mu}(x)$. With ℓ the angular quantum number, $\lambda_F = \sqrt{2|\epsilon|}$ with ϵ a single-particle energy and $Q' = Q_{\text{tot}}/\epsilon_E$ with Q_{tot} the total charge in the nanoshell and ϵ_E the permittivity of the environment, we have

$f_1(\lambda_F, Q'; r)$	$f_2(\lambda_F, Q'; r)$
$e^{-\lambda_F r} r^\ell \sum_{k=0}^{\infty} \frac{\left(\ell - \frac{Q'}{\lambda_F} + 1\right)_k}{k!(2\ell+2)_k} (2\lambda_F r)^k$	/
$e^{-\lambda_F r} r^\ell M\left(\ell - \frac{Q'}{\lambda_F} + 1; 2\ell + 2; 2\lambda_F r\right)$	$e^{-\lambda_F r} r^\ell U\left(\ell - \frac{Q'}{\lambda_F} + 1; 2\ell + 2; 2\lambda_F r\right)$
$\frac{\mathcal{M}_{\frac{Q'}{\lambda_F}, \ell + \frac{1}{2}}(2\lambda_F r)}{r}$	$\frac{\mathcal{W}_{\frac{Q'}{\lambda_F}, \ell + \frac{1}{2}}(2\lambda_F r)}{r}$

If $Q'/\lambda_E = \mathbf{n}$, the linearly independent functions are given by

$f_1(\lambda_F, Q'; r) \propto f_2(\lambda_F, Q'; r)$	$f_3(\lambda_F, Q'; r)$
$e^{-\frac{Q'}{\mathbf{n}}r} r^\ell L_{\mathbf{n}-\ell-1}^{(2\ell+1)}\left(2\frac{Q'}{\mathbf{n}}r\right)$	$\left[C_3 \int_0^r \frac{e^{2\frac{Q'}{\mathbf{n}}r}}{\left[r^{\ell+1} L_{\mathbf{n}-\ell-1}^{(2\ell+1)}\left(2\frac{Q'}{\mathbf{n}}r\right) \right]^2} dr + C_4 \right] f_1(\lambda_F, Q'; r)$

A.1.3 Limiting behavior as $r \rightarrow \infty$

Solution $f_1(\lambda_E, Q'; r)$

If $Q'/\lambda_E \neq \mathbf{n}$ the solution $f_1(\lambda_E, Q'; r)$ is not quadratically integrable if $r \rightarrow \infty$. If $Q'/\lambda_E = \mathbf{n}$, the solution is finite in this limit and $f_1(\lambda_E, Q'; r) \propto f_2(\lambda_E, Q'; r)$. The solution (A.4) that is linearly independent of this solution diverges as $r \rightarrow \infty$.

Solution $f_2(\lambda_E, Q'; r)$

This solution is finite if $r \rightarrow \infty$ for all values of the parameters [86]:

$$\lim_{r \rightarrow \infty} f_2(\lambda_E, Q'; r) = \lim_{r \rightarrow \infty} \frac{\mathcal{W}_{\frac{Q'}{\lambda_E}, \ell + \frac{1}{2}}(2\lambda_E r)}{r} \propto r^{\frac{Q'}{\lambda_E} - 1} e^{-\lambda_E r} \xrightarrow{r \rightarrow \infty} 0.$$

Conclusion

The only solution of differential equation (A.1) that is quadratically integrable as $r \rightarrow \infty$ for all values of the parameters is $f_2(r) = \mathcal{W}_{\frac{B}{2A}, \ell + \frac{1}{2}}(2Ar) / r$.

A.2 Implementation of the basis functions and their derivatives

In orbital-based calculations for a nanoshell the radial single-particle Schrödinger equation

$$\frac{1}{r^2} \frac{d}{dr} \left(r^2 \frac{d}{dr} \right) \mathbf{R}(r) + \left[2\epsilon - \left(2u_{\text{eff}}(r) + \frac{\ell(\ell+1)}{r^2} \right) \right] \mathbf{R}(r) = 0$$

has to be solved. In this equation, $\mathbf{R}(r)$ is the (unnormalized) single-particle wave function, ϵ the single-particle energy, $u_{\text{eff}}(r)$ the effective potential energy (consisting of a Hartree, an exchange and a correlation contribution) and ℓ the angular quantum number. In section 5.3.3 we described the Transfer Matrix Method to derive piecewise wave functions for different regions in some models that we considered for a nanoshell: an ideal Fermi gas in a spherically symmetric (in)finite potential well and interacting electrons moving in the field of a uniform background in the shell. In this appendix we explain how we have performed the implementation of some of the basis functions and of their derivative with respect to r which is needed in the recurrence relations and boundary conditions as explained in section 5.3.2. The basis functions we will discuss are the spherical Bessel functions $j_\ell(x)$ and $y_\ell(x)$, the modified spherical Bessel functions $i_\ell(x)$ and $k_\ell(x)$, and the Whittaker function $\mathcal{W}_{\kappa, \mu}(x)$.

We first briefly repeat in which context these functions occur.

The spherical Bessel functions $j_\ell(x)$ and $y_\ell(x)$ are used inside the infinite and finite spherically symmetric potential well if the centrifugal term is not approximated.

The modified spherical Bessel function of the first kind $i_\ell(x)$ occurs in the model of non-interacting fermions in a finite potential well and in the model of interacting electrons. It is used in the region $[0, r_O]$ in which the potential energy is constant and the centrifugal term cannot be approximated. In the case of the finite well $r_O = R_C$. The energy-dependent parameter in this region is $\lambda_O = \sqrt{2|\epsilon - u_C|}$ with u_C the constant potential in the interval $[0, r_O]$.

The modified spherical Bessel function of the third kind $k_\ell(x)$ is only used in the model of the finite potential well where it describes the wave function in the region $[R_S, \infty[$ in which the potential energy is a constant equal to $u_{\text{eff}}(r) = u_E$. This region is characterized by $\lambda_E = \sqrt{2|\epsilon - u_E|}$.

The Whittaker function $\mathcal{W}_{\kappa, \mu}(x)$ is only used in the model of interacting electrons where it describes the wave function in the “free-of-charge” region denoted as $[r_F, \infty[$. The energy-dependent parameter in this region is $\lambda_F = \sqrt{2|\epsilon|}$.

A.2.1 (Modified) spherical Bessel functions

Spherical Bessel functions

For the calculation of the spherical Bessel functions $j_\ell(x)$ and $y_\ell(x)$ and their derivatives we used the routine “sphbes” of Ref. [97].

Modified spherical Bessel functions

In the region of interest (small x -values for $i_\ell(x)$ and large x -values for $k_\ell(x)$) the standard routine for the modified Bessel functions quickly leads to underflow. Because it is not per se true that the normalized wave function in those x -values is equal to zero, it is better not to calculate the modified Bessel functions directly. We now discuss how this problem can be solved. The explanation is worked out for the case of forward recurrence, but it is analogous for the case of backward recurrence. In the recurrence relations “rescaled derivatives”, $i'_\ell(X)/i_\ell(X)$ and $k'_\ell(X)/k_\ell(X)$, and “rescaled modified Bessel functions”, $i_\ell(x)/i_\ell(X)$ and $k_\ell(x)/k_\ell(X)$ appear. How these are implemented is explained after the basic exposition.

The (unnormalized) wave function has the following form in the region that contains the origin:

$$R_O(r) = a_O u_1(0, \epsilon, r) = a_O i_\ell(\lambda_O r).$$

We set as initial value of a_O for the forward recurrence:

$$a_O = \frac{1}{i_\ell(\lambda_O r_O)}$$

so that $R_O(r_O) = 1$ and the values of the wave function in the core are calculated relative to the value at the shell boundary:

$$R_O(0 < r \leq r_O) = \frac{i_\ell(\lambda_O r)}{i_\ell(\lambda_O r_O)}$$

$$R_O(r = 0) = \begin{cases} \frac{1}{i_0(\lambda_O r_O)} & \ell = 0 \\ 0 & \ell > 0 \end{cases}.$$

It follows that the coefficients a_{j_O+1} and b_{j_O+1} in the interval with as lower bound r_O can be determined by using equations (5.9) and (5.12) as

$$a_{j_O+1} = \frac{u'_2(j_O + 1, \epsilon, r_O) - \lambda_O \frac{i'_\ell(\lambda_O r_O)}{i_\ell(\lambda_O r_O)} u_2(j_O + 1, \epsilon, r_O)}{D(j_O + 1, \epsilon, r_O)}$$

$$b_{j_O+1} = \frac{\lambda_O \frac{i'_\ell(\lambda_O r_O)}{i_\ell(\lambda_O r_O)} u_1(j_O + 1, \epsilon, r_{j_O+1}) - u'_1(j_O + 1, \epsilon, r_{j_O+1})}{D(j_O + 1, \epsilon, r_O)}$$

and the contribution to the normalization integral can be calculated from equation (5.24) as

$$\int_0^{r_O} |R_O(r)|^2 r^2 dr = \frac{r_O^3}{2} \left[\left(1 + \frac{\ell(\ell+1)}{\lambda_O^2 r_O^2} \right) - \left(\frac{i'_\ell(\lambda_O r_O)}{i_\ell(\lambda_O r_O)} + \frac{1}{\lambda_O r_O} \right) \frac{i'_\ell(\lambda_O r_O)}{i_\ell(\lambda_O r_O)} \right].$$

In these expressions $i'_\ell(x)$ denotes the derivative with respect to the argument, $i'_\ell(x) = di_\ell(x)/dx$. We will discuss below how the “rescaled derivative” $i'_\ell(X)/i_\ell(X)$ and the “rescaled modified Bessel function” $i_\ell(x)/i_\ell(X)$ are implemented.

For the boundary condition with the region which contains $r \rightarrow \infty$, we again only need the “rescaled derivative” of the basis function (equation (5.14)) which for $u_1(j_S, \epsilon, r) = k_\ell(\lambda_E r)$ becomes:

$$f_E(\epsilon) = \frac{u'_1(j_S - 1, \epsilon, R_S) - u_1(j_S - 1, \epsilon, R_S) \lambda_E \frac{k'_\ell(\lambda_E R_S)}{k_\ell(\lambda_E R_S)}}{u'_2(j_S - 1, \epsilon, R_S) - u_2(j_S - 1, \epsilon, R_S) \lambda_E \frac{k'_\ell(\lambda_E R_S)}{k_\ell(\lambda_E R_S)}} a_{j_S-1} + b_{j_S-1}$$

with j_S the index of the region outside the nanoshell. For the calculations of the piecewise wave function $R_E(r)$ and the normalization constant, it is useful to write the unnormalized wave function in the form

$$R_E(r) = b_E \frac{k_\ell(\lambda_E r)}{k_\ell(\lambda_E R_S)}.$$

The constant b_E can be defined from the continuity of the wave function at $r = R_S$ as $b_E = R_E(R_S) = a_{j_S-1} u_1(j_S - 1, \epsilon, R_S) + b_{j_S-1} u_2(j_S - 1, \epsilon, R_S)$. The contribution to the normalization integral can then be written as

$$\int_{R_S}^{\infty} |R_E(r)|^2 r^2 dr = b_E^2 \frac{R_S^3}{2} \left[\left(\frac{k'_\ell(\lambda_E R_S)}{k_\ell(\lambda_E R_S)} + \frac{1}{\lambda_E R_S} \right) \frac{k'_\ell(\lambda_E R_S)}{k_\ell(\lambda_E R_S)} - \left(1 + \frac{\ell(\ell+1)}{\lambda_E^2 R_S^2} \right) \right].$$

The implementation of the “rescaled derivative” $k'_\ell(\lambda_E R_S)/k_\ell(\lambda_E R_S)$ and the “rescaled modified Bessel function” $k_\ell(\lambda_E r)/k_\ell(\lambda_E R_S)$ are explained in the following paragraphs.

Calculation of the “rescaled derivatives” We wrote routines to calculate the “rescaled derivatives” $i'_\ell(X)/i_\ell(X)$ and $k'_\ell(X)/k_\ell(X)$ based on the routine “bessik” of Ref. [97] in which the modified Bessel function $I_\nu(x)$ and $K_\nu(x)$ and their derivatives $I'_\nu(x)$ and $K'_\nu(x)$ are calculated.

With the use of the relation between the modified spherical Bessel functions $z_\ell(x)$ and their “non-spherical” counterparts $Z_\ell(x)$:

$$\begin{aligned} z_\ell(x) &= \sqrt{\frac{\pi}{2x}} Z_{\ell+\frac{1}{2}}(x) \\ z'_\ell(x) &= \sqrt{\frac{\pi}{2x}} Z'_{\ell+\frac{1}{2}}(x) - \frac{z_\ell(x)}{2x}, \end{aligned} \tag{A.5}$$

the rescaled derivatives of the basis functions can be written as

$$\begin{aligned} \frac{i'_\ell(X)}{i_\ell(X)} &= \frac{I'_{\ell+\frac{1}{2}}(X)}{I_{\ell+\frac{1}{2}}(X)} - \frac{1}{2X} \\ \frac{k'_\ell(X)}{k_\ell(X)} &= \frac{K'_{\ell+\frac{1}{2}}(X)}{K_{\ell+\frac{1}{2}}(X)} - \frac{1}{2X}. \end{aligned}$$

To calculate the ratios $I'_{\ell+\frac{1}{2}}(X)/I_{\ell+\frac{1}{2}}(X)$ and $K'_{\ell+\frac{1}{2}}(X)/K_{\ell+\frac{1}{2}}(X)$ we have made use of intermediate steps in the routine “bessik” [97]. One of the intermediate steps provides directly what we need [98]:

$$f_\nu(X) \equiv \frac{I'_\nu(X)}{I_\nu(X)}.$$

So for calculating $I'_{\ell+\frac{1}{2}}(X)/I_{\ell+\frac{1}{2}}(X)$ we used the code of “bessik” upto the calculation of $f_\nu(X)$.

Another intermediate step in the routine “bessik” gives the ratio $K_{\nu+1}(X)/K_\nu(X)$. We used this piece of code to calculate $K_{\nu+1}(X)/K_\nu(X)$ and extended it to derive $K'_\nu(X)/K_\nu(X)$ which is equal to

$$\frac{K'_\nu(X)}{K_\nu(X)} = \frac{\nu}{X} - \frac{K_{\nu+1}(X)}{K_\nu(X)}.$$

This identity can be found by setting $\mathcal{Z}_\nu(X) = e^{i\pi\nu}K_\nu(X)$ in the recurrence relation [1, 86]

$$\mathcal{Z}'_\nu(X) = \mathcal{Z}_{\nu+1}(X) + \frac{\nu}{X}\mathcal{Z}_\nu(X)$$

from which

$$K'_\nu(X) = -K_{\nu+1}(X) + \frac{\nu}{X}K_\nu(X).$$

Calculation of the “rescaled modified Bessel functions” To calculate the “rescaled modified Bessel function” we have made use of relation (A.5) and the logarithm:

$$\begin{aligned} \frac{z_\ell(x)}{z_\ell(X)} &= \sqrt{\frac{X}{x}} \exp \left[\ln \left(\frac{Z_{\ell+\frac{1}{2}}(x)}{Z_{\ell+\frac{1}{2}}(X)} \right) \right] \\ &= \sqrt{\frac{X}{x}} \exp \left[\ln \left(Z_{\ell+\frac{1}{2}}(x) \right) - \ln \left(Z_{\ell+\frac{1}{2}}(X) \right) \right]. \end{aligned}$$

The function $\ln(Z_\nu(x))$ was calculated by modifying the routine “bessik” of Ref. [97] so that it returned the logarithm of $Z_\nu(x)$ instead of $Z_\nu(x)$ itself. Therefore we extensively used the following identities:

$$\begin{aligned} a &= s_a e^{l_a} \text{ with } \begin{cases} s_a = \text{signum}(a) \\ l_a = \log|a| \text{ if } s_a \neq 0; \text{ arbitrary, say 1, otherwise.} \end{cases} \\ c &= ab \rightarrow c = s_c e^{l_c} \text{ with } \begin{cases} s_c = s_a s_b \\ l_c = l_a + l_b \end{cases} \\ c = a + b \rightarrow c = s_c e^{l_c} \text{ with } &\begin{cases} s_c = s_a; l_c = l_a \text{ if } s_b = 0 \\ s_c = s_b; l_c = l_b \text{ if } s_a = 0 \\ s_c = 0; l_c = \text{arbitrary} \text{ if } s_a = -s_b \ \& \ l_a = l_b \\ s_c = s_M; l_c = l_M + \log(1 + s_a s_b \exp(l_m - l_M)) \end{cases} \\ &\text{with } \begin{cases} M = a; m = b \text{ if } l_b < l_a \\ M = b; m = a \text{ if } l_a < l_b \end{cases} \end{aligned}$$

A.2.2 Whittaker function $\mathcal{W}_{\kappa,\mu}(x)$

Because of the boundary conditions only basis function $u_1(j, \epsilon, r)$ is of interest in the free-of-charge region. This function is given by

$$u_1(j, \epsilon, r) = \begin{cases} \frac{\mathcal{W}_{\frac{Q'}{\lambda_F}, \ell + \frac{1}{2}}(2\lambda_F r)}{r} & \text{if } \frac{Q'}{\lambda_F} \notin \mathbb{N} \\ e^{-\frac{Q'}{p}r} r^\ell L_{p-\ell-1}^{(2\ell+1)}\left(2\frac{Q'}{p}r\right) & \text{if } \frac{Q'}{\lambda_F} = p \in \mathbb{N} \end{cases}$$

with $Q' = Q_{\text{tot}}/\epsilon_E$ with Q_{tot} the total charge in the system and ϵ_E the permittivity of the environment. The expression with the Laguerre polynomial is a special case of the expression with the Whittaker function so we only discuss the latter. Just like in the case of the modified spherical Bessel functions, a routine for the Whittaker function would lead to underflow for

values of the argument in which the normalized wave function is still substantial. In this section we explain how we have solved this problem for forward recurrence.

If the boundary condition in the smallest radius r_F of the free-of-charge region is written in the form as was given by equation (5.14), only the “rescaled derivative” has to be calculated:

$$f_F(\epsilon) = \frac{u'_1(j_F - 1, \epsilon, r_F) - u_1(j_F - 1, \epsilon, r_F) \frac{u'_1(j_F, \epsilon, r_F)}{u_1(j_F, \epsilon, r_F)}}{u'_2(j_F - 1, \epsilon, r_F) - u_2(j_F - 1, \epsilon, r_F) \frac{u'_1(j_F, \epsilon, r_F)}{u_1(j_F, \epsilon, r_F)}} a_{j_F-1} + b_{j_F-1}$$

with

$$\frac{u'_1(j_F, \epsilon, r_F)}{u_1(j_F, \epsilon, r_F)} = 2\lambda_F \frac{\mathcal{W}'_{\frac{Q'}{\lambda_F}, \ell + \frac{1}{2}}(2\lambda_F r)}{\mathcal{W}_{\frac{Q'}{\lambda_F}, \ell + \frac{1}{2}}(2\lambda_F r)} - \frac{1}{r}.$$

How we implemented the “rescaled derivative” of the Whittaker function will be explained after the exposition on how we calculated the unnormalized wave function.

To calculate the unnormalized wave function in the free-of-charge region we applied the following trick. Because of the continuity in the smallest radius r_F of the free-of-charge region, the unnormalized wave function in r_F can be written with the use of the basis functions in the last interval before the free-of-charge region:

$$\mathbf{R}_F(r_F) = a_{j_F} u_1(j_F, \epsilon, r_F) = a_{j_F-1} u_1(j_F - 1, \epsilon, r_F) + b_{j_F-1} u_2(j_F - 1, \epsilon, r_F).$$

With a good scaling of the coefficients a_j and b_j , the value $\mathbf{R}_F(r_F)$ has a size appropriate to the problem. Now we will derive an expression of the form

$$\mathbf{R}_F(r_j) \propto \mathbf{R}_F(r_{j-1}) \tag{A.6}$$

so that the wave function $\mathbf{R}_F(r_j)$ in radius $r_j > r_F$ can be calculated from the wave function $\mathbf{R}_F(r_{j-1})$ in radius r_{j-1} , with $\mathbf{R}_F(r_j) < \mathbf{R}_F(r_{j-1})$. This is somewhat more straightforward than using logarithms as we did for the modified spherical Bessel functions, see section A.2.1, and applying the logarithm would be of no use because for the Whittaker function there does not exist an analytical expression for the contribution to the normalization integral. To derive a relation like relation (A.6), we make use of the equalities

$$\begin{aligned} \frac{f'(x)}{f(x)} &= \frac{d}{dx} \ln f(x) \\ &\Downarrow \\ f(x) &= f(X) \exp\left(\int_X^x \frac{f'(y)}{f(y)} dy\right). \end{aligned}$$

The radial wave function in a point $r_j > r_F$ can thus be calculated from

$$\begin{aligned} \mathbf{R}_F(r_j > r_F) &= a_F \frac{\mathcal{W}'_{\frac{Q'}{\lambda_F}, \ell + \frac{1}{2}}(2\lambda_F r_j)}{r_j} \\ &= a_F \frac{\mathcal{W}'_{\frac{Q'}{\lambda_F}, \ell + \frac{1}{2}}(2\lambda_F r_{j-1})}{r_j} \exp\left(\int_{2\lambda_F r_{j-1}}^{2\lambda_F r_j} \frac{\mathcal{W}'_{\frac{Q'}{\lambda_F}, \ell + \frac{1}{2}}(x)}{\mathcal{W}_{\frac{Q'}{\lambda_F}, \ell + \frac{1}{2}}(x)} dx\right) \\ &\Downarrow \\ \mathbf{R}_F(r_j > r_F) &= \mathbf{R}_F(r_{j-1}) \frac{r_{j-1}}{r_j} \exp\left(\int_{2\lambda_F r_{j-1}}^{2\lambda_F r_j} \frac{\mathcal{W}'_{\frac{Q'}{\lambda_F}, \ell + \frac{1}{2}}(x)}{\mathcal{W}_{\frac{Q'}{\lambda_F}, \ell + \frac{1}{2}}(x)} dx\right). \end{aligned}$$

To calculate the integral in the exponent we used linear interpolation for the integrand. For the contribution to the normalization integral we used linear interpolation for the unnormalized wave function.

In the rest of this section we will deal with the most difficult problem of the determination of the piecewise radial wave function in the free-of-charge region and the only topic we have not discussed yet: the calculation of the “rescaled derivative” $\mathcal{W}'_{\kappa,\mu}(x)/\mathcal{W}_{\kappa,\mu}(x)$. For the calculation of this term we will make use of continued fractions (as is used in the routine “bessik” of Ref. [98] to calculate the ratio $I'_\nu(x)/I_\nu(x)$). A **continued fraction** has the form [20, 86]

$$\mathcal{C} = b_0 + \frac{a_1}{b_1 + \frac{a_2}{b_2 + \frac{a_3}{b_3 + \dots}}} = b_0 + \frac{a_1}{b_1 +} \frac{a_2}{b_2 +} \dots = b_0 + \underset{j=1}{\overset{\infty}{\text{K}}} \left(\frac{a_j}{b_j} \right) \quad (\text{A.7})$$

with a_j and b_j complex numbers and the condition

$$\forall j : a_j \neq 0. \quad (\text{A.8})$$

The approximation of the continued fraction by only taking into account the first q terms,

$$\mathcal{C}^{(q)} = b_0 + \underset{j=1}{\overset{q}{\text{K}}} \left(\frac{a_j}{b_j} \right) = \frac{A_q}{B_q},$$

is called the q 'th **approximant** or the q 't convergent for \mathcal{C} .

In what follows we derive two different continued fractions for the rescaled derivative, we compare the calculation of $\mathcal{W}'_{\kappa,\mu}(x)/\mathcal{W}_{\kappa,\mu}(x)$ based on these two continued fractions and finally we mention which one is to be preferred.

First continued fraction

Using expressions [86]

$$\begin{aligned} \frac{d^n}{dx^n} \left(e^{-\frac{1}{2}x} x^{-\mu-\frac{1}{2}} \mathcal{W}_{\kappa,\mu}(x) \right) &= (-1)^n e^{-\frac{1}{2}x} x^{-\mu-\frac{1}{2}n-\frac{1}{2}} \mathcal{W}_{\kappa+\frac{1}{2}n, \mu+\frac{1}{2}n}(x) \\ \frac{\mathcal{W}_{\kappa,\mu}(x)}{\sqrt{x} \mathcal{W}_{\kappa-\frac{1}{2}, \mu-\frac{1}{2}}(x)} &= 1 + \frac{v_1/x}{1+} \frac{v_2/x}{1+} \dots \text{ with } \begin{cases} v_{2i+1} = \frac{1}{2} + \mu - \kappa + i, \\ v_{2i} = \frac{1}{2} - \mu - \kappa + i \end{cases} \end{aligned}$$

with $i \in \mathbb{N}$, we can derive the following continued fraction for the rescaled derivative:

$$\frac{\mathcal{W}'_{\kappa,\mu}(x)}{\mathcal{W}_{\kappa,\mu}(x)} = \mathcal{C}_1 = -\frac{1}{2} + \frac{\mu + \frac{1}{2}}{x} - \frac{t_1/x}{1+} \frac{t_2/x}{1+} \dots \text{ with } \begin{cases} t_{2i+1} = -\kappa + \mu + \frac{1}{2} + i, \\ t_{2i} = -\kappa - \mu - \frac{1}{2} + i \end{cases}. \quad (\text{A.9})$$

The coefficients of the continued fraction as defined in (A.7) are in this case given by

$$\begin{aligned} b_0 &= -\frac{1}{2} + \frac{\mu + \frac{1}{2}}{x} \\ b_{j>0} &= 1 \\ a_1 &= -\frac{-\kappa + \mu + \frac{1}{2}}{x} \\ a_{j=2i} &= \frac{-\kappa - \mu - \frac{1}{2} + i}{x} \\ a_{j=2i+1} &= \frac{-\kappa + \mu + \frac{1}{2} + i}{x}. \end{aligned} \quad (\text{A.10})$$

This continued fraction can also be derived from

- 1) the relation between the Whittaker function $\mathcal{W}_{\kappa,\mu}(x)$ and the confluent hypergeometric function $U(a; c; x)$ given by [86] $\mathcal{W}_{\kappa,\mu}(x) = \exp(-x/2) x^{\mu+1/2} U(\mu - \kappa + 1/2, 1 + 2\mu, x)$,
- 2) formula (13.4.25) of Ref. [1] from which the following equality can be written down: $U'(a; c; x)/U(a; c; x) = 1 - U(a; c + 1; x)/U(a; c; x)$, and
- 3) the continued fraction (13.5.3-4) of Ref. [86] for $U(a; c; x)/U(a; c - 1; x)$.

The condition (A.8) for existence of the continued fraction with $\mu = \ell + 1/2$ is from expressions (A.10)

$$\begin{aligned} \kappa + \ell + 1 &\neq i & j \text{ even} \\ \kappa - (\ell + 1) &\neq i & j \text{ odd} \end{aligned} .$$

This condition is always fulfilled if $\kappa \neq p \in \mathbb{N}$. In the rare case that $\kappa = p \in \mathbb{N}$, the condition is only fulfilled for a certain number of approximants. The condition for j even is always satisfied for the first $2(p + \ell)$ approximants (for which $p + \ell + 1 < i$). The fulfillment of the condition for j odd can lead to a quicker breakdown. We distinguish the following two cases:

1. $p = \kappa < \ell + 1$: the condition for j odd is always fulfilled because $i \geq 0$. The continued fraction can be calculated up to the $2(p + \ell)$ 'th approximant.
2. $p \geq \ell + 1$: the condition for j odd is fulfilled up to the $[2(p - \ell) - 1]$ 'th approximant (for which $p - \ell - 1 < i$). Because the number of approximants that can be calculated for j even is bigger than the number of approximants that can be calculated for j odd, $2(p + \ell) > 2(p - \ell) - 1$, the condition for j odd is the most restrictive. The continued fraction can be calculated up to the $[2(p - \ell) - 1]$ 'th approximant.

Note that if $p \geq \ell + 1$, the series in $U(a; c; x)$ cuts down to a Laguerre polynomial, as in the case of the hydrogen atom. Then the ratio $\mathcal{W}'_{\kappa,\mu}(x)/\mathcal{W}_{\kappa,\mu}(x)$ is a ratio of polynomials where the polynomial in the numerator is of one order less than the polynomial in the denominator.

Second continued fraction

The second continued fraction can be derived by using the relations [1, 20, 86]

$$\begin{aligned} \mathcal{W}_{\kappa,\mu}(x) &= e^{-\frac{x}{2}} x^{\mu+\frac{1}{2}} U\left(\mu - \kappa + \frac{1}{2}; 2\mu + 1; x\right) \\ U(a - 1; c; x) &= (a - c + x) U(a; c; x) - xU'(a; c; x) \\ \frac{U(a; c; x)}{U(a + 1; c; x)} &= 2a - c + 2 + z - \mathop{\text{K}}_{j=1}^{\infty} \left(\frac{(a + j)(c - a - j - 1)}{c - 2a - 2j - x} \right). \end{aligned} \quad (\text{A.11})$$

We then find the following continued fraction for the rescaled derivative:

$$\frac{\mathcal{W}'_{\kappa,\mu}(x)}{\mathcal{W}_{\kappa,\mu}(x)} = \mathcal{C}_2 = -\frac{1}{2} + \frac{1}{x} \left[\kappa + \mathop{\text{K}}_{j=1}^{\infty} \left(\frac{\mu^2 - (\kappa + \frac{1}{2} - j)^2}{2(\kappa - j) - x} \right) \right] \quad (\text{A.12})$$

with the expressions for the coefficients a_j and b_j of the general form (A.7) of the continued fraction given by:

$$\begin{aligned} b_0 &= -\frac{1}{2} + \frac{\kappa}{x} \\ a_1 &= \frac{\mu^2 - (\kappa - \frac{1}{2})^2}{x} \\ b_{j>0} &= 2(\kappa - j) - x \\ a_j &= \mu^2 - \left(\kappa + \frac{1}{2} - j \right)^2. \end{aligned} \quad (\text{A.13})$$

The same continued fraction was derived in a different way in Ref. [20].

The condition (A.8) for existence of the continued fraction with $\mu = \ell + 1/2$ is now

$$\begin{aligned}\kappa - \ell &\neq j \\ \kappa + \ell + 1 &\neq j.\end{aligned}$$

This condition is again always fulfilled if $\kappa \neq p \in \mathbb{N}$. In the rare case that $\kappa = p \in \mathbb{N}$ the condition is again only fulfilled for a certain number of approximants, but now the situation is different than for the first continued fraction. The number of approximants is again determined by the relative magnitude of p and ℓ , but in this case we have the following possibilities:

1. $p = \kappa < \ell + 1$: because $j \geq 1$ the second condition is the most restrictive. The first $p + \ell$ approximants can be calculated.
2. $p \geq \ell + 1$: the first $p - \ell - 1$ approximants can be calculated.

About half of the number of approximants can be calculated as compared to the first continued fraction.

Remark

Although the construction of the solution of the differential equation in the approximation $u_{\text{eff}}(r) = -Q'/r$ makes use of the rule of l'Hôpital to evaluate the Whittaker function (see section A.1), it appears to be possible to fill in integer values for μ directly into the continued fractions.

Implementation and comparison

For the implementation of the rescaled derivative $\mathcal{W}'_{\kappa,\mu}(x)/\mathcal{W}_{\kappa,\mu}(x)$ based on the continued fractions, we used the modified Lentz's method (see e.g. Ref. [98] section 5.2 for an explanation of the method and a sketch of the algorithm). The algorithm is stopped if for a certain $j = J$ one has $\mathcal{C}^{(J)}/\mathcal{C}^{(J-1)} \simeq 1$. The result is thus the J -th approximant $\mathcal{C}^{(J)}$ of the continued fraction.

The relations between the parameters $\{\kappa, \mu, x\}$ of the Whittaker functions and the physical parameters of the problem (the total charge Q_{tot} , the permittivity of the environment ε_E , the single-electron energy ϵ , the angular quantum number ℓ and the smallest radius of the free-of-charge region r_F) are:

$$\mu = \ell + \frac{1}{2}; \quad \kappa = \frac{Q_{\text{tot}}}{\varepsilon_E \sqrt{2|\epsilon|}}; \quad x = 2\sqrt{2|\epsilon|r_F}.$$

The test values of κ, μ and x were constructed as follows:

- value for Q_{tot} and ε_E : for simplicity we have taken $Q_{\text{tot}} = 1$ and $\varepsilon_E = 1$ (these variables will have an order of magnitude equal to 1 in the considered problem);
- values for ℓ : we have taken the testing values $\ell = 0, \dots, 20$;
- values for r_F : the value for r_F is approximately equal to the value for R_S . Because R_S varies approximately between 40 nm en 120 nm, these values were also used for r_F . In atomic units this means that $r_F \simeq 700, \dots, 2300$;
- values for ϵ : the energy values were taken to be $|\epsilon| = 1/r_F$.

This analysis led to the use of the following Whittaker parameters for testing:

$$\begin{aligned}\kappa &\simeq \sqrt{\frac{r_F}{2}} \in [19, 34] \\ \mu &= \ell + \frac{1}{2} = 0.5, 1.5, \dots, 20.5 \\ x &\simeq 2\sqrt{2r_F} \in [75, 135].\end{aligned}$$

First, tests for $\kappa \notin \mathbb{N}$ were performed. The results of the continued fractions only differed in the sixth to eighth digit with each other and with results from Mathematica[®]. The calculations with \mathcal{C}_1 needed about two times more iterations than those with \mathcal{C}_2 before the stopping criterion $\mathcal{C}^{(j)}/\mathcal{C}^{(j-1)} \simeq 1$ was met and so the calculations with \mathcal{C}_2 are much faster than those with \mathcal{C}_1 .

The case $\kappa \in \mathbb{N}$ could cause problems because the continued fraction can only be calculated up to a certain approximant. That is why this case was tested separately to check whether in practice

- the continued fraction reaches convergence before it breaks down because for the j 'th approximant the condition $a_j \neq 0$ is not fulfilled.
- a possible break down leads to erroneous results.

The results were compared with results of Mathematica[®] in which the basis function was calculated as $\exp(-Q'r/p)r^\ell L_{p-\ell-1}^{(2\ell+1)}(2Q'r/p)$. The results only differed in the sixth to ninth digit. We conclude that a possible break down of the continued fraction does not lead to erroneous results so the continued fraction implementation can also be used for $\kappa \in \mathbb{N}$.

Choice of continued fraction

Because both continued fractions lead to comparable results and the calculations based on \mathcal{C}_2 are faster than those based on \mathcal{C}_1 , the implementation with \mathcal{C}_2 is to be preferred. The parameters of this continued fraction for $\mathcal{W}'_{\kappa,\mu}(x)/\mathcal{W}_{\kappa,\mu}(x)$ are

$$\begin{aligned} b_0 &= -\frac{1}{2} + \frac{\kappa}{x} \\ a_1 &= \frac{\mu^2 - \left(\kappa - \frac{1}{2}\right)^2}{x} \\ b_{j>0} &= 2(\kappa - j) - x \\ a_{j>1} &= \mu^2 - \left(\kappa + \frac{1}{2} - j\right)^2. \end{aligned}$$

Appendix B

Regarding part III - Orbital-free calculations

B.1 Hartree energy for spherically symmetric systems

To derive an expression for the Hartree energy $u_H(r)$ due to a spherically symmetric excess charge distribution $\rho_{exc}(r)$, we used the following key relations:

$$\left. \begin{array}{l} u_H(\mathbf{r}) = -\phi_H(\mathbf{r}) \\ \nabla\phi_H(\mathbf{r}) = -\mathbf{E}(\mathbf{r}) \end{array} \right\} \implies \nabla u_H(\mathbf{r}) = \mathbf{E}(\mathbf{r}) \quad (\text{B.1})$$

$$\mathbf{E}_k(r) = \frac{D(r)}{\varepsilon_k} \quad (\text{B.2})$$

$$\nabla \cdot \mathbf{D}(\mathbf{r}) = 4\pi\rho_{exc}(\mathbf{r}) \quad \text{Gauss's law} \quad (\text{B.3})$$

with $\phi_H(\mathbf{r})$ the Hartree (electrostatic) potential, $\mathbf{E}(\mathbf{r})$ the electric field, k the index of a layer of a given material of a spherically symmetric system, $\mathbf{E}_k(r)$ and $D_k(r)$ the electric field and displacement vector in layer k , ε_k the permittivity of the material of layer k and $\mathbf{D}(\mathbf{r})$ the displacement vector.

B.1.1 Expression for $u_H(r)$ as a double integral

We will first derive an expression for the displacement vector $D(r)$ and the electric field $E(r)$ in a spherically symmetric system using relations (B.3) and (B.2) and the appropriate boundary conditions. Afterwards we will derive an expression for the Hartree single-particle energy $u_H(r)$ from the derived expression for $E(r)$ using relation (B.1).

For a spherically symmetric system, Gauss's law (B.3) can be written as

$$\frac{1}{r^2} \frac{\partial [r^2 D(r)]}{\partial r} = 4\pi\rho_{exc}(r)$$

from which the following expression for the displacement vector can be found:

$$D(r) = 4\pi \frac{1}{r^2} \int_0^r r'^2 \rho_{exc}(r') dr' + \frac{c}{r^2} \quad (\text{B.4})$$

with c a constant. From relation (B.2), the electric field in layer k (so $k = 1$ for the core, $k = 2$ for the shell and $k = 3$ for the environment) is then given by

$$\mathbf{E}_k(r) = \frac{4\pi}{\varepsilon_k} \frac{1}{r^2} \int_0^r r'^2 \rho_{exc}(r') dr' + \frac{c}{\varepsilon_k r^2}.$$

The boundary conditions are the following:

$$\mathbf{E}(r=0) = 0 \quad (\text{B.5})$$

for a spherically symmetric system and [48]

$$D_S(R_C) - D_C(R_C) = 0 \quad (\text{B.6})$$

$$D_E(R_S) - D_S(R_S) = 0 \quad (\text{B.7})$$

for boundaries with external surface charge density σ_{ext} equal to zero, like for the interfaces of an unperturbed nanoshell. From the boundary condition (B.5) on the electric field in the origin it follows that $c = 0$ and so the electric field in the core is given by

$$\mathbf{E}_C(r) = \frac{4\pi}{\varepsilon_C} \frac{1}{r^2} \int_0^r r'^2 \rho_{exc}(r') dr'.$$

From the boundary conditions (B.6) and (B.7) we find eventually that the electric field in layer k is given by

$$\mathbf{E}_k(r) = \frac{4\pi}{\varepsilon_k} \frac{1}{r^2} \int_0^r r'^2 \rho_{exc}(r') dr'. \quad (\text{B.8})$$

Combining relation (B.1) with expression (B.8) gives

$$\frac{\partial u_H(r)}{\partial r} = \mathbf{E}(r) \Rightarrow u_H(r) = \int_0^r \mathbf{E}(r'') dr'' + C = \int_0^r \frac{4\pi}{\varepsilon(r'')} \frac{1}{r''^2} \int_0^{r''} \rho_{exc}(r') r'^2 dr' dr'' + C$$

with C a constant. We now choose the zero point energy at $r \rightarrow \infty$ which leads to the following expression for the Hartree single-particle energy as a double integral:

$$u_H(r) = -4\pi \int_r^{+\infty} \frac{1}{\varepsilon(r'')} \frac{1}{r''^2} \left(\int_0^{r''} \rho_{exc}(r') r'^2 dr' \right) dr''. \quad (\text{B.9})$$

The Hartree potential energy $u_H(r)$ is calculated in two steps: first the electric field $\mathbf{E}(r)$ is calculated and then $u_H(r)$ is calculated as the integral over the electric field:

$$\mathbf{E}_k(r) = \frac{4\pi}{\varepsilon_k} \frac{1}{r^2} \int_0^r \rho_{exc}(r') r'^2 dr' \implies u_H(r) = \int_{+\infty}^r \mathbf{E}(r') dr'.$$

The zero point of the potential energy was chosen such that $u_H(r \rightarrow \infty) = 0$. Now the calculations are performed on a finite mesh with maximum radius R_{\max} . In the case of a charge neutral system we can set $u_H(R_{\max}) = 0$ to start the ‘backward’ integration $\int_{+\infty}^r \mathbf{E}(r') dr'$. However, if the system is not charge neutral, then $u_H(R_{\max}) \neq 0$. Because the radius R_{\max} is chosen such that $\rho_{exc}(r > R_{\max}) = 0$, the value for the electric field for $r \geq R_{\max}$ is equal to

$$\mathbf{E}(r \geq R_{\max}) = \frac{4\pi}{\varepsilon_E} \frac{1}{r^2} \int_0^{R_{\max}} \rho_{exc}(r') r'^2 dr' = \frac{1}{\varepsilon_E} \frac{Q_{\text{tot}}}{r^2}$$

with Q_{tot} the total charge in the system. We thus find that the Hartree potential energy in the last mesh point R_{\max} is in general given by

$$u_H(R_{\max}) = \frac{Q_{\text{tot}}}{\varepsilon_E} \int_{+\infty}^{R_{\max}} \frac{1}{r'^2} dr' = -\frac{Q_{\text{tot}}}{\varepsilon_E} \frac{1}{R_{\max}}.$$

B.1.2 Expression for $u_H(r)$ as a sum of two single integrals

Expression (B.9) can be rewritten as a sum of two single integrals. This can be done by first interchanging the integration sequence, which leads to the expression

$$u_H(r) = -4\pi \left[\int_0^r \rho_{exc}(r') r'^2 \left(\int_{\varepsilon(r'')}^{\frac{1}{r'^2}} \frac{1}{r''^2} dr'' \right) dr' + \int_r^{\infty} \rho_{exc}(r') r'^2 \left(\int_{\varepsilon(r'')}^{\frac{1}{r'^2}} \frac{1}{r''^2} dr'' \right) dr' \right].$$

This sum of double integrals can be converted to a sum of single integrals by using the fact that in each layer the permittivity is a constant. Elementary algebra then yields the following expressions for $u_H(r)$:

- in the environment:

$$u_H^{(E)}(r) = -\frac{4\pi}{\varepsilon_E} \left(\frac{1}{r} \int_0^r \rho_{exc}(r') r'^2 dr' + \int_r^{\infty} \rho_{exc}(r') r' dr' \right)$$

- in the shell:

$$u_H^{(S)}(r) = -4\pi \left\{ \frac{1}{\varepsilon_S} \left(\frac{1}{r} \int_0^r \rho_{exc}(r') r'^2 dr' + \int_r^{R_S} \rho_{exc}(r') r' dr' \right) + \left(\frac{1}{\varepsilon_E} - \frac{1}{\varepsilon_S} \right) \frac{1}{R_S} \int_0^{R_S} \rho_{exc}(r') r'^2 dr' + \frac{1}{\varepsilon_E} \int_{R_S}^{\infty} \rho_{exc}(r') r' dr' \right\}$$

- in the core:

$$u_H^{(C)}(r) = -4\pi \left\{ \frac{1}{\varepsilon_C} \left[\frac{1}{r} \int_0^r \rho_{exc}(r') r'^2 dr' + \int_r^{R_C} \rho_{exc}(r') r' dr' \right] + \left(\frac{1}{\varepsilon_S} - \frac{1}{\varepsilon_C} \right) \frac{1}{R_C} \int_0^{R_C} \rho_{exc}(r') r'^2 dr' + \frac{1}{\varepsilon_S} \int_{R_C}^{R_S} \rho_{exc}(r') r' dr' + \left(\frac{1}{\varepsilon_E} - \frac{1}{\varepsilon_S} \right) \frac{1}{R_S} \int_0^{R_S} \rho_{exc}(r') r'^2 dr' + \frac{1}{\varepsilon_E} \int_{R_S}^{\infty} \rho_{exc}(r') r' dr' \right\}.$$

The expressions can easily be generalized to multiple-shell structures. With k the index of a material layer - so in the case of a single nanoshell $k_{\max} = 3$, $\{\varepsilon_1, \varepsilon_2, \varepsilon_3\} = \{\varepsilon_C, \varepsilon_S, \varepsilon_E\}$ and $\{R_1, R_2, R_3\} = \{R_C, R_S, +\infty\}$ - we can write the Hartree energy in layer k as:

$$u_H^{(k)}(r) = -4\pi \left\{ \frac{1}{\varepsilon_k} \left[\frac{1}{r} \int_0^r \rho_{exc}(r') r'^2 dr' + \int_r^{R_k} \rho_{exc}(r') r' dr' \right] + \sum_{k'=k}^{k_{\max}-1} \left[\left(\frac{1}{\varepsilon_{k'+1}} - \frac{1}{\varepsilon_{k'}} \right) \frac{1}{R_{k'}} \int_0^{R_{k'}} \rho_{exc}(r') r'^2 dr' + \frac{1}{\varepsilon_{k'+1}} \int_{R_{k'}}^{R_{k'+1}} \rho_{exc}(r') r' dr' \right] \right\}. \quad (\text{B.10})$$

B.2 Difference in Hartree energy ΔE_H

In section 9.3.4 we mentioned an expression for the difference ΔE_H in Hartree energy due to the move of a walker to an adjacent interval. An expression for the difference ΔE_H in Hartree energy due to the removal of a walker from the system was given in section 9.3.7. In this appendix the derivation of these expressions is provided.

B.2.1 Key formulas

The derivation of an expression for ΔE_H is quite straightforward if the following key formulas are collected.

We can make use of the specific implementation of the diffusion process with Bernoulli walkers. Denoting by J the lowest index of the interval in which the density has changed, we get for the new number of walkers $(N_w)'_j$ in interval j due to (re)moving of a number of walkers ΔN_w :

$$(N_w)'_J = (N_w)_J \pm \Delta N_w = (N_w)_J - \mathbf{sgn} \times \Delta N_w \quad (\text{B.11})$$

$$(N_w)'_{J+1} = (N_w)_{J+1} \mp \Delta N_w = (N_w)_{J+1} + \mathbf{sgn} \times \Delta N_w \quad (\text{B.12})$$

$$(N_w)'_{j \neq J, J+1} = (N_w)_{j \neq J, J+1} \quad (\text{B.13})$$

with

$$\mathbf{sgn} \equiv \begin{cases} -1 & \text{if move to left} \\ +1 & \text{if move to right} \end{cases} .$$

Now we know from expression (8.1) that

$$n_j = \frac{N}{N_w} \frac{(N_w)_j}{V_j}. \quad (\text{B.14})$$

Combining expressions (B.11), (B.12), (B.13) and (B.14) and using the uniform background approximation, we get the following useful identities for the change in excess charge density $\Delta \rho_j$ in interval j :

$$\Delta \rho_J = -\Delta n_J = -\mathbf{sgn} \times \frac{3}{4\pi} \frac{N}{N_w} \frac{\Delta N_w}{r_{J+1}^3 - r_J^3} = -\mathbf{sgn} \cdot \eta_J \Delta N_w \quad (\text{B.15})$$

$$\Delta \rho_{J+1} = -\Delta n_{J+1} = \mathbf{sgn} \times \frac{3}{4\pi} \frac{N}{N_w} \frac{\Delta N_w}{r_{J+2}^3 - r_{J+1}^3} = \mathbf{sgn} \cdot \eta_{J+1} \Delta N_w \quad (\text{B.16})$$

$$\Delta \rho_{j \neq J, J+1} = 0. \quad (\text{B.17})$$

The often encountered combination $A(\Delta \rho)_J + B(\Delta \rho)_{J+1}$ can then easily be written out as

$$A(\Delta \rho)_J + B(\Delta \rho)_{J+1} = -\mathbf{sgn} \times \frac{3}{4\pi} \frac{N}{N_w} \Delta N_w \left(\frac{A}{r_{J+1}^3 - r_J^3} - \frac{B}{r_{J+2}^3 - r_{J+1}^3} \right). \quad (\text{B.18})$$

For the integration over the energy density, in each interval the excess charge density $\rho_{exc}(r)$ is considered to be constant and for the Hartree potential energy $u_H(r)$ linear interpolation is used. Then the Hartree part of the energy functional takes on the following discretized form:

$$E_H[n(r)] = C_H \sum_{j=0}^{j_{\max}-1} \rho_j \left(u_j I_j^{(1)} + u_{j+1} I_j^{(2)} \right) \quad (\text{B.19})$$

with ρ_j the value of $\rho_{exc}(r)$ in the j -th interval, u_j the value of the single-particle Hartree energy $u_H(r)$ in mesh point j and

$$\begin{aligned} C_H &= -\frac{\pi}{6} \\ I_j^{(1)} &= (r_{j+1}^2 + 2r_j r_{j+1} + 3r_j^2) h_j \\ I_j^{(2)} &= (3r_{j+1}^2 + 2r_j r_{j+1} + r_j^2) h_j. \end{aligned}$$

In calculating the difference ΔE_H , the difference Δu_j in Hartree single-particle energy in mesh point j will appear. It is for the derivation of Δu_j that the formula (9.10), or (B.10), for $u_H(r)$ as a sum of single integrals comes into play. It is useful for the derivation that this expression is rewritten with obvious distinction between integral parts of the different layers. After reordering and discretizing we get for the Hartree energy in mesh point j (with square brackets [] around multiple lines referring to the same layer):

$$u_j^{(E)} = -4\pi \left\{ \begin{aligned} &\frac{1}{3r_j} \frac{1}{\varepsilon_E} \sum_{j_1=0}^{j_{RC}-1} \rho_{j_1} (r_{j_1+1}^3 - r_{j_1}^3) \\ &+ \frac{1}{3r_j} \frac{1}{\varepsilon_E} \sum_{j_1=j_{RC}}^{j_{RS}-1} \rho_{j_1} (r_{j_1+1}^3 - r_{j_1}^3) \\ &+ \left[\begin{aligned} &\frac{1}{3r_j} \frac{1}{\varepsilon_E} \sum_{j_1=j_{RS}}^{j-1} \rho_{j_1} (r_{j_1+1}^3 - r_{j_1}^3) \\ &+ \frac{1}{2} \frac{1}{\varepsilon_E} \sum_{j_1=j}^{j_{\max}-1} \rho_{j_1} (r_{j_1+1}^2 - r_{j_1}^2) \end{aligned} \right] \end{aligned} \right\} \quad (\text{B.20})$$

$$u_j^{(S)} = -4\pi \left\{ \begin{aligned} &\frac{1}{3} \left[\frac{1}{r_j} \frac{1}{\varepsilon_S} + \left(\frac{1}{\varepsilon_E} - \frac{1}{\varepsilon_S} \right) \frac{1}{R_S} \right] \sum_{j_1=0}^{j_1=j_{RC}-1} \rho_{j_1} (r_{j_1+1}^3 - r_{j_1}^3) \\ &+ \left[\begin{aligned} &\frac{1}{3r_j} \frac{1}{\varepsilon_S} \sum_{j_1=j_{RC}}^{j-1} \rho_{j_1} (r_{j_1+1}^3 - r_{j_1}^3) \\ &+ \frac{1}{2\varepsilon_S} \sum_{j_1=j}^{j_1=j_{RS}-1} \rho_{j_1} (r_{j_1+1}^2 - r_{j_1}^2) \\ &+ \left(\frac{1}{\varepsilon_E} - \frac{1}{\varepsilon_S} \right) \frac{1}{3R_S} \sum_{j_1=j_{RC}}^{j_1=j_{RS}-1} \rho_{j_1} (r_{j_1+1}^3 - r_{j_1}^3) \end{aligned} \right] \\ &+ \frac{1}{2\varepsilon_E} \sum_{j_1=j_{RS}}^{j_1=j_{\max}-1} \rho_{j_1} (r_{j_1+1}^2 - r_{j_1}^2) \end{aligned} \right\} \quad (\text{B.21})$$

$$u_j^{(C)} = -4\pi \left\{ \begin{aligned} &\left[\begin{aligned} &\frac{1}{3r_j} \frac{1}{\varepsilon_C} \sum_{j_1=0}^{j_1=j-1} \rho_{j_1} (r_{j_1+1}^3 - r_{j_1}^3) \\ &+ \frac{1}{2\varepsilon_C} \sum_{j_1=j}^{j_1=j_{RC}-1} \rho_{j_1} (r_{j_1+1}^2 - r_{j_1}^2) \end{aligned} \right] \\ &+ \frac{1}{3} \left(\begin{aligned} &\left(\frac{1}{\varepsilon_S} - \frac{1}{\varepsilon_C} \right) \frac{1}{R_C} \\ &+ \left(\frac{1}{\varepsilon_E} - \frac{1}{\varepsilon_S} \right) \frac{1}{R_S} \end{aligned} \right) \sum_{j_1=0}^{j_1=j_{RC}-1} \rho_{j_1} (r_{j_1+1}^3 - r_{j_1}^3) \\ &+ \left[\begin{aligned} &\frac{1}{2\varepsilon_S} \sum_{j_1=j_{RC}}^{j_1=j_{RS}-1} \rho_{j_1} (r_{j_1+1}^2 - r_{j_1}^2) \\ &+ \left(\frac{1}{\varepsilon_E} - \frac{1}{\varepsilon_S} \right) \frac{1}{3R_S} \sum_{j_1=j_{RC}}^{j_1=j_{RS}-1} \rho_{j_1} (r_{j_1+1}^3 - r_{j_1}^3) \end{aligned} \right] \\ &+ \frac{1}{2\varepsilon_E} \sum_{j_1=j_{RS}}^{j_1=j_{\max}-1} \rho_{j_1} (r_{j_1+1}^2 - r_{j_1}^2) \end{aligned} \right\}. \quad (\text{B.22})$$

B.2.2 Difference ΔE_H due to walker movement

In this section we calculate Δu_j and ΔE_H due to the move of one walker between the intervals J and $J + 1$.

Single-particle Hartree energy

The derivation of Δu_j due to the movement of one walker, $\Delta N_w = 1$, to a neighboring mesh point is straightforward with the use of expressions (B.17), (B.18), (B.20), (B.21) and (B.22). We show the derivation for j in one particular material layer and one particular value of J . The derivation for other values is completely analogous.

Let $J = j_{R_S} - 1$, so J is the index of the last interval in the shell and $J + 1$ is the index of the first interval in the environment, and let us have a look at the difference in Hartree energy in a mesh point in the shell. Using the relations (B.17) and (B.18) we then easily find from expression (B.21) that

$$\begin{aligned} \Delta u_{j;J=j_{R_S}-1}^{(S)} &= -4\pi \left\{ \left[+ \left(\frac{1}{\varepsilon_E} - \frac{1}{\varepsilon_S} \right) \frac{1}{3R_S} (r_{J+1}^3 - r_J^3) \right] \Delta \rho_J \right. \\ &\quad \left. + \frac{1}{2\varepsilon_E} (r_{J+2}^2 - r_{J+1}^2) \Delta \rho_{J+1} \right\} \\ &= \text{sgn} \times 3 \frac{N_e}{N_w} \left[+ \frac{1}{2} \left(\frac{1}{\varepsilon_S} \frac{r_{J+1}^2 - r_J^2}{r_{J+1}^3 - r_J^3} - \frac{1}{\varepsilon_E} \frac{r_{J+2}^2 - r_{J+1}^2}{r_{J+2}^3 - r_{J+1}^3} \right) \right]. \end{aligned}$$

Proceeding this way for all kinds of combinations for j and J , we find eventually the general expressions

$$\begin{aligned} (\Delta u)_{j \leq J} &= \text{sgn} \times (\Delta \mathcal{U})_J \\ &= \text{sgn} \times 3 \frac{N}{N_w} \left[+ \frac{1}{2} \left(\frac{1}{\varepsilon_{J+1}} \frac{r_{J+1}^2 - r_J^2}{r_{J+1}^3 - r_J^3} - \frac{1}{\varepsilon_J} \frac{r_{J+2}^2 - r_{J+1}^2}{r_{J+2}^3 - r_{J+1}^3} \right) \right] \quad (\text{B.23}) \\ (\Delta u)_{J+1} &= \text{sgn} \times (\Delta \mathcal{U})_{J+1} = \text{sgn} \times 3 \frac{N}{N_w} \frac{1}{\varepsilon_{J+1}} \left(\frac{1}{3r_{J+1}} - \frac{1}{2} \frac{r_{J+2}^2 - r_{J+1}^2}{r_{J+2}^3 - r_{J+1}^3} \right) \\ (\Delta u)_{j > J+1} &= 0. \end{aligned}$$

Hartree energy functional

Because the density changes only in interval J and $J + 1$, we have from expression (B.19)

$$\begin{aligned} \frac{1}{C_H} \Delta E_H [n(r)] &= \sum_{j=0}^{J-1} \rho_j \left((\Delta u)_j I_j^{(1)} + (\Delta u)_{j+1} I_j^{(2)} \right) \\ &\quad + \rho_J \left(u_J I_J^{(1)} + u_{J+1} I_J^{(2)} \right) - \rho'_J \left(u'_J I_J^{(1)} + u'_{J+1} I_J^{(2)} \right) \\ &\quad + \left[\begin{aligned} &\rho_{J+1} \left(u_{J+1} I_{J+1}^{(1)} + u_{J+2} I_{J+1}^{(2)} \right) \\ &- \rho'_{J+1} \left(u'_{J+1} I_{J+1}^{(1)} + u'_{J+2} I_{J+1}^{(2)} \right) \end{aligned} \right] \\ &\quad + \sum_{j=J+2}^{j_{\max}-1} \rho_j \left((\Delta u)_j I_j^{(1)} + (\Delta u)_{j+1} I_j^{(2)} \right). \end{aligned}$$

With use of the expressions (B.23) for the difference in Hartree single-particle energy and

$$u'_j = u_j - (\Delta u)_j,$$

we find after some rearranging that

$$\begin{aligned} \frac{1}{C_H} \Delta E_H [n(r)] &= \text{sgn} \times (\Delta \mathcal{U})_J \sum_{j=0}^{J-1} \rho_j \left(I_j^{(1)} + I_j^{(2)} \right) \\ &\quad + [(\Delta \rho)_J u_J + \text{sgn} \times \rho'_J (\Delta \mathcal{U})_J] I_J^{(1)} \\ &\quad + [(\Delta \rho)_J u_{J+1} + \text{sgn} \times \rho'_J (\Delta \mathcal{U})_{J+1}] I_J^{(2)} \\ &\quad + [(\Delta \rho)_{J+1} u_{J+1} + \text{sgn} \times \rho'_{J+1} (\Delta \mathcal{U})_{J+1}] I_{J+1}^{(1)} \\ &\quad + (\Delta \rho)_{J+1} u_{J+2} \cdot I_{J+1}^{(2)} \end{aligned}$$

If we now use the expressions (B.15) and (B.16), we finally get

$$\Delta E_H [n(r)] = \text{sgn} \times C_H \left[(\Delta \mathcal{U})_J S_J + \begin{pmatrix} [-\eta_J u_J + \rho'_J (\Delta \mathcal{U})_J] I_J^{(1)} \\ + [-\eta_J u_{J+1} + \rho'_J (\Delta \mathcal{U})_{J+1}] I_J^{(2)} \\ + [\eta_{J+1} u_{J+1} + \rho'_{J+1} (\Delta \mathcal{U})_{J+1}] I_{J+1}^{(1)} \\ + \eta_{J+1} u_{J+2} \cdot I_{J+1}^{(2)} \end{pmatrix} \right]$$

with S_j defined as

$$S_j = \sum_{j_1=0}^{j-1} \rho_{j_1} \left(I_{j_1}^{(1)} + I_{j_1}^{(2)} \right). \quad (\text{B.24})$$

Values of S_j and the single-particle Hartree potential energy u_j can be quickly updated after acceptance of a move by

$$\begin{aligned} S'_{J+1} &= S_{J+1} + \text{sgn} \times \eta_J \left(I_J^{(1)} + I_J^{(2)} \right) \\ S'_{j>J+1} &= S_{j>J+1} + \text{sgn} \times \eta_J \left(I_J^{(1)} + I_J^{(2)} \right) - \text{sgn} \times \eta_{J+1} \left(I_{J+1}^{(1)} + I_{J+1}^{(2)} \right) \end{aligned}$$

$$\begin{aligned} u'_{j \leq J} &= u_j - \text{sgn} \times (\Delta \mathcal{U})_J \\ u'_{J+1} &= u_{J+1} - \text{sgn} \times (\Delta \mathcal{U})_{J+1}. \end{aligned}$$

B.2.3 Difference ΔE_H due to walker removal

In this section we calculate Δu_j and ΔE_H due to the removal of ΔN_w walkers from interval J . The derivation is analogous as the derivation of the difference due to moving of a walker.

Single-particle Hartree energy

The solution for the three different possibilities for the location of J ,

- J in environment

$$\begin{aligned} \Delta u_{j>J}^{(E)} &= \frac{1}{r_j} \frac{1}{\varepsilon_E} \frac{N}{N_w} \Delta N_w \\ \Delta u_{j \leq J} &= \frac{3}{2\varepsilon_E} \frac{N}{N_w} \frac{r_{J+1}^2 - r_J^2}{r_{J+1}^3 - r_J^3} \Delta N_w, \end{aligned}$$

- J in shell

$$\begin{aligned}\Delta u_j^{(E)} &= \frac{1}{r_j} \frac{1}{\varepsilon_E} \frac{N}{N_w} \Delta N_w \\ \Delta u_{j>J}^{(S)} &= \frac{N}{N_w} \left[\frac{1}{\varepsilon_S} \frac{1}{r_j} + \left(\frac{1}{\varepsilon_E} - \frac{1}{\varepsilon_S} \right) \frac{1}{R_S} \right] \Delta N_w \\ \Delta u_{j\leq J} &= \frac{N}{N_w} \left[\frac{3}{2\varepsilon_S} \frac{r_{J+1}^2 - r_J^2}{r_{J+1}^3 - r_J^3} + \left(\frac{1}{\varepsilon_E} - \frac{1}{\varepsilon_S} \right) \frac{1}{R_S} \right] \Delta N_w,\end{aligned}$$

- J in core

$$\begin{aligned}\Delta u_j^{(E)} &= \frac{1}{r_j} \frac{1}{\varepsilon_E} \frac{N}{N_w} \Delta N_w \\ \Delta u_j^{(S)} &= \frac{N}{N_w} \left[\frac{1}{r_j} \frac{1}{\varepsilon_S} + \left(\frac{1}{\varepsilon_E} - \frac{1}{\varepsilon_S} \right) \frac{1}{R_S} \right] \Delta N_w \\ \Delta u_{j>J}^{(C)} &= \frac{N}{N_w} \left[\frac{1}{r_j} \frac{1}{\varepsilon_C} + \left(\frac{1}{\varepsilon_S} - \frac{1}{\varepsilon_C} \right) \frac{1}{R_C} + \left(\frac{1}{\varepsilon_E} - \frac{1}{\varepsilon_S} \right) \frac{1}{R_S} \right] \Delta N_w \\ \Delta u_{j\leq J} &= \frac{N}{N_w} \left[\frac{3}{2\varepsilon_C} \frac{r_{J+1}^2 - r_J^2}{r_{J+1}^3 - r_J^3} + \left(\frac{1}{\varepsilon_S} - \frac{1}{\varepsilon_C} \right) \frac{1}{R_C} + \left(\frac{1}{\varepsilon_E} - \frac{1}{\varepsilon_S} \right) \frac{1}{R_S} \right] \Delta N_w,\end{aligned}$$

can be summarized and generalized as

$$\Delta u_j^{(k)} = \frac{N}{N_w} \Delta N_w \left[\sum_{k'=k}^{k_{\max}-1} \left(\frac{1}{\varepsilon_{k'+1}} - \frac{1}{\varepsilon_{k'}} \right) \frac{1}{R_{k'}} + \begin{cases} \frac{3}{2\varepsilon_k} \frac{r_{J+1}^2 - r_J^2}{r_{J+1}^3 - r_J^3} & j \leq J \\ \frac{1}{\varepsilon_k} \frac{1}{r_j} & j > J \end{cases} \right] \quad (\text{B.25})$$

if j is located in layer k ; for a single nanoshell we still have $\{\varepsilon_1, \varepsilon_2, \varepsilon_3\} = \{\varepsilon_C, \varepsilon_S, \varepsilon_E\}$, $\{R_1, R_2, R_3\} = \{R_C, R_S, +\infty\}$ and $k_{\max} = 3$.

Hartree energy functional

The removal of ΔN_w walkers from interval J leads to a change $\Delta \rho_j$ in the excess charge density in the interval J only, but it leads to a change Δu_j in Hartree energy in all intervals as can be seen from expression (B.25). We then have

$$\begin{aligned}\frac{1}{C_H} \Delta E_H &= \sum_{j=0}^{J-1} \rho_j \left(I_j^{(1)} \Delta u_j + I_j^{(2)} \Delta u_{j+1} \right) \\ &\quad + \left[\rho'_J \left(I_J^{(1)} u'_J + I_J^{(2)} u'_{J+1} \right) - \rho_J \left(I_J^{(1)} u_J + I_J^{(2)} u_{J+1} \right) \right] \\ &\quad + \sum_{j=J+1}^{j_{\max}-1} \rho_j \left(I_j^{(1)} \Delta u_{j>J} + I_j^{(2)} \Delta u_{j+1>J} \right).\end{aligned}$$

By using the fact that $\Delta u_{j\leq J} = \Delta u_J$, the relation (B.15) between $\Delta \rho_j$ and ΔN_w , the definition (B.24) of S_j and with some rearranging of terms, we can rewrite this expression as

$$\Delta E_H = C_H \left[\begin{aligned} &\Delta u_J S_J + \sum_{j=J+1}^{j_{\max}-1} \rho_j \left(I_j^{(1)} \Delta u_{j>J} + I_j^{(2)} \Delta u_{j+1>J} \right) \\ &+ (-\text{sgn} \times \eta_J \Delta N_w u_J + \rho'_J \Delta u_J) I_J^{(1)} \\ &+ (-\text{sgn} \times \eta_J \Delta N_w u_{J+1} + \rho'_J \Delta u_{J+1}) I_J^{(2)} \end{aligned} \right].$$

Bibliography

- [1] Abramowitz M., Stegun I. A., *Handbook of mathematical functions*, 9th ed. (Dover Publications, Inc., New York, 1972)
- [2] Aden A. L., Kerker M., J. Appl. Phys. **22**, 1242 (1951)
- [3] Arfken G. B., Weber H. J., *Mathematical Methods for Physicists*, 5th. ed. (Harcourt/Academic Press, USA, 2001)
- [4] Ashcroft N. W., Mermin N. D., *Solid State Physics* (Saunders College, Philadelphia, Pennsylvania, 1976).
- [5] Atwater H. A., *The promise of plasmonics*, Scientific American.com (2007)
- [6] Atwater H. A., Polman A., Nature Materials **9**, 205 (2010)
- [7] Averitt R. D., Sarkar D., Halas N. J., Phys. Rev. Lett. **78**, 4217 (1997)
- [8] Bachelier G., Mlayah A., Phys. Rev. B **69**, 205408 (2004)
- [9] Baer B. J., Chang M. E., Evans W. J., J. Appl. Phys. **104**, 034504 (2008)
- [10] Bardhan R., Lal S., Joshi A., Halas N. J., Acc. Chem. Res. **44**, 936 (2011)
- [11] Barnes W. L., Dereux A., Ebbesen T. W., Nature **424**, 824 (2003)
- [12] Bohren C. F., Huffman D. R., *Absorption and scattering of light by small particles* (Wiley-VCH, Germany 2004), p.82-104.
- [13] Born M., Oppenheimer J. R., Ann. Physik **84**, 457 (1927); English translation by Blinder S.M. can be found at <http://www.ulb.ac.be/cpm/people/scientists/bsutclif/bornop.pdf> .
- [14] Boyd J., Medical News Today, June 22, 2004
- [15] Brongersma M. L., Nature materials **2**, 296 (2003)
- [16] Ceperley D., Phys. Rev. B **18**, 3126 (1978)
- [17] Ceperley D. M., Alder B. J., Phys. Rev. Lett. **45**, 566 (1980)
- [18] Chen N. H., Silvera I. F., Rev. Sci. Instrum. **67**, 4275 (1996)
- [19] Chijioke A., Nellis W. J., Soldatov A., Silvera I. F., J. Appl. Phys. **98**, 114905, (2005)
- [20] Cuyt A., Petersen V., Verdonk B., Waadeland H., Jones W. B., "*Handbook of continued fractions for special functions*", Chapter 16, Springer (Berlijn 2008)

- [21] De Greef T., *Breking van licht verstrooid aan nanoschillen op een silicium oppervlak - Refraction of scattered light from nanoshells on a Silicon surface*, bachelor thesis, supervisor: J. Tempere, mentor: N. Van den Broeck (Universiteit Antwerpen, 2011)
- [22] Dewaele A., Egert J. H., Loubeyre P., Le Toullec R., Phys. Rev. B **67**, 094112 (2003)
- [23] Dhara A.K., Ghosh S.K., Phys. Rev. A **35**, 442 (1987)
- [24] Dirac P. A. M., Proc. Cambridge Philos. Soc. **26**, 376 (1930)
- [25] Dreizler R. M., Gross E. K. U., *Density-functional theory, an approach to the quantum many-body problem* (Springer-Verlag, Berlin Heidelberg, 1990)
- [26] Driver K. P., Cohen R. E., Wu Z., Militzer B., Rios P. L., Towler M. D., Needs R. J., Wilkins J. W., Proc. Natl. Acad. Sci. USA **107**, 9519 (2010)
- [27] Dubrovinskaia N., Dubrovinsky L., Caracas R., Hanfland M., Appl. Phys. Letters **97**, 251903 (2010)
- [28] Dueck T., Scheuer J., Comput. Phys. **90**, 161 (1990)
- [29] Ekardt W., Phys. Rev. B **29**, 1558 (1984)
- [30] Eggert J.H., Goetel K. A., Silvera I. F., Appl. Phys. Letters **53**, 2489 (1988)
- [31] Evans W. J., Silvera I. F., Phys. Rev. B **57**, 14105 (1998)
- [32] Fermi E., Atti Accad. Naz. Lincei Rend. Cl. Sci. Fis. Mat. Natur. **6**, 602 (1927)
- [33] Fock V. A., Zeit. für Phys. **61**, 126 (1930)
- [34] Gell-Mann M., Brueckner K. A., Phys. Rev. **106**, 364 (1957)
- [35] Goodman A. M., Phys. Rev. **144**, 588 (1966)
- [36] Gray A., Mathews G. B., MacRobert T. M., *A treatise on Bessel Functions and their applications to physics*, 2nd edition, Dover Publications Inc, New York (1966)
- [37] Haes A. J., Van Duyne R. P., Anal. Bioanal. Chem. **379**, 920 (2004)
- [38] Halas N., Optics & Photonics News, August 2002, p. 26 (2002)
- [39] Hartree D. R., Proc. Cam. Phil. Soc. **24**, 89 (1928); Proc. Cam. Phil. Soc. **24**,111 (1928); Proc. Cam. Phil. Soc. **24**, 426 (1928)
- [40] Haynes W. M., ed., *CRC Handbook of Chemistry and Physics*, 92nd Edition (Internet Version 2012), CRC Press/Taylor and Francis, Boca Raton, FL (2012)
- [41] Hiep H. M., Science and technology of advanced materials **8**, 331 (2007)
- [42] Hirsch L. R., Gobin A. M., Lowery A. R., Tam F., Drezek R. A., Halas N. J., West J. L., Annals of biomedical engineering **34**, 15 (2006)
- [43] Ho Gregory S., Huang Chen, Carter Emily A., Current Opinion in Solid State and Materials Science **11**, 57 (2007)
- [44] Hohenberg P., Kohn W., PR **136**, B864 (1964)

- [45] Huang C., Carter E. A., Phys. Rev. B **85**, 045126 (2012)
- [46] IMEC (Interuniversitair Micro-Elektronica Centrum) annual report 2006
- [47] Jackson J. B., Westcott S. L., Hirsch L. R., West J. L., Halas N. J., Appl. Phys. Letters **82**, 257 (2003)
- [48] Jackson J. D., *Classical electrodynamics*, 2nd ed. (John Wiley & Sons, New York, 1975)
- [49] <http://www.earth.northwestern.edu/research/jacobsen/>
- [50] Jayaraman A., Rev. Mod. Phys **55**, 65 (1983)
- [51] Jin D., “A fermi gas of atoms”, PhysicsWorld (April 4, 2002)
- [52] Johnson P. B., Christy R. W., Phys. Rev. B **6**, 4370 (1972)
- [53] Kalele S., Gosavi S. W., Urban J., Kulkarni S. K., Current science **19**, 1038 (2006)
- [54] Kalele S. A., et al., Small **2**, 335 (2006)
- [55] Karasiev V. V., Sjostrom T., Trickey S. B., Phys. Rev. B **86**, 115101 (2012)
- [56] Khlebtsov B. N., Khanadeyev V. A., Ye Jian, Mackowski D. W., Borghs G., Khlebtsov N. G., Phys. Rev. B **77**, 035440 (2008)
- [57] Kirkpatrick S., Gelatt Jr. C. D., Vecchi M. P., Science **220**, 671 (1983)
- [58] Kittel C., *Introduction to solid state physics, fifth edition* (John Wiley & Sons, USA 1976) p.410
- [59] Kittel C., *Quantum theory of solids, second edition* (John Wiley & Sons, New York 1967)
- [60] Kohn W., Sham L. J., Phys. Rev. **140**, A1133 (1965)
- [61] Kohn W., in *Proceedings of the International School of Physics, “Enrico Fermi”*, Course LXXXIX, p.4 (1985)
- [62] Kohn W., Rev. Mod. Phys. **71**, 1253 (1999)
- [63] Kreuzer M. P., Analytical and Bioanalytical Chemistry **391**, 1813 (2008)
- [64] Kulkarni V., Nordlander P., private communication
- [65] Lal S., Link S., Halas N. J., Nature photonics **1**, 641 (2007)
- [66] Lal S., private communication (July 7, 2011)
- [67] Lang N. D., Kohn W., Phys. Rev. B **1**, 4555 (1970)
- [68] Lang N. D., Kohn W., Phys. Rev. B **3**, 1215 (1971)
- [69] Le F., Lwin N. Z., Halas N. J., Nordlander P., Phys. Rev. B **76**, 165410 (2007)
- [70] Lieb E. H., Liniger W., Phys. Rev. **130**, 1605 (1963)
- [71] Lindhard J., Kgl. Danske Videnskab. Selskab, Mat.-Fys. Medd. **28**, No. 8 (1954)
- [72] Magnus W., Schoenmaker W., JAP **88**, 5833 (2000)

- [73] Maier S. A., Atwater H. A., J. Appl. Phys. **98**, 011101 (2005)
- [74] Malynych S., Luzinov I., Chymanov G., J. Phys. Chem. B **106**, 1280 (2002)
- [75] Mao H. K., Xu J., Bell P. M., Journal of geophysical research **91**, 4673 (1986)
- [76] Mathews J., Walker R.L., *Mathematical methods of physics, second edition* (Addison-Wesley, New York, 1970)
- [77] Mermin N. D., Phys. Rev. **137**, A1441 (1965)
- [78] Metropolis N., Rosenbluth A.W., Rosenbluth M.N., Teller A.H., Teller E., J. Chem. Phys. **21**, 1087 (1953)
- [79] Mie G., Ann. Phys. **25**, 377 (1908)
- [80] Morse P. M., Feshbach H., *Methods of theoretical physics, part I* (McGraw-Hill Book Company, New York, 1953)
- [81] Moscato P., Fontanari J., Phys. Lett. A **146**, 204 (1990)
- [82] <http://www.nanospectra.com/> : the website of Nanospectra Biosciences Inc.
- [83] Nehl C. L., Grady N. K., Goodrich G. P., Tam F., Halas N. J., Hafner J. H., Nano Letters **4**, 2355 (2004)
- [84] Nelson J., *The physics of solar cells* (Imperial College Press, UK, 2007)
- [85] Neuhauser D., Pistinner S., Coomar A., Zhang Xu, Lu Gang, J. Chem. Phys. **134**, 144101 (2011)
- [86] NIST Digital Library of Mathematical Functions, <http://dlmf.nist.gov/>
- [87] Nordlander P., Prodan E., arXiv:cond-mat/0307289v1 [cond-mat.mtrl-sci]
- [88] Oldenburg S.J., Averitt R.D., Westcott S.L., Halas N.J., Chem. Phys. Lett. **288**, 243 (1998)
- [89] Parr R. G., Yang Weitao, *Density-functional theory of Atoms and Molecules*, part 16 of the International Series of Monographs on Chemistry (Oxford University Press, New York, 1989)
- [90] Perdew J. P., Zunger Alex, Phys. Rev. B **23**, 5048 (1981)
- [91] Perdew J. P., Wang Yue, Phys. Rev. B **38**, 12228 (1988)
- [92] Perdew J. P., Ruzsinszky A., Tao Jianmin, Staroverov V. N., Scuseria G. E., Csonka G. I., J. Chem. Phys. **123**, 062201 (2005)
- [93] Perdew J. P., Constantin L. A., Phys. Rev. B **75**, 155109 (2007)
- [94] Peuckert V., J. Phys. C **11**, 4945 (1978)
- [95] Piermarini G. J., Block S. J., Barnett J. D., Forman R. A., J. Appl. Phys., **46**, 2774 (1975)
- [96] Pino R., Markvoort A. J., Hilbers P. A. J., Physica B **325**, 149 (2003)

- [97] Press William H., Teukolsky Saul A., Vetterling William T., Flannery Brian P., *Numerical Recipes in Fortran 90: The Art of Parallel Scientific Computing*, Second Edition (Numerical Recipes Software, New York, 1996)
- [98] Press William H., Teukolsky Saul A., Vetterling William T., Flannery Brian P., *Numerical Recipes in Fortran 90: The Art of Parallel Scientific Computing*, Second Edition (Cambridge University Press, New York, 1996)
- [99] Prodan E., Nordlander P., J. Math. Phys. **42**, 3390 (2001); J. Math. Phys. **42**, 3407 (2001); J. Stat. Phys. **111**, 967 (2003)
- [100] Prodan E., Nordlander P., Chem. Phys. Lett. **349**, 153 (2001);
- [101] Prodan E., Nordlander P., Chem. Phys. Lett. **352**, 140 (2002);
- [102] Prodan E., Lee Allen, Nordlander P., Chem. Phys. Lett. **360**, 325 (2002)
- [103] Prodan E., Nordlander P., Halas N. J., Chem. Phys. Lett. **368**, 94 (2003)
- [104] Prodan E., Nordlander P., Nano Letters **3**, 543 (2003)
- [105] Prodan E., Nordlander P., Halas N. J., Nano Letters **3**, 1411 (2003)
- [106] Prodan E., *Theoretical investigations of the electronic structure and optical properties of metallic nanoshells*, PhD thesis (Proquest Information and Learning Company, Rice University, Houston, Texas 2003); <http://scholarship.rice.edu/handle/1911/18599>
- [107] Prodan E., Radloff C., Halas N. J., Nordlander P., Science **302**, 419 (2003)
- [108] Prodan E., Nordlander P., J. Chem. Phys. **120**, 5444 (2004)
- [109] Prudnikov A. P., Brychkov Yu A., Marichev O. I., *Integrals and series volume 2: special functions* (Gordon and Breach Science Publishers, Amsterdam 1992)
- [110] Radloff C., Halas N. J., Nano Letters **4**, 1323 (2004)
- [111] Rayford II C. E., Schatz G., Shuford K., Nanoscape **2**, 27 (2005)
- [112] Rotondo M., Rueda Jorge A., Ruffini Remo, Xue She-Sheng, Phys. Rev. C **83**, 045805 (2011)
- [113] Runge E., Gross E.K.U., Phys. Rev. Lett. **52**, 997 (1984)
- [114] Ruppin R., Phys. Rev. Lett. **31**, 1434 (1973)
- [115] Ruppin R., Phys.Rev. B **11**, 2871 (1975)
- [116] Shklyarefskii I. N., Pakhmov P. L., USSR optika i Spektroskopiya **34**, 163 (1973); also at <http://www.mit.edu/~6.777/matprops/gold.htm>.
- [117] Silvera I. F., Chijioke A. D., Nellis W. J., Soldatov A., Tempere J., Phys. Stat. Sol (b) **244**, 460 (2007)
- [118] Stakenborg T., Van Dorst B., private communication (2010)
- [119] Stober W., Fink A. Bohn E. J., Colloid Interface Sci. **26**, 62 (1968).

- [120] Stockman M. I., *Spacer as nanoscale quantum generator and ultrafast amplifier*, arXiv.org > Condensed matter > Mesoscale and nanoscale physics (2009)
- [121] Stratton J. A., *Electromagnetic theory* (McGraw-Hill book company, New York and London 1941), p.563-573
- [122] Svedendahl M., et al., *Nano Letters* **9**, 4428 (2009)
- [123] Thomas L. H., *Proc. Camb. Phil. Soc.* **23** (5), 542 (1927)
- [124] Van den Broeck N., *Metallische nanoschillen op een zonnecel - Metallic nanoshells on a solar cell*, master thesis, supervisor: J. Tempere, mentor: K. Putteneers (Universiteit Antwerpen, 2010); available at <http://www.ua.ac.be/main.aspx?c=.TQC&n=83691>
- [125] Van den Broeck N., Putteneers K., Tempere J., Silvera I. F., *J. Appl. Phys.* **110**, 114318 (2011)
- [126] Vinet P., Ferrante J., Rose J. H., Smith J. R., *Journal of geophysical research* **92**, 9319 (1987)
- [127] Wang Y. A., Carter E. A., Orbital-free kinetic energy density-functional, in: *Theoretical methods in condensed phase chemistry*, edited by S.D. Schwartz, within the series: Progress in theoretical chemistry and physics (Kluwer, New York, 2000)
- [128] Wang H., Brandl D. W., Le F., Nordlander P., Halas N. J., *Nano Lett.* **6**, 827 (2006)
- [129] Wang H., Brandl D. W., Nordlander P., Halas N. J., *Acc. Chem. Res.* **40**, 53 (2007)
- [130] Wang Y., et al., *Biosensors and Bioelectronics* **23**, 1166 (2008)
- [131] Wood D. M., *Phys. Rev. Lett.* **46**, 749 (1981)
- [132] Wong Kin, Vongehr S., Kresin V.V., *Phys. Rev. B* **67**, 035406 (2003)
- [133] Xu Bu-Xing, Rajagopal A. K., *Phys. Rev. A* **31**, 2682 (1985)
- [134] Yang J., Lee J., Kang J., Oh S. J., Ko H.-J., Son J.-H., Lee K., Suh J.-S., Huh Y.-M., Haam S., *Adv. Mater.* **21**, 4339 (2009)
- [135] Ye Jian, Van Dorpe P., Van Roy W., Lodewijks K., De Vlaminc I., *J. Phys. Chem. C* **113**, 3110 (2009)
- [136] Yokoo M., Kawai N., Nakamura K.G., Kondo K.-I., Tange Y., Tsuchiya T., *Phys. Rev. B* **80**, 104114 (2009)
- [137] Yonzon C. R., et al., *Spectroscopy* **22**, 42 (2007)
- [138] Zia R., Schuller J. A., Chandran A., Brongersma M. L., *Materials Today* **9**, 20 (2006)
- [139] Zhou H. S., Honma I., Komiyama H., Haus J. W., *Phys. Rev. B* **50**, 12052 (1994)